

Support Stability and
Strong Metal-Support Effects in Catalysis:
From Nanoparticles to Single Atoms

Fang Liu

The research in this thesis was performed at the Inorganic Chemistry and Catalysis group, Debye Institute for Nanomaterials Science, Utrecht University, the Netherlands.

ISBN: 978-90-393-7070-4

Layout and printing: Off Page, Amsterdam

Cover design: Fang/Off Page

Copyright © 2018 by Fang Liu. All rights reserved. No part of this thesis may be reproduced without prior permission of the author.

Activity, selectivity and stability (three colors of the ball in the cover) are three important parameters of supported catalysts (cat.). A good cat. plays a key role in green energy production.

Support Stability and
Strong Metal-Support Effects in Catalysis:
From Nanoparticles to Single Atoms

Dragerstabiliteit en
sterke metaal-dragereffecten in katalyse:
Van nanodeeltjes tot afzonderlijke atomen
(met een samenvatting in het Nederlands)

Proefschrift

ter verkrijging van de graad van doctor aan de Universiteit Utrecht op gezag van de rector
magnificus, prof. dr. H.R.B.M. Kummeling, ingevolge het besluit van het college voor
promoties in het openbaar te verdedigen
op maandag 17 december 2018 des middags te 4.15 uur

door

Fang Liu
geboren op 15 juli 1988 te Henan, China

Promotoren: Prof. dr. ir. B.M. Weckhuysen
Prof. dr. P.C.A. Bruijninx

This thesis was financially supported by the China Scholarship Council and the Netherlands Center for Multiscale Catalytic Energy Conversion (MCEC), an NWO Gravitation program funded by the Ministry of Education, Culture and Science of the government of the Netherlands.

Table of Contents

Chapter 1	General Introduction	7
Chapter 2	Silica Deposition Improves the Hydrothermal Stability of an Alumina Support During Glycerol Aqueous Phase Reforming	27
Chapter 3	Phase-Dependent Stability and Substrate-Induced Deactivation by Strong Metal-Support Interaction of Ru/TiO ₂ Catalysts for the Hydrogenation of Levulinic Acid	55
Chapter 4	Highly Stable Ru/ZrO ₂ Single Atom Catalysts: Structure, Genesis, Stability and Application in CO Oxidation	81
Chapter 5	ZrO ₂ Supported Noble Metal Catalysts: Influence of Isolated Atoms on Catalyst Performance	113
Chapter 6	Summary and Outlook	145
Appendix	Nederlandse Samenvatting	157
	List of Publications	165
	Acknowledgements	166
	Curriculum Vitae	169

1

General Introduction

1.1. Heterogeneous Catalysis and its Importance

In our society, catalysts, heterogeneous catalysts in particular, play a key role in many manufacturing processes, including the production of transportation fuels, plastics and pharmaceutical intermediates. A specific class of these heterogeneous catalysts consist of metal (oxide) nanoparticles stabilized by a high-surface-area support material.[1,2] Compared to homogeneous catalysts and biocatalysts, heterogeneous catalysts have several merits, major ones being their thermal and chemical stability and the fact that they can be easily separated from the reactants and reaction products. As a consequence, over 80% of our industrial chemical processes are conducted by using one or more heterogeneous catalyst (Fig. 1.1).[3,4]

In last two decades, the production of renewable chemicals and fuels from bio-based feedstocks has emerged as potential green alternatives for the manufacturing processes involving fossil resources.[5–7] Processes for biomass or platform molecules conversion are often run in the liquid phase at high temperature and pressure given the low volatility and high polarity of those substrates.[8,9] Again, supported metal catalysts are here preferred and extensively used for biomass conversion due to their high stability and ease of recyclability, allowing high temperature operating and regeneration conditions. Many of these catalysts contain expensive Pt group metals as active metal phase, materials that are widely used for hydrogenation, dehydrogenation, oxidation and catalytic reforming reactions, amongst others.[10–13] Given the low natural abundance of these precious metals, such catalysts are expensive and can be more precious than the reaction products they are able to produce. Indeed, the price of heterogeneous catalysts is often in a range of \$40-200/kg, whereas the price of commodity chemicals is in the order of \$1-2/kg. This price difference and overall economic considerations suggests that industrially viable catalysts need to produce at least over a 1000 times their own weight in product.[14] Therefore, the central task in catalysis research is to develop cost competitive

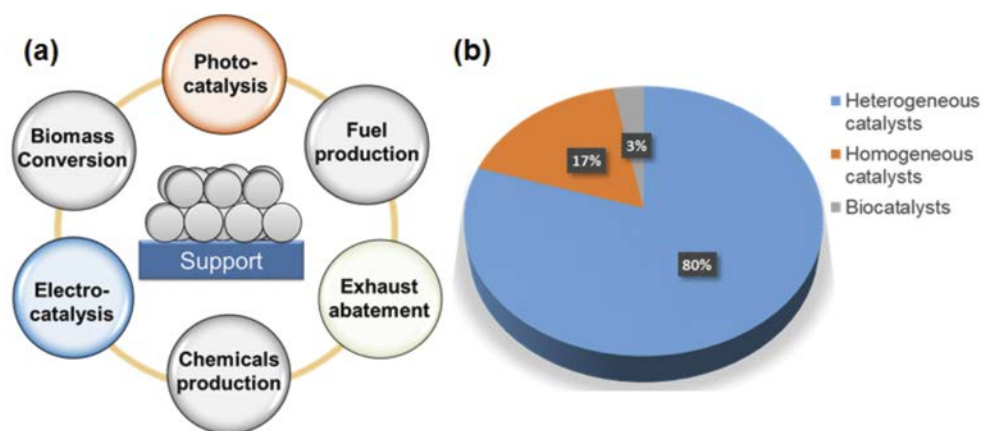


Fig. 1.1. (a) The various applications of heterogeneous catalysis, exemplified here by supported (noble) metal catalysts, and (b) the contribution of heterogeneous catalysis in comparison to other catalytic processes in industry.[4]

catalysts that are highly active, selective to a desired product and stable over sufficiently long periods of operation. However, development of such catalysts is not an easy task. Foremost, a good understanding of the parameters that control catalyst performance, such as particle size and support effects, as well as insight into the mechanisms of catalyst deactivation are crucial to develop stable, high-performing and cost-effective solid catalysts. As the work described in this thesis focuses on understanding the effects of metal dispersion, the interaction between metal and support and the (in)stability of metal oxide supports on catalyst performance, the deactivation of metal oxide supported precious metal catalysts, including by strong metal support interaction (SMSI), and the effect of catalyst morphology on catalyst performance are briefly discussed.

1.2. Different Modes of Catalyst Deactivation

In chemical industry, the lifetime of catalysts is an important parameter.[15] For industrial applications, an eligible catalyst should produce 10^3 - 10^4 times its own weight in product before it can be discarded. For example, a catalyst of moderate activity, e.g. $0.2 \text{ t}_{\text{product}}/\text{t}_{\text{catalyst}}/\text{h}$, would have to be stable under operating conditions for at least one year.[16] However, regardless of the window of operation, solid catalysts will eventually inevitably start to lose their activity with increasing time-on-stream, with rates of deactivation depending on the intrinsic properties of the catalyst material and on the severity of the process conditions applied. In the quest for the development of cost effective catalysts, deactivation should be postponed and, when activity is lost, deactivation is preferably reversible, allowing the catalyst material to be regenerated. Therefore, understanding the causes of catalyst deactivation is crucial. Here, we shortly discuss catalyst deactivation originating from coke deposition, metal sintering, active site poisoning as well as the structural change or collapse of the support oxide structure.

Coke formation. Coke formation is a very common cause for catalyst deactivation, in particular when processing fossil-based resources.[17] A recent review by Maraf *et al.* illustrated some examples of deactivation of noble metals containing catalysts as a result of coke formation in various hydroprocessing (HPR) applications, including hydrodenitrogenation, hydrodeoxygenation and hydrocracking (HCR) of tight oils and Fischer-Tropsch syn-crude.[12]



Fig. 1.2. Different modes of catalyst deactivation.

Also in the methanol-to-olefins process carbon deposition on the zeolite catalyst material is considered as one of the main reason for deactivation, as the large and inactive carbonaceous deposits formed lead to zeolite pore filling or/and surface coverage.[18,19] Likewise, coke deposition-induced deactivation is also found for dehydrogenation reactions. For example, Li *et al.* systemically investigated coke formation on a $\text{PtSn}/\text{Al}_2\text{O}_3$ catalyst used for propane dehydrogenation by extensive characterization of the deactivated catalyst.[20] Coke deposition was found to take place on both the metal phase and the support oxide, with the former being more in character and the latter more aromatic.[20]

Compared to the more conventional fossil feedstock, biomass and the bio-oils and platform molecules obtained therefrom typically have a high oxygen content and catalytic upgrading is needed to reduce this oxygen content to make them useful for practical applications, in particular when transportation fuel (additives) are targeted, but typically also for (commodity) chemicals production.[21] Such catalytic deoxygenation is particularly prone to coke formation on the catalyst surface as well, and is often the cause of activity loss. For example, Shao *et al.* attributed the deactivation of zeolite ZSM-5 seen in the catalytic deoxygenation of furfural, a major component present in bio-oil and important renewable platform molecule, to both active and inert coke formation, with the former still being an active participant in the reaction and the latter obviously causing the reduction in catalytic activity.[22] Wang *et al.* systemically investigated the deactivation of a sulfided Ru/C catalyst in the upgrading of bio-oil from pyrolysis of lignocellulosic biomass. X-ray photoelectron spectroscopy and thermogravimetric analysis confirmed that carbon deposition was the major form of deactivation of the sulfided Ru/C material, with 31 wt.% carbonaceous species being detected on the spent catalyst after 90 h treatment.[23]

Metal sintering. During catalytic reactions, the well-dispersed metal nanoparticles of solid catalysts are intrinsically thermodynamically unstable and indeed oftentimes tend to grow into larger metal nanoparticles. As catalysis is a surface phenomenon, the resulting loss of active metallic surface, a process known as sintering, is expected to lead to loss of catalytic activity. Naturally, as metal mobility is required, metal sintering is especially encountered for solid catalysts when exposed to high reaction temperatures.[24] Pham *et al.* demonstrated that a $\text{Pt}/\gamma\text{-Al}_2\text{O}_3$ catalyst suffered from continuous, irreversible deactivation in propane dehydrogenation at 600 °C, even though a regeneration step was applied between different catalytic runs to remove deposited coke. Indeed, the formation of large Pt nanoparticles was found to be the cause of the gradual loss of activity upon reuse.[25] Jones *et al.* also showed that a La-alumina-supported Pt catalyst lost its catalytic ability to convert CO into CO_2 after the system had been treated under diesel oxidation catalysis conditions at 800 °C, again due to the formation of large Pt crystallites.[26] Under such reaction conditions, metallic Pt can transform into volatile PtO_2 , causing the mobility of the supported Pt species,[27] which is also one of principal mechanisms of sintering apart from metal crystallite and atomic migration mechanisms.[28]

In addition to high temperature, this metal nanoparticle growth can also take place under more mild reaction conditions, for example in a water solution or in the presence of water

vapor.[29–31] For instance, a Ru/SiO₂ catalyst suffered from significant metal sintering upon treatment in a H₂-saturated water solution at 100 °C, leading to a 3 fold increase in Ru-Ru coordination number.[31] Abdelrahman *et al.* studied catalyst deactivation in the aqueous-phase hydrogenation of levulinic acid at 50 °C under 24 bar H₂ with water as solvent. The authors were able to discern both reversible and irreversible loss of activity for Ru supported on C, TiO₂, SiO₂ and Al₂O₃, with reversible deactivation being related to coke deposition and irreversible deactivation with Ru sintering.[32] Meng *et al.* evidenced a gradual activity loss for a Pd/Al₂O₃ catalyst upon reuse in the liquid phase decarbonylation of 5-hydroxymethylfurfural at 180 °C. TEM analysis of the reused catalyst confirmed that the Pd nanoparticle size had increased from 5.3 to 6.6 nm after three cycles of reaction.[33]

Active site poisoning. Rather than generic coverage and resulting inaccessibility of the active sites by deposition of coke, the performance of solid catalysts can also be impacted by selective poisoning by biogenic or process-derived impurities.[16] Such impurities can bind strongly to the active sites on a catalyst surface, thereby hindering the absorption of reactants. Sulfur species are notorious examples and have been shown to significantly impair the reactivity of many metal-based catalysts, including those of the platinum group metals. This can happen at very low impurity concentrations, in the case of S-containing species due to the formation of strong metal-S bonds. Besides, the formation of stable bonds between metal and an impurity adsorbate can also lead to undesired side reactions and catalyst deactivation.[15,34,35] Boga *et al.* investigated the influence of impurities present in crude glycerol feedstocks on the catalytic performance of Pt-based catalysts in the aqueous phase reforming of glycerol.[36] The authors found that the catalyst deactivated rapidly due to both reversible coke formation and the irreversible deposition of long-chain alkanes and olefins, side products originating from the fatty acid derivatives in the crude feedstock.[36] Contaminants introduced externally during upstream processing steps can also poison or foul a solid catalyst that is used further downstream in the overall production process. For example, levulinic acid can be obtained from different biomass sources, by hydrolysis/(de)hydration of the carbohydrate fraction using various mineral acids (e.g. HCl or H₂SO₄), with the latter being preferred due to its lower price. [37] Ftouni *et al.* demonstrated that minor amounts of a sulfuric acid impurity in the levulinic acid feed are enough to inhibit the catalytic activity of Ru/C in levulinic acid hydrogenation.[38]

Support destruction. In addition to changes to the active metal phase, loss of support integrity, for example by structure collapse, phase change, or surface modification, is also a common cause of irreversible catalyst deactivation. Changes in support morphology, crystallinity or composition can be expected in particular when catalytic reactions are run in the aqueous phase at elevated temperature and pressure, i.e. under hydrothermal conditions.[39] While metal oxides are often used as supports on the account of their good (thermal) stability, allowing high temperature operating and regeneration conditions, such metal oxides are often not inert in the presence of water and can, as function of pH, temperature, pressure and particular substrates offered, be attacked by water, something which may ultimately lead to structural changes. Calculated Pourbaix diagrams illustrating the stability windows for different (bulk) metal oxides in hot water at 200 °C, showing Al₂O₃, ZrO₂, SiO₂ appear to be unstable under demanding conditions,

with the first two supports tend to transform into the corresponding hydroxides and the latter into silica gel, respectively.[16] Aqueous Phase Reforming (APR) is a typical process to convert biomass-derived oxygenates to hydrogen and is performed under polar liquid-phase reaction conditions, oxidic supports such as γ -alumina, can be hydrated, leading to phase changes in the support and, as a result, deactivation.[40,41] The γ -alumina support in a $\text{Pt}/\text{Al}_2\text{O}_3$ catalyst is well-known to transform into boehmite under typical APR conditions, for instance. Indeed, Ravenelle *et al.* [42] demonstrated that when bare γ - Al_2O_3 was exposed to hot water, it completely converted into crystalline boehmite with a significant loss of surface area. During this process, supported metal particles can lose contact with their original binding sites leading to sintering or encapsulation, both of which are detrimental for catalyst activity.[42] Likewise, Jongerius *et al.* also reported similar phase transformation of an alumina support under typical liquid phase reforming condition, the presence of oxygenates, such as ethanol and guaiacol, can slow down the phase transformation process to some extent, but rehydration to boehmite was still observed after 1 h treatment.[43] Acidic supports such as silicate-alumina and zeolite are more stable than alumina, however, can still suffer from degradation as a result of Si-O-Si hydrolysis in hot liquid water.[44,45]

At elevated temperatures, the reducing conditions employed in both gas and liquid reduction/hydrogenation condition can in principle present another stability challenge for reducible oxides. Such support oxides can suffer from noble-metal mediated H spillover onto the support, resulting in surface reduction and support rearrangement and ultimately coverage of the metal nanoparticle by the support, a phenomenon described as Strong Metal Support Interactions (SMSI).[46–48] More often than not, the reduced support oxide overcoating of an active metal phase caused by the SMSI effect is considered detrimental and therefore best to be avoided. [49,50] Ko and Garten pointed out that TiO_2 supported group VIII metals always exhibited a much lower reactivity in ethane hydrolysis of up to several orders of magnitude compared to their SiO_2 counterparts as a result of SMSI formation caused by catalyst pre-reduction at 500 °C. Sa *et al.* demonstrated that the CO uptake ability of a Pd/TiO_2 catalyst decreased after H_2 reduction at 200 °C, attributing this to SMSI already at this temperature. Upon increasing the reduction temperature to 350 °C, a visible surface coating of the Pd particles by patches of a Ti_4O_7 phase was observed by TEM.[46]

The insights gained into the causes of catalyst deactivation serve as input for the development of more robust catalysts materials. For example, a protective layer deposition strategy has been demonstrated to be useful in limiting coking formation, metal sintering and support structure change.[51–53] Indeed, Pham *et al.* deposited a thin, sucrose-derived carbonaceous layer on fumed alumina and demonstrated that the carbon coating led to improved thermal stability.[51] Similarly, Xiong *et al.* found that the formation of a graphitic carbon layer on pelletized γ -alumina by chemical vapor deposition of methane can enhance catalyst thermal stability significantly.[54] Dumesic and co-workers demonstrated that metal sintering and leaching observed in furfural liquid hydrogenation can be suppressed significantly by porous Al_2O_3 layer deposition through atomic layer deposition method.[55] Alternatively, the stability of the catalysts against deactivation resulting from metal sintering or structural changes in

the support can be improved by doping the support with a various other element.[56,57] As for the active metal phase, promotion with an additional metal can aid stability, as shown for example by the addition of Sn to a Pt/Al₂O₃ catalyst, which helped to redisperse Pt nanoclusters back to small sub-nanoparticles by providing nucleation sites on the catalyst surface. As a result, high propene selectivity was observed in propane dehydrogenation together with a minimization of coke formation as a result of the reduced extent of unwanted side reactions.[25] In another example, ConocoPhillips showed that the use of dopants, such as silicon, cobalt, magnesium and others, is beneficial to enhance the hydrothermal stability of alumina-supported catalysts for Fischer-Tropsch Synthesis.[56,57] More research is still needed, however, to develop efficient strategies to improve catalyst stability without compromising activity and selectivity.

1.3. Size Effects of Supported Metal Nanoparticles on Catalyst Performance

As heterogeneous catalysis is a surface process, the nanoparticle size and shape of the metal in supported metal catalysts is expected to influence catalytic performance.[58–61] Numerous reviews are indeed available that illustrate the importance of nanoparticle size and shape on catalyst performance.[62–64] That control over the size of the supported metal nanoparticles can give rise to remarkable changes in catalytic behavior, is shown for example by gold-based catalysts. It is well known that gold is chemically inert in bulk, but can catalyze numerous chemical reactions under quite mild conditions if it is more highly dispersed at the nanoscale.[65–67] At the nanometer scale, generally three types of particle size-activity relationship can be discerned: (1) catalytic activity increases as metal particle size increases, (2) catalytic activity increases as metal particle size decreases, and (3) the activity is independent of metal particle size (Fig. 1.3).[68] Indeed, the overall increase in coordinative unsaturation that occurs upon downsizing the metal phase can be beneficial, but smaller is not always better, as certain sites required for some catalytic reaction are less or not available with smaller particles.

Many examples are nevertheless available of increasing catalyst reactivity and selectivity by downsizing the metal nanoparticles to increase the number of under-coordinated surface atoms.[69–71] For example, Vajda *et al.* demonstrated that small Pt clusters, consisting of 8-10 atoms and supported by high-surface-area supports, are 40-100 times more active than Pt- and V- based catalysts with extended metal surfaces in the oxidative dehydrogenation of propane, without compromising the high selectivity of propene production.[71] Wei *et al.* extensively studied the size/dispersion effect of Pt nanoparticles supported onto different oxides, such as ZrO₂, ZrO₂-CeO₂ and γ -Al₂O₃, for the oxidative reforming of methane.[72] The authors pointed out that the turnover frequency regarding methane conversion was governed by the dispersion of Pt rather than by the support type. More specifically, it was found that the activity increased with increasing Pt dispersion, i.e. decreasing Pt particle size. In addition to Pt catalysts, a similar size effect on turnover rates in methane reforming was also observed for other supported noble metals (i.e. Rh, Ir and Ru). This particle size-activity dependence was rationalized by the fact that the more coordinatively unsaturated single atoms active site are more prevalent in small

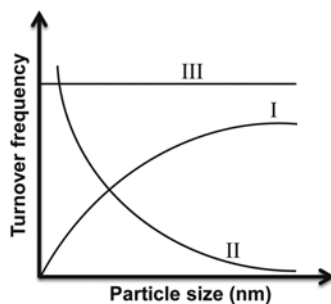


Fig. 1.3. Three types of particle size-performance relationship. The Figure is adapted from ref. [68].

metal nanoparticles significantly, leading to an increase in activity for the rate determining step (more specifically C-H bond activation) as compared to the those systems possessing low-index planes, which are predominately exposed in large metal nanocrystallites.[72] An extreme example of metal particle size downsizing is to have single, isolated atoms dispersed on a solid support, i.e. the limit of single atom catalysts (SAC). As will be discussed in Section 1.4, SACs indeed can show better catalytic performance than their nanoparticulate counterparts in various chemical reactions.[70,73–75]

On the other hand, a volcano-like size-activity dependence was reported by Liu *et al.* for the aerobic oxidation of cyclohexane to cyclohexanol and cyclohexanone using sub-2 nm Au supported by hydroxyapatite (Au_n/HAP , $n = 10, 18, 25, 39$ and 89).[21] The turnover frequency increased continuously from $n = 10$ up to $n = 39$, reaching a maximum turnover frequency of $18\,500\text{ h}^{-1}\text{ Au atom}^{-1}$, after which it dropped again for $n = 89$. [21] Likewise, Ojeda *et al.* reported a noticeable Rh particle size influence in CO hydrogenation to C_2 -oxygenates over a series of Rh/ $\gamma\text{-Al}_2\text{O}_3$. [76] The authors found that larger Rh particles were preferred to convert CO and the turnover frequency of the reaction increased fourfold when Rh particle size increased from 5 to 30 nm. [76] In general, previous reports suggest that activation a π bond in molecules such as CO, O_2 and N_2 requires double step-edge sites and therefore, bigger metal particles are required for those molecules dissociation. [68,77]

The structure insensitive relationship shown in Fig. 1.3 is illustrated by benzene hydrogenation at low temperatures. Dorling *et al.* found that the intrinsic activity of C_6H_6 hydrogenation was constant for the tested Pt/ SiO_2 catalysts with different Pt particle sizes. [78] Likewise, Rioux *et al.* investigated the Pt size effect (1.7–7.1 nm) on catalytic performance in hydrogenation of cyclohexene to cyclohexane over a series of Pt/SBA-15 catalysts at different temperatures, and found similar turnover frequencies at a temperature below $150\text{ }^\circ\text{C}$ regardless of the Pt particle size. [79] The same observation was also reported by Segal *et al.* in the vapor-phase hydrogenation of cyclohexene over a Pt/ SiO_2 catalyst, with the rate expression derived by the authors suggesting that the combination of hydrogen and adsorbed alkyl intermediate was rate limiting step, and independent of particle size changes. [80]

In addition to catalytic activity, selectivity can be also governed by controlling the particle size and local environment of supported metal catalysts. Matsubu *et al.* investigated the structure-

function relationships for CO₂ hydrogenation over TiO₂ supported Rh catalysts.[81] Knowledge of the size of the supported Rh nanoparticles was obtained from diffuse reflectance infrared Fourier transform spectroscopy with CO as probe molecule. The authors found that isolated Rh atoms catalyzed the formation of CO, while CH₄ production was preferred over supported Rh nanoparticles.[81] Xiong *et al.* reported that CeO₂ supported Pt single atoms showed exclusive production of methane rather than the desired propene in the catalytic dehydrogenation of propane, this in contrast to supported Pt nanoparticles, which are very active for this reaction.[82]

1.4. The Advent of Single Atom Catalysis

The examples listed in the previous section illustrate that control over particle size of supported metal particles is highly important for steering the overall catalytic performance of solid catalysts. Some of the examples also showed that the ultimate limit of dispersion, i.e. a single supported metal atom can give highly interesting catalyst materials. These catalysts containing such isolated metal atoms, or better, metal ions dispersed on a solid support, are known as Single Atom Catalysts (SAC) (Fig. 1.4a).[83] The SAC concept was first proposed by Zhang *et al.*,[73] and many efforts are now being devoted to construct new types of SACs and to get fundamental insight into their genesis, properties and performance. Indeed, SAC has become a very active new frontier in heterogeneous catalysis, not only because of the very promising performance shown by some of these materials, but also because conceptually they fill the gap between homogeneous and heterogeneous catalysts.[84]

So far, many routes have been developed for the synthesis of fully dispersed single atom catalysts, for example mass-selected soft-landing, high temperature atom trapping, atomic layer deposition (ALD) and wet chemical approaches.[26,86–88] By the careful choice of the type of supports as well as metal precursors, isolated atoms can be formed and anchored onto various kinds of supports via a Strong Metal Support Interaction (SMSI).[89] First, high-surface-area support oxides, such as zeolites, were exploited for their pore architecture to obtain the earliest examples of SAC materials, while defect sites in reducible oxides, such as CeO₂ and TiO₂, have been used for synthesizing and stabilizing single atoms sites onto their surfaces. SACs

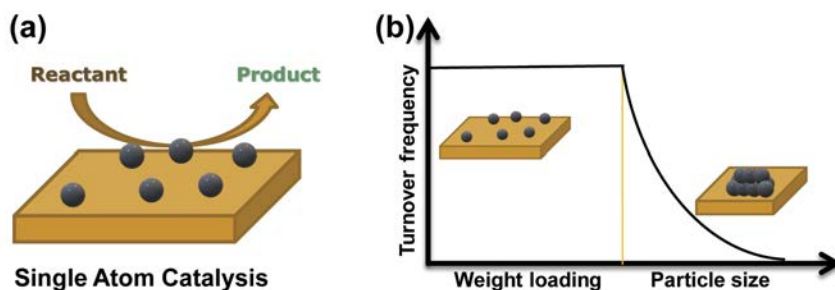


Fig. 1.4. (a) A schematic depiction of Single Atom Catalysis (SAC) and (b) the specific activity of Au/ZrO₂ SAC in 1,3-butadiene hydrogenation is independent of metal loading. Fig. 1.4b is adapted from ref. [85].

with other types of supports, including non-reducible oxides such as Al_2O_3 or carbon-based materials (e.g. graphene), have also been reported, with the former for example making use of unsaturated Al^{3+} sites for metal ion anchoring and the latter using doped N or S atoms as electron donors to stabilize the isolated metal atoms.[90–94] The physical deposition and ALD approaches are able to precisely control the location and SAC layer growing, however, normally are costly and less efficient for batch manufacturing of catalysts. On the other hand, wet chemical preparation methods are easy to execute and have a great potential for real industrial applications.[95] However, it is usually difficult to fabricate a catalyst of fully monoatomic nature with conventional wet chemical methods. For example, a mixture of isolate atoms, tiny clusters and nanoparticles was observed in the Aberration-corrected Scanning Transmission Electron Microscopy (AC-STEM) images of a Pt/ZnO material prepared by a modified deposition-precipitation method.[96]

In order to evaluate if SACs are successfully fabricated, several techniques have been extensively employed.[95] Both Aberration-corrected High-angle Annular Dark-field Scanning Transmission Electron Microscopy (AC-HAADF-STEM) and Scanning Tunneling Microscopy (STM) can afford a direct observation of the presence of single metal atoms on supports. However, STEM techniques can not provide any information on the local environment of active species unless the support is well defined.[97] A more important drawback of STEM is that this approach can only analyze a few locations rather than the whole catalyst and therefore might not be representative for the bulk. For this reason, it is necessary to combine STEM with other bulk techniques to better understand the architecture of fabricated SAC.

X-ray Absorption Spectroscopy (XAS) is known as a powerful technique to identify the nature of supported metals.[98] According to the definition, SAC contains only individual metal atoms on the catalyst surface, i.e. no metal-metal coordination should be observed. Therefore, if the metal-metal scattering is absent in the Extended X-ray Absorption Fine Structure (EXAFS) data, one can conclude that the metal phase is fully atomically dispersed. Wei *et al.* reported a series of Pt/ FeO_x SAC, with Pt-Pt coordination number decreasing gradually upon decreasing metal loading. When the Pt loading was decreased to 0.08 wt.%, the Pt-Pt scatter had completely vanished, with Pt-O bonding being observed instead.[75] By coupling XAS data with STEM analysis, the authors then concluded that the 0.08 wt.% Pt/ FeO_x was monoatomical and that the Pt atoms were positively charged.[75]

Fourier-transform infrared (FT-IR) spectroscopy after CO absorption could also provide useful information on active metal surface properties, such as the oxidation state and degree of dispersion, of the catalyst.[99] Qiao *et al.* compared the CO absorption behavior of FeO_x supported Pt nanoparticles and Pt isolated atoms using FT-IR techniques. After interacting with CO molecules, three bands at 2030, 1860 and 1950 cm^{-1} were observed for the nanoparticle containing catalyst. The authors attributed the former two to CO linear and bridged adsorbed on metallic Pt, respectively, and the latter to CO adsorbed on the interface between Pt clusters and the support. On the other hand, only a single band centered at 2080 cm^{-1} was observed for the Pt SAC and assigned to Pt^{n+} -CO vibration. While the Pt-CO vibration blue shifted as function of CO pressure for the nanoparticle containing catalyst, no shift of the location of

the maximum of the band associated with the $\text{Pt}^{\text{n+}}$ -CO vibration in SAC was observed, given that dipole-dipole interactions are absent in the latter.[73]

Single atom catalysts have been shown to be active in various chemical reactions, such as the water-gas shift reaction, electro-oxidation, selective hydrogenation and photo-catalysis,[74,85] although for some of these this is still debated.[100,101] Some notable examples of increased catalyst performance for SAC include an increase in catalytic efficiency for the selective hydrogenation of 1,3-butadiene upon downsizing the Au particle size, with the turnover frequency being the highest for isolated Au^{3+} atoms. The TOF was found to be independent of Au loading when fully atomically dispersed, as expected for such catalysts (Fig. 1.4b).[102] Hackett *et al.* have constructed mesoporous alumina-supported palladium catalysts with different loadings and compared their catalytic performance in the aerobic oxidation of alcohol. It was found that the catalysts with extremely low Pd weight loading, for which full monoatomicity is ensured, outperformed the normal Pd-based catalysts.[103] In the past several years, Zhang and co-workers synthesized a series of iron oxide supported single atom catalysts, which were demonstrated to be highly active and selective in various reactions, such as the low temperature CO oxidation, water gas shift reaction, NO reduction and the chemoselective hydrogenation of functionalized nitroarenes.[70,73–75] Xing *et al.* reported that noble metals (i.e. Pt, Pd, Ru and Rh) loaded TiO_2 SACs were able to increase the catalytic activity in photo-catalysis towards H_2 evolution 6 to 13 times compared to metal nanoparticles decorated TiO_2 materials.[104] Specifically, isolated noble metal atoms also exhibited excellent product selectivity.[105] Important examples are provided by graphene supported isolated Pd atoms, γ -alumina supported Pd-Cu single-atom alloy and mesoporous Al_2O_3 supported Pt single atom catalysts, which were demonstrated to be highly selective towards alkenes hydrogenation in alkene-rich streams, whereas the corresponding nanoscale catalysts gave rise to over-hydrogenation and the subsequent formation of alkanes.[87,88,106]

However, stability is a key issue with SAC materials when used in practical applications. Indeed, single, supported atoms may be expected to easily aggregate and grow into bigger metal nanoparticles due to their high surface energy. However, numerous examples have now shown that single atoms can be sufficiently stabilized by a suitable support oxide and are stable in many catalytic applications, due to the strong chemical bonding between the isolated atoms and the support. For example, Qiao *et al.* reported a highly active and ultra-stable Au/FeO_x catalyst for CO oxidation.[74] No CO conversion drop was observed for the single atom decorated catalysts at 200 °C even after 100 h time-on-stream. In contrast, the catalyst prepared by the same method but containing both Au clusters and single Au atoms lost its activity continuously with CO conversion having decreased from ~95 % to ~76 % within 63 h of operation. High resolution TEM analysis confirmed that the Au nanoparticles had sintered, whereas the single Au atoms in both two catalysts remained stable.[74] More recently, a Pt SAC supported by mesoporous Al_2O_3 was reported by Zhang *et al.*[88] This catalyst showed outstanding stability in several reactions (i.e., CO oxidation, selective hydrogenation of 1,3-butadiene and hydro-reforming of n-hexane) under demanding reaction conditions. The catalyst was shown to maintain its catalytic activity for CO oxidation up to 60 cycles in a temperature range of 100-400 °C, whereas a commercial

Pt/Al₂O₃ catalyst tested for comparison, deactivated in the first several runs as a result of metal sintering. Besides, no apparent catalytic performance change was observed for the catalyst in the selective hydrogenation of 1,3-butadiene even after exposure to a H₂ atmosphere at 200 °C for 24 h. Moreover, this SAC system was also found to be more coke and sintering resistant in n-hexane hydro-reforming compared than its nanoparticulate counterparts. As demonstrated by long-term stability tests, a loss of activity of only 12% was observed for the SAC system after reacting at 550 °C for 48 h, while a 72% loss in activity was found for a commercial Pt/Al₂O₃ catalyst tested for comparison.[88]

1.5. Scope and Outline of the PhD Thesis

This PhD Thesis aims to study the effect of choice of catalyst support, support modification and metal dispersion on the performance of metal oxide supported, precious metal based catalysts. Based on catalyst performance in a range of different gas- and liquid-phase reactions and catalyst characterization results, insights are gained into the structure-performance relationships governing these reactions, and the modes of catalyst deactivation, knowledge that can aid the further development of stable and more cost-effective precious-metal catalysts for targeted applications.

It has been demonstrated in previous work that an oxidic support, for example Al₂O₃, will suffer from hydrolytic attack under polar hydrothermal conditions that are typical in catalytic biomass conversion processes. In order to improve catalyst stability for such applications, in **Chapter 2**, silica deposition on a benchmark Aqueous Phase Reforming (APR) catalyst, namely Pt/γ-Al₂O₃, is studied. The physicochemical properties, catalytic performance, including stability, of the catalysts before and after silica deposition are systemically compared.

High temperature reducing conditions, employed in hydrogenation reactions, can in principle present another stability challenge to reducible oxide-based catalysts such as TiO₂, as this can result in deactivation by Strong Metal Support Interaction (SMSI). The SMSI concept was first developed by Tauster *et al.* in 1978 to refer to the dramatic suppression of metal chemisorption ability.[107] The SMSI effect then proved to be either advantageous for or detrimental to the activity of the catalyst. For instance, SMSI generation over TiO₂ supported catalysts has a beneficial effect on various reactions, such as, the hydrogenation of carbonyl groups toward alcohols,[108–111] nitrate reduction to nitrite[112] and photocatalytic bio-hydrogen production from glucose solution.[113] Notably, SMSI is also widely employed for fabrication stable single atom catalysts.[89]

However, as discussed in Section 1.2, in other cases, SMSI effects have been detrimental for catalytic activity and better to be avoided. Indeed, previous work from our group demonstrated that a Ru/TiO₂-P25 catalyst suffered from deactivation resulting from SMSI surface coverage in the hydrogenation of levulinic acid (LA) into γ-valerolactone (GVL).[114] Therefore, in **Chapter 3**, we studied the effect of TiO₂ type on the stability of Ru-based catalysts in the selective hydrogenation of LA to GVL. A set of Ru/TiO₂ catalysts with similar metal loading and metal particle size were prepared via wet impregnation and their stability was assessed by

multiple recycling reactions under various conditions. The extent and origin of SMSI formation encountered for the Ru/TiO₂ catalysts under such mild liquid hydrogenation condition is reported.

Single Atom Catalysts (SAC), materials that contain isolated metal atoms on a support, are attractive as they offer to combine efficient metal use with new catalytic performance. In **Chapter 4**, we report a stable ZrO₂ supported Ru SAC with high metal loading. The genesis of the single Ru atoms on the ZrO₂ support and the stability of this SAC material have been systematically studied by both *ex-situ* and *in-situ* X-ray absorption spectroscopy and CO-FT-IR spectroscopy under different gas atmospheres at elevated temperatures. The catalytic performance of this Ru SAC under oxidation conditions is also investigated using CO oxidation as a probe reaction.

In **Chapter 5**, we have extended the ZrO₂ supported family of SAC from Ru to also include Pd and Pt as the active metals. In order to build structure-performance relationship, a series of Pd and Pt SAC with different loading and metal dispersion were prepared via a simple wet impregnation procedure. The catalytic performance of these catalysts was assessed in CO oxidation, propane dehydrogenation, cinnamaldehyde hydrogenation as well as 1,3-butadiene hydrogenation in a propene-rich steam.

The PhD Thesis ends with a summary of the main results, as well as with some perspectives on potential future research in **Chapter 6**.

References

1. P. Kumbhar, J. Sawant, A. Ghosalkar, in: *Ind. Catal. Process. Fine Spec. Chem.*, Elsevier, Amsterdam, 2016, 597–662.
2. G.A. Somorjai, R.M. Rioux, *Catal. Today* 100 (2005) 201–215.
3. J.M. Thomas, K.D.M. Harris, *Energy Environ. Sci.* 9 (2016) 687–708.
4. S. Wacławek, V.V.T. Padil, M. Černík, *Ecol. Chem. Eng. S* 25 (2018) 9–34.
5. J.Q. Bond, A.A. Upadhye, H. Olcay, G.A. Tompsett, J. Jae, R. Xing, D.M. Alonso, D. Wang, T. Zhang, R. Kumar, A. Foster, S.M. Sen, C.T. Maravelias, R. Malina, S.R.H. Barrett, R. Lobo, C.E. Wyman, J.A. Dumesic, G.W. Huber, *Energy Environ. Sci.* 7 (2014) 1500–1523.
6. D.M. Alonso, J.Q. Bond, J.A. Dumesic, *Green Chem.* 12 (2010) 1493–1513.
7. G.W. Huber, J.A. Dumesic, *Catal. Today* 111 (2006) 119–132.
8. S.V. Pisupati, A.H. Tchapda, in: *Adv. Bioprocess Technol.*, Springer International Publishing, 2015, 277–314.
9. A.R.K. Gollakota, N. Kishore, S. Gu, *Renew. Sustain. Energy Rev.* 81 (2018) 1378–1392.
10. S. Saerens, M.K. Sabbe, V.V. Galvita, E.A. Redekop, M.F. Reyniers, G.B. Marin, *ACS Catal.* 7 (2017) 7495–7508.
11. Y. Wang, H. Arandiyán, J. Scott, A. Bagheri, H. Dai, R. Amal, *J. Mater. Chem. A* 5 (2017) 8825–8846.
12. M. Marafi, E. Furimsky, *Energy & Fuels* 31 (2017) 5711–5750.
13. M.R. Rahimpour, M. Jafari, D. Iranshahi, *Appl. Energy* 109 (2013) 79–93.
14. J.P. Lange, *Catal. Sci. Technol.* 6 (2016) 4759–4767.
15. R.J. Farrauto, in: *Handb. Ind. Chem. Biotechnol.*, Springer International Publishing, 2017, 1995–2035.
16. J.P. Lange, *Angew. Chem. Int. Ed.* 54 (2015) 13186–13197.
17. A. Devaraj, M. Vijayakumar, J. Bao, M.F. Guo, M.A. Derewinski, Z. Xu, M.J. Gray, S. Prodingier, K.K. Ramasamy, *Sci. Rep.* 6 (2016) 37586–37592.
18. J. Goetze, I. Yarulina, J. Gascon, F. Kapteijn, B.M. Weckhuysen, *ACS Catal.* 8 (2018) 2060–2070.
19. J. Goetze, F. Meirer, I. Yarulina, J. Gascon, F. Kapteijn, J. Ruiz-Martínez, B.M. Weckhuysen, *ACS Catal.* 7 (2017) 4033–4046.
20. Q. Li, Z. Sui, X. Zhou, Y. Zhu, J. Zhou, D. Chen, *Top. Catal.* 54 (2011) 888–896.
21. Y. Liu, H. Tsunoyama, T. Akita, S. Xie, T. Tsukuda, *ACS Catal.* 1 (2011) 2–6.
22. S. Shao, H. Zhang, Y. Wang, R. Xiao, L. Heng, D. Shen, *Energy & Fuels* 29 (2015) 1751–1757.
23. H. Wang, Y. Wang, *Top. Catal.* 59 (2016) 65–72.
24. F. Héroguel, B. Rozmysłowicz, J.S. Luterbacher, *Chimia* 69 (2015) 582–591.
25. H.N. Pham, J.J.H.B. Sattler, B.M. Weckhuysen, A.K. Datye, *ACS Catal.* 6 (2016) 2257–2264.
26. J. Jones, H. Xiong, A.T. DeLaRiva, E.J. Peterson, H. Pham, S.R. Challa, G. Qi, S. Oh, M.H. Wiebenga, X.I. Pereira Hernandez, Y. Wang, A.K. Datye, *Science* 353 (2016) 150–154.
27. C.B. Alcock, G.W. Hooper, *Proc. R. Soc. A Math. Phys. Eng. Sci.* 254 (1960) 551–561.
28. M. Argyle, C. Bartholomew, *Catalysts* 5 (2015) 145–269.
29. J.H. Vleeming, B.F.M. Kuster, G.B. Marin, F. Oudet, P. Courtine, *J. Catal.* 166 (1997) 148–159.
30. W.C. Ketchie, E.P. Maris, R.J. Davis, *Chem. Mater.* 19 (2007) 3406–3411.
31. E.P. Maris, W.C. Ketchie, V. Oleshko, R.J. Davis, *J. Phys. Chem. B* 110 (2006) 7869–7876.
32. O.A. Abdelrahman, H.Y. Luo, A. Heyden, Y. Román-Leshkov, J.Q. Bond, *J. Catal.* 329 (2015) 10–21.
33. Q. Meng, H. Zheng, Y. Zhu, Y. Li, J. Mol. Catal. A Chem. 421 (2016) 76–82.

34. N.S. Nasri, J.M. Jones, V.A. Dupont, A. Williams, *Energy & Fuels* 12 (1998) 1130–1134.
35. J. Dunleavy, *Platin. Met. Rev.* 50 (2006) 110–110.
36. D.A. Boga, F. Liu, P.C.A. Bruijninx, B.M. Weckhuysen, *Catal. Sci. Technol.* 6 (2016) 134–143.
37. Q. Fang, M.A. Hanna, *Bioresour. Technol.* 81 (2002) 187–192.
38. J. Ftouni, H.C. Genuino, A. Muñoz-Murillo, P.C.A. Bruijninx, B.M. Weckhuysen, *ChemSusChem* 10 (2017) 2891–2896.
39. H. Xiong, H.N. Pham, A.K. Datye, *Green Chem.* 16 (2014) 4627–4643.
40. G. Lefèvre, M. Duc, P. Lepeut, R. Caplain, M. Fédoroff, *Langmuir* 18 (2002) 7530–7537.
41. D.D. MacDonald, P. Butler, *Corros. Sci.* 13 (1973) 259–274.
42. R.M. Ravenelle, J.R. Copeland, W.G. Kim, J.C. Crittenden, C. Sievers, *ACS Catal.* 1 (2011) 552–561.
43. A.L. Jongerius, J.R. Copeland, G.S. Foo, J.P. Hofmann, P.C.A. Bruijninx, C. Sievers, B.M. Weckhuysen, *ACS Catal.* 3 (2013) 464–473.
44. R.M. Ravenelle, F. Schüßler, A. D'Amico, N. Danilina, J.A. van Bokhoven, J.A. Lercher, C.W. Jones, C. Sievers, *J. Phys. Chem. C* 114 (2010) 19582–19595.
45. M.W. Hahn, J.R. Copeland, A.H. van Pelt, C. Sievers, *ChemSusChem* 6 (2013) 2304–2315.
46. J. Sá, J. Bernardi, J.A. Anderson, *Catal. Lett.* 114 (2007) 91–95.
47. L.B. Xiong, J.L. Li, B. Yang, Y. Yu, *J. Nanomater.* 2012 (2012) 1–13.
48. Y. Zhu, D. Liu, M. Meng, *Chem. Commun.* 50 (2014) 6049–6051.
49. O. Dulub, W. Hebenstreit, U. Diebold, *Phys. Rev. Lett.* 84 (2000) 3646–3649.
50. J.C. Matsubu, S. Zhang, L. DeRita, N.S. Marinkovic, J.G. Chen, G.W. Graham, X. Pan, P. Christopher, *Nat. Chem.* 9 (2016) 120–127.
51. H.N. Pham, A.E. Anderson, R.L. Johnson, K. Schmidt-Rohr, A.K. Datye, *Angew. Chem. Int. Ed.* 51 (2012) 13163–13167.
52. M. Piernavieja-Hermida, Z. Lu, A. White, K.B. Low, T. Wu, J.W. Elam, Z. Wu, Y. Lei, *Nanoscale* 8 (2016) 15348–15356.
53. J. Lu, B. Fu, M.C. Kung, G. Xiao, J.W. Elam, H.H. Kung, P.C. Stair, *Science* 335 (2012) 1205–1208.
54. H. Xiong, T.J. Schwartz, N.I. Andersen, J.A. Dumesic, A.K. Datye, *Angew. Chem. Int. Ed.* 54 (2015) 7939–7943.
55. B.J. O'Neill, D.H.K. Jackson, A.J. Crisci, C.A. Farberow, F. Shi, A.C. Alba-Rubio, J. Lu, P.J. Dietrich, X. Gu, C.L. Marshall, P.C. Stair, J.W. Elam, J.T. Miller, F.H. Ribeiro, P.M. Voyles, J. Greeley, M. Mavrikakis, S.L. Scott, T.F. Kuech, J.A. Dumesic, *Angew. Chem. Int. Ed.* 52 (2013) 13808–13812.
56. R. Espinoza, K. Jothimurugesan, Y. Jin, B.C. Ortego, K. Fjare, *Stabilized Boehmite-Derived Catalyst Supports, Catalysts, Methods of Making and Using*, US 20080039539 A1, 2007.
57. Y. Jin, R. Espinoza, N. Srinivasan, O.P. Ionkina, *Stabilized Transition Alumina Catalyst Support from Boehmite and Catalysts Made Therefrom*, US7402612 B2, 2003.
58. J.M. González-Carballo, F.J. Pérez-Alonso, M. Ojeda, F.J. García-García, J.L.G. Fierro, S. Rojas, *ChemCatChem* 6 (2014) 2084–2094.
59. G.L. Bezemer, J.H. Bitter, H.P.C.E. Kuipers, H. Oosterbeek, J.E. Holewijn, X. Xu, F. Kapteijn, A.J. van Dillen, K.P. de Jong, *J. Am. Chem. Soc.* 128 (2006) 3956–3964.
60. M. Behrens, F. Studt, I. Kasatkin, S. Kuhl, M. Havecker, F. Abild-Pedersen, S. Zander, F. Girgsdies, P. Kurr, B.L. Knief, M. Tovar, R.W. Fischer, J.K. Nørskov, R. Schlögl, *Science* 336 (2012) 893–897.
61. A.T. Bell, *Science* 299 (2003) 1688–1691.
62. B. Roldan Cuenya, F. Beharfarid, *Surf. Sci. Rep.* 70 (2015) 135–187.
63. Y. Liu, G. Zhao, D. Wang, Y. Li, *Natl. Sci. Rev.* 2 (2015) 150–166.
64. S. Cao, F.F. Tao, Y. Tang, Y. Li, J. Yu, *Chem. Soc. Rev.* 45 (2016) 4747–4765.
65. A.S.K. Hashmi, G.J. Hutchings, *Angew. Chem. Int. Ed.* 45 (2006) 7896–7936.

66. G.J. Hutchings, M. Haruta, *Appl. Catal. A Gen.* 291 (2005) 2–5.
67. A. Stephen, K. Hashmi, *Gold Bull.* 37 (2004) 51–65.
68. M. Che, C.O. Bennett, in: *Adv. Catal.*, 1989, pp. 55–172.
69. M. Turner, V.B. Golovko, O.P.H. Vaughan, P. Abdulkina, A. Berenguer-Murcia, M.S. Tikhov, B.F.G. Johnson, R.M. Lambert, *Nature* 454 (2008) 981–983.
70. J. Lin, B. Qiao, N. Li, L. Li, X. Sun, J. Liu, X. Wang, T. Zhang, *Chem. Commun.* 51 (2015) 7911–7914.
71. S. Vajda, M.J. Pellin, J.P. Greeley, C.L. Marshall, L.A. Curtiss, G.A. Ballentine, J.W. Elam, S. Catillon-Mucherie, P.C. Redfern, F. Mehmood, P. Zapol, *Nat. Mater.* 8 (2009) 213–216.
72. J. Wei, E. Iglesia, *J. Phys. Chem. B* 108 (2004) 4094–4103.
73. B. Qiao, A. Wang, X. Yang, L.F. Allard, Z. Jiang, Y. Cui, J. Liu, J. Li, T. Zhang, *Nat. Chem.* 3 (2011) 634–641.
74. B. Qiao, J.X. Liang, A. Wang, C.Q. Xu, J. Li, T. Zhang, J.J. Liu, *Nano Res.* 8 (2015) 2913–2924.
75. H. Wei, X. Liu, A. Wang, L. Zhang, B. Qiao, X. Yang, Y. Huang, S. Miao, J. Liu, T. Zhang, *Nat. Commun.* 5 (2014) 5634.
76. M. Ojeda, S. Rojas, M. Boutonnet, F.J. Pérez-Alonso, F. Javier García-García, J.L.G. Fierro, *Appl. Catal. A Gen.* 274 (2004) 33–41.
77. M.P. Andersson, F. Abild-Pedersen, I.N. Remediakis, T. Bligaard, G. Jones, J. Engbæk, O. Lytken, S. Hørch, J.H. Nielsen, J. Sehested, *J. Catal.* 255 (2008) 6–19.
78. T. Dorling, *J. Catal.* 7 (1967) 378–385.
79. C.L. Padró, S.R. de Miguel, A.A. Castro, O.A. Scelza, in: *Catal. Deactiv.*, 1997, 191–198.
80. E. Segal, *J. Catal.* 52 (1978) 45–49.
81. J.C. Matsubu, V.N. Yang, P. Christopher, *J. Am. Chem. Soc.* 137 (2015) 3076–3084.
82. H. Xiong, S. Lin, J. Goetze, P. Pletcher, H. Guo, L. Kovarik, K. Artyushkova, B.M. Weckhuysen, A.K. Datye, *Angew. Chem. Int. Ed.* 56 (2017) 8986–8991.
83. A. Wang, J. Li, T. Zhang, *Nat. Rev. Chem.* 2 (2018) 65–81.
84. L. Zhang, Y. Ren, W. Liu, A. Wang, T. Zhang, *Natl. Sci. Rev.* (2018), DOI: 10.1093/nsr/nwy077.
85. X.F. Yang, A. Wang, B. Qiao, J. Li, J. Liu, T. Zhang, *Acc. Chem. Res.* 46 (2013) 1740–1748.
86. P. Liu, Y. Zhao, R. Qin, S. Mo, G. Chen, L. Gu, D.M. Chevrier, P. Zhang, Q. Guo, D. Zang, B. Wu, G. Fu, N. Zheng, *Science* 352 (2016) 797–800.
87. H. Yan, H. Cheng, H. Yi, Y. Lin, T. Yao, C. Wang, J. Li, S. Wei, J. Lu, *J. Am. Chem. Soc.* 137 (2015) 10484–10487.
88. Z. Zhang, Y. Zhu, H. Asakura, B. Zhang, J. Zhang, M. Zhou, Y. Han, T. Tanaka, A. Wang, T. Zhang, N. Yan, *Nat. Commun.* 8 (2017) 16100–16110.
89. C.T. Campbell, *Nat. Chem.* 4 (2012) 597–598.
90. B.C. Gates, M. Flytzani-Stephanopoulos, D.A. Dixon, A. Katz, *Catal. Sci. Technol.* 7 (2017) 4259–4275.
91. L. DeRita, S. Dai, K. Lopez-Zepeda, N. Pham, G.W. Graham, X. Pan, P. Christopher, *J. Am. Chem. Soc.* 139 (2017) 14150–14165.
92. G. Spezzati, Y. Su, J.P. Hofmann, A.D. Benavidez, A.T. DeLaRiva, J. McCabe, A.K. Datye, E.J.M. Hensen, *ACS Catal.* 7 (2017) 6887–6891.
93. K. Ding, A. Gulec, A.M. Johnson, N.M. Schweitzer, G.D. Stucky, L.D. Marks, P.C. Stair, *Science* 350 (2015) 189–92.
94. H. Li, H. Zhang, X. Yan, B. Xu, J. Guo, *New Carbon Mater.* 33 (2018) 1–11.
95. J. Liu, *ACS Catal.* 7 (2017) 34–59.
96. J. Liu, *Microsc. Microanal.* 18 (2012) 354–355.
97. J.D. Kistler, N. Chotigkrai, P. Xu, B. Enderle, P. Praserthdam, C.Y. Chen, N.D. Browning, B.C. Gates, *Angew. Chem. Int. Ed.* 53 (2014) 8904–8907.
98. I. Ogino, *Chin. J. Catal.* 38 (2017) 1481–1488.
99. C. Asokan, L. DeRita, P. Christopher, *Chin. J. Catal.* 38 (2017) 1473–1480.
100. M.D. Rossell, F.J. Caparrós, I. Angurell, G. Muller, J. Llorca, M. Seco, O. Rossell, *Catal. Sci. Technol.* 6 (2016) 4081–4085.

101. C.K. Narula, L.F. Allard, M. Moses-DeBusk, G.M. Stocks, Z. Wu, *Sci. Rep.* 7 (2017) 560.
102. Z.P. Liu, C.M. Wang, K.N. Fan, *Angew. Chem. Int. Ed.* 45 (2006) 6865–6868.
103. S.F.J. Hackett, R.M. Brydson, M.H. Gass, I. Harvey, A.D. Newman, K. Wilson, A.F. Lee, *Angew. Chem. Int. Ed.* 119 (2007) 8747–8750.
104. J. Xing, J.F. Chen, Y.H. Li, W.T. Yuan, Y. Zhou, L.R. Zheng, H.F. Wang, P. Hu, Y. Wang, H.J. Zhao, Y. Wang, H.G. Yang, *Chem. Eur. J.* 20 (2014) 2138–2144.
105. H. Zhang, G. Liu, L. Shi, J. Ye, *Adv. Energy Mater.* 8 (2018) 1701343.
106. F.R. Lucci, J. Liu, M.D. Marcinkowski, M. Yang, L.F. Allard, M. Flytzani-Stephanopoulos, E.C.H. Sykes, *Nat. Commun.* 6 (2015) 8550.
107. S. Tauster, *J. Catal.* 55 (1978) 29–35.
108. M.A. Vannice, D. Poondi, J. Catal. 169 (1997) 166–175.
109. D. Poondi, M.A. Vannice, *J. Mol. Catal. A Chem.* 124 (1997) 79–89.
110. P. Mäki-Arvela, J. Hájek, T. Salmi, D.Y. Murzin, *Appl. Catal. A Gen.* 292 (2005) 1–49.
111. T. Ekou, L. Ekou, A. Vicente, G. Lafaye, S. Pronier, C. Especel, P. Marécot, *J. Mol. Catal. A Chem.* 337 (2011) 82–88.
112. M.S. Kim, S.H. Chung, C.J. Yoo, M.S. Lee, I.H. Cho, D.W. Lee, K.Y. Lee, *Appl. Catal. B Environ.* 142–143 (2013) 354–361.
113. J.C. Colmenares, A. Magdziarz, M.A. Aramendia, A. Marinas, J.M. Marinas, F.J. Urbano, J.A. Navio, *Catal. Commun.* 16 (2011) 1–6.
114. J. Ftouni, A. Muñoz-Murillo, A. Goryachev, J.P. Hofmann, E.J.M. Hensen, L. Lu, C.J. Kiely, P.C.A. Bruijninx, B.M. Weckhuysen, *ACS Catal.* 6 (2016) 5462–5472.

2

**Silica Deposition Improves
the Hydrothermal Stability of an
Alumina Support During Glycerol
Aqueous Phase Reforming**

Abstract

Silica deposition on the benchmark aqueous phase reforming (APR) catalyst Pt/ γ -Al₂O₃ is studied to prevent or limit hydrolytic attack of the support under hydrothermal APR conditions, for which boehmite formation by support hydration is a known cause for catalyst deactivation. Tetraethyl orthosilicate (TEOS) is employed as a silicon source in a straightforward liquid-phase, silylation process followed by catalyst calcination and reduction. Characterization by X-ray diffraction, temperature-programmed desorption of NH₃, infrared, ²⁷Al nuclear magnetic resonance and X-ray photoelectron spectroscopy of the fresh catalysts suggests that silica addition occurs preferentially on the support surface, resulting in the formation of weak Brønsted acid sites as well as the Si-O-Al linkages at the expense of specific surface Lewis acid sites. Silylation and calcination of Pt/ γ -Al₂O₃ causes partial blockage of the metal surface area (12% loss), whereas γ -Al₂O₃ surface silica modification prior to Pt deposition makes controlled metal deposition difficult. Catalytic performance tests show the overcoated samples to be active in the APR of 5 wt.% glycerol, albeit with lower H₂ production rates compared to the benchmark catalyst. Characterization of spent APR catalysts clearly demonstrates that silylation/calcination treatments effectively slows down the transformation of the γ -Al₂O₃ support due to the formation of a Si-O-Al interface. Overall, the lifetime of the catalyst is increased three-fold as a result of the surface overcoating treatment, with repetitive recycling ultimately leading to loss of the protective silica layer.

This chapter is on the following manuscript: F. Liu, C. Okolie, R.M. Ravenelle, J.C. Crittenden, C. Sievers, P.C.A. Bruijninx, B.M. Weckhuysen, *Appl. Catal. A Gen.* 551 (2018) 13–22.

2.1. Introduction

The unsustainable consumption of fossil fuel reserves and continuously increasing energy demands are big challenges currently faced by our society.[1–3] Alternative and efficient routes for the production of energy and chemicals from sustainable resources, such as biomass, are therefore needed. Biomass can serve as a source of renewable hydrogen, a clean energy carrier but also a key reagent for the chemical industry. As a result, hydrogen production from glycerol via so-called Aqueous Phase Reforming (APR) has received considerable attention.[4–8] Glycerol has been identified as an attractive biomass-derived feedstock being produced in large amounts as a by-product of biodiesel production.[9–11] Compared to more conventional hydrogen production routes, such as steam reforming, partial oxidation and autothermal reforming, APR is usually operated at a relative low temperature in a single reaction step. Under these conditions, the water-gas shift reaction is thermodynamically favorable, resulting in efficient H₂ production and a lower CO concentration in the product stream.[11,12]

A large variety of (supported) metal-based catalysts, including Raney Ni, noble and non-noble metals on oxidic and carbon supports, have been used for hydrogen production by APR from glycerol and other oxygenated, renewable substrates.[13–17] Pt/ γ -Al₂O₃ is commonly used as APR catalyst,[14,18] showing good activity, high H₂ selectivity and limited alkane formation, albeit that this catalyst is unstable under the applied hydrothermal conditions.[19,20] It has been demonstrated that supported metal particles can suffer irreversible sintering under the high temperature and pressure conditions often applied in biomass reactions.[20] Besides, under APR conditions, oxidic supports, such as γ -alumina, can be hydrated, leading to phase changes in the support and, as a result, deactivation[21,22]. The γ -alumina in Pt/Al₂O₃ is well-known to transform to boehmite under typical APR conditions. For example, Ravenelle *et al.* demonstrated that bare γ -Al₂O₃ was rehydrated in hot water and completely converted into crystalline boehmite within 10 h with a significant loss of surface area.[23] During this structural modification, supported metal particles can loose contact with their original binding sites leading to sintering or encapsulation, both of which are detrimental for catalyst activity.[23] Previous studies suggested this transformation to start with hydrolytic attack of the Lewis acid sites of the alumina support.[24,25] Indeed, supported metal particles as well as biomass-derived oxygenates in the reaction solution were reported to have a beneficial effect on catalyst stability by “capping” specific, coordinatively unsaturated surface Al atoms.[26,27] For example, Copeland *et al.* found that biomass-derived polyols can block Lewis acidic Al sites of γ -Al₂O₃ by formation of multidentate alkoxy surface species that protect the alumina from hydrolytic attack[25]. Similarly, Absi-Halabi *et al.*[28] proposed the improved hydrothermal stability of γ -Al₂O₃ in acetic acid solution to be related to the formation of acetate bridges by alumina acetylation, again emphasizing the protection of such primary rehydration sites as the reason for improved hydrothermal stability.

Various other approaches to γ -alumina support stabilization have been reported, including stabilization by doping with a broad range of other materials. For example, ConocoPhillips studied the use of dopants, such as silicon, cobalt, magnesium and others, to enhance

the hydrothermal stability of alumina-supported catalysts for Fischer–Tropsch synthesis.[29,30] Byrd *et al.* reported that the stability of γ - Al_2O_3 treated in supercritical water at 500 °C could be improved by inclusion of CeO_2 . [31] Alternatively, catalyst surface coating can also be used to limit or preclude the phase transformation process to boehmite. Pham *et al.* deposited a thin, sucrose-derived carbonaceous layer on fumed alumina and demonstrated that the carbon coating led to improved thermal stability.[32] Similarly, it was reported that the formation of a graphitic carbon layer on pelletized γ -alumina by chemical vapor deposition of methane can enhance catalyst thermal stability significantly.[33]

Silylation of metal oxide surfaces has also emerged as a promising route to tune the surface properties of inorganic materials, such as silica, zeolites and alumina.[34–36] Zapata *et al.* reported that hydrophobization of HY zeolites by functionalization with organosilanes could protect the material from structural collapse in hot liquid water due to increased hydrophobicity. [37] In case of γ - Al_2O_3 , silylation followed by high temperature calcination could block the surface Lewis acid Al sites that serve as initial hydration sites for boehmite formation via coordinative saturation and the formation of Al-O-Si bonds, inhibiting water absorption.[36]

In this PhD thesis Chapter, we explore surface silylation of a Pt/ γ - Al_2O_3 APR catalyst with tetraethylorthosilicate (TEOS) followed by calcination as a means of protecting the support against hydrolytic attack to ultimately increase the stability of the catalyst under glycerol APR conditions. Recycle tests show that the silica deposition does indeed reduce boehmite formation and extends the catalyst lifetime, but cannot prevent eventual deactivation by dehydration entirely.

2.2. Experimental Section

2.2.1. Catalyst synthesis

The 1 wt.% Pt/ γ - Al_2O_3 catalyst was prepared via wet impregnation. A slurry of $\text{H}_2\text{Pt}(\text{OH})_6$ (99.9% metals basis, Alfa Aesar) and commercial γ - Al_2O_3 (3 μm APS powder, 99.97% metals basis, Alfa Aesar) was stirred at 40 °C for 24 h. The catalysts were dried at 110 °C under vacuum overnight and calcined right after at 500 °C with a heating ramp rate of 1 °C/min for 4 h (starting from room temperature) under a 20% O_2/N_2 flow. Prior to the silylation treatment, the catalyst was reduced in 10% H_2/N_2 flow at 300 °C (ramp rate 5 °C/min) for 3 h (starting from room temperature).

The silylation procedure was performed according to a literature protocol.[38] In a typical experiment, a mixture of 2.4 g tetraethyl orthosilicate (TEOS, 98% Alfa Aesar), 30 g ethanol, 8 g milli-Q water and 1 g of 1 wt.% Pt/ Al_2O_3 was stirred at 40 °C for the designated time. The quantity of precursor added corresponded to a theoretical loading of 40% silicon by weight (if all silicon was deposited). The solid was collected by centrifugation at 5000 rpm for 10 min and washed three times with ethanol, followed by drying at 60 °C and then 120 °C overnight, respectively. Prior to catalytic activity experiments, the samples were calcined and reduced under the conditions mentioned above. The effect of silylation time on catalyst performance

was tested by using three different silylation times of 4 h, 8 h and 12 h and the obtained catalyst materials named as Pt/Al₂O₃-4, Pt/Al₂O₃-8 and Pt/Al₂O₃-12, respectively.

One additional reference catalyst, further denoted as Pt/Al₂O₃-8R, was prepared in a reverse order compared to Pt/Al₂O₃-8 sample. The support alumina was first silylated for 8 h under conditions otherwise identical to the silylation procedure for the Pt/Al₂O₃-8 sample, followed by calcination and reduction. Subsequently, the wet impregnation method described above was employed to prepare 1 wt.% Pt/Al₂O₃-8R with the pre-modified alumina as support. Subsequent calcination and reduction conditions were again identical to those used in the preparation of Pt/Al₂O₃-8.

2.2.2. Catalyst testing

Aqueous phase reforming (APR) of a 5 wt.% glycerol solution was performed in a 40 mL stainless Parr batch autoclave equipped with a back-pressure regulator and magnetic stirrer. In a typical experiment, 300 mg of catalyst and 10 g of the 5 wt.% glycerol solution were loaded into the reactor and the system was pressurized to 30 bar with helium. The reaction mixture was then heated to 225 °C and reacted for 12 h. An online dual channel micro-GC (Varian CP4900) equipped with thermal conductivity detector was employed to analyze the gas phase composition. A COX column with back flush was used for quantification of the gases and N₂ was added as internal standard. The composition of the liquid phase was measured using a Shimadzu 2010A GC with flame ionization detector. The spent catalyst was collected by filtration using a 0.45 µm Nylon filter membrane, followed by ethanol washing and drying. Glycerol conversion (*X*), yield (*Y*) and selectivities (*S*) of liquid phase products and H₂ are defined as follows:

$$X_{gly}(\%) = \frac{C_{0,gly} - C_{t,gly}}{C_{0,gly}} \times 100\% \quad (1)$$

$$Y_{t,i}(\%) = \frac{C_{t,i}}{C_{0,gly}} \times \frac{M_i}{M_o} \times 100\% \quad (2)$$

$$S_{t,i}(\%) = \frac{C_{t,i}}{C_{0,gly} - C_{t,gly}} \times \frac{M_i}{M_o} \times 100\% \quad (3)$$

$$S_{H_2}(\%) = \frac{n_{H_2}}{X_{gly} \times n_{gly}} \times \frac{1}{7} \times 100\% \quad (4)$$

where $C_{0,gly}$ is initial glycerol concentration, $C_{t,gly}$ is glycerol concentration at time t , $C_{i,gly}$ is the concentration of product i at time t , M_o and M_i are the moles of carbon in glycerol and product i , respectively, n_{H_2} and n_{gly} are the moles of H₂ produced and initial moles of glycerol, respectively.

For the recycle tests, the spent catalyst was retrieved after a standard run, rinsed, dried at 60 °C overnight and reused directly without any regeneration step. All (recycle) runs were carried

out at 225 °C for 12 h under 30 bar of He. The recovery of each catalyst after every run was close to 100% and the amount of glycerol in every subsequent run was scaled to the amount of catalyst recovered with the constant total reaction weight (10 g) to allow for a proper comparison of the runs, the H₂ production rates were normalized to the intake of the recycled catalysts.

2.2.3. Catalyst characterization

X-Ray Diffraction (XRD) patterns measured using on a Bruker-AXS D2 Phaser powder X-ray diffractometer using Co K_{α1,2} with $\lambda=1.79026 \text{ \AA}$. Measurements were carried out between 10-85° 2 θ using a step size of 0.04° and a scan speed of 1 s. Part of the XRD patterns were recorded with Cu K α radiation with an incident angle ranging from 2 θ = 5-70° with a step size of 0.02° with a scan speed of 1 s.

Scanning Transmission Electron Microscopy (STEM) and Energy Dispersive X-ray (EDX) analyses were conducted with a JEOL 100CX microscope at a 100 kV acceleration voltage. The samples were prepared by applying three drops of a catalyst in ethanol slurry onto a graphene-coated, 200 mesh copper grid. The slurry was homogenized using sonication prior to applying to the sample grid.

The Pt loading was determined using an inductively coupled plasma optical emission spectrometry (ICP-OES). The sample was prepared by dissolving 100 mg of the catalyst samples in aqua regia at 90 °C overnight. After evaporation of the aqua regia at 160 °C, the samples were dissolved in 20 mL HCl at 90 °C. The silicon content analysis was performed by Mikroanalytisches Laboratorium Kolbe (Mikrolab Kolbe), Germany.

Hydrogen chemisorption experiments were performed on a Micromeritics ASAP 2020 instrument. The catalyst was reduced at 250 °C for 2 h. After reduction, the sample was degassed for 1 h at 250 °C. The sample was then cooled to 40 °C at which the H₂ adsorption isotherm was measured. The same procedure was applied for measurements with the spent recycled overcoated catalysts. A H₂/Pt stoichiometric ratio of 0.5 was used to calculate the metal dispersion. The metallic surface area was calculated by dividing the amount of surface platinum atoms (determined from the amount of hydrogen adsorbed) by the area density of surface platinum. The particle size d was determined using the equation below:

$$d = \frac{6}{s} * \rho$$

where s = metallic surface area per gram of metal, ρ = density of the metal.[39]

Solid state ²⁷Al Magic Angle Spinning (MAS) Nuclear Magnetic Resonance (NMR) spectra were taken using a Bruker AV3 400 solid spectrometer. A high MAS rate of 12 kHz and a high magnetic field of 9.4 T helped to ensure that the spectra were quantitatively reliable. The samples were packed into a 4 mm zirconia rotor. A $\pi/12$ pulse was used for excitation, and a recycling delay of 250 ms was used. For each spectrum, a minimum of 2400 scans were

recorded. The fractions of tetrahedrally and octahedrally coordinated Al nuclei were obtained by fitting the spectra using dmfit.

Thermal Gravimetric Analysis (TGA) was performed using a Perkin–Elmer Pyris 1 apparatus. 15 mg of catalyst sample was heated with a ramp of 5 °C/min to 850 °C in a 10 mL/min air flow.

Temperature Programmed Desorption (TPD) of ammonia measurements were measured using a Micromeritics ASAP 2920 apparatus. First, about 100 mg of sample was dried *in situ* using a He flow of 10 cm³/min with a temperature ramp of 5 °C/min up to 600 °C. Subsequently, the sample was cooled to 100 °C, at this point, NH₃ was fed at 25.3 cm³/min. The sample was then heated to 600 °C with a ramp of 5 °C/min to induce desorption of NH₃. The desorbed NH₃ was quantified using a Thermal Conductivity Detector (TCD). A cold trap was used to prevent water passing through the TCD.

N₂ physisorption isotherms were measured to determine surface areas and pore volumes using a Micromeritics Tristar 3000 setup. The samples were outgassed at 150 °C overnight under a N₂ flow prior to performing the measurements at liquid nitrogen temperature. Surface areas were determined using the Brunauer–Emmett–Teller (BET) theory.

Fourier-Transform Infra-Red (FT-IR) spectra in transmission mode were measured using a Perkin-Elmer 2000 FT-IR instrument. Approximately 15 mg of the catalyst were pressed into a self-supported pellet and placed into a well-sealed cell with CaF₂ window. The wafer was first activated at 500 °C (5 °C/min) for 1 h under high vacuum (10⁻⁶ mbar). Subsequently, the cell was cooled down to 150 °C to record the spectra. After that, the sample was dosed with excess pyridine vapor, followed by high vacuum evacuation for 40 min. Literature values were used for the integrated molar extinction coefficients for quantitative determination of the Brønsted acid and Lewis acid site contents.[40]

The X-ray Photoelectron Spectroscopy (XPS) measurements were carried out on a Thermo Scientific K-Alpha spectrometer, equipped with a monochromatic small-spot X-ray source and a 180° double-focusing hemispherical analyzer with a 128-channel detector. XPS spectra were obtained using an aluminum anode (Al K α = 1486.6 eV) operating at 72 W and a spot size of 400 μ m; samples were not handled under an inert atmosphere and should be considered passivated. Survey scans were measured at constant pass energy of 200 eV and region scans at 50 eV. The background pressure of the Ultra-High Vacuum (UHV) chamber was 2 \times 10⁻⁸ mbar.

2.3. Results and Discussion

2.3.1. Catalyst characterization

To improve the hydrothermal stability of a benchmark 1 wt.% Pt/Al₂O₃ APR catalyst, the material was silylated with TEOS according to the method of Sato *et al.*[38] using three different silylation times (i.e., 4, 8 and 12 h), followed by calcination and reduction. It was previously shown that the deposited silicon content was proportional to the amount of TEOS charged, resulting in reported weight loadings of 3.8-15.6 wt.% silicon on alumina.[38]

The physicochemical properties of the overcoated materials are summarized in Table 2.1. XPS analysis showed the near-surface silicon (Si) loading in Pt/Al₂O₃-4, 8 and 12 to be 6.2, 18.0 and 33.7 wt.%, respectively. The steady increase with increased silylation time occurred as expected. On the other hand, ICP-OES analysis of the Pt/Al₂O₃-4, Pt/Al₂O₃-8 and Pt/Al₂O₃-12 samples showed bulk Si loadings of 1.1, 2.2 and 2.6 wt.%, respectively. Taken together, the results suggest preferential deposition of silica on the catalyst surface. The lower silicon loading compared to a previous report might be due to the lower surface area of the γ -alumina used in our work.[38] To investigate the effect of the sequence of synthesis steps, one reference catalyst, namely Pt/Al₂O₃-8R, was also prepared with the silylation and calcination steps preceding Pt deposition. ICP-OES analysis showed that the silicon in Pt/Al₂O₃-8R was 1.0 wt.%, which is surprisingly lower than Pt/Al₂O₃-8.

No obvious differences were seen in the XRD diffractograms of the freshly reduced catalyst before and after silylation, calcination and reduction indicating that the deposited silica layer was insufficiently thick to cause Bragg diffraction (Fig. 2.1). STEM showed that the Pt nanoparticles were highly dispersed on the parent Al₂O₃ support, with an average particle size of 1.3 ± 0.8 nm (Fig. 2.2). After silylation, calcination and reduction, the particle size in Pt/Al₂O₃-8 increased slightly to 1.5 ± 1.1 nm, indicating that the mean Pt particle sizes in the catalysts before and after surface treatment are very similar, which is in line with the H₂ chemisorption data (Table 2.1).

Table 2.1. Physicochemical properties of the different catalysts under study before and after silica deposition.

Catalyst	Pt/Al ₂ O ₃	Pt/Al ₂ O ₃ -4	Pt/Al ₂ O ₃ -8	Pt/Al ₂ O ₃ -12	Pt/Al ₂ O ₃ -8R
Pt loading ^a (wt.%)	0.83	0.76	0.71	0.68	1.0
Si content ^a (wt.%)	0	1.1	2.1	2.6	1.0
Si content ^b (wt.%)	0	1.0	2.9	5.4	ND
Metal dispersion ^c (%)	30.9	31.7	27.0	29.5	21.1
Metallic surface area ^c (m ² *g ⁻¹)	0.63	0.59	0.47	0.49	0.43
Pt particle size ^c (nm)	3.7	3.6	4.2	3.8	5.4
Pt particle size ^d (nm)	1.3	ND	1.5	ND	2.8
BET surface area ^e (m ² *g ⁻¹)	64	57	59	58	60
Acid concentration ^f (mmol*g ⁻¹)	0.35	0.30	0.27	0.18	0.25

a obtained from ICP-OES; b obtained from XPS; c obtained from H₂ chemisorption; d obtained from TEM; e obtained from N₂ physisorption; f obtained from TPD-NH₃.

A 12% decrease in accessible metal surface area was observed for sample that was treated for 8 h, and there was little change in metal surface area when the silylation time was increased to 12 h, showing that silica overcoating only leads to a limited reduction in accessible Pt surface area. As the particle size distribution did not change upon surface modification as seen by STEM (Fig. 2.2), the drop in accessible Pt surface area is attributed to partial coverage by the deposited siliceous species. One could envision that metal impregnation after overcoating would prevent such blockage of active metal surface area, but for Pt/Al₂O₃-8R, some large, agglomerated Pt nanoparticles were observed (Fig. 2.2). The larger particle size and the lower accessible metal surface area seen for Pt/Al₂O₃-8R showed that Pt dispersion is more difficult to control on the pre-modified support than on pure alumina. Similarly, studies have shown some difficulty in controlling Pt dispersion on a SiO₂ support. Lin *et al.* reported, for example, a bimodal Pt particle size distribution (1-1.5 and 4-7 nm) for SiO₂ supported catalysts, whereas Pt/Al₂O₃ showed a unimodal Pt size distribution with a mean size of 1.5 nm.[41]

The BET surface area dropped slightly as expected from 64 m²/g for the non-modified sample to 57-59 m²/g after silica deposition. Surface silica modification of γ -Al₂O₃ before Pt deposition led to an initial decrease in surface area from 70 m²/g to 61 m²/g, after which Pt impregnation led to little further change.

The ²⁷Al MAS NMR spectra of the solid catalysts before and after treatment are shown in Fig. 2.3. The ²⁷Al MAS NMR spectrum of Pt/Al₂O₃ shows the typical resonances at 8 ppm and 65 ppm, attributed to octahedrally and tetrahedrally coordinated aluminum species, respectively. [23] Expectedly, surface overcoating followed by precursor decomposition did not lead to obvious differences in the ²⁷Al MAS NMR spectrum. No peaks corresponding to pentahedrally coordinated aluminum species were observed, indicating that silica deposition leads to a surface modification only, rather than the formation of any detectable (bulk) silica-alumina phases.[42]

The effect of overcoating treatment on the total acidity of the catalyst materials, as determined by TPD-NH₃, is compared in Fig. 2.4. One broad peak of NH₃ desorption was observed in all samples. The maxima located at ~280 °C can be assigned to weak and medium strength acid sites.[43] Acid site concentration (Table 2.1) decreased with increasing modification time, similar to previous observations of selective consumption of the strong Al Lewis acid sites upon

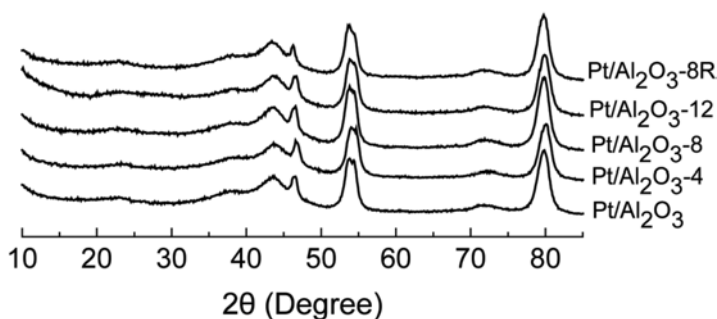


Fig. 2.1. XRD patterns of the different fresh catalysts before and after silylation.

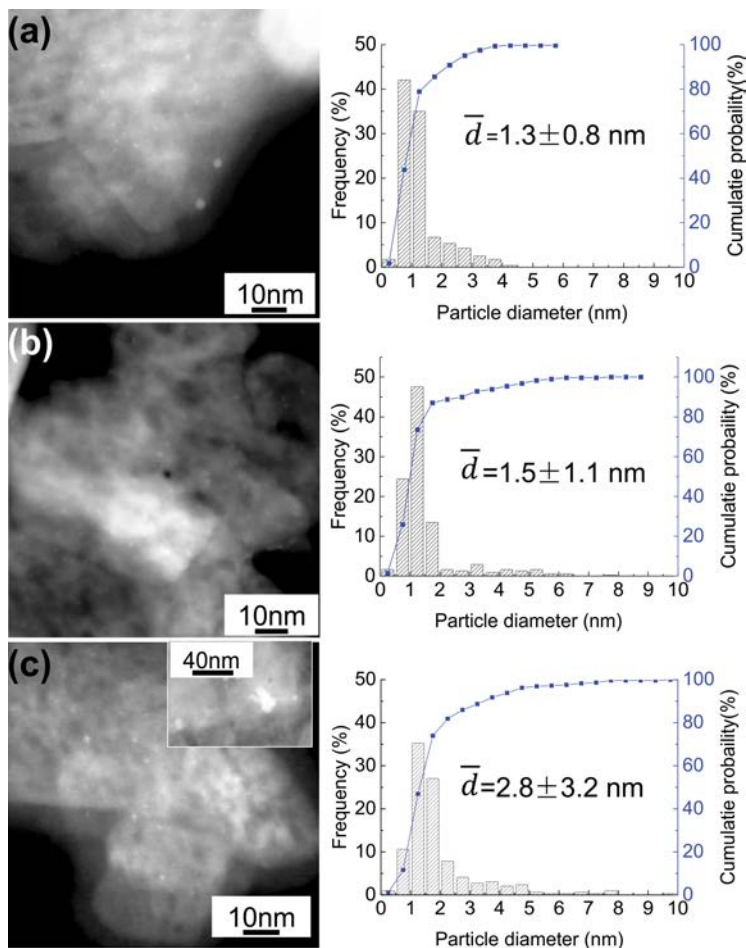


Fig. 2.2. STEM images and Pt particle size distributions of fresh (a) Pt/Al₂O₃, (b) Pt/Al₂O₃-8 and (c) Pt/Al₂O₃-8R.

exposure to TEOS.[44] Pyridine adsorption followed by FT-IR spectroscopy indicated that only Lewis Acid Sites (LAS) were present in the parent Pt/Al₂O₃ catalyst (Fig. 2.5a). However, silica deposition led to a decrease in Lewis acidity, with only about 25% of the LAS remaining in Pt/Al₂O₃-12. On the other hand, Brønsted Acid Sites (BAS) were detected for the 8 and 12 h overcoated samples, as evidenced by the appearance of the vibration at around 1545 cm⁻¹ that is characteristic for BAS.[45] Regardless of BAS formation, the amount of total acid sites of the overcoated samples dropped significantly upon modification (Table 2.2), in line with the NH₃-TPD results.

The OH region of the FT-IR spectrum of Pt/Al₂O₃ (Fig. 2.5b) shows 4 distinct peaks, corresponding to different coordination environments of the OH groups.[46] The peaks at 3765, 3725 and 3672 cm⁻¹ were assigned to terminal, doubly-bridged and triply-bridged OH groups,

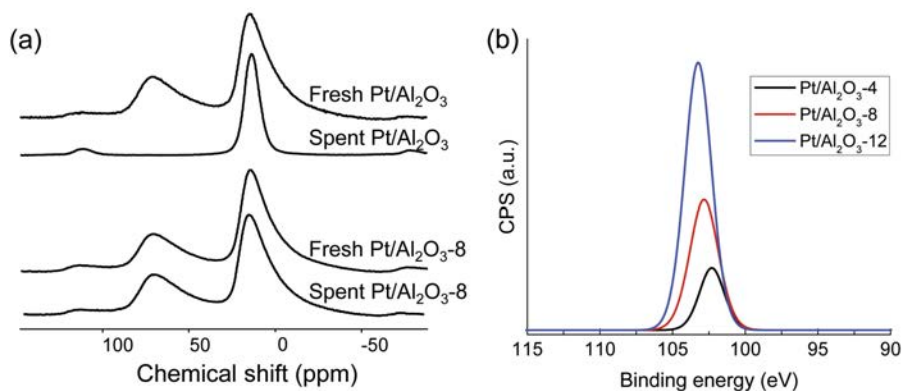


Fig. 2.3. (a) ^{27}Al NMR spectra of the Si-free catalyst and the catalyst treated by silylation, calcination and reduction before (fresh) and after (spent) APR, and (b) Si 2p XP spectra of fresh modified catalysts after background subtraction.

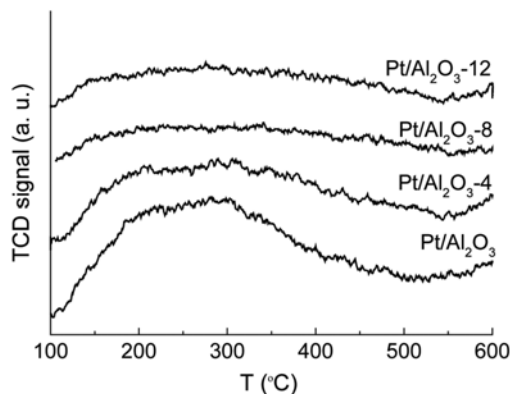


Fig. 2.4. TPD- NH_3 profiles of the different catalysts under study before and after silylation.

Table 2.2. Acid site concentration of the different catalysts under study as measured by Pyridine-IR spectroscopy.

Catalyst	Acid site concentrations ($\mu\text{mole/g}$)		
	C_{total}	Brønsted	Lewis
Pt/ Al_2O_3	618	0	618
Pt/ Al_2O_3 -4	575	0	575
Pt/ Al_2O_3 -8	365	35	330
Pt/ Al_2O_3 -12	232	59	173

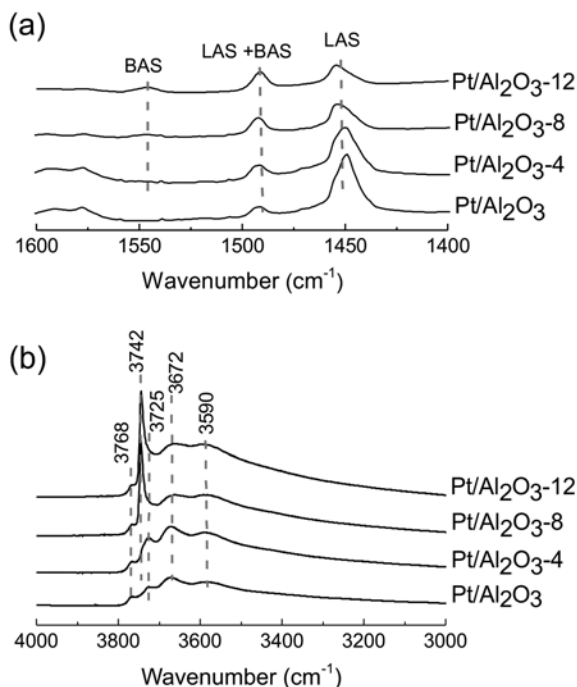


Fig. 2.5. (a) FT-IR spectra after pyridine adsorption of all catalysts under study, (b) selected OH region of the FT-IR spectra of the fresh catalysts before and after silylation.

respectively. The broad peak at 3590 cm^{-1} has been attributed to hydrogen-bonded OH groups. [47,48] Upon modification with TEOS, a sharp peak centered at 3742 cm^{-1} appeared, attributed to isolated silanols, considered to be Brønsted acid sites. [44,49] The FT-IR spectra of Pt/Al₂O₃-8 and Pt/Al₂O₃-12 showed a decrease in intensity of the absorption bands at 3672 and 3725 cm^{-1} compared to pristine Pt/Al₂O₃, suggesting that surface unsaturated Al atoms were consumed in the overcoating process. No obvious C-H vibrations were observed in the region of 2800 to 3000 cm^{-1} of any of the spectra (data not shown), indicative of complete decomposition of TEOS during calcination. [50] Given the change in catalyst acidity before and after modification, it can be inferred that Al-O-Si linkages were formed successfully at the expense of specific surface Lewis acid sites, which serve as original hydration sites for the undesired conversion to boehmite. Similarly, Mouat *et al.* suggested that TEOS modification of a γ -alumina surface preferentially occurs on strong LAS, also observing the formation of “mild” BAS. [44] As stated above, silica deposition was hypothesized to inhibit water absorption of Al₂O₃ by Al coordinative saturation of unsaturated Al species and the formation of Al-O-Si bonds, with the characterization data now suggesting that improved stability under hydrothermal conditions can indeed be anticipated.

2.3.2. Catalyst testing

In a second phase of our study, we have investigated the effect of the silica overcoating treatment on catalyst performance in the APR reaction of pure glycerol. Standard reaction conditions entailed 12 h runs of a 5 wt.% aqueous glycerol solution at 225 °C. Catalyst performance was compared in a semi-batch reactor setup, which allows for an initial assessment of activity and, upon catalyst recycling, possible catalyst deactivation.[51,52] As shown above, catalyst synthesis using silica overcoating prior to metal impregnation made controlled Pt deposition difficult and the Pt/Al₂O₃-8R sample was therefore not included in the APR tests. Fig. 2.6a shows glycerol conversion as a function of time over the different catalysts under study before and after modification. The Pt/Al₂O₃ catalyst had 100% conversion of glycerol in 5 h of reaction time. Overcoated catalysts were slower to convert glycerol, and the conversion decreased with increasing modification time. For the Pt/Al₂O₃-4 and Pt/Al₂O₃-8 catalysts, glycerol was converted completely after roughly 7 h and 11 h, respectively, whereas after 12 h 23% glycerol had not reacted over the Pt/Al₂O₃-12 catalyst.

The liquid phase composition was determined as a function of time by HPLC analysis (Fig. 2.7 and Table 2.3). The same products and intermediates were observed for non-modified and modified catalysts, including Lactic Acid (LA), Acetic Acid (AA), Ethylene Glycol (EG), Hydroxy-Acetone (HA), 1,2-Propane-Diol (1,2-PD), Acetaldehyde (Ac) and Ethanol (EtOH). Overall, the total amount of liquid products formed during APR increased upon surface modification and as a function of modification time. For instance, the yields of the liquid products for Pt/Al₂O₃ and Pt/Al₂O₃-4, Pt/Al₂O₃-8, Pt/Al₂O₃-12 were 11%, 16%, 24% and 29%, respectively, at ~60% glycerol conversion. Among those liquid products, the amount of HA and 1,2-PD increased significantly as a function of modification time. In particular, the selectivity to HA was 8 times higher for the 12 h treated sample than the non-modified sample due to the increased Brønsted acidity of the silica-containing samples. Online gas phase analysis showed the expected formation of H₂ and CO₂, as well as some minor amounts of methane. Only trace amounts of CO were detected in all experiments, illustrative of efficient water-gas shift activity. Fig. 2.6b shows the H₂ production rate as a function of reaction time over the bare and overcoated

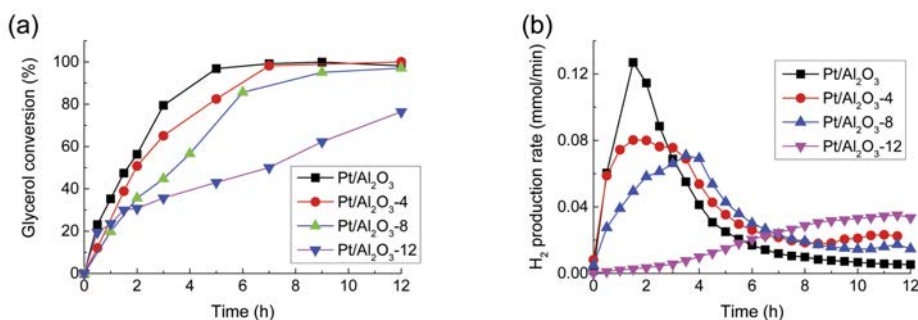


Fig. 2.6. Time profiles of (a) glycerol conversion and (b) H₂ production rate over the different catalysts under study before and after silylation.

fresh catalysts, with hydrogen formation clearly decreasing with increasing modification time. The H_2 selectivity of the Pt/Al_2O_3 -4 catalyst was 73%, which is comparable to that of the parent catalyst (72%). However, longer treatment time resulted in a drop in H_2 selectivity to 66% and 47% for the Pt/Al_2O_3 -8 and Pt/Al_2O_3 -12 catalysts. This decreased selectivity for H_2 production is in line with the increase in the production of liquid products.

H_2 production requires high reforming and water-gas shift activities, with the initial step being the dehydrogenation of glycerol to generate glyceraldehyde/pyruvaldehyde, followed rapid C-C bond cleavage by decarbonylation.[53] Dehydration reactions and reactions consuming hydrogen, such as the transformation of glycerol to 1,2-Propylene-Glycol (1,2-PG) by acid-catalyzed dehydration to HA followed by hydrogenation, should be avoided.[54,55] Obviously, higher selectivity towards HA and 1,2-PD leads to lower H_2 production as they are the products formed by an initial dehydration rather than dehydrogenation step.[55] Of course, Brønsted acid sites play a key role in promoting such dehydration reactions.[56] In our case, silica deposition resulted in the generation of Brønsted acid sites at the expense of Lewis acid sites, causing the increase in undesired dehydration side reactions, hindering H_2 production with the silylated samples.

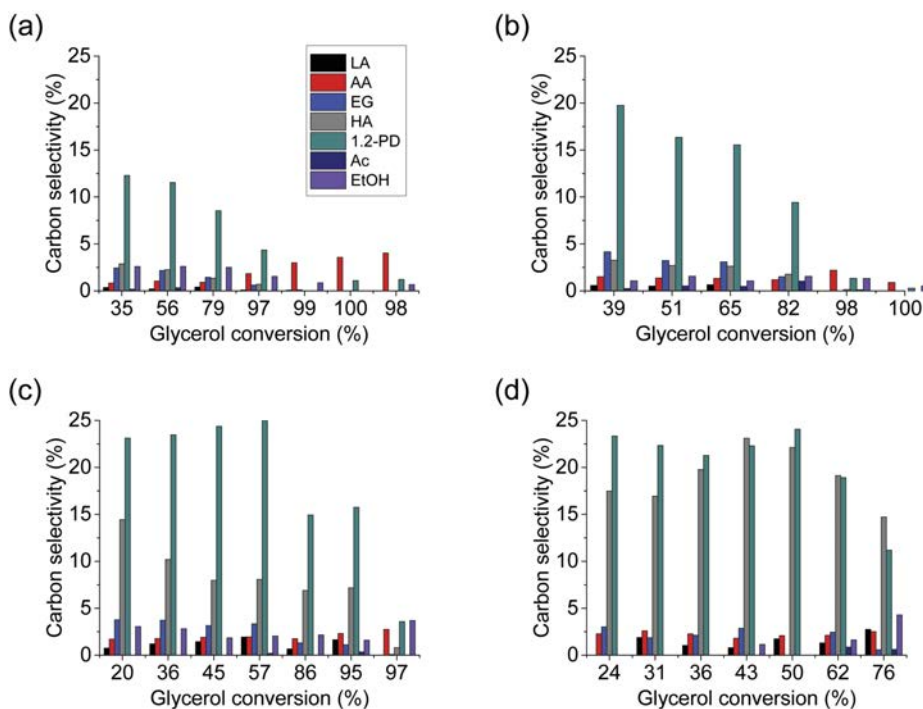


Fig. 2.7. Product distributions as a function of glycerol conversion for (a) Pt/Al_2O_3 , (b) Pt/Al_2O_3 -4, (c) Pt/Al_2O_3 -8 and (d) Pt/Al_2O_3 -12.

Table 2.3. Liquid phase product selectivities (S) and yields (Y) as a function of glycerol conversion (X) for Pt/Al₂O₃, Pt/Al₂O₃-4, Pt/Al₂O₃-8 and Pt/Al₂O₃-12 APR.^a

Time (h)	Gly	LA		AA		EG		HA		1, 2-PD		Ac		EtOH	
	X	S	Y	S	Y	S	Y	S	Y	S	Y	S	Y	S	Y
Pt/Al ₂ O ₃															
0	0	0	0	0	0	0	0	0	0	0	0	0	0	0	0
1	35	<1	<1	1	<1	2	1	3	1	12	4	0	0	3	1
2	56	<1	<1	1	<1	2	1	2	1	12	7	<1	<1	3	1
3	79	<1	<1	1	<1	1	1	1	1	9	7	<1	<1	3	2
5	97	<1	<1	2	<1	1	1	1	1	4	4	0	0	2	1
7	99	<1	<1	3	<1	0	0	0	0	0	0	0	0	1	1
9	100	0	0	4	4	0	0	0	0	1	1	0	0	0	0
12	98	0	0	4	4	0	0	0	0	1	1	0	0	1	1
Pt/Al ₂ O ₃ -4															
0	0	0	0	0	0	0	0	0	0	0	0	0	0	0	0
1.5	39	1	<1	2	1	4	2	3	1	20	8	<1	<1	1	<1
2	51	1	<1	1	1	3	2	3	1	16	8	1	<1	2	1
3	65	1	<1	1	1	3	2	3	2	16	10	<1	<1	1	1
5	82	0	0	1	1	2	1	2	1	9	8	1	1	2	1
7	98	0	0	2	2	0	0	0	0	1	1	<1	<1	1	1
12	100	0	0	1	1	0	0	0	0	0	0	0	0	1	1
Pt/Al ₂ O ₃ -8															
0	0	0	0	0	0	0	0	0	0	0	0	0	0	0	0
1	20	1	<1	2	<1	4	1	14	3	23	5	0	0	3	1
2	36	1	<1	2	1	4	1	10	4	23	8	0	0	3	1
3	45	1	1	2	1	3	1	8	4	24	11	0	0	2	1
4	57	2	1	2	1	3	2	8	5	25	14	<1	<1	2	1
6	86	1	1	2	2	1	1	7	6	15	13	0	0	2	2
9	95	2	2	2	2	1	1	7	7	16	15	<1	<1	2	2
12	97	0	0	3	3	<1	<1	1	1	4	3	0	0	4	4
Pt/Al ₂ O ₃ -12															
0	0	0	0	0	0	0	0	0	0	0	0	0	0	0	0
1	24	0	0	2	1	3	1	17	4	23	5	0	0	0	0
2	31	2	1	3	1	2	1	17	5	22	7	0	0	0	0
3	36	1	0	2	1	2	1	20	7	21	8	0	0	0	0
5	43	1	0	2	1	3	1	23	10	22	10	0	0	1	0
7	50	2	1	2	1	0	0	22	11	24	12	0	0	0	0
9	62	1	1	2	1	2	2	19	12	19	12	1	1	2	1
12	76	3	2	3	2	1	<1	15	11	11	9	1	<1	4	3

^a see experimental section for definitions of C, Y, and S; Gly, glycerol; LA, lactic acid; AA, acetic acid; EG, ethylene glycol; HA, hydroxyacetone; 1, 2-PD, 1, 2-propanediol; Ac, acetaldehyde; EtOH, ethanol.

The spent APR catalysts were characterized by XRD, ^{27}Al NMR, TGA, STEM and N_2 physisorption to better understand the impact of surface silica deposition on the support layer stability of the catalyst during the APR reaction.

As expected, after 12 h of APR, $\text{Pt}/\text{Al}_2\text{O}_3$ catalyst was fully converted to boehmite. Fig. 2.8 shows the sharp diffraction peaks at $2\theta = 16.8^\circ$, 32.9° , 44.9° , 57.5° and 57.9° , which correspond to the (020), (120), (140), (031), (051) and (200) crystal planes of boehmite, respectively.[23,27] Boehmite formation was also seen for $\text{Pt}/\text{Al}_2\text{O}_3$ -4, albeit to a much lesser extent given the low intensity and broadness of the boehmite diffraction peaks. In contrast, no sign of crystalline boehmite was detected in the XRD patterns of the samples that were overcoated for 8 and 12 h. This clearly shows that, depending on the degree of modification, boehmite formation can be slowed down or prevented. As mentioned above, the support phase transformation should lead to a severe loss of surface area. Indeed, an 86% decrease in surface area was observed for the spent non-modified catalyst (Table 2.4), in line with the XRD results. Additionally, this decrease is associated with a significant decrease of pore volume (Table 2.4). The surface area of the spent $\text{Pt}/\text{Al}_2\text{O}_3$ -4 catalyst increased remarkably up to $69 \text{ m}^2/\text{g}$, which is attributed to surface pitting, as a result of small boehmite particle formation.[57] Conversely, there was no significant drop in surface area seen for the 8 h overcoated sample.

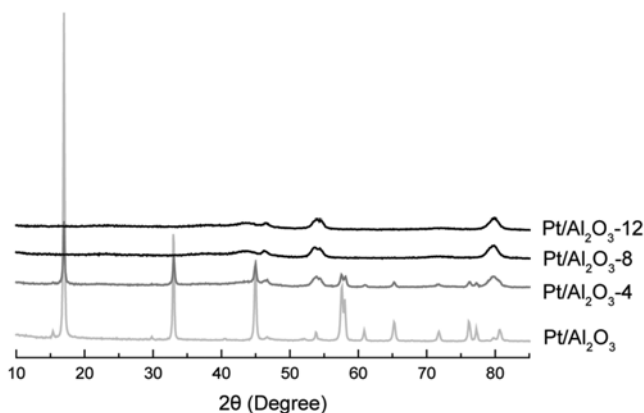


Fig. 2.8. XRD patterns of recovered, spent (non-)silylated catalysts after 12 h of APR reaction.

Table 2.4. Physicochemical properties of the spent APR catalysts before and after silylation.

Catalyst		BET surface area (m^2g^{-1})	Pore volume (cm^3g^{-1})
$\text{Pt}/\text{Al}_2\text{O}_3$	Fresh	64	0.23
	Spent	10	0.03
$\text{Pt}/\text{Al}_2\text{O}_3$ -8	Fresh	59	0.20
	Spent	53	0.25

STEM images of the Pt/ Al_2O_3 and Pt/ Al_2O_3 -8 spent catalysts corroborate the differences seen by XRD and N_2 physisorption (Fig. 2.9). After 12 h of APR reaction, flake-like boehmite patches are seen for Pt/ Al_2O_3 catalyst, with sharp edges suggesting crystallinity. Large black clusters, identified by an EDX line scan as Pt, show that significant metal sintering happened during the APR process along with the support transformation. In stark contrast, no obvious differences in support morphology are seen for the 8 h overcoated sample before and after reaction. Some minor sintering did occur, though, with the mean particle size increasing from 1.5 ± 1.1 to 2.2 ± 1.6 nm for the spent Pt/ Al_2O_3 -8 catalyst, similar to previous observations in which Pt sintering was suppressed by protective layers deposited by atomic layer deposition or liquid-phase methods.[58–61]

The TGA profiles of the spent catalysts after 12 h APR reaction are shown in Fig. 2.10. The TGA traces can be roughly divided into 4 temperature regions based on the Differential Thermal Gravimetric Analysis (DTG) (Table 2.5). Weight loss between 50–180 °C is attributed to removal of adsorbed water. The second weight loss event occurs at 180–390 °C due to the desorption of interstitial H_2O and/or the desorption or decomposition of any adsorbed carbon-containing species, including carbonaceous deposits.[62] In the third temperature range of 390–650 °C, weight loss is normally attributed to water release due to the dehydration that occurs upon the phase transition of the support from boehmite back to $\gamma\text{-Al}_2\text{O}_3$.[63] Weight loss at temperatures above 650 °C may be assigned to dehydroxylation of the support.[21] The weight loss in the temperature range from 390–650 °C, indicative for the extent of boehmite formation, drops with increasing modification time, with only 0.9% weight loss being detected

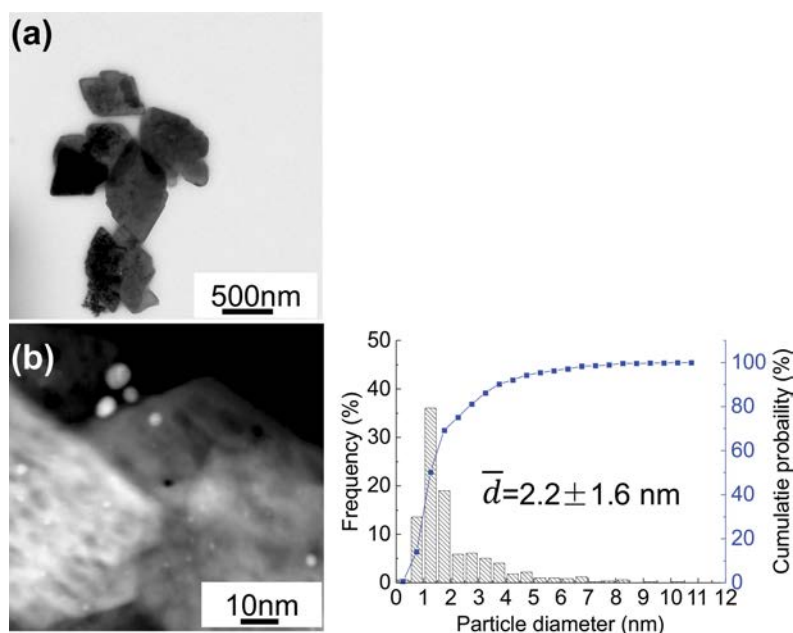


Fig. 2.9. STEM images of the spent (a) Pt/ Al_2O_3 and (b) Pt/ Al_2O_3 -8 catalysts.

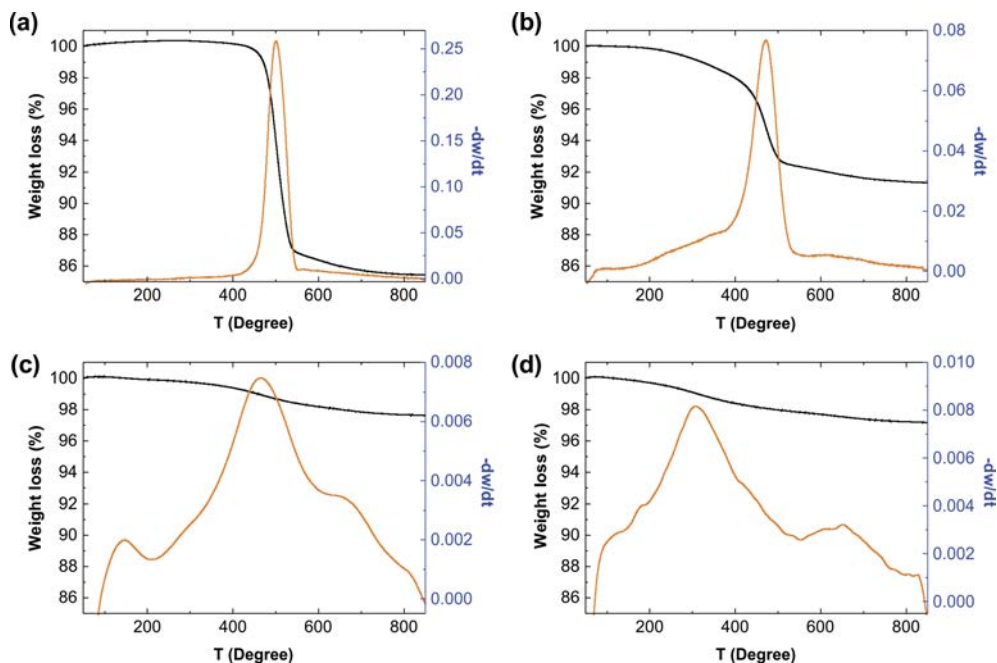


Fig. 2.10. TGA (black) and inverted DTG (orange) curves of the spent (a) Pt/Al₂O₃, (b) Pt/Al₂O₃-4, (c) Pt/Al₂O₃-8 and (d) Pt/Al₂O₃-12 catalyst materials.

Table 2.5. Weight loss divided over four temperature regions for the spent catalysts after APR reaction.

Spent catalyst	Weight loss (%)				
	Total	50-180 °C	180-390 °C	390-650 °C	650-850 °C
Pt/Al ₂ O ₃	14.6	0.0	0.0	14.0	0.6
Pt/Al ₂ O ₃ -4	8.7	0.1	1.8	6.3	0.5
Pt/Al ₂ O ₃ -8	2.4	0.1	0.5	1.4	0.4
Pt/Al ₂ O ₃ -12	2.8	0.2	1.3	0.9	0.4

for the spent Pt/Al₂O₃-12 catalyst, compared to 14.6% for the non-overcoated catalyst material. Besides, there is no weight loss in the temperature range of 180-390 °C for ethanol-washed Pt/Al₂O₃, indicating that carbonaceous deposits do not contribute to the deactivation seen for Pt/Al₂O₃.

Boehmite formation was further quantified by ²⁷Al MAS NMR spectroscopy, with the boehmite fraction being determined by linear combination of the spectra of γ-Al₂O₃ and boehmite. The NMR spectrum of spent Pt/Al₂O₃ exhibited only octahedrally coordinated aluminum, suggesting quantitative conversion of the alumina support (Fig. 2.3 and Table 2.6) into boehmite.[64] In contrast, the octahedrally coordinated aluminum fraction in Pt/Al₂O₃-8

increased slightly from 68% to 70%, indicating that only 6% of the Al nuclei were present as boehmite. A previous study demonstrated that the formation of organic acids can have a negative effect on alumina catalyst stability.[65] In our case, the total yield of organic acids (LA+AA) is higher for overcoated catalysts than for the parent catalyst. This again suggests that surface silica deposition does indeed increase the hydrothermal stability of the catalyst, with the Pt/Al₂O₃-8 catalyst showing the best results in terms of both activity and stability.

2.3.3. Catalyst recycling experiments

The hydrolytic stability of the APR catalyst materials, taking the Pt/Al₂O₃-8 catalyst as a showcase, was further evaluated by reusing this catalyst during subsequent recycle tests. Normalized H₂ production rates are given to compare the catalytic activity after reusing the catalyst material several times. Obviously, H₂ production was inhibited completely for non-modified Pt/Al₂O₃ catalyst after first use (Fig. 2.11a). In contrast, the Pt/Al₂O₃-8 catalyst showed essentially the same hydrogen productivity profile for the first reuse (Fig. 2.11b). Interestingly, upon second reuse,

Table 2.6. Summary of boehmite formation characteristics for spent and recycled Pt/Al₂O₃ and Pt/Al₂O₃-8 materials.

		Octahedral Al (%)	Tetrahedral Al (%)	Boehmite fraction (%)
Pt/Al ₂ O ₃	Fresh	67	33	0
	Spent	100	0	100
Pt/Al ₂ O ₃ -8	Fresh	68	32	0
	Spent	70	30	6
	Recycle 1	69	38	4
	Recycle 2	71	29	10
	Recycle 4	84	16	51

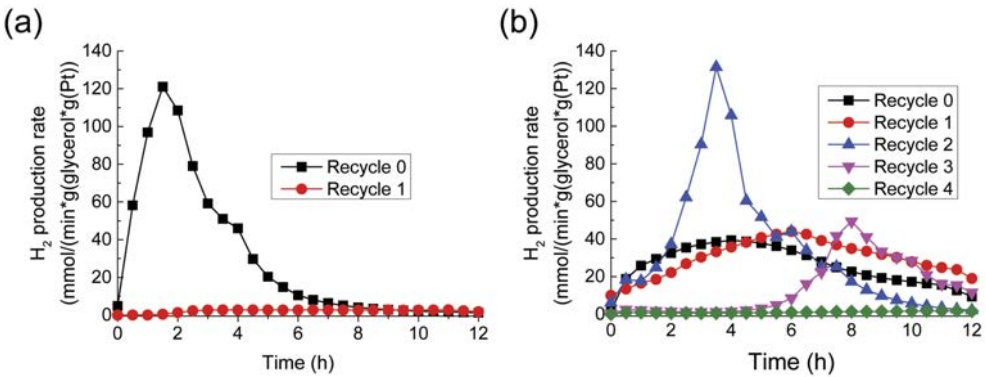


Fig. 2.11. Time profiles of H₂ production rate in recycle tests of the (a) Pt/Al₂O₃ and (b) Pt/Al₂O₃-8 catalyst material.

a clear increase in H_2 production rate was observed, showing a profile similar to the fresh, non-modified Pt/Al_2O_3 sample. Upon further recycling, hydrogen productivity drops greatly, with essentially no hydrogen being produced in the fourth recycle run. These results thus show that catalyst lifetime could be prolonged from 12 h to 36 h, but also that deactivation, presumably by removal of the protective layers by Si-O-Si and Si-O-Al bond hydrolysis and eventually boehmite formation, ultimately does occur.

The spent Pt/Al_2O_3 -8 catalyst recovered after recycling was characterized by various physicochemical techniques, including XRD, STEM, TGA and ^{27}Al MAS-NMR. The XRD patterns clearly show that the spent catalyst after the first recycle still did not exhibit any evidence for the formation of new crystalline structures (Fig. 2.12). However, after the second reuse, the first evidence of boehmite formation was seen, with boehmite peaks increasing in intensity upon further recycling.

^{27}Al MAS-NMR spectroscopic analysis of the reused catalysts provided insight into the extent of boehmite formation upon recycling (Fig. 2.13 and Table 2.6). The amount of octahedrally coordinated aluminum in the spent catalysts recovered the first and second recycle were 69% and 71%, corresponding to 4% and 10% boehmite formation, respectively. However, the fraction of octahedrally coordinated aluminum increased greatly to 84% after the fourth recycle, indicating

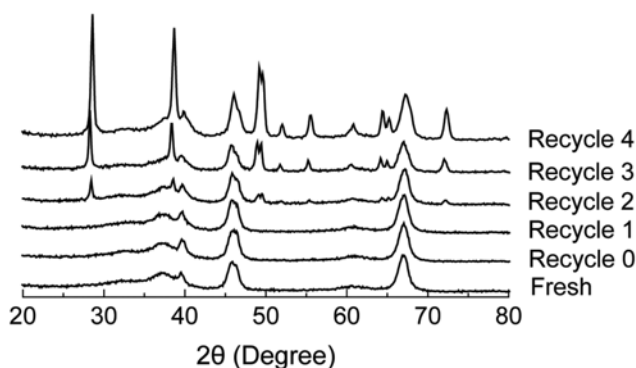


Fig. 2.12. XRD patterns of the fresh Pt/Al_2O_3 -8 and spent Pt/Al_2O_3 -8 after different recycle tests.

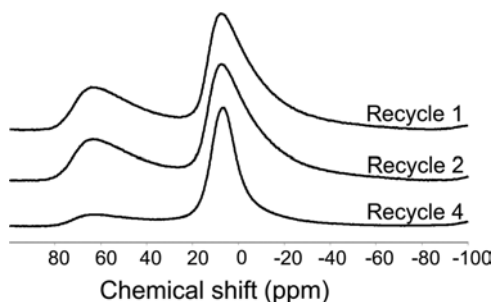


Fig. 2.13. ^{27}Al NMR spectra of the spent Pt/Al_2O_3 -8 catalyst from different recycle tests.

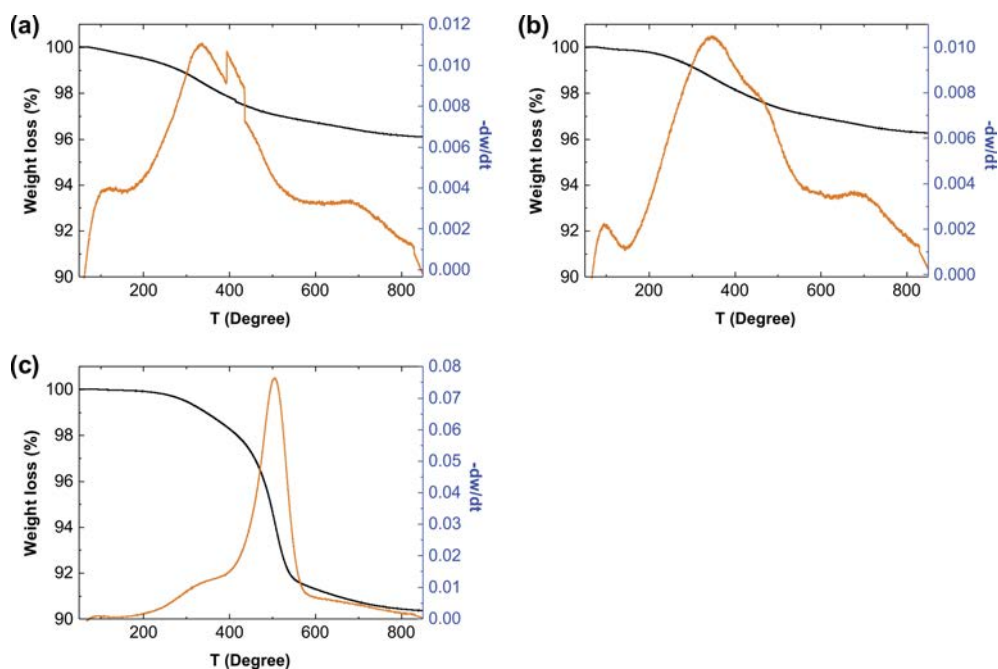
Table 2.7. Physicochemical properties of the Pt/Al₂O₃-8 catalyst after subsequent recycle tests.

	Recycle number			
	0	1	2	4
BET surface area (m ² *g ⁻¹) ^a	53	56	66	52
Pore volume (cm ³ *g ⁻¹) ^a	0.25	0.24	0.28	0.25
Leached Si (mg*kg _(reaction solution) ⁻¹) ^b	0.02	0.01	0.01	0.01

a obtained from N₂ physisorption; b obtained from ICP-OES test on reaction solutions.

Table 2.8. Weight loss in the four temperature regions for the Pt/Al₂O₃-8 samples after subsequent recycle tests.

Recycle number	Weight loss (%)				
	Total	50-180 °C	180-390 °C	390-650 °C	650-850 °C
1	3.9	0.4	1.7	1.3	0.5
2	3.7	0.2	1.6	1.5	0.5
4	9.6	0.0	1.5	7.4	0.6


Fig. 2.14. TGA (black) and inverted DTG (orange) curves of the spent Pt/Al₂O₃-8 catalyst from different recycle tests.

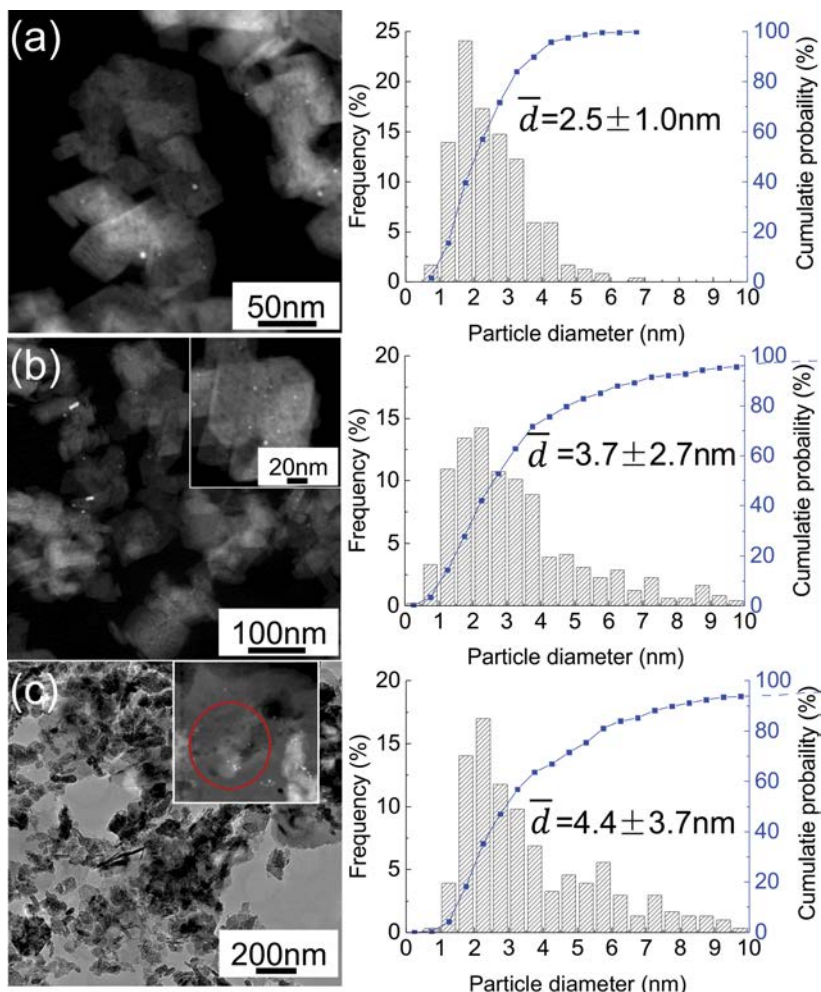


Fig. 2.15. STEM images and the corresponding particle size distribution for the spent Pt/Al₂O₃-8 catalyst from (a) 1st recycle, (b) 2nd recycle and (c) 4th recycle.

that 51% of the support had transformed. In accordance with NMR analysis, the weight loss in the temperature range of 180-390 °C from TGA analysis of reused catalysts showed similar changes (Fig. 2.14 and Table 2.8). Compared to the fresh Pt/Al₂O₃-8 catalyst, little variation was observed for the surface area of the spent catalysts during the original reaction and the first recycle (Table 2.7). However, the surface area of spent Pt/Al₂O₃-8 after the second recycle increased remarkably up to 66 m²/g, which is comparable to that of the fresh non-overcoated catalyst. This surface area increase is attributed to surface pitting, as a result of small boehmite particle formation.[57] After that, the surface area of the spent catalyst decreased again due to structural collapse of alumina support, consistent with the transformation observed by XRD and NMR.

STEM analysis of the reused catalysts (Fig. 2.15) showed the mean size of Pt particles in Pt/ Al_2O_3 -8 to increase from 1.5 nm for the fresh catalyst to 2.5, 3.7 and 4.4 nm for the spent catalyst after the first, second and fourth recycle, respectively. The spent Pt/ Al_2O_3 -8 catalyst obtained after the first and second recycles showed morphologies similar to the fresh sample (Fig. 2.15). However, after the fourth recycle, clear differences in the morphology of the alumina support can be seen. Specifically, the amorphous alumina phase of the fresh catalyst changed to flake-like boehmite patches. In addition, the Pt particles and bulk alumina phase seem enveloped by a thin layer (red circle in Fig. 2.15c). The STEM images are consistent with previous studies that showed the encapsulation of Pt nanoparticles by boehmite after APR reaction.[66,67] As a result of alumina phase collapse, the accessible metal surface area of Pt/ Al_2O_3 -8 decreased by 60% from 0.47 m^2/g to 0.19 m^2/g after the fourth recycle. ICP-OES analysis of the solution after reaction did not show any Pt leaching, but low concentrations of silicon were detected upon recycling (Table 2.7). Evidently, the deposited silica species are gradually hydrolyzed from the support under APR conditions, as a result of Si-O bond cleavage due to the nucleophilic attack of water.[68] Taken together, the results suggest that even though surface silica deposition is not a permanent solution against catalyst deactivation during reactions in hot liquid water, it does have a positive effect on catalyst lifetime.

2.4. Conclusions

In this PhD chapter we have shown that the hydrothermal stability of a Pt/ Al_2O_3 APR catalyst is enhanced by silylation, followed by calcination and reduction with tetraethylorthosilicate as silicon source. Catalyst characterization shows that silica deposition does not significantly alter the catalyst parent morphology, but results in a partial coverage of the active Pt metal phase. Silica deposition on Pt/ Al_2O_3 rather than the bare support is preferred, as controlled Pt deposition on silica-containing Al_2O_3 is difficult. FT-IR analysis shows that Al-O-Si bonds are generated at the expense of specific LAS of the alumina support, giving rise to the generation of BAS. Total acidity, however, is found to decrease upon surface modification. As a result of BAS formation and partial Pt metal blockage, the catalytic activity for APR of glycerol, as evidenced by the H_2 production rates, decreases upon modification. Based on XRD, STEM, ^{27}Al NMR and TGA characterization of the (recycled) catalysts, silica modification is shown to retard the support transformation process significantly. An 8 h overcoating treatment increases the lifetime of the catalyst three times from 12 to 36 h compared to the non-modified catalyst. These results clearly show that silica deposition can considerably improve catalyst stability in polar aqueous media, but also that more efficient methods of anchoring protective layers are needed.

References

1. J.Q. Bond, A.A. Upadhye, H. Olcay, G.A. Tompsett, J. Jae, R. Xing, D.M. Alonso, D. Wang, T. Zhang, R. Kumar, A. Foster, S.M. Sen, C.T. Maravelias, R. Malina, S.R.H. Barrett, R. Lobo, C.E. Wyman, J.A. Dumesic, G.W. Huber, *Energy Environ. Sci.* 7 (2014) 1500–1523.
2. D.M. Alonso, J.Q. Bond, J.A. Dumesic, *Green Chem.* 12 (2010) 1493–1513.
3. G.W. Huber, J.A. Dumesic, *Catal. Today* 111 (2006) 119–132.
4. M.C. Kim, T.W. Kim, H.J. Kim, C.U. Kim, J.W. Bae, *Renew. Energy* 95 (2016) 396–403.
5. N.D. Subramanian, J. Callison, C.R.A. Catlow, P.P. Wells, N. Dimitratos, *Int. J. Hydrog. Energy* 41 (2016) 18441–18450.
6. G. Wen, Y. Xu, H. Ma, Z. Xu, Z. Tian, *Int. J. Hydrog. Energy* 33 (2008) 6657–6666.
7. N.H. Tran, G.S.K. Kannangara, *Chem. Soc. Rev.* 42 (2013) 9454–9479.
8. A. Seretis, P. Tsiakaras, *Renew. Energy* 85 (2016) 1116–1126.
9. M. Pagliaro, R. Ciriminna, H. Kimura, M. Rossi, C. Della Pina, *Angew. Chem. Int. Ed.* 46 (2007) 4434–4440.
10. J.J. Bozell, G.R. Petersen, *Green Chem.* 12 (2010) 539–554.
11. C.H. Zhou, H. Zhao, D.S. Tong, L.M. Wu, W.H. Yu, *Catal. Rev.* 55 (2013) 369–453.
12. Y.C. Lin, *Int. J. Hydrogen Energy* 38 (2013) 2678–2700.
13. A. Ciftci, D.A.J.M. Ligthart, E.J.M. Hensen, *Green Chem.* 16 (2014) 853–863.
14. I. Coronado, M. Stekrova, M. Reinikainen, P. Simell, L. Lefferts, J. Lehtonen, *Int. J. Hydrogen Energy* 41 (2016) 11003–11032.
15. R.R. Davda, J.A. Dumesic, *Chem. Commun.* 10 (2004) 36–37.
16. T. Nozawa, Y. Mizukoshi, A. Yoshida, S. Naito, *Appl. Catal. B Environ.* 146 (2014) 221–226.
17. R.R. Davda, J.W. Shabaker, G.W. Huber, R.D. Cortright, J.A. Dumesic, *Appl. Catal. B Environ.* 43 (2003) 13–26.
18. C. Chizallet, P. Raybaud, *Catal. Sci. Technol.* 4 (2014) 2797–2813.
19. J.P. Lange, *Angew. Chem. Int. Ed.* 54 (2015) 13187–13197.
20. F. Héroguel, B. Rozmysłowicz, J.S. Luterbacher, *Chimia* 69 (2015) 582–591.
21. G. Lefèvre, M. Duc, P. Lepeut, R. Caplain, M. Fédoroff, *Langmuir* 18 (2002) 7530–7537.
22. D.D. MacDonald, P. Butler, *Corros. Sci.* 13 (1973) 259–274.
23. R.M. Ravenelle, J.R. Copeland, W.G. Kim, J.C. Crittenden, C. Sievers, *ACS Catal.* 1 (2011) 552–561.
24. C. Sievers, Y. Noda, L. Qi, E.M. Albuquerque, R.M. Rioux, S.L. Scott, *ACS Catal.* 6 (2016) 8286–8307.
25. J.R. Copeland, X.R. Shi, D.S. Sholl, C. Sievers, *Langmuir* 29 (2013) 581–593.
26. R.M. Ravenelle, J.R. Copeland, A.H. Van Pelt, J.C. Crittenden, C. Sievers, *Top. Catal.* 55 (2012) 162–174.
27. A.L. Jongerius, J.R. Copeland, G.S. Foo, J.P. Hofmann, P.C.A. Bruijninx, C. Sievers, B.M. Weckhuysen, *ACS Catal.* 3 (2013) 464–473.
28. M. Absi-Halabi, A. Stanislaus, H. Al-Zaid, *Appl. Catal. A Gen.* 101 (1993) 117–128.
29. R. Espinoza, K. Jothimurugesan, Y. Jin, B.C. Ortego, K. Fjare, *Stabilized Boehmite-Derived Catalyst Supports, Catalysts, Methods of Making and Using*, US 20080039539 A1, 2007.
30. Y. Jin, R. Espinoza, N. Srinivasan, O.P. Ionkina, *Stabilized Transition Alumina Catalyst Support from Boehmite and Catalysts Made Therefrom*, US7402612 B2, 2003.
31. A.J. Byrd, R.B. Gupta, *Appl. Catal. A Gen.* 381 (2010) 177–182.
32. H.N. Pham, A.E. Anderson, R.L. Johnson, K. Schmidt-Rohr, A.K. Datye, *Angew. Chem. Int. Ed.* 51 (2012) 13163–13167.

33. H. Xiong, T.J. Schwartz, N.I. Andersen, J.A. Dumesic, A.K. Datye, *Angew. Chem. Int. Ed.* 54 (2015) 7939–7943.
34. M.C. Capel-Sanchez, L. Barrio, J.M. Campos-Martin, J.L.G. Fierro, *J. Colloid Interface Sci.* 277 (2004) 146–153.
35. A.M. Fidalgo, L.M. Ilharco, *Microporous Mesoporous Mater.* 158 (2012) 39–46.
36. L.A.S.A. Prado, M. Sriyai, M. Ghislandi, A. Barros-Timmons, K. Schulte, J. Braz. Chem. Soc. 21 (2010) 2238–2245.
37. P.A. Zapata, J. Faria, M.P. Ruiz, R.E. Jentoft, D.E. Resasco, *J. Am. Chem. Soc.* 134 (2012) 8570–8578.
38. S. Sato, R. Takahashi, T. Sodesawa, D. Shin, N. Ichikawa, K. Ogura, *Bull. Chem. Soc. Jpn.* 79 (2006) 649–655.
39. A.G. Shastri, J. Schwank, *J. Catal.* 95 (1985) 271–283.
40. J. Datka, *J. Catal.* 135 (1992) 186–199.
41. W. Lin, A.A. Herzing, C.J. Kiely, I.E. Wachs, *J. Phys. Chem. C* 112 (2008) 5942–5951.
42. M. Williams, B. Fonfe, C. Sievers, A. Abraham, J. Vanbokhoven, A. Jentys, J. Vanveen, J. Lercher, *J. Catal.* 251 (2007) 485–496.
43. D. Huang, M. Ke, X. Bao, H. Liu, *Ind. Eng. Chem. Res.* 55 (2016) 1192–1201.
44. A.R. Mouat, C. George, T. Kobayashi, M. Pruski, R.P. van Duyne, T.J. Marks, P.C. Stair, *Angew. Chem. Int. Ed.* 54 (2015) 13346–13351.
45. C.A. Emeis, *J. Catal.* 141 (1993) 347–354.
46. M. Digne, P. Sautet, P. Raybaud, P. Euzen, H. Toulhoat, *J. Catal.* 211 (2002) 1–5.
47. T. Armaroli, T. Bécue, S. Gautier, *Oil Gas Sci. Technol.* 59 (2004) 215–237.
48. G. Busca, V. Lorenzelli, G. Ramis, R.J. Willey, *Langmuir* 9 (1993) 1492–1499.
49. E. Brunner, *Catal. Today* 38 (1997) 361–376.
50. M. Guisnet, P. Andy, N.S. Gnep, C. Travers, E. Benazzi, *Progress in Zeolite and Microporous Materials*, 1st ed., Elsevier, Amsterdam, 1996.
51. G.W. Huber, J.W. Shabaker, S.T. Evans, J.A. Dumesic, *Appl. Catal. B Environ.* 62 (2006) 226–235.
52. D.A. Boga, R. Oord, A.M. Beale, Y.M. Chung, P.C.A. Bruijninx, B.M. Weckhuysen, *ChemCatChem* 5 (2013) 529–537.
53. A. Wawrzetz, B. Peng, A. Hrabar, A. Jentys, A.A. Lemonidou, J.A. Lercher, *J. Catal.* 269 (2010) 411–420.
54. R.D. Cortright, R.R. Davda, J.A. Dumesic, *Nature* 418 (2002) 964–967.
55. A. Ciftci, B. Peng, A. Jentys, J.A. Lercher, E.J.M. Hensen, *Appl. Catal. A Gen.* 431–432 (2012) 113–119.
56. R. Weingarten, G.A. Tompsett, W.C. Conner, G.W. Huber, *J. Catal.* 279 (2011) 174–182.
57. H. Xiong, H.N. Pham, A.K. Datye, *Green Chem.* 16 (2014) 4627–4643.
58. J.W. Han, C. Kim, J.S. Park, H. Lee, *ChemSusChem* 7 (2014) 451–456.
59. J. Lu, B. Fu, M.C. Kung, G. Xiao, J.W. Elam, H.H. Kung, P.C. Stair, *Science* 335 (2012) 1205–1208.
60. F. Héroguel, B.P. Le Monnier, K.S. Brown, J.C. Siu, J.S. Luterbacher, *Appl. Catal. B Environ.* 218 (2017) 643–649.
61. B.J. O'Neill, D.H.K. Jackson, A.J. Crisci, C.A. Farberow, F. Shi, A.C. Alba-Rubio, J. Lu, P.J. Dietrich, X. Gu, C.L. Marshall, P.C. Stair, J.W. Elam, J.T. Miller, F.H. Ribeiro, P.M. Voyles, J. Greeley, M. Mavrikakis, S.L. Scott, T.F. Kuech, J.A. Dumesic, *Angew. Chem. Int. Ed.* 52 (2013) 13808–13812.
62. M. El Doukkali, A. Iriondo, J.F. Cambra, I. Gandarias, L. Jalowiecki-Duhamel, F. Dumeignil, P.L. Arias, *Appl. Catal. A Gen.* 472 (2014) 80–91.
63. M. El Doukkali, A. Iriondo, J.F. Cambra, P.L. Arias, *Top. Catal.* 57 (2014) 1066–1077.
64. M. Trueba, S.P. Trasatti, *Eur. J. Inorg. Chem.* (2005) 3393–3403.
65. D.J.M. de Vlieger, L. Lefferts, K. Seshan, *Green Chem.* 16 (2014) 864–xxx.
66. K. Koichumanova, A.K.K. Vikla, D.J.M. de Vlieger, K. Seshan, B.L. Mojét, L. Lefferts, *ChemSusChem* 6 (2013) 1717–1723.
67. D.J.M. de Vlieger, B.L. Mojét, L. Lefferts, K. Seshan, *J. Catal.* 292 (2012) 239–245.

Chapter 2

68. R.M. Ravenelle, F. Schüßler, A. D'Amico, N. Danilina, J.A. van Bokhoven, J.A. Lercher, C.W. Jones, C. Sievers, J. Phys. Chem. C 114 (2010) 19582–19595.

3

**Phase-Dependent Stability and
Substrate-Induced Deactivation by
Strong Metal-Support
Interaction of Ru/TiO₂ Catalysts for
the Hydrogenation of Levulinic Acid**

Abstract

The choice of support and solvent has a profound influence on catalyst performance in liquid phase hydrogenation reactions, including the catalytic hydrogenation of biomass-derived levulinic acid (LA) to γ -valerolactone (GVL). Here, we report on the effect of the type of TiO_2 support on catalyst stability of Ru-based catalysts used for conversion of LA to GVL in both dioxane and water as solvents. Catalytic performance, including stability, of three Ru/ TiO_2 catalysts, having a similar Ru mean particle size but supported on three types of TiO_2 , namely P25, rutile and anatase, is evaluated by multiple reuse under batch reactor conditions and the catalysts' physiochemical properties before and after recycling are characterized by XRD, STEM, TGA and FT-IR after CO stepwise adsorption. The results show that the deactivation seen for (mixed) anatase-supported catalysts in dioxane can be attributed to strong metal-support interaction (SMSI) rather than coke formation or metal sintering, with the rutile-based catalyst being more resistant against such support reduction. Notably, SMSI formation under the applied, relatively mild conditions only occurs in the presence of the organic acids, such as LA or valeric acid. Continuous flow experiments further demonstrate that the rutile phase supported catalyst performed best over a three day run, showing some signs of gradual deactivation, possibly by coke deposition. In water as solvent, SMSI formation is less of an issue, but Ru sintering is observed for all three catalysts instead.

3.1. Introduction

As part of the transition to a more sustainable chemical industry, the use of non-edible biomass as feedstock for the production of renewable chemical building blocks, or platform chemicals, is desired.[1] Two platform molecules of particular potential are biomass-derived levulinic acid (LA) and γ -valerolactone (GVL), both of which received much attention given their relative ease of synthesis and manifold potential applications.[2,3] Indeed, LA can be obtained in one step from lignocellulosic biomass by a simple hydrolysis process[4] and can be converted to GVL in another single step, with GVL finding possible application as a green solvent,[5] food additive[6] and as intermediate for the production of bulk polymers and advanced biofuels.[4,7]

The production of GVL by hydrogenation of LA has received much attention, having been extensively studied both in the gas and liquid phase and with different reductants, including molecular hydrogen, formic acid and alcohols.[8–11] Numerous heterogeneous metal-based hydrogenation catalysts, such as Raney Ni, noble metals on oxidic and carbon supports were developed to facilitate GVL synthesis.[12–14] Of these, Ru based catalysts have shown particularly excellent hydrogenation capacity.[15,16] In an early example, Manzer *et al.* assessed the performance of 5 wt.% Ir, Rh, Pd, Ru, Pt, Re and Ni catalysts loaded on activated carbon in LA hydrogenation at 150 °C under 55 bar (H₂) in 1,4-dioxane as solvent and found Ru/C to perform best, whereas the Pt, Re and Ni systems rendered low LA conversions ($\leq 15\%$).[17] Tan *et al.* showed that Ru/TiO₂ (P25) could convert LA into GVL (selectivity > 99%) with a turnover frequency as high as 7676 h⁻¹ under relative mild reaction conditions (70 °C, 40 bar H₂) with water as solvent.[18] Luo *et al.* also demonstrated that Ru/TiO₂ (P25) exhibited good catalytic performance in terms of GVL generation even under harsh reaction conditions in the LA mimic 2-ethylhexanoic acid, as well as in neat GVL as solvent.[19]

Next to productivity, long-term stability is known to be an equally critical parameter for a catalyst, but typically receives much more limited attention.[3] When run in the liquid phase, the catalyst is exposed to highly polar, high temperature LA hydrogenation conditions, with the added difficulty of having an acidic substrate.[4] As a result of these harsh conditions, catalysts can be expected to deactivate as a result of metal sintering/leaching, and/or support collapse or destruction.[20] In addition, some intermediates involved tend to polymerize and form carbonaceous deposits and biogenic or process-derived impurities can poison the catalyst, both also leading to deactivation.[3] While carbon-based supports are known to be stable under hydrothermal and acidic hydrogenation conditions,[21–23] they cannot, however, withstand the high temperature, oxidative conditions required for catalyst reactivation by coke burn off.[20] Indeed, metal oxide-based supports are more widely employed in industrial processes on account of their good stability against such gas phase regeneration conditions. If such metal oxides are stable also under the liquid phase conditions typical for biomass conversion and platform molecule generation still needs to be firmly established, however, and will strongly depend on the actual severity of the process (e.g., solvent choice, temperature, pressure, atmosphere, pH, etc.). TiO₂, for example, has been shown to resist aggressive aqueous media, especially hydrothermal and acidic hydrogenation conditions. Indeed, it has been calculated that

(bulk) TiO_2 is stable in hot water at 200 °C, over almost the entire pH range.[20] Ru/TiO_2 (P25) was indeed found to maintain its catalytic activity and selectivity towards LA hydrogenation up to 6 batch recycling test at 70 °C under 40 bar H_2 with water as solvent.[18] TiO_2 has also shown good performance in other solvents, for example in a continuous flow screening study of the LA hydrogenation activity of 50 different supported noble metal catalysts, performed at 200 °C under 40 bar H_2 using LA dissolved in GVL as feedstock.[4] Pt on TiO_2 (P25) proved to be 10 times more active than its SiO_2 and C counterparts, giving a very stable GVL production (>95% selectivity) up to 100 h time-on-stream.[4] On the other hand, Abdelrahman *et al.* found that Ru/TiO_2 (P25) lost its catalytic activity with time-on-time in LA hydrogenation at 50 °C under 24 bar H_2 in a continuous flow reactor with H_2O as solvent, the deactivation was attributed to Ru sintering and coke formation rather than change on TiO_2 support, however.[13] Ftouni *et al.* also reported on the deactivation for Ru/TiO_2 (P25) catalyst towards LA hydrogenation at 150 °C under 30 bar H_2 with dioxane as solvent, with activity gradually dropping upon batch recycling. Surprisingly, characterization on the reused catalysts confirmed that neither Ru sintering, leaching nor coke were responsible for deactivation, but rather Ru nanoparticle overcoating by TiO_{2-x} species.[24]

Indeed, the elevated temperature, reducing conditions employed in hydrogenation reactions can in principle present another stability challenge for reducible oxides such as TiO_2 . Such supports can suffer from noble-metal mediated H spillover onto the support, resulting in surface reduction and support rearrangement and ultimately coverage of the metal nanoparticle by the support, a phenomenon described as Strong Support Metal Interaction (SMSI).[25–27] The SMSI concept was first developed by Tauster *et al.* in 1978 to refer to the dramatic suppression of metal chemisorption ability[28] and has been extensively studied since then. For TiO_2 supported systems, such SMSI formation processes typically require an elevated temperature (above 300 °C) in a pure or dilute H_2 atmosphere.[29,30] The most benign conditions we could find for SMSI generation over a Ru loaded TiO_2 (P25) catalyst were reported by Badyal *et al.* showing support reduction and metal nanoparticle overcoating after a gas phase H_2 treatment at 250 °C for 2 h.[31]

SMSI can exert different effects on different reactions.[31,32] For instance, it has been documented that SMSI generation over TiO_2 supported catalysts benefited activity in the hydrogenation of carbonyl groups toward alcohols,[33–36] nitrate reduction to nitrite[37] and photocatalytic bio-hydrogen production from glucose solution.[38] More often than not, however, the overcoat caused by the SMSI effect is considered detrimental for the activity of the metal phase and is best to be avoided.[39,40] For example, Ko and Garten pointed out that TiO_2 supported group VIII metals always exhibited a much lower reactivity, up to several magnitude orders in ethane hydrolysis compared to their SiO_2 counterparts, due to SMSI formation when the catalyst was pre-reduced at 500 °C.[41] Sa *et al.* demonstrated with FT-IR that reduced CO uptake due to SMSI was already seen for Pd/TiO_2 catalyst after H_2 reduction at 200 °C. Upon increasing the reduction temperature to 350 °C, patches of a Ti_4O_7 phase on the Pd particles could be observed by TEM.[25] In addition to high temperature H_2 reduction, surface

decoration can also occur by vacuum treatment, for which, again, high temperatures are needed (e.g. 327-527 °C).[26,42,43]

The deactivation of the Ru/TiO₂ catalyst reported by Ftouni *et al.* in LA hydrogenation was also attributed to such an SMSI. Indeed, Ru nanoparticles were found to be blanketed by a disordered titania surface layer of 1-3 nm thick, as could be clearly seen by Aberration Corrected Scanning Transmission Electron Microscopy (AC-STEM) after repeated reuse.[24] Compared to the above examples, the mode of deactivation was somewhat unexpected given the relatively mild hydrogenation conditions of 150 °C in dioxane.[24] The underlying reasons for SMSI formation under such mild conditions remain to be elucidated.

The ease and extent of TiO₂ reduction, aided by SMSI or not, do depend on the particular TiO₂ phase that is studied. Indeed, the vast amounts of studies on the generation of 'black' titania for photochemical/physical applications have shown that anatase reduces more readily than rutile.[28,29] In addition, the type of TiO₂ support used has also been shown to have a pronounced effect on catalyst hydrogenation performance. For example, Hernandez-Mejia *et al.* used a series of Ru catalysts supported on different TiO₂ phases for the catalytic hydrogenation of xylose and found metal dispersion to depend on the titania crystal structure used, with a rutile supported Ru catalyst performing better than its anatase counterpart.[44] Carballo *et al.* also noted that support structure, rather than Ru precursor or support surface area determined Ru particle dispersion and further catalytic efficiency.[45] Al-Shaal *et al.* compared the catalytic efficiency of rutile and P25 supported Ru catalysts in LA hydrogenation and found that no LA was hydrogenated over Ru/TiO₂ (rutile) in neither ethanol nor ethanol-water as solvent, whereas Ru/TiO₂ (P25) could produce GVL in good yields of up to 72%.[23] The higher activity of the TiO₂-P25 supported catalyst was thought to be the result of its higher surface area, facilitating either reactant adsorption or Ru dispersion.[23] Ruppert *et al.* studied the effect of titania phase on LA hydrogenation in detail as function of rutile/anatase ratio and morphology.[46] A high GVL yield was obtained with 20/80 and 10/90 rutile/anatase mixture while pure anatase supported catalysts were much less active, and activity was related to Ru dispersion and the electronic and surface properties of two chosen phases.[46] However, the examples available of titania phase-dependent LA hydrogenation performance give limited information on the influence of the type of TiO₂ support on the stability of the catalyst, including the support. For example, the extent to which the SMSI-induced support reduction is phase and solvent dependent is an open question.

This PhD chapter reports a systematic investigation of the influence of different parameters on catalyst performance in LA hydrogenation. Three different TiO₂ types, rutile, anatase and P25 (mixture of anatase and rutile), were studied under typical liquid phase LA hydrogenation conditions in both water and dioxane with catalyst stability being assessed by multiply recycling tests. Catalytic activity and characterization results show that the anatase(-containing) supported catalysts suffer from deactivation due to SMSI formation, whereas pure rutile is more stable against support reduction in dioxane. Deactivation by SMSI was much less evident in water, but metal sintering in this solvent was more severe than in dioxane. Notably, support reduction (and

by inference catalyst deactivation) by SMSI was found to be organic acid-induced, as it occurred only in the presence of the LA substrate or an added acid such as valeric acid.

3.2. Experimental Section

3.2.1. Catalyst synthesis

All chemicals were used as received. For catalyst preparation: ruthenium(III) nitrosyl nitrate ($\text{RuNO}(\text{NO}_3)_3/\text{Ru}$ 31.3%) and $\text{RuCl}_3 \cdot x\text{H}_2\text{O}$ were purchased from Alfa Aesar and Sigma-Aldrich, respectively. The support TiO_2 (P25) was purchased from Degussa, while TiO_2 (rutile, nanopowder, <100 nm particle size, 99.5% trace metals basis) and TiO_2 (anatase) were from Sigma-Aldrich. For the catalytic tests: levulinic acid (98%), 1,4-dioxane (99+%, containing 0.05% of H_2O) were obtained from Alfa Aesar. Anisole (99%), used as an internal standard, was purchased from Acros Organics. Technical grade acetone (> 99%), used for washing the catalyst, was purchased from Interchema. The water used as solvent was purified by a Milli-Q system.

Preparation of 1 wt.% Ru/P25 and Ru/Rutile. The catalysts were prepared via wet impregnation following a previous report.[24] In short, the supports were first dried at 120 °C for 2 h to remove humidity. Subsequently, a slurry of support and demi-water was stirred at room temperature for 30 min, followed by dropwise addition of 10 mL of a Ru precursor ($\text{RuNO}(\text{NO}_3)_3/\text{Ru}$ 31.3%) solution after which the slurry was stirred for 3 h. After evaporation of the water under vacuum at 60 °C, the catalyst was dried at 60 °C overnight in air, calcined at 500 °C for 3.5 h with a heating ramp of 5 °C/min under a pure N_2 flow of 100 mL/min, followed by its reduction at 450 °C with a ramp rate of 5 °C/min, for 5 h, under a pure H_2 flow at 80 mL/min.

Preparation of 1 wt.% Ru/Anatase. The catalyst was prepared following the work of Piskun *et al.*[47] In a typical experiment, 1 g anatase support was first dried at 120 °C for 4 h to remove humidity. The metal precursor ($\text{RuCl}_3 \cdot x\text{H}_2\text{O}$) was dissolved in 25 mL water and stirred for 30 min at 30 °C, followed by a gradually addition of support to the precursor solution under stirring. Afterwards, the temperature was heated to 85 °C and kept at this temperature until all water was evaporated. Subsequently, the catalysts were reduced directly, i.e. without intermediate calcination, at 450 °C with a heating ramp of 2 °C/min under a 10% H_2/N_2 flow with a total flow of 200 mL/min.

3.2.2. Characterization

X-ray powder diffraction (XRD) patterns measured using a Bruker-AXS D2 Phaser powder X-ray diffractometer using $\text{Co K}_{\alpha 1,2}$ with $\lambda = 1.79026 \text{ \AA}$. Measurements were carried out between 20-55° 2θ using a step size of 0.04° and a scan speed of 1 s.

Transmission Electron Microscopy (TEM) analyses were operated with JEOL 100CX microscope at a 100 kV acceleration voltage. The samples were prepared by applying three drops of a catalyst in ethanol slurry on a graphene-coated, 200 mesh copper grid.

N_2 physisorption isotherms were recorded to determine surface areas and pore volumes with a Micromeritics Tristar 3000 setup. The samples were outgassed prior to performing

the measurement overnight at 200 °C in a N₂ flow. Surface areas were determined using the Brunauer-Emmett-Teller (BET) theory, while microspores volumes (cm³/g) were determined by *t*-plot analysis for *t* between 3.5 and 5.0 Å to ensure inclusion of the minimum required pressure points.

Fourier-transform infrared (FT-IR) spectra in transmission mode were recorded on a Perkin-Elmer 2000 instrument. Samples were pressed under 3.5 tons for 15 s to achieve self-supporting wafers (12–28 mg/13 mm diameter). The wafer was positioned in a well-sealed cell with CaF₂ window and posteriorly activated at 550 °C (5 °C/min) under high vacuum (10⁻⁶ mbar). Subsequently, the cell was cooled down to -188 °C with liquid nitrogen. Spectra were taken upon CO (10% in He, purity 99.9%) adsorption on the sample, at elevated pressures.

Thermal gravimetric analysis (TGA) was performed with a Perkin-Elmer Pyris 1 apparatus. 15 mg of catalyst sample was heated with a ramp of 5 °C/min to 150 °C for 1 h in a 20 mL/min flow of argon to eliminate physisorbed humidity and any acetone remaining from the washing step, followed by a ramp of 5 °C/min to 600 °C in a 10 mL/min flow of oxygen to burn off deposited organic species.

3.2.3. Catalyst testing

Catalyst activity and stability were analyzed in both 1,4-dioxane and water. All batch reactions were run in a 40 mL Parr batch autoclave for 3 h at a stirring speed of 1250 rpm. In a typical reaction, the batch autoclave reactor was loaded with the catalyst, substrate and solvent. Then the autoclave was purged three times with argon after which the reaction mixture was heated to reaction temperature and charged with H₂. This was taken as the starting point of the reaction, during the reaction samples were collected at different intervals, filtered and internal standard was added to the samples. At the end of the reaction, the autoclave was cooled rapidly to room temperature in an ice bath, after which the remaining H₂ was released. The catalyst was separated by filtration (filters of 0.45 µm), washed with acetone and dried overnight at 60 °C in air.

For the reactions in dioxane, the tests were performed using 1,4-dioxane (27 g) as solvent at 150 °C under 30 bar H₂ pressure, 10 wt.% of levulinic acid (3 g, 25.8 mmol) over a series of 1 wt.% of Ru supported catalysts (0.19 g).[24] One reference run without the addition of levulinic acid was also operated for 18 h under otherwise identical conditions over Ru/P25. The reaction products were analyzed using a Shimadzu GC-2010A gas chromatograph equipped with a CPWAX 57-CB column (25 m × 0.2 mm × 0.2 µm) and FID detector, using authentic samples for calibration.

For the reactions in water, 2.2 g LA, 27.8 g H₂O and 1.2 g catalyst were introduced in the autoclave and reacted at 90 °C under 45 bar H₂ pressure for 3 h.[47] The composition of the reaction solution was analyzed on a Shimadzu HPLC, using a 5mM aqueous H₂SO₄ solution as eluent. The presence of 4-hydroxypentanoic acid (4-HPA) was confirmed by ¹H NMR with D₂O as solvent.

Continuous flow reactions were performed under identical dioxane reaction conditions with a stainless steel, fixed-bed flow reactor (42.5 cm in length, 0.9 cm in outer diameter and

0.8 cm in inner diameter). 0.5 g (70-150 μm) of catalyst was packed in the center of the reactor tube and plugged with quartz wood. Prior to heating, H_2 pressure was built up slowly by flowing 100 Standard Cubic Centimeter per Minute (sccm) of pure H_2 gas to 30 bar, after which the H_2 flow kept as 10 sccm. Then 10 wt.% LA/dioxane feedstock was introduced into the reactor in an upflow configuration by an HPLC pump with a weight hourly space velocity of $1.2 \text{ g}_{\text{LA}} \text{ g}_{\text{catalyst}}^{-1} \text{ h}^{-1}$ and the system was heated to 150 $^\circ\text{C}$ with a ramp of 2 $^\circ\text{C}/\text{min}$. Once the temperature reached the desired value, this was taken as the starting point of the reaction. Samples of the product solution were taken manually and analyzed offline on a Shimadzu GC-2010A gas chromatograph.

3.3. Results and Discussion

3.3.1. Characterization of the fresh catalysts

To investigate the effect of TiO_2 phase composition on catalyst stability in liquid phase LA hydrogenation, three different types of TiO_2 (P25, anatase and rutile) were selected. 1 wt.% Ru/P25 and Ru/Rutile were prepared by wet impregnation with $\text{RuNO}(\text{NO}_3)_3$ followed by calcination and high temperature (450 $^\circ\text{C}$) reduction according to the method reported by Ftouni *et al.* [24] The Ru/Anatase catalyst was instead prepared following the report of Piskun *et al.* [47], in which $\text{RuCl}_3 \cdot x\text{H}_2\text{O}$ is used as precursor followed by direct H_2 reduction. These methods were selected in order to obtain similar mean Ru particle sizes, of around 2.0-2.5 nm (see below), allowing any particle size effects on performance and deactivation to be discarded. The physicochemical properties of the fresh (and recycled) catalysts are summarized in Table 3.1, showing BET surface areas of the fresh P25, anatase and rutile supported materials of 75, 11 and 25 m^2/g , respectively. The characteristic diffraction peaks seen by XRD for Ru/Rutile and Ru/Anatase showed them to be phase pure, while, diffraction signals of both pure anatase and rutile phases, with an anatase:rutile ratio of 80:20, were observed for Ru/P25. No Ru diffraction peaks were observed in the XRD patterns of any of the three Ru-based catalysts (Fig. 3.1), indicative of the low loading and small Ru particle size. Fig. 3.2 shows the TEM images and Ru particle size distribution for all three fresh Ru catalysts. The mean Ru particle diameters of Ru/P25, Ru/Rutile and Ru/Anatase were found to be similar ranging from $2.5 \pm 0.9 \text{ nm}$, $2.3 \pm 0.8 \text{ nm}$ and $2.0 \pm 0.6 \text{ nm}$ (Fig. 3.2), respectively. As can be viewed in the TEM image of freshly reduced Ru/P25 catalyst, two differently shaped crystalline phases can be observed. The rectangular-shaped fragments are identified as rutile and the smaller, round fragments as anatase, in line with the observation of Ohno *et al.* that the particle size of rutile in Degussa P25 is about four times larger than that of its anatase component. [48] The TEM images furthermore showed that Ru was not found equally dispersed over all titania crystallites in the Ru/P25 catalyst. Indeed, the majority of Ru particles were located on the rutile phase (Fig. 3.2a), in line with the observation of Ruppert *et al.*, who prepared a Ru/ TiO_2 (P25) via incipient wet impregnation from $\text{Ru}(\text{acac})_3$. [46] In our case, a small portion of Ru particles was also found at the surface of the anatase component (Fig. 3.2a, yellow round circle). On the other hand, for the Ru/Anatase and Ru/Rutile samples, the TEM images showed a homogeneous distribution of Ru particles over the support.

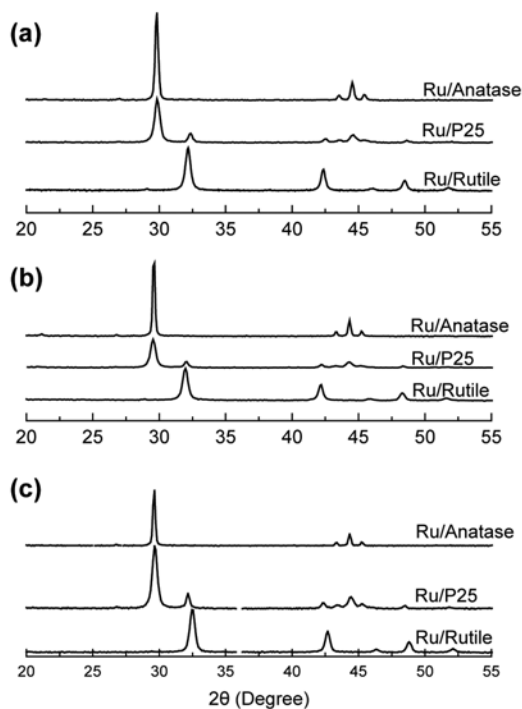


Fig. 3.1. XRD patterns of (a) fresh Ru/TiO₂ catalysts, reused Ru/TiO₂ catalysts recycled 5 times (b) in dioxane and (c) in water.

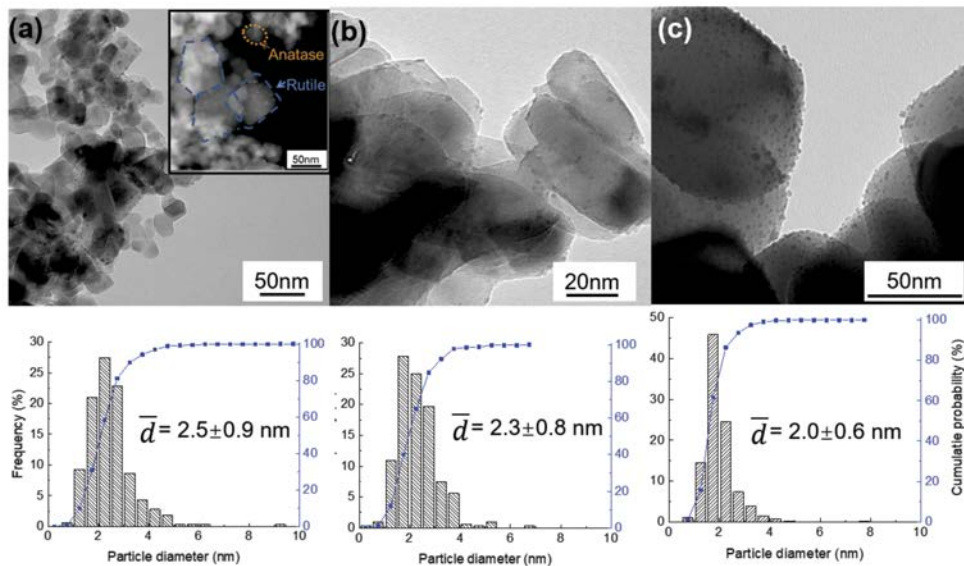


Fig. 3.2. TEM images and Ru size distributions of fresh (a) Ru/P25, (b) Ru/Rutile and (c) Ru/Anatase.

FT-IR analysis after CO adsorption is a powerful method to monitor active metal surface properties, such as the oxidation state and degree of dispersion, of the catalyst.[49] Fig. 3.3 shows the FT-IR spectra of the fresh catalysts after CO adsorption at liquid nitrogen temperature. A series of characteristic CO-Ti species is seen, in line with the results reported by Hadjiivanov *et al.*[50] The low intensity bands centered at 2208 and 2190 cm^{-1} were attributed to CO interacting with electrophilic, pentacoordinated Ti^{4+} α and five-coordinated β' sites, respectively. At higher CO coverage, a gradual red shift from 2190 cm^{-1} to 2180 cm^{-1} is seen, as next to the CO- β' sites also the β'' sites adsorb CO. With increased CO pressure, one more kind of Ti^{4+} site, five-coordinated Ti^{4+} cations (γ sites) of very low acidity, was detected as well at around 2160 cm^{-1} . [50] The bands centered at 2150-2155 and 2140 cm^{-1} were attributed to CO adsorbed on surface OH groups and physisorbed CO, respectively.[51] That a CO-OH band ($\sim 2150 \text{ cm}^{-1}$) was absent for the Ru/P25 sample is indicative of the high degree of surface dehydroxylation after outgassing at 550 $^{\circ}\text{C}$, whereas a large amount of residual hydroxyl groups were still present on the surface of Ru/Rutile and Ru/Anatase after annealing.[52] In addition, broad bands centered at 2040, 2043 and 2046 cm^{-1} were observed for Ru/P25, Ru/Rutile and Ru/Anatase, respectively, assigned to CO linearly adsorbed on metallic Ru particles.[53]

3.3.2. Catalyst performance in 1,4-dioxane

The standard reaction conditions for LA hydrogenation in 1,4-dioxane as solvent consisted of a run at 150 $^{\circ}\text{C}$ under 30 bar H_2 in a batch autoclave, with catalyst stability being assessed by multiple recycling tests. GVL is the only product detected after reaction, no intermediates such as α -angelicalactone or GVL overhydrogenation products (e.g. 1,4-pentanediol and valeric acid) were observed. As the mass balance of substrate and products (LA + GVL) was always higher than 95% as determined by GC analysis, only GVL yields are given below to compare catalytic activity between runs. The production of GVL as a function of time (Fig. 3.4a) varied as in the following order: Ru/Anatase > Ru/Rutile > Ru/P25. This trend is different from a previous observation that a P25-based catalyst was more reactive than rutile-based one in LA hydrogenation in ethanol as solvent.[23]

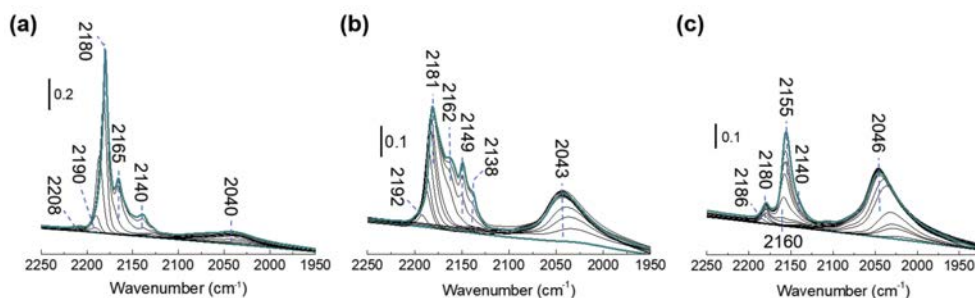


Fig. 3.3. FT-IR spectra of fresh (a) Ru/P25, (b) Ru/Rutile and (c) Ru/Anatase after CO adsorption as function of pressure at -188 $^{\circ}\text{C}$.

The production of GVL for the three catalysts under study as a function of recycle number is presented in Fig. 3.4b, c and d. In line with previous observations,[24] Ru/P25 deactivated upon recycling, showing a considerable drop in GVL yield from 69% to 24%, again as previously, attributed to a detrimental SMSI (see discussion below). Likewise, GVL yield over Ru/Anatase was also found to decrease from full conversion to 49% after the 3rd recycle. To properly see any deactivation in the first runs, recycling tests were also performed at lower conversion (LC), using a higher LA/Ru ratio, again showing the pure anatase support to exhibit similar behavior to the anatase-rutile mixture (P25), with the yield gradually going down upon reuse. In sharp contrast, Ru/Rutile proved to be more stable in term of GVL production upon recycling. Under standard conditions, GVL yield over Ru/Rutile actually went up upon first reuse and kept constant until the 2nd recycle, as observed in low conversion runs. Gradual deactivation was still observed also for the Ru/Rutile material upon further recycling.

To get further insight into the differences in catalyst behavior seen upon recycling, the 5-times recycled Ru/P25, Ru/Anatase and Ru/Rutile catalysts were recovered and characterized. XRD analysis confirmed that the bulk titania phase composition did not change upon recycling (Fig. 3.1), giving an identical anatase:rutile ratio of 80:20 for Ru/P25 before and after reuse. N₂ physisorption measurements showed a dramatic difference, however (Table 3.1). The recycled Ru/P25 showed a drop of ~40% in surface area compared to its fresh counterpart. A similar

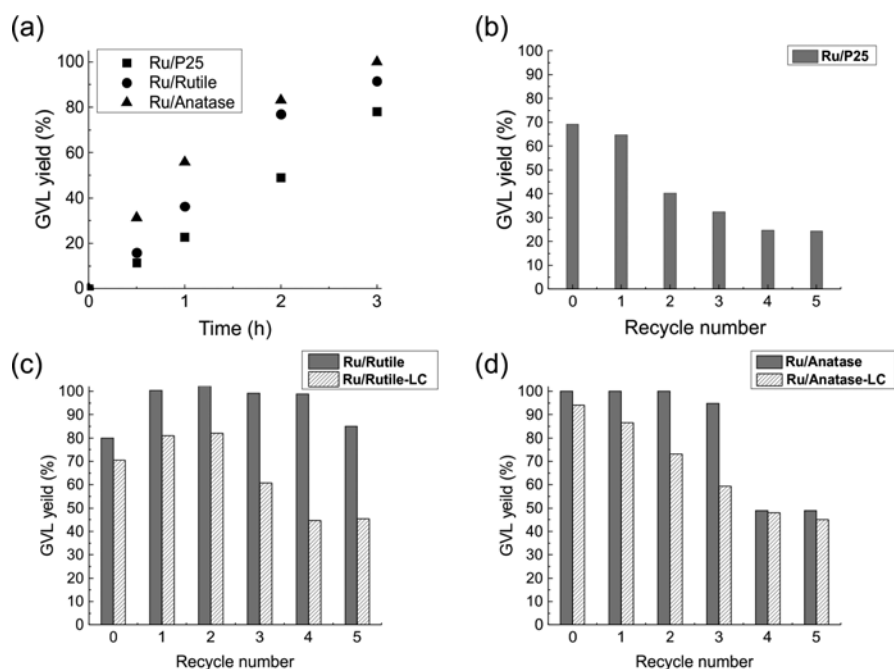


Fig. 3.4. (a) GVL yield as function of reaction time, GVL yield as a function of recycling number for (b) Ru/P25, (c) Ru/Rutile and (d) Ru/Anatase in dioxane. Experimental conditions: $T = 150\text{ }^{\circ}\text{C}$, $P(\text{H}_2) = 30\text{ bar}$ and $t = 3\text{ h}$, $\text{LA}/\text{Ru} = 1400$; $\text{LA}/\text{Ru} = 3300$ for Ru/Rutile LC (low conversion) and Ru/Anatase LC recycle.

drop in surface area had been seen before for Ru/TiO₂ (P25) upon recycling and was attributed to support reduction and partial (surface) amorphization.[24] Instead, almost no change in surface area was seen for both Ru/Rutile and Ru/Anatase. TGA analysis revealed weight losses of 0.3%, 0.6% and 0.3% for the recycled Ru/P25, Ru/Rutile and Ru/Anatase materials (Table 3.1), respectively, indicating coke formation is limited. The mean Ru particle size in Ru/P25 and Ru/Rutile remained the same before and after recycling, whereas some sintering was observed for Ru/Anatase with average Ru particle size increasing from 2.0 ± 0.6 nm to 3.1 ± 2.7 nm (Table 3.1 and Fig. 3.5). TEM image of the 5-times recycled Ru/P25 showed the Ru particles still preferentially deposited on the rutile phase (Fig. 3.5a). ICP analysis demonstrated no detectable levels of Ru in the reaction solution, showing leaching to be very limited as well. Taken together, these results suggest that the observed phase-dependent deactivation of the Ru/TiO₂ catalysts is not linked to metal particle growth, leaching or the result of coke deposition.

Table 3.1. Physicochemical properties of fresh and recycled Ru-based catalysts used for LA hydrogenation in 1,4-dioxane as solvent.

		BET (m ² g ⁻¹)	Particle size (nm)	TGA (%)
Ru/P25	Fresh	75	2.5±0.9	ND
	Spent 5x Recycled	46	2.5±1.0	0.3
Ru/Rutile	Fresh	25	2.3±0.8	ND
	Spent 5x Recycled	23	2.3±0.9	0.6
Ru/Anatase	Fresh	11	2.0±0.6	ND
	Spent 5x Recycled	12	3.1±2.7	0.3

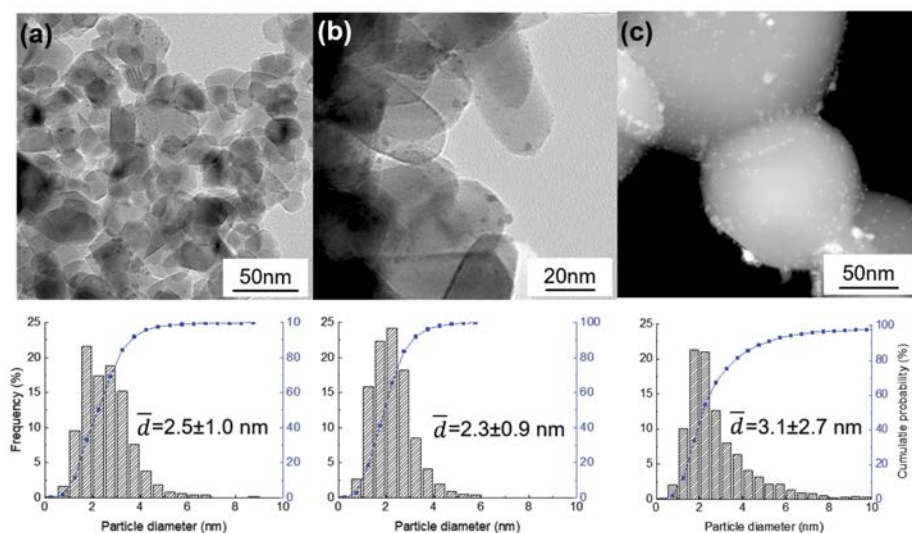


Fig. 3.5. TEM images and Ru size distributions of reused (a) Ru/P25, (b) Ru/Rutile and (c) Ru/Anatase recycled 5 times in dioxane.

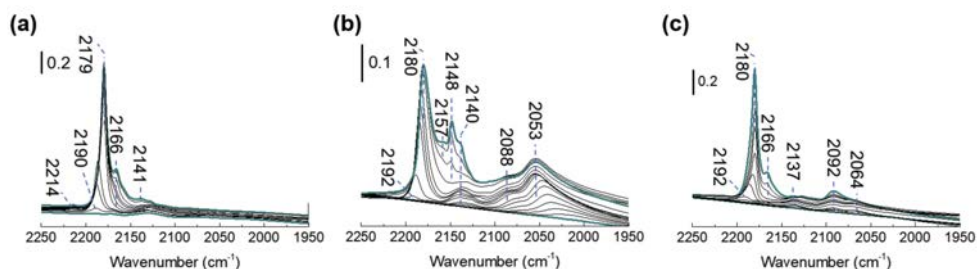


Fig. 3.6. FT-IR spectra of 5 times reused (a) Ru/P25, (b) Ru/Rutile and (c) Ru/Anatase obtained from the high conversion runs in dioxane after CO adsorption as function of pressure at -188 °C.

Fig. 3.6a-c show the FT-IR spectra upon CO adsorption at liquid nitrogen temperature of the recycled Ru catalysts. After five recycle runs in dioxane, it can be seen clearly that the CO-Ru⁰ signal vanished in the spectrum of recycled Ru/P25, in line with the results (obtained for a three times reused Ru/P25) reported by Ftouni *et al.*[24] Given the limited coke formation and Ru metal sintering, this decrease in CO adsorption ability is thought to be characteristic of SMSI formation.[30] Indeed, it was previously shown by AC-STEM that the TiO₂ (P25) support developed a continuous disordered surface layer of reduced Ti species varying in thickness between 1 and 2 nm after three recycles under LA hydrogenation reaction conditions similar to the one used here which was performed with more recycling and a higher LA/Ru ratio.[24] A similar, nearly full decrease in CO adsorption on Ru was also observed for the 5-times recycled Ru/Anatase catalyst, again pointing at loss of adsorption capacity as a result of SMSI. Although some Ru sintering did occur upon recycling, this is not considered sufficient to account for the severe loss on CO adsorption of recycled Ru/Anatase catalyst. Indeed, as can be seen clearly below in the CO-IR spectra of a five-times recycled anatase catalyst used in water rather than dioxane (Fig 3.11, see section 3.3.4), this catalyst showed a better CO adsorption ability than this dioxane recycled anatase sample, despite having a much larger Ru mean particle size of 4.1 ± 4.7 nm. Therefore, the significant loss of CO adsorption capacity observed for the dioxane-recycled anatase catalyst is also most likely attributed to Ru surface coverage by SMSI formation. In line with this, as a result of SMSI formation, the peak centered at 2155 cm⁻¹ related to CO-OH adsorption seen in the fresh catalyst, was absent after recycling of Ru/Anatase, as also seen previously.[54–56] Indeed, Chen *et al.* found H₂-reduced black TiO₂ material to exhibit much less surface hydroxyl groups compared to pristine white TiO₂. [55] Likewise, no band related to OH adsorption was observed in the CO-FT-IR spectrum of hydrogenated TiO₂ nanocrystals obtained after gas phase H₂ (5 bar) reduction at 450 °C for 4 h, whereas clear CO-OH bands were detected with the untreated TiO₂ nanocrystals.[54] Disordered surfaces were also seen for these two reduced titanias. In contrast, considerable peak intensity associated with CO adsorbed on Ru was still observed for Ru/Rutile after five times recycling in dioxane, suggesting that pure rutile is more stable against support reduction than a (mixed) anatase phase. A similar conclusion was drawn by Li *et al.* using Electron Paramagnetic Resonance (EPR) as a means to

compare the SMSI formation for anatase and rutile supported palladium catalysts. Irreversible support reduction was observed for anatase, but not for a rutile supported catalyst after H_2 reduction at 200 °C.[29]

Notably, two new bands centered appeared at 2137/2140 and 2092/2088 cm^{-1} in the FT-IR spectra of the recycled Ru/Anatase and Ru/Rutile catalysts, respectively, associated with tightly bound CO species as they were stable upon high vacuum desorption (Fig. 3.7).[57] These bands positions are very similar to those observed by Robbins and attributed to $(TiO)_2Ru(CO)_3$ surface species based on a CO-induced oxidation experiment on fully reduced Ru/ TiO_2 at 37 °C, indicating TiO_{2-x} -Ru ligand formation after recycling.[58]. De la Peña O'Shea *et al.* demonstrated that such amorphous Ti-metal mixed species can be indeed generated as a result of SMSI formation. In their work, layers a few atoms thick of TiO_x moieties were detected on the surface of a Co/ TiO_2 catalyst after H_2 reduction at 500 °C, indicative of SMSI surface decoration, these layers were accompanied by the formation of Co-O-Ti linkages as suggested by XPS analysis.[59] Reduced Ti species were proposed to be stabilized by reaction with reduced cobalt, giving rise to an amorphous mixed oxide on the catalyst surface.[59] Based on the work of Robbins and De la Peña O'Shea *et al.*, it can be inferred in our case that the appearance of these bands at high frequency support the evolution of surface TiO_{2-x} -Ru species resulting from SMSI.

Summarizing, the above experiments clearly shows that the choice of TiO_2 support has a big influence on catalyst performance in dioxane. Under typical LA hydrogenation conditions, the reactivity of the anatase-supported catalyst outperforms the rutile one, which in turn shows better performance than the P25 catalyst. Upon recycling, (mixed) anatase catalysts show a fast and continuous deactivation in terms of GVL production, whereas, an initial jump in catalytic activity is observed for rutile phase supported catalyst. Differences in ease of reducibility and resulting extent of SMSI seem to be the origin of these support effects. The CO adsorption ability is significantly depressed for P25 and anatase supported catalysts after recycling as revealed by the CO-FT-IR spectra, whereas considerable CO-Ru adsorption intensity is still observed for

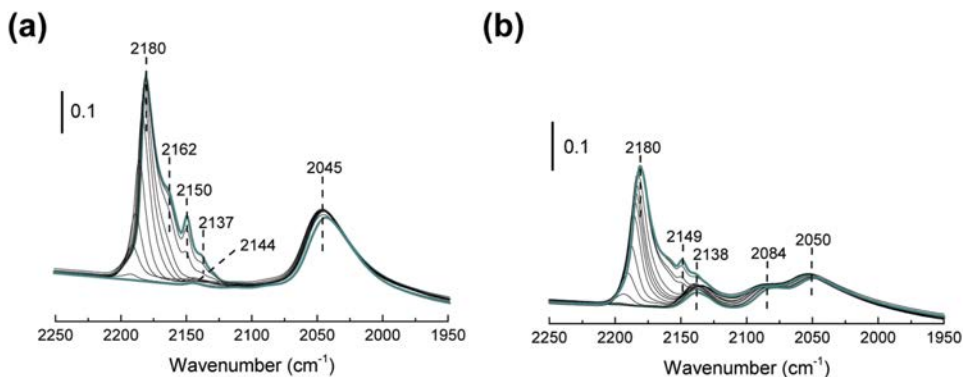


Fig. 3.7. FT-IR spectra of CO desorption on (a) fresh and (b) recycled Ru/Rutile from 1.4 to 10^{-5} mbar at -188 °C.

recycled Ru/Rutile, making the latter support more stable against deactivation under dioxane LA hydrogenation conditions.

3.3.3. Adsorbate-induced Strong Metal Support Interaction.

Under gas phase reduction conditions, support reduction by H₂ spillover is considered the main reason for SMSI formation.[60] In this mechanism, adsorbed H₂ is dissociated by the supported metal, spilled over onto the TiO₂ support that gets reduced to TiO_{2-x} suboxides that eventually migrate over the surface of the metal particles. Such processes, however, typically require an elevated temperature (above 350 °C) in a pure or diluted H₂ gas atmosphere.[29] In our case, the Ru/TiO₂ materials are exposed to much milder liquid phase conditions (150 °C), yet still suffered from deactivation by SMSI as demonstrated above and previously.[24] We therefore investigated what the necessary conditions are to induce SMSI in the liquid phase.

To test the role of H₂ alone on SMSI formation for the Ru/TiO₂ catalysts under mild liquid hydrogenation conditions, fresh Ru/P25, without LA substrate, was treated in H₂ saturated dioxane solution (30 bar) at 150 °C for 18 h, equivalent to the time the catalyst was exposed to reducing conditions over the five recycle runs. Surprisingly, no evidence of SMSI was observed for the spent Ru/P25 material obtained after this run. N₂ physisorption revealed that the surface area of this spent catalyst is similar to that of fresh Ru/P25 (Table 3.2), while the CO-FT-IR spectrum of this treated Ru/P25 showed the CO-Ru⁰ vibration to be equal to comparable to the fresh counterpart (Fig. 3.8b), suggesting spent Ru/P25 did not lose its CO adsorption ability. Given that these results are opposite to those found for recycling the same catalyst in the presence of LA, after which Ru/P25 had suffered an obvious decrease in CO adsorption intensity, (Fig. 3.6a) it can be speculated that LA may be involved in catalyst deactivation by SMSI.

Indeed, previous studies have shown that formic acid and generated formates adsorbed on TiO₂ support can generate an Adsorbate-induced SMSI state (A-SMSI) under relatively mild conditions.[40,61,62] For example, Rui *et al.* found SMSI to occur not only upon high temperature H₂ reduction of Pt/TiO₂, but also when an as-calcined TiO₂ catalyst was reduced by a 35 wt.% formic acid water solution at 70 °C without any H₂ present. Very recently, such an adsorbate-mediated SMSI was also reported by Matsubu *et al.*, [40] who found that, depending on the reaction and pretreatment conditions, a reduced Rh/TiO₂ catalyst could be blanketed by a thin, yet permeable support layer after appropriate treatment under 20% CO₂/2% H₂ at 250 °C. High coverage of HCO_x species was observed by *in-situ* DRIFT spectroscopy and, after comparison to formic acid decomposition on TiO₂, these HCO_x were held responsible for oxygen vacancy formation and for driving the A-SMSI.

To determine the effect of having an organic acid on SMSI formation under liquid hydrogenation conditions, a non-reducible acid, valeric acid was used instead of LA and reacted with fresh Ru/P25 under the same acid/Ru ratio under 30 bar H₂ in dioxane for 18 h. No pressure drop was observed during the reaction, indicating that indeed no hydrogenation reaction occurred. The surface area of this spent catalyst dropped to 40 m²/g, comparable to the five-time recycled Ru/P25 after the LA runs (46 m²/g). TEM analysis confirmed that the mean

Ru particle size before and after valeric acid treatment was the same (Table 3.2). However, no CO-Ru⁰ vibration was seen in the CO-IR spectrum of the recovered Ru/P25 material (Fig. 3.8c), again similar to Ru/P25 after repetitive LA runs, indicative of A-SMSI. Matsubu *et al.* pointed out that different surface properties were observed for A-SMSI and traditional SMSI overlayers. [40] Unlike the crystalline fully reduced metal-oxide layer observed for traditional SMSI, an amorphous and partially reduced metal-oxide overlayer was formed in the A-SMSI state, in line with our previous observations on the AC-STEM images of three times recycled Ru/P25 catalyst. [24] It is also worth to emphasize that, as shown above (Fig. 3.4), LA conversion for Ru/TiO₂ catalysts leveled off upon recycling, which might suggest that a semipermeable, equilibrium state is reached for the formed amorphous overcoat. Indeed, the overlayer originating from A-SMSI was thought to be porous enough to allow molecules to interact with the metal surface in the work of Matsubu *et al.*[24]

While the mechanism of A-SMSI formation is still unclear, several similarities with monocarboxylic acid-induced oxygen vacancy formation on titania can be discerned.[63,64] For example, formic acid is known to adsorb dissociatively on TiO₂, with dissociated protons combining with nearby bridging oxygens, producing bridging hydroxyl groups, followed by H₂O dissociation and oxygen vacancy formation.[62,63] This finally results in a HCO_x-covered, disordered and reduced titania surface. Such a disordered surface on TiO₂ (110) surface was also reported by Henderson with the help of High-Resolution Electron Energy Loss Spectroscopy (HREELS) after formic acid decomposition, as a result of bridging surface hydroxyl group condensation.[62] White *et al.* further demonstrated that the thermal decomposition of trimethylacetic acid on TiO₂ largely mirrored that of formic acid, also generating oxygen vacancies on the surface of TiO₂ material as revealed by ¹⁸O isotope labelling experiments.[65] Based on those studies and the experimental results presented above, it is hypothesized that an adsorbate-induced SMSI rather than a direct support reduction resulting from classical H₂ spillover occurred under the mild liquid LA hydrogenation conditions and that the organic acid substrate LA plays a key role in this process.

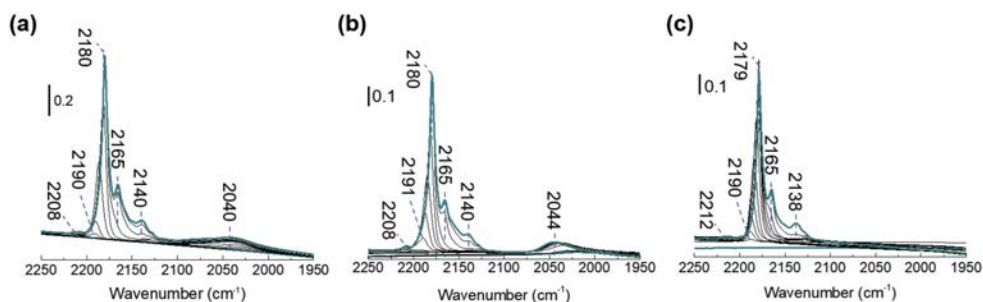


Fig. 3.8. FT-IR spectra of (a) fresh Ru/P25, (b) Ru/P25 treated without LA and (c) Ru/P25 treated with valeric acid under H₂ (30 bar) for 18 h after CO adsorption as function of pressure at -188 °C.

Table 3.2. Physicochemical properties of fresh, recycled and spent Ru/P25 from different runs in dioxane.

		BET (m ² *g ⁻¹)	Particle size (nm)	TGA (%)
Ru/P25	Fresh	75	2.5±0.9	ND
	Dioxane 5x Recycled	46	2.5±1.0	0.3
	Without LA	70	2.6±1.4	0.3
	With valeric acid	40	2.2±1.1	ND

3.3.4. Catalyst stability in H₂O

In a subsequent of experiments, catalyst stability was also tested in LA hydrogenation, but now with H₂O as solvent. A typical reaction was performed at 90 °C under 45 bar H₂ in a batch reactor for 3 h.[47] NMR analysis confirmed that both 4-hydroxypentanoic acid (4-HPA) and GVL are formed, as expected (data not shown). As the reactions cleanly proceed with GVL as only product and HPA as only reaction intermediate and with the focus being on deactivation/stability, further analyses were performed by HPLC, for which the GVL yield obtained should be considered as the summed yield of GVL and HPA. The production of GVL as a function of time is shown in Fig. 3.9a. Under these standard conditions, Ru/Anatase outperformed Ru/Rutile and Ru/P25, similar to the results observed in the dioxane experiments. 90% conversion of LA was achieved for Ru/Anatase after 1 h reaction whereas conversions of 25% and 47% were seen for Ru/Rutile and Ru/P25, respectively. Interestingly, different from the catalytic activity order observed in dioxane, Ru/P25 catalyst showed higher hydrogenation activity than its rutile counterpart in H₂O. A similar observation was made by Ruppert *et al.*[46] who showed that anatase-rutile (P25) and a micropore-free anatase supported Ru catalysts were more reactive than a pure rutile supported one at various reaction temperatures in H₂O.[46]

Catalyst stability in H₂O was again evaluated by recycling (Fig. 3.9). GVL production for Ru/P25 catalyst decreased gradually by about 30% after 3 recycles after which there was little variation, in line with our results in dioxane and a previous study.[13] Abdelrahman *et al.* also found Ru/TiO₂ (P25) lost its catalytic activity with time-on-stream in LA hydrogenation at 50 °C under 24 bar H₂ in a continuous flow reactor with H₂O as solvent due to both irreversible Ru sintering and reversible carbon deposition.[13] A similar, yet smaller drop was seen for Ru/Anatase with LA conversion dropping from full to 90%. Lower LA conversion (LC) recycling tests, which were performed under the identical conditions yet with a higher LA/Ru ratio, confirmed that Ru/Anatase suffered a continuous deactivation in terms of GVL production. Notably, the deactivation seen in water for the Ru/P25 and Ru/Anatase catalysts was less than in dioxane, even though severe Ru sintering is seen for the catalysts recovered from water (Fig. 3.9). Different from the catalytic efficiency increase seen at early recycles in dioxane, Ru/Rutile also showed gradual deactivation, with an overall drop of around 14% in GVL yield after recycling.

The XRD patterns of the Ru catalysts after 5 recycles in water did not show any evidence for structural change (Fig. 3.1). TGA analysis gave 1.2%, 0.6% and 0% weight loss for five times water recycled Ru/P25, Ru/Rutile and Ru/Anatase (Table 3.3), respectively, indicating that

carbonaceous deposition formation on Ru/Rutile and anatase samples during the recycling was limited, Ru/P25 nevertheless accumulated about 4 times as much coke when recycled in water instead of in dioxane. Changes in surface area were similar to those seen in dioxane. Ru/P25 also showed a decrease in surface area from 75 to 46 m²/g after its fifth recycle in H₂O, whereas the pure phase supported Ru catalysts showed little variation on the surface area upon recycling compared to the fresh catalysts. Obvious sintering as well as an increase in Ru particle size polydispersity was found for all spent catalysts after recycling in H₂O (Fig. 3.10). Especially for

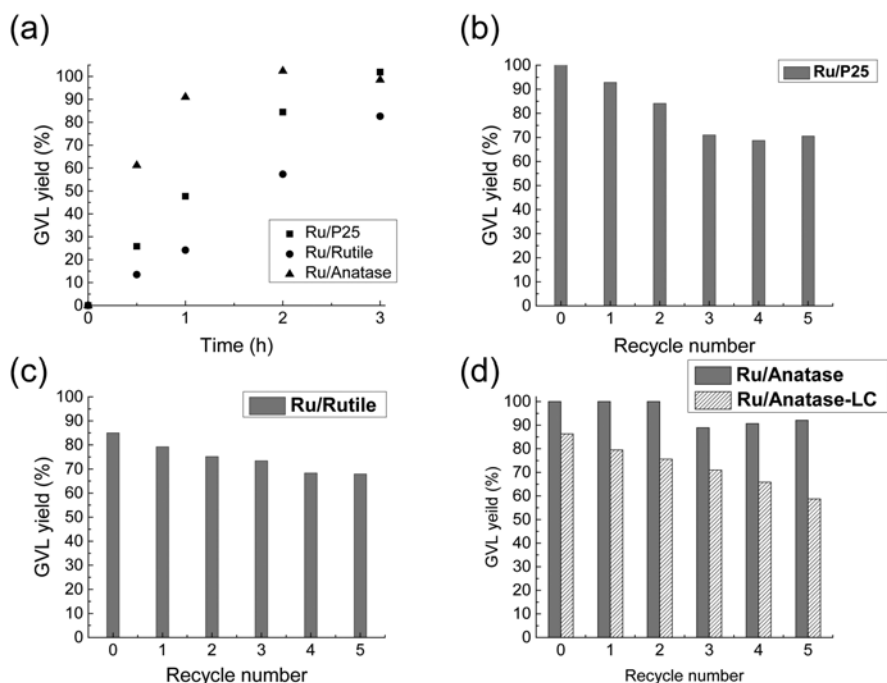


Fig. 3.9. (a) GVL yield as function of reaction time, GVL yield as a function of recycling number for (b) Ru/P25, (c) Ru/Rutile and (d) Ru/Anatase in H₂O. Experimental conditions: T = 90 °C, P(H₂) = 45 bar and t = 3 h. LA/Ru = 1600 for experiment runs, LA/Ru = 3800 for Ru/Anatase LC (low conversion) recycle.

Table 3.3. Physiochemical properties of the recycled Ru-based catalysts after LA hydrogenation with H₂O as solvent.

		BET (m ² g ⁻¹)	Particle size (nm)	TGA (%)
Ru/P25	Fresh	75	2.5±0.9	ND
	Spent 5x Recycled	46	2.9±1.5	1.2
Ru/Rutile	Fresh	25	2.3±0.8	ND
	Spent 5x Recycled	26	3.0±1.7	0.6
Ru/Anatase	Fresh	10	2.1±0.6	ND
	Spent 5x Recycled	12	4.0±4.7	0.0

Ru/Anatase, the mean Ru particle size almost doubled after recycling. It has been reported that noble metal particles could coalesce into larger particles on various supports, such as SiO₂, Al₂O₃ and C, under mild conditions in water solution.[66–68] For instance, a Ru/SiO₂ catalyst suffered significantly from metal sintering upon treatment in a H₂-saturated water solution at 100 °C, leading to the Ru-Ru coordination number to increase about three fold.[68] In the same study, the authors also noted that the addition of carbohydrates could help to stabilize Ru particles against sintering to some extent under otherwise identical conditions.[68] Similarly Ru metal sintering in LA hydrogenation in water as solvent was also reported by Abderlrahman *et al.* on various supports, including TiO₂ (P25), Ru sintering was thought to be governed by the support and exacerbated by the presence of water rather than LA interaction.[13].

Fig. 3.11a-c show the FT-IR spectra upon CO adsorption at liquid nitrogen temperature of the water recycled Ru catalysts. The frequency of the broad CO-Ru band red shifted to around 2000 cm⁻¹ for the recycled Ru/P25 catalyst, due to decreased CO adsorption and coverage (Fig. 3.11).[49] For five times recycled Ru/Anatase, the metallic Ru-CO band also shifted to a lower wavenumber of 2030 cm⁻¹ with decreased intensity. Again, the absence of a band related to CO adsorption on OH groups (2155 cm⁻¹) and appearance of new peaks located at 2123 and 2073 cm⁻¹ attributed to (TiO)₂Ru(CO)₃ species according to Robbins were observed for reused Ru/Anatase,[58] which might suggest that SMSI occurs also in water to some extent. However, the experimental data obtained so far do not allow one to discern between CO adsorption reduction resulting from Ru sintering or SMSI formation. Notably, the CO-Ru band is still present, albeit at reduced intensity, and is higher in intensity for the P25 and Ru/Anatase

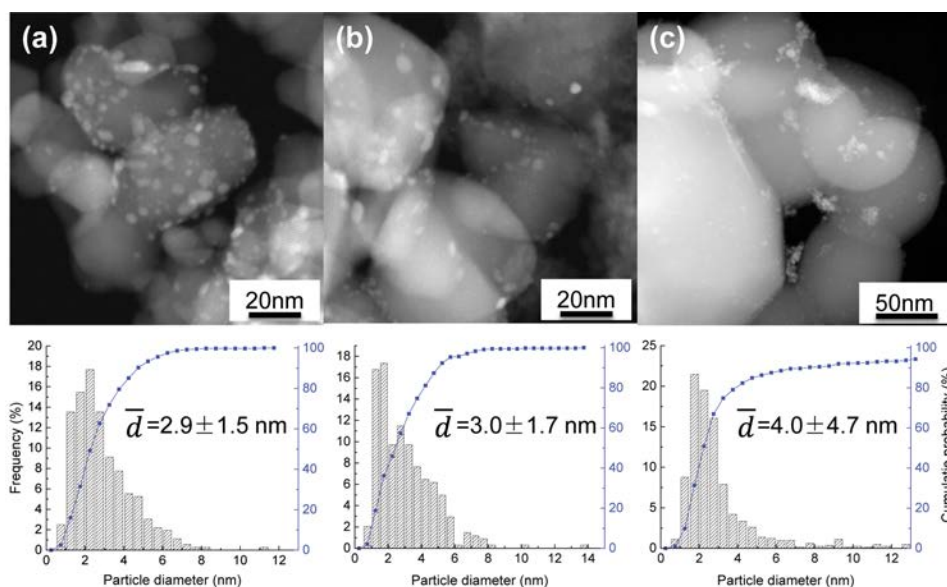


Fig. 3.10. TEM images and Ru size distributions of recycled (a) Ru/P25, (b) Ru/Rutile and (c) Ru/Anatase in H₂O as solvent.

samples recycled in water than for those used in dioxane. This result suggested that any SMSI formation must be much weaker in water. Reused Ru/Rutile, which exhibited the best stability against support reduction in dioxane, showed a much decreased CO-Ru adsorption ability after use in water. Given that rutile should be the hardest to reduce, this drop in intensity is thought to be mainly due to Ru sintering.

Taken together, in a water rich environment, the catalytic activity is in the order: Ru/Anatase > Ru/P25 > Ru/Rutile. The results showed above suggest that the reactions in water as solvent do not show the strong SMSI effects seen in dioxane, but give rise to metal sintering for all Ru catalysts.

3.3.5. Long term stability of catalysts in dioxane

As shown above, the rutile supported catalyst is most stable against deactivation by A-SMSI support reduction when used in a batch reactor with dioxane as solvent. To assess longer term stability performance of the Ru/TiO₂ catalysts, the materials were tested in a continuous flow reactor under similar dioxane LA hydrogenation conditions (Fig. 3.12). Similar to the catalytic result in batch reaction, the initial catalytic activity of the catalysts follows the order: Ru/Anatase > Ru/Rutile > Ru/P25. The LA conversion decreased continuously and significantly for Ru/P25 and Ru/Anatase (Fig. 3.12), in line with the observations made for the recycling tests in batch. Interestingly, Ru/P25 and Ru/Anatase exhibited similar catalytic activity after 20 h reaction, even though big differences in initial catalytic efficiency were seen. In sharp contrast, an initial jump in LA conversion was again seen for Ru/Rutile, similar to the increase seen in batch recycling, after which a slow decrease in activity was noted, leveling off after 56 h of treatment. It also worth to notice that, after 32 h reaction, all catalysts exhibited the same slope of deactivation. As shown above in the dioxane batch recycling experiments, for all catalysts a plateau is reached after an initial jump or drop in activity, suggesting that an equilibrium in terms of SMSI coverage is reached. Given that also no obvious metal sintering was observed for spent Ru/P25 and Ru/Rutile after 72 h time-on-stream (Fig. 3.13), the similar deactivation shown by all catalysts after 32 h in continuous flow reactor can presumably be attributed to

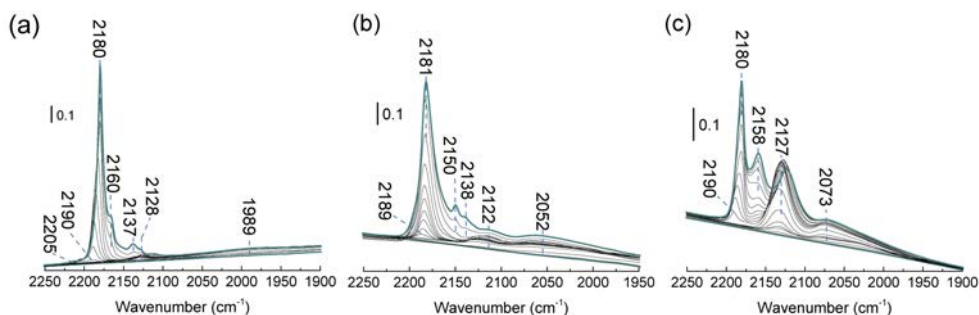


Fig. 3.11. FT-IR spectra of the 5 times recycled (a) Ru/P25, (b) Ru/Rutile and (f) Ru/Anatase obtained from high conversion runs in H₂O after CO adsorption at -188 °C.

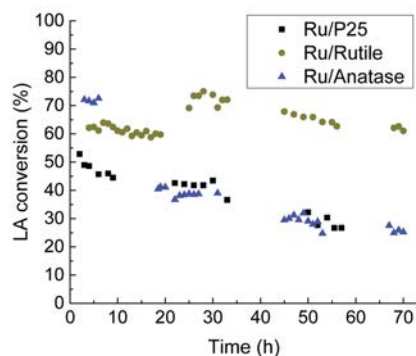


Fig. 3.12. LA conversion as a function of time over Ru/P25, Ru/Rutile and Ru/Anatase. Experimental conditions: $T = 150\text{ }^{\circ}\text{C}$, $P(\text{H}_2) = 30\text{ bar}$ and $t = 72\text{ h}$, $\text{WHSV} = 1.2\text{ g}_{\text{LA}}\text{ g}_{\text{catalyst}}^{-1}\text{ h}^{-1}$, up-stream configuration.

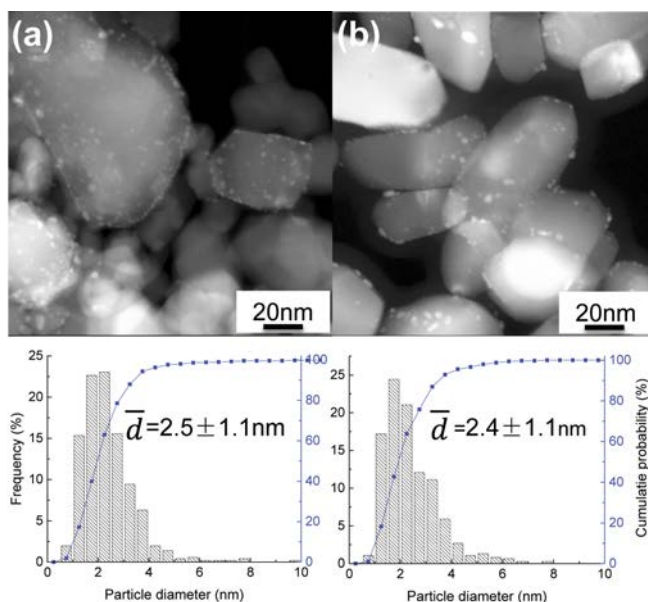


Fig. 3.13. TEM images and Ru particle size distribution of (a) Ru/P25 and (b) Ru/Rutile after 72 h time-on-stream treatment in dioxane as solvent.

a gradual coke buildup. These results again show that Ru/Rutile performed better than the Ru/(mixed)Anatase materials.

3.4. Conclusions

In this PhD thesis Chapter, we examined the effect of TiO₂ support type on Ru catalyst performance under typical LA hydrogenation reaction conditions. Rutile, anatase and the mixture of these two titania phases, i.e. P25, were selected as support oxides to disperse

the supported Ru nanoparticles. A set of Ru/TiO₂ catalysts with similar metal loading and Ru particle size was prepared via wet impregnation method and their stability assessed by multiple recycling under batch reactor conditions. With dioxane as reaction solvent, both the benchmark catalyst Ru/P25 and Ru/Anatase show a continuous decrease in GVL yield upon recycling. In contrast, rutile supported catalyst exhibited an initial jump on LA conversion in the recycling test. Characterization by TEM, TGA, FT-IR spectroscopy after CO adsorption demonstrated that the observed deactivation for (mixed) anatase supported catalysts can be attributed to SMSI formation rather than coke formation and metal sintering, with the rutile phase showing better stability against this support reduction. Also in continuous flow catalysis testing experiments, the Ru/Rutile catalyst showed the best catalyst performance over 3 days time-on-stream. The SMSI seen under the applied, relatively mild conditions is shown to require an organic acid, such as LA and valeric acid, to be present, suggesting that these organic acids play a key role in inducing SMSI formation. In a water-rich reaction environment, however, the strong effect of SMSI is not seen to the same extent, but obvious Ru particle growth is observed for all three catalyst materials under study. These results clearly show that catalyst performance highly depends on the support structure as well as the solvent employed, and are useful for the selection of efficient catalysts for catalytic biomass conversion processes.

References

1. W.R.H. Wright, R. Palkovits, *ChemSusChem* 5 (2012) 1657–1667.
2. S. De, B. Saha, R. Luque, *Bioresour. Technol.* 178 (2015) 108–118.
3. J. Ftouni, H.C. Genuino, A. Muñoz-Murillo, P.C.A. Bruijninx, B.M. Weckhuysen, *ChemSusChem* 10 (2017) 2891–2896.
4. J.P. Lange, R. Price, P.M. Ayoub, J. Louis, L. Petrus, L. Clarke, H. Gosselink, *Angew. Chem. Int. Ed.* 49 (2010) 4479–4483.
5. M.A. Mellmer, C. Sener, J.M.R. Gallo, J.S. Luterbacher, D.M. Alonso, J.A. Dumesic, *Angew. Chem. Int. Ed.* 53 (2014) 11872–11875.
6. B.L. Oser, S. Carson, M. Oser, *Food Cosmet. Toxicol.* 3 (1965) 563–569.
7. Z. Zhang, *ChemSusChem* 9 (2016) 156–171.
8. H. Xiong, S. Lin, J. Goetze, P. Pletcher, H. Guo, L. Kovarik, K. Artyushkova, B.M. Weckhuysen, A.K. Datye, *Angew. Chem. Int. Ed.* 56 (2017) 8986–8991.
9. F. Liguori, C. Moreno-Marrodan, P. Barbaro, *ACS Catal.* 5 (2015) 1882–1894.
10. A.M. Ruppert, M. Jędrzejczyk, O. Sneka-Plątek, N. Keller, A.S. Dumon, C. Michel, P. Sautet, J. Grams, *Green Chem.* 18 (2016) 2014–2028.
11. M. Varkolu, V. Velpula, D.R. Burri, S.R.R. Kamaraju, *New J. Chem.* 40 (2016) 3261–3267.
12. S. Xu, D. Yu, T. Ye, P. Tian, *RSC Adv.* 7 (2017) 1026–1031.
13. O.A. Abdelrahman, H.Y. Luo, A. Heyden, Y. Román-Leshkov, J.Q. Bond, *J. Catal.* 329 (2015) 10–21.
14. A. Piskun, J. Winkelman, Z. Tang, H. Heeres, *Catalysts* 6 (2016) 131–151.
15. P.P. Upare, J.M. Lee, D.W. Hwang, S.B. Halligudi, Y.K. Hwang, J.S. Chang, *J. Ind. Eng. Chem.* 17 (2011) 287–292.
16. C. Michel, P. Gallezot, *ACS Catal.* 5 (2015) 4130–4132.
17. L.E. Manzer, *Appl. Catal. A Gen.* 272 (2004) 249–256.
18. J. Tan, J. Cui, T. Deng, X. Cui, G. Ding, Y. Zhu, Y. Li, *ChemCatChem* 7 (2015) 508–512.
19. W. Luo, U. Deka, A.M. Beale, E.R.H. van Eck, P.C.A. Bruijninx, B.M. Weckhuysen, *J. Catal.* 301 (2013) 175–186.
20. J.P. Lange, *Angew. Chem. Int. Ed.* 54 (2015) 13187–13197.
21. D. Ding, J. Wang, J. Xi, X. Liu, G. Lu, Y. Wang, *Green Chem.* 16 (2014) 3846–3854.
22. A.M.R. Galletti, C. Antonetti, V. De Luise, M. Martinelli, *Green Chem.* 14 (2012) 688–694.
23. M.G. Al-Shaal, W.R.H. Wright, R. Palkovits, *Green Chem.* 14 (2012) 1260–1263.
24. J. Ftouni, A. Muñoz-Murillo, A. Goryachev, J.P. Hofmann, E.J.M. Hensen, L. Lu, C.J. Kiely, P.C.A. Bruijninx, B.M. Weckhuysen, *ACS Catal.* 6 (2016) 5462–5472.
25. J. Sá, J. Bernardi, J.A. Anderson, *Catal. Lett.* 114 (2007) 91–95.
26. L.B. Xiong, J.L. Li, B. Yang, Y. Yu, *J. Nanomater.* 335 (2012) 187–195.
27. Y. Zhu, D. Liu, M. Meng, *Chem. Commun.* 50 (2014) 6049–6051.
28. S. Tauster, *J. Catal.* 55 (1978) 29–35.
29. Y. Li, Y. Fan, H. Yang, B. Xu, L. Feng, M. Yang, Y. Chen, *Chem. Phys. Lett.* 372 (2003) 160–165.
30. Z. Rui, S. Wu, C. Peng, H. Ji, *Chem. Eng. J.* 243 (2014) 254–264.
31. J. Badyal, *J. Catal.* 129 (1991) 486–496.
32. M. Sanchez, *J. Catal.* 104 (1987) 120–135.
33. M.A. Vannice, D. Poondi, *J. Catal.* 169 (1997) 166–175.
34. D. Poondi, M.A. Vannice, *J. Mol. Catal. A Chem.* 124 (1997) 79–89.
35. P. Mäki-Arvela, J. Hájek, T. Salmi, D.Y. Murzin, *Appl. Catal. A Gen.* 292 (2005) 1–49.
36. T. Ekou, L. Ekou, A. Vicente, G. Lafaye, S. Pronier, C. Especel, P. Marécot, *J. Mol. Catal. A Chem.* 337 (2011) 82–88.
37. M.S. Kim, S.H. Chung, C.J. Yoo, M.S. Lee, I.H. Cho, D.W. Lee, K.Y. Lee, *Appl. Catal. B Environ.* 142–143 (2013) 354–361.

38. J.C. Colmenares, A. Magdziarz, M.A. Aramendia, A. Marinas, J.M. Marinas, F.J. Urbano, J.A. Navio, *Catal. Commun.* 16 (2011) 1–6.
39. O. Dulub, W. Hebenstreit, U. Diebold, *Phys. Rev. Lett.* 84 (2000) 3646–3649.
40. J.C. Matsubu, S. Zhang, L. DeRita, N.S. Marinkovic, J.G. Chen, G.W. Graham, X. Pan, P. Christopher, *Nat. Chem.* 9 (2016) 120–127.
41. E.I. Ko, R.L. Garten, *J. Catal.* 68 (1981) 233–236.
42. M. Bowker, P. Stone, P. Morrall, R. Smith, R. Bennett, N. Perkins, R. Kvon, C. Pang, E. Fourre, M. Hall, *J. Catal.* 234 (2005) 172–181.
43. M. Bowker, R. Sharpe, *Catal. Struct. React.* 1 (2015) 140–145.
44. C. Hernandez-Mejia, E.S. Gnanakumar, A. Olivos-Suarez, J. Gascon, H.F. Greer, W. Zhou, G. Rothenberg, N. Raveendran Shiju, *Catal. Sci. Technol.* 6 (2016) 577–582.
45. J.M. González Carballo, E. Finocchio, S. García, S. Rojas, M. Ojeda, G. Busca, J.L.G. Fierro, *Catal. Sci. Technol.* 1 (2011) 1013–1023.
46. A.M. Ruppert, J. Grams, M. Jędrzejczyk, J. Matras-Michalska, N. Keller, K. Ostojka, P. Sautet, *ChemSusChem* 8 (2015) 1538–1547.
47. A.S. Piskun, J. Ftouni, Z. Tang, B.M. Weckhuysen, P.C.A. Bruijninx, H.J. Heeres, *Appl. Catal. A Gen.* 549 (2018) 197–206.
48. T. Ohno, K. Sarukawa, K. Tokieda, M. Matsumura, *J. Catal.* 203 (2001) 82–86.
49. K. Hadjiivanov, J.C. Lavalley, J. Lamotte, F. Maugé, J. Saint-Just, M. Che, *J. Catal.* 176 (1998) 415–425.
50. K. Hadjiivanov, J. Lamotte, J.C. Lavalley, *Langmuir* 13 (1997) 3374–3381.
51. K. Hadjiivanov, *Appl. Surf. Sci.* 135 (1998) 331–338.
52. L. Mino, G. Spoto, S. Bordiga, A. Zecchina, J. Phys. Chem. C 116 (2012) 17008–17018.
53. D. Liuzzi, F.J. Pérez-Alonso, F.J. García-García, F. Calle-Vallejo, J.L.G. Fierro, S. Rojas, *Catal. Sci. Technol.* 6 (2016) 6495–6503.
54. T. Xia, C. Zhang, N.A. Oyler, X. Chen, *Adv. Mater.* 25 (2013) 6905–6910.
55. X. Chen, L. Liu, Z. Liu, M.A. Marcus, W.C. Wang, N.A. Oyler, M.E. Grass, B. Mao, P.A. Glans, P.Y. Yu, J. Guo, S.S. Mao, *Sci. Rep.* 3 (2013) 1510–1517.
56. X. Chen, L. Liu, F. Huang, *Chem. Soc. Rev.* 44 (2015) 1861–1885.
57. M. Sankar, Q. He, S. Dawson, E. Nowicka, L. Lu, P.C.A. Bruijninx, A.M. Beale, C.J. Kiely, B.M. Weckhuysen, *Catal. Sci. Technol.* 6 (2016) 5473–5482.
58. J. Robbins, *J. Catal.* 115 (1989) 120–131.
59. V.A. de la Peña O’Shea, M. Consuelo Álvarez Galván, A.E. Platero Prats, J.M. Campos-Martin, J.L.G. Fierro, *Chem. Commun.* 47 (2011) 7131–7133.
60. Y. Zhu, D. Liu, M. Meng, *Chem. Commun.* 50 (2014) 6049–51.
61. Z. Rui, L. Chen, H. Chen, H. Ji, *Ind. Eng. Chem. Res.* 53 (2014) 15879–15888.
62. M.A. Henderson, J. Phys. Chem. B 101 (1997) 221–229.
63. C.L. Pang, R. Lindsay, G. Thornton, *Chem. Soc. Rev.* 37 (2008) 2328–2353.
64. B.D. Chandler, *Nat. Chem.* 9 (2017) 108–109.
65. J.M. White, J. Szanyi, M.A. Henderson, *J. Phys. Chem. B* 108 (2004) 3592–3602.
66. J.H. Vleeming, B.F.M. Kuster, G.B. Marin, F. Oudet, P. Courtine, *J. Catal.* 166 (1997) 148–159.
67. W.C. Ketchie, E.P. Maris, R.J. Davis, *Chem. Mater.* 19 (2007) 3406–3411.
68. E.P. Maris, W.C. Ketchie, V. Oleshko, R.J. Davis, *J. Phys. Chem. B* 110 (2006) 7869–7876.

4

**Highly Stable Ru/ZrO₂ Single
Atom Catalysts: Structure,
Genesis, Stability and
Application in CO Oxidation**

Abstract

Single atom catalysts (SACs), consisting of isolated metal atoms, or better, ions dispersed on a solid support, are attractive due to their efficient metal use and distinct catalytic performance in various reactions. Here, the structure, stability and performance of Ru/ZrO₂ single atom catalysts are reported. The structure of these catalysts was studied with aberration-corrected HAADF-STEM, FT-IR after CO adsorption and Extended X-ray Absorption Fine Structure (EXAFS) to confirm the loading-dependent dispersion of the metal phase. The nature of single atom sites and the associated CO-FT-IR spectra were investigated by DFT calculations. The genesis of single Ru atoms during the catalyst synthesis procedure and the stability of the SAC were studied by *in-situ* EXAFS analysis under H₂, CO and O₂ atmosphere at elevated temperature. The characterization results demonstrate that fully atomically dispersed catalysts were successfully prepared via a simple wet impregnation method and the single Ru atoms carry a positive charge. Furthermore, the 1 wt.% Ru/ZrO₂ single atom catalyst was highly stable in the gas phase under oxidizing conditions, whereas a nanoparticle-based Ru/ZrO₂ material, synthesized for comparison, suffered from metal sintering. More interestingly, the Ru speciation in the single atom catalyst can be fine-tuned reversibly from small clusters to isolated atoms by simply changing the reduction/oxidization conditions. The catalytic activity of the Ru SACs was tested in CO oxidation, with activity increasing significantly with decreasing Ru-Ru coordination number. The T_{50%} (temperature 50% CO conversion) was lowered by 90 °C to 150 °C, going from nanoparticulate Ru/ZrO₂ to the analogous SACs. Recycling tests furthermore showed the Ru SACs to be highly stable under a strongly oxidizing reaction environment, which make them promising candidates for other oxidation catalysis applications.

This chapter is in part on the following manuscript: H.V. Thang, S. Tosoni, F. Liu, P.C.A. Bruijninx, G. Pacchioni, ChemCatChem 10 (2018) 2634–2645.

4.1. Introduction

Noble metal based heterogeneous catalysts are heavily employed in industry due to their high activity and selectivity for various important commercial processes.[1–3] As many (but not all) catalytic reactions are structure sensitive, the size and shape of supported noble metal phases play a key role in their catalytic performance.[4] Several comprehensive reviews are available on such size and shape effects in some key catalytic processes, including CO oxidation.[5–7] Depending on the type of reaction catalyzed, downsizing of the metal phase often increases activity, with subnanometer clusters for example being more reactive and selective than their nanoparticulate counterparts.[8–10] The ultimate limit of downsizing the metal phase is to have isolated, supported single metal atoms, a limit at which the electronic properties of the metal active sites can be expected to be considerably different from supported nanoparticles, offering the potential of new chemistry and catalysis. Recently this has been increasingly recognized and single atom catalysis has evolved into a rapidly developing frontier in catalysis research.[11,12]

Single atom catalysts (SACs) have now been reported with various combinations of metal phase and support and have been applied in several different hydrogenation and oxidation reactions.[12,13] For example, an increase in catalytic efficiency for butadiene hydrogenation was reported upon downsizing Au particle size, with the turnover frequency being the highest for isolated Au³⁺ atoms and independent of the Au loading when fully atomically dispersed.[14] Zhang and co-workers synthesized a series of iron oxide supported single atom catalysts (Pt, Au and Ir), which were demonstrated to be highly active and selective in various reactions, such as low temperature CO oxidation, water gas shift (WGS), NO reduction and chemoselective hydrogenation of functionalized nitroarenes.[9,13,15,16] Hackett *et al.* reported mesoporous alumina-supported palladium catalysts with different loadings and compared their catalytic performance in aerobic alcohol oxidation, demonstrating that the SAC obtained at very low Pd weight loading outperformed the nanoparticle-based catalysts.[17] More recently, isolated Pt atoms on mesoporous-Al₂O₃ were also reported to show excellent performance in selective butadiene hydrogenation, n-hexane hydro-reforming and CO oxidation.[18] These are just a few of the many reported examples of single atom catalysis and the range of reactions catalyzed by SAC is rapidly expanding.[19]

So far, many routes have been explored for the fabrication of fully dispersed SACs, including physical vapor deposition, atomic layer deposition as well as wet chemical approaches.[18,20–22] Of these reported methods, traditional wet impregnation may be most attractive, given the simplicity of the preparation process and its potential to be employed in realistic industrial catalyst preparation applications. By judicious choice of the type of supports and metal precursors, isolated atoms can be anchored on supports via wet impregnation through Strong Metal Support Interactions (SMSI).[23] Zeolites have been exploited for their pore architecture to obtain early examples of SACs,[24] defect sites in reducible oxides such as CeO₂[25] and TiO₂[23] have been used for synthesizing and stabilizing single atoms sites and SACs with non-reducible oxides, such as Al₂O₃, have also been reported, for example making use of unsaturated Al³⁺ sites for anchoring.[26,27] Given that anchoring sites are often limited on the supports,

SACs with higher loadings are often, but not always more difficult to achieve, which might hinder their practical application.[21,28]

Supported single metal atoms, or better ions, although stabilized by solid supports, can still be rather mobile due to their intrinsically high surface-free energy, and consequently can easily sinter into clusters or bigger metal nanoparticles under reactive (catalytic) conditions, especially at elevated temperatures.[29–31] For example, Duan *et al.* investigated the stability of Pt₁/Fe₂O₃ SAC under various gas atmospheres relevant to CO oxidation, water-gas shift, and hydrogenation reactions at 250 °C by imaging the spent catalysts afterwards with HAADF-STEM.[30] While Pt single atoms were found to be stable under O₂ atmosphere, they aggregated into larger Pt clusters after exposure to CO or H₂. This sintering processes could be further accelerated by the addition of water to the reducing gases.[30] Deng *et al.* also reported a fully atomically dispersed Au/CeO₂ catalyst, which turned out to be unstable under WGS reaction conditions. The positively charged Au single atoms were reduced and transformed into metal nanoparticles with an average size of 6.5 nm at 100 °C in a gas flow containing 5% CO-3% H₂O in He, with particle size further increasing to 8.7 nm upon increasing the temperature to 200 °C.[32] Kwak *et al.* also pointed out that γ -Al₂O₃ supported isolated Pt atoms converted into metallic Pt nanoparticles at temperatures higher than 400 °C, even under oxidizing conditions despite the increasing number of anchoring sites with increasing temperature.[31] Peterson *et al.* found that isolated Pd atoms dispersed on La₂O₃-modified alumina were partially reduced into metallic nanoparticles during CO oxidation when the reaction temperature got above 100 °C, as revealed by *operando* X-ray Absorption Spectroscopy (XAS).[33]

Among those reported reactions that are catalyzed by SACs, CO oxidation is of particular interest for both its practical applications, such as in exhaust abatement for automobiles and CO removal for proton exchange membrane fuel cells,[34–36] and as model reaction to assess catalyst performance and gain structural and mechanistic understanding. A range of SACs, including Pt, Pd, Au and Ag based ones, supported on reducible support oxides (e.g. iron oxide, hollandite, CeO₂, TiO₂) or inert support oxides (e.g. Al₂O₃ and zeolites) have been reported for the CO oxidation, often showing enhanced performance as compared to their metal nanoparticle counterparts.[13,16,24,37–40] To the best of our knowledge, CO oxidation activity for Ru SAC has not yet been reported. In general, Ru based catalysts, including Ru single crystals, thin films or nanoparticles are much less studied as they often do not perform well in this reaction. [41,42] Besides, Ru based catalysts would be expected to suffer from activity loss with increasing time-on-stream in CO oxidation, as a result of the formation of an inactive bulk RuO_x phase in oxygen-rich media.[43,44] It is not known yet, however, how Ru SAC would behave under such oxidizing conditions.

Previously, we found that a 1 wt.% Ru/ZrO₂ catalyst, prepared via a conventional, simple wet impregnation method, was fully monoatomically dispersed, as demonstrated by aberration-corrected HAADF-STEM.[45] This catalyst was applied in a liquid phase levulinic acid hydrogenation reaction and, surprisingly, the Ru single atoms were to a large extent found to survive the severe, highly polar and reducing reactions condition after consecutive recycling, although accompanied by some limited sintering.[45] In this PhD thesis chapter, we further

study these Ru/ZrO₂ SAC materials and report on the genesis of the single Ru atoms on the ZrO₂ support, study the structure of the Ru sites by DFT and explore the stability of this SAC under different gas atmospheres at elevated temperatures by both *ex-situ* and *in-situ* XAS and CO-FT-IR analysis. In this chapter, we show that the Ru/ZrO₂ SAC also performs well under gas phase, oxidative conditions, being highly active and stable in CO oxidation. A comparison with a Ru/ZrO₂ catalyst containing Ru metal nanoparticles revealed that the single atoms are much more active in catalysis.

4.2. Experimental Section

4.2.1. Catalyst synthesis

All chemicals were used as received without any further purification. For the preparation of the catalysts, the following chemicals have been used: ruthenium(III) nitrosyl nitrate (RuNO(NO₃)₃/Ru 31.3%) was obtained from Alfa Aesar, while the support ZrO₂ (monoclinic, Daiichi Kikenso RC-100) was obtained from Degussa. All gases were provided by Linde.

The SAC catalyst was prepared via wet impregnation following a previous report.[45] The ZrO₂ support was first dried at 120 °C for 2 h to remove humidity. Subsequently, the slurry of support and demi-water was stirring at room temperature for 0.5 h, followed by the dropwise addition of a 10 mL Ru precursor (RuNO(NO₃)₃/Ru 31.3%) water solution after which the slurry was stirred for at least 3 h. After elimination of water under vacuum at 60 °C, the solid catalyst was dried at 60 °C overnight in air, calcined at 500 °C for 3.5 h with a heating ramp of 5 °C/min under a pure N₂ flow of 100 mL/min, followed by its reduction at 450 °C with a ramp rate of 5 °C/min for 5 h, under a pure H₂ flow of 80 mL/min. Catalysts with weight loadings ranging from 0.5 to 5 wt.% were prepared with this protocol and named as XRu-SAC in which X is equal to the Ru weight loading.

A 1 wt.% Ru/ZrO₂ catalyst with Ru metal nanoparticles, labeled as 1Ru-NP, was prepared following the above wet impregnation protocol, but applying more severe calcination and reduction conditions: 10 h calcination at 500 °C in a 100 mL/min of N₂ flow with a ramp of 1 °C/min, followed by 7 h reduction at 500 °C in a 100 mL/min pure H₂ flow with a ramp of 1 °C/min. This catalyst was used as a reference system, to benchmark the activity of the SACs.

4.2.2. Catalyst characterization

Samples for examination by scanning transmission electron microscopy (STEM) were prepared by dry dispersing the catalyst powder onto holey carbon supported by a 300 mesh copper STEM grid. Aberration corrected HAADF-STEM images were taken at Lehigh University (USA) by using an aberration-corrected JEM ARM 200CF microscope operating at 200 kV.

Fourier-transform infrared (FT-IR) spectra were recorded on a Perkin-Elmer 2000 instrument. The FT-IR measurements after CO adsorption were conducted on a freshly reduced, inertly handled catalyst sample unless specific statement, the tube used for calcination/reduction was flushed with pure N₂ for 30 min, sealed and transported into a nitrogen-filled glovebox immediately to avoid any potential air oxidation or water adsorption. A self-supported

wafer (10-15 mg) was pressed at 3-3.5 tons for 10 s and positioned in a well-sealed transmission FT-IR cell equipped with CaF_2 windows inside the glovebox. The cell was evacuated to 10^{-6} mbar and cooled down to -188°C with liquid nitrogen. Spectra were taken upon CO (10% in He, purity 99.9%) adsorption on the sample at stepwise increasing pressures. CO desorption was studied under high vacuum (10^{-6} mbar) by temperature programmed desorption with a ramp of $5^\circ\text{C}/\text{min}$ from -188 to 400°C . CO-FT-IR spectroscopy of reduced but air-stored 1Ru-SAC was carried out as follows: 15-20 mg of the catalyst was pressed into a self-supported pellet and placed into a well-sealed cell with CaF_2 window. The wafer was activated at 500°C ($10^\circ\text{C}/\text{min}$) under high vacuum (10^{-6} mbar) to remove the adsorbed water. Subsequently, the cell was cooled down to -188°C to record the FT-IR spectra.

X-ray Absorption Spectroscopy (XAS) measurements were performed at ESRF (Grenoble, France) on the DUBBLE BM26 beamline. Two Ru reference samples were measured, metallic Ru and Ru(IV)O_2 . Both references were diluted in boron nitride and pressed into a pellet, after which they were measured in transmission mode. The catalyst samples, with a sieve fraction of 75-150 μm , were packed in a quartz capillary (1 mm external diameter, 0.01 mm wall thickness) and supported with two plugs of quartz wool to give a catalyst bed length of 0.8 cm. Both *ex-situ* and *in-situ* samples were measured in fluorescence mode.

For *in-situ* measurements, the samples were placed in the reactor cell. 1 mL/min of gas was flown through the reactor during the measurements. Calcined 1Ru-SAC was treated in a pure H_2 flow at 450°C for 5 h. Reduced 1Ru-SAC was treated in a gas flow of CO (10% in He) or pure O_2 for 2 h at 250 and 300°C , respectively. In order to compare the stability of a Ru-based catalyst in an oxidizing environment, a reduced 1Ru-NP catalyst was also heated in O_2 atmosphere at 250°C for 2 h. The ramping rate of the heating process in all *in-situ* measurements was $5^\circ\text{C}/\text{min}$. In order to get high quality XANES spectra during the heating process, heating processes were repeated and the targeted temperature was held for 20 min to collect multiple spectra. All the acquired XAS spectra were subsequently processed in Athena and analyzed in Artemis, both part of a XAS data analysis software package using IFEFFIT.[46] For the EXAFS spectra the R-space was determined and the EXAFS parameters (coordination number, Debye-Waller factor, radial distance and E_0) were determined by fitting the R-space of the various samples to the Ru and RuO_2 standards using a correction parameter (S_0^2) of 0.69 and 0.95 for Ru-Ru and Ru-O scattering respectively. A k -weight of 3 was used in the analysis to optimize the parameters, then for comparison the fit was double-checked with a k -weight of 1.

Hydrogen chemisorption experiment was performed on a Micromeritics ASAP 2020 instrument. The catalyst was reduced at 250°C for 2 h. After reduction, the sample was degassed for 1 h at 250°C . The sample was then cooled to 40°C at which the H_2 adsorption isotherm was measured.

4.2.3. Theoretical calculations

DFT calculations were performed at the University of Milano-Bicocca (Italy). Spin-polarized DFT+U calculations have been performed using the VASP code. The core regions are treated

with the Projector Augmented Wave scheme. The PBE functional was adopted, together with a Hubbard's penalty parameter U to improve the description of the electronic structure of zirconia (in particular the band gap). The U parameter, applied to the Zr(4d) orbitals, was empirically set to 4 eV. Electronic and ionic relaxations were performed with a tolerance of 10^{-5} eV and 0.01 eV/Å, respectively. The sampling of the reciprocal space reduces, in all cases, to the Γ point. The SCF tolerance was tightened to 10^{-6} eV to ensure good numerical accuracy.

The most stable surfaces of the tetragonal (t-ZrO₂) and monoclinic (m-ZrO₂) polymorphs were studied, namely (101) for t-ZrO₂ and (11) for m-ZrO₂. In the case of t-ZrO₂, we extended the study to the (156) stepped surface, consisting of subsequently stacked t-ZrO₂ (101) planes connected by steps exposing three-coordinated oxygen ions. In order to simulate adsorption phenomena at a reasonable dilution, large supercells were adopted: for t-ZrO₂ (101) a 3x2 supercell (Zr₆₀O₁₂₀); for t-ZrO₂ (156) a 2x1 supercell (Zr₁₀₀O₂₀₀), and for m-ZrO₂ (11), a 2x2 supercell (Zr₆₄O₁₂₈). The CO stretching frequencies were calculated with the finite difference numerical scheme, performing three displacements for every degree of freedom. The active fragment in frequencies calculations was restricted to the CO molecule and its first neighbors on the surface. The vibrational properties of adsorbed CO have been computed using the harmonic approximation. At the PBE level the free CO molecule displays a C-O bond distance of 1.144 Å and a stretching frequency of 2125 cm^{-1} , to be compared with the experimental $\omega_e = 2143\text{ cm}^{-1}$. In the following the computed frequencies were scaled by a factor $a = 2143/2125 = 1.0085$ to facilitate the comparison with the experimental bands. The adsorption energy was defined as the energy difference between the unbound moieties and the CO/RuO_x-ZrO₂ complex. Positive adsorption energies, E_{ad} , indicate a bound complex. The data concerning CO adsorption on (RuO_x) ZrO₂ are summarized and shown in Tables 4.1, 4.2 and 4.3.

4.2.4. Catalyst performance testing

Catalytic tests were performed in a fixed bed plug flow set-up. Typically, a fixed amount of 0.5 mg of Ru (sieve fraction of 75-150 μm) was packed in a 1 cm OD rectangular quartz tube reactor (ID = 3 mm \times 6 mm) and diluted with SiC (sieve fraction of 212-425 μm) to a total volume of 0.4 mL. After that, the catalysts were exposed to reacting gas consisting of 20 mL CO (10% in He, purity 99.9%) and 20 mL pure O₂. Light-off curves of catalyst activity were determined using a temperature gradient from 30 to 300 °C with a ramp of 2 °C/min. Catalyst stability was tested by temperature cycling. The output gas was analyzed by nondispersive FT-IR gas analysis and mass spectrometry. The gas concentration was calibrated with different concentration of CO in O₂. Temperature for 50% CO conversion ($T_{50\%}$) was used an index to evaluate the catalyst activity. Turnover frequency (TOF) is defined as the number of molecules reacted per catalytic site per time.[33,47] TOF and CO conversion (X) calculated following the equations:

$$TOF = \frac{\text{Flowrate of CO (mol/min)} * (1\text{mol}/22400) * \text{Fraction converted}}{\text{Moles of Ru} * 60(\text{sec/min})} \div \text{Dispersion} \quad (1)$$

Table 4.1. CO on RuO_x species dispersed on tetragonal ZrO₂ (101) surface. Formal Ru oxidation state, adsorption energy (E_{ad} , eV), C-O bond length (R_{CO} , Å), C-Ru distance (R_{Cru} , Å), Ru Bader charge (Q_{Ru} , |e|), scaled CO harmonic stretching frequency, (ω_e , cm⁻¹) and frequency shift with respect to the gas-phase ($\Delta\omega_e$, cm⁻¹).

RuO _x species	CO site	E _{ad} (eV)	R _{CO} (Å)	R _{Cru} (Å)	Q _{Ru} (e)	ω _e (cm ⁻¹) ^a	Δω _e (cm ⁻¹)
Single CO molecule							
t-ZrO ₂ (101)	Zr ^{IV}	0.26	1.143	2.556	-	2145	+2
(Ru) _{ad} /t-ZrO ₂	Ru ⁰	1.86	1.173	1.869	+0.20	1946	-197
(RuO) _{ad} / t-ZrO ₂	Ru ^I	2.05	1.168	1.901	+0.92	1986	-157
(RuO ₂) _{ad} / t-ZrO ₂	Ru ^{II}	1.48	1.170	1.801	+1.53	2018	-125
(RuO ₃) _{ad} / t-ZrO ₂	Ru ^{IV}	0.50	1.143	2.108	+1.91	2130	-13
(Ru) _{lattice} / t-ZrO ₂	Ru ^{IV}	1.91	1.158	1.870	+1.65	2057	-86
Geminal CO molecules							
(RuO) _{ad} / t-ZrO ₂	Ru ^I	2.05	1.165	1.872	+1.13	2039	-104
		2.19	1.171	1.813	+1.13	1972	-171
Three CO molecules							
(RuO) _{ad} / t-ZrO ₂	Ru ^I	2.05	1.156	1.954	+1.18	2097	-46
		2.19	1.157	1.973	+1.18	2012	-131
		0.56	1.163	1.894	+1.18	1999	-144

^a In the gas-phase, the CO molecule exhibits a bond distance of 1.144 Å and a stretching frequency of 2125 cm⁻¹. Frequencies scaled by 2143/2125 = 1.0085

Table 4.2. CO on RuO_x species dispersed on tetragonal ZrO₂ (156) stepped surface. Formal Ru oxidation state, adsorption energy (E_{ad} , eV), C-O bond length, (R_{CO} , Å), C-M distance, (M=Zr, Ru), (R_{CM} , Å), Ru Bader charge (Q_{Ru} , |e|), scaled CO harmonic stretching frequency, (ω_e , cm⁻¹) and frequency shift with respect to the gas-phase ($\Delta\omega_e$, cm⁻¹).

RuO _x species	CO site	E_{ad} (eV)	R_{CO} (Å)	R_{Cru} (Å)	Q_{Ru} (e)	ω_e (cm ⁻¹) ^a	$\Delta\omega_e$ (cm ⁻¹)
Single CO molecule							
t-ZrO ₂ (156)	Zr ^{IV}	0.54	1.139	2.556	-	2178	+35
(RuO) _{ad} /t-ZrO ₂	Ru ^I	2.11	1.165	1.893	+1.02	1994	-149
(RuO ₂) _{ad} /t-ZrO ₂	Ru ^{II}	1.93	1.116	1.831	+1.51	2020	-123
(RuO ₃) _{ad} /t-ZrO ₂	Ru ^{III}	2.61	1.164	1.867	+1.59	2030	-113
(Ru) _{lattice} /t-ZrO ₂	Ru ^{IV}	2.07	1.165	1.834	+0.84	2022	-121
Geminal CO molecules							
(RuO) _{ad} /t-ZrO ₂	Ru ^I	2.11	1.164	1.865	+1.20	2044	-99
		1.92	1.172	1.815	+1.20	1975	-168
(RuO ₂) _{ad} /t-ZrO ₂	Ru ^{II}	1.93	1.147	2.051	+1.53	2114	-29
		0.64	1.161	1.864	+1.53	2034	-109

^a In the gas-phase, the CO molecule exhibits a bond distance of 1.144 Å and a stretching frequency of 2125 cm⁻¹. Frequencies scaled by 2143/2125 = 1.0085.

Table 4.3. CO adsorption on RuO species dispersed on monoclinic ZrO₂ ($\bar{1}11$) surface. Formal Ru oxidation state, adsorption energy (E_{ad} , eV), C-O bond length, (R_{CO} , Å), C-M (M=Zr, Ru) distance, (R_{CM} , Å), Ru Bader charge (Q_{Ru} , |e|), scaled CO harmonic stretching frequency, (ω_e , cm⁻¹) and frequency shift with respect to the gas-phase ($\Delta\omega_e$, cm⁻¹).

RuO _x species	CO site	E_{ad} (eV)	R_{CO} (Å)	R_{Cru} (Å)	Q_{Ru} (e)	ω_e (cm ⁻¹) ^a	$\Delta\omega_e$ (cm ⁻¹)
Single CO molecule							
m-ZrO ₂ ($\bar{1}11$)	Zr1	0.36	1.142	2.556	-	2152	+9
	Zr2	0.07	1.143	3.871	-	2146	+3
	Zr3	0.34	1.141	2.587	-	2161	+18
	Zr4	0.40	1.140	2.578	-	2169	+26
RuO _{ca4} /m-ZrO ₂ ($\bar{1}11$)	Ru ^I	2.71	1.162	1.1913	+0.91	2013	-130
RuO _{a4} /m-ZrO ₂ ($\bar{1}11$)	Ru ^I	2.67	1.167	1.875	+0.88	1994	-149
RuO _{a3} /m-ZrO ₂ ($\bar{1}11$)	Ru ^I	2.49	1.174	1.824	+1.13	1966	-177
Geminal CO molecules							
RuO _{ca4} /m-ZrO ₂ ($\bar{1}11$)	Ru ^I	2.71	1.164	1.860	+1.12	2041	-107
		1.82	1.172	1.832	+1.12	1963	-180

^a In the gas-phase, the CO molecule exhibits a bond distance of 1.144 Å and a stretching frequency of 2125 cm⁻¹. Frequencies scaled by 2143/2125 = 1.0085.

$$X = \frac{\text{Moles of CO inlet} - \text{Moles of CO outlet}}{\text{Moles of CO inlet}} \times 100\% \quad (2)$$

In which the dispersion of 1Ru-NP was determined by H₂ chemisorption, while for 0.5Ru-SAC the dispersion was assumed to be 100%.

4.3. Results and Discussion

4.3.1. Catalyst performance in CO oxidation

The CO oxidation activity of a series of Ru/ZrO₂ catalysts of different weight loadings (0.5-5 wt.%) prepared by the method that previously gave a fully monoatomic 1 wt.% Ru/ZrO₂ material (XRu-SAC) is compared to a nanoparticle containing 1 wt.% Ru/ZrO₂ catalyst (1Ru-NP) (Fig. 4.2).[45] CO oxidation was selected as a probe reaction to evaluate catalyst performance, the effect of dispersion and catalyst stability under oxidizing condition. Light-off curves were determined for each catalyst material over a temperature range of 30 to 300 °C, keeping the molar amount of noble metal fixed between runs, using a gas feed composition with a CO/O₂ ratio of 1:10 and a GHSV of 6000 h⁻¹.

The activity of the catalyst materials is shown in Fig. 4.1a in terms of CO conversion. The 1Ru-NP material exhibited a 50% CO conversion temperature ($T_{50\%}$) of 240 °C. The series

of Ru-SAC proved to be much more active at lower temperatures, showing a significant, continuously decreasing $T_{50\%}$, from 185 °C for the 5Ru-SAC catalyst to 150 °C for the 1 and 0.5Ru-SAC catalysts (Table 4.4). The gradual shift in $T_{50\%}$ as well as the observation that the 0.5 and 1 wt.% Ru-SAC materials are equally active, suggests that catalytic performance depends on dispersion and that Ru single atom sites are more active than their nanoparticles in CO oxidation. The turnover frequency (TOF) at 10% CO conversion and the given space velocity

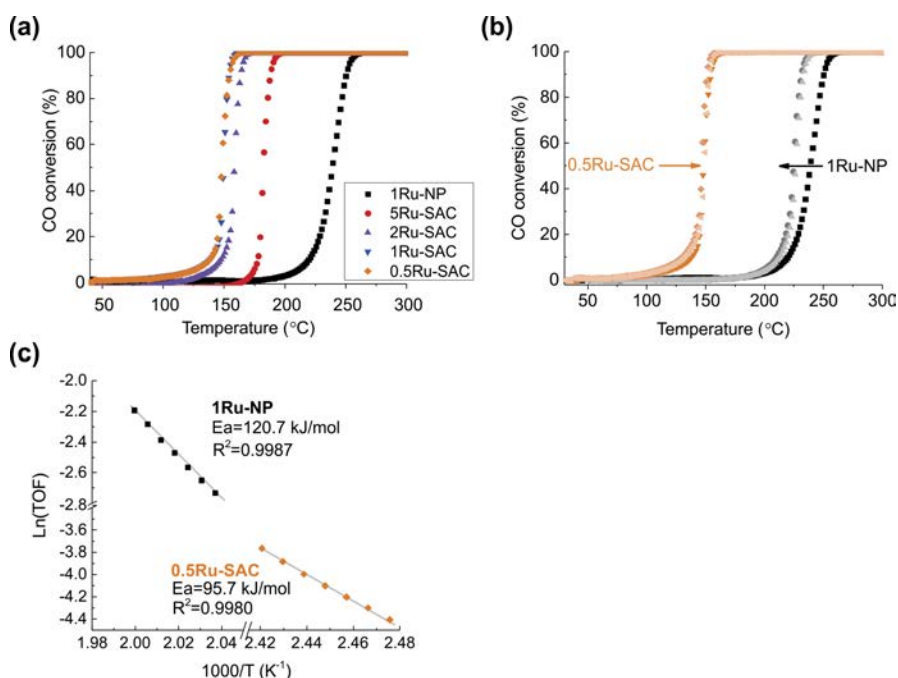


Fig. 4.1. (a) Catalytic activity in CO oxidation over the reduced Ru-based catalysts as a function of temperature, (b) catalyst stability upon recycling and (c) Arrhenius plots for CO oxidation over Ru SAC and NP catalysts.

Table 4.4. Catalytic performance of Ru single atom and nanoparticle catalysts.

	1Ru-NP	1Ru-NP ^a	1Ru-SAC	0.5Ru-SAC	2Ru-SAC	5Ru-SAC
Cycle No.	$T_{50\%}$ (°C)					
1	240	ND	150	148	158	182
2	226	226	149	146	160	173
3	226	226	151	148	161	173
	TOF (s ⁻¹)					
1	0.17 ^b			0.03 ^c		

^a 1Ru-NP was treated in a pure O₂ flow in cycle 1, b and c were obtained at 220 and 142 °C, respectively.

for 1Ru-NPs (220 °C) and 1Ru-SAC (142 °C) were 0.17 and 0.03 s⁻¹, respectively, which are similar to that of a KLTL zeolite supported Pt SAC catalyst (0.012 s⁻¹, 150 °C) under comparable reaction conditions.[24]

In addition to catalytic activity, differences in stability were also observed for Ru SAC and NP catalysts (Fig. 4.1b and Table 4.4). Interestingly, upon recycling, an improvement in catalytic activity was observed for both the 1Ru-NP and 5Ru-SAC catalysts. For example, after a first run, the $T_{50\%}$ for 1Ru-NP shifted to lower temperature from 240 to 226 °C, after which the activity remained constant upon further recycling. Notably, a control run using O₂ only as gas feed in cycle 1 also generated the same positive effect on catalytic activity of the Ru nanoparticulate catalyst (Table 4.4, column 2), which is attributed to the partial oxidation of the Ru metal nanoparticles under these conditions. Indeed, Aßmann *et al.* previously reported a detailed investigation into the deactivation of polycrystalline RuO₂ powder during CO oxidation, observing that a Ru/RuO₂ core-shell model catalyst was most reactive and stable.[48] Joo *et al.* further corroborated this by comparing the catalytic activity of a series of size-controlled Ru NPs from 2 to 6 nm in CO oxidation under oxidizing condition. They found that larger supported Ru metal nanoparticles gave rise to a higher activity due to the formation of stable Ru/RuO₂ core-shell particles, whereas small Ru metal nanoparticles were prone to transform into highly oxidized, but inactive bulk RuO_x species.[49] The similar formation of a disordered oxidic platinum shell on a metallic Pt core during the CO oxidation process has also been seen over a nanoparticulate Pt/Al₂O₃ catalyst.[50] The temperature-resolved XANES experiments discussed below (see section 4.3.4.2) also point at partial oxidation under an O₂ rich environment, with the reduced metal nanoparticles of 1Ru-NP converting into RuO_x species supported on metallic Ru, in line with the above. Although some improvement of catalytic activity was found for 1Ru-NP upon recycling, STEM analysis did reveal that significant metal sintering had occurred (Fig. 4.2h). The mean Ru particle after recycling more than doubled (7.9 ± 3.3 nm) compared to the fresh counterpart (3.2 ± 2.5 nm). In contrast, the 0.5Ru-SAC catalyst proved to be thermally stable, as evidenced by its constant catalytic activity upon recycling (Fig. 4.1b). No Ru nanoparticles could be detected in the STEM images of the recycled 0.5Ru-SAC catalyst (Fig. 4.2g).

Activation energies (E_a) were determined for 1Ru-NP and 0.5Ru-SAC, presenting the two extremes in dispersion (Fig. 4.1c). The Arrhenius plots give an activation energy of 120.7 kJ/mol for 1Ru-NP, similar to data reported data for a RuO₂ (110) crystal, in line with the suggested partial oxidation.[44] In contrast, the fully atomically dispersed Ru on ZrO₂ catalyst showed a distinctly lower activation energy of 95.7 kJ/mol, highlighting the differences in catalytic pathway and active sites involved in this reaction for the two types of catalysts.

4.3.2. Characterization of fresh catalysts

Having established that the SAC catalysts perform much better than the nanoparticulate reference catalyst in CO oxidation and that the CO oxidation activity depends on weight loading for the SAC series, we turned to the extensive characterization of the metal phase in these materials, including the evolution of these structures during synthesis and under reactive conditions. Fig. 4.2 shows STEM images of the catalysts obtained by the SAC synthesis method

and the nanoparticle-containing catalyst. We previously showed that AC-STEM analysis of a 1 wt.% Ru/ZrO₂ sample showed only isolated Ru atoms, marked by white arrows in Fig. 4.2a, well dispersed on the surface of ZrO₂.^[45] In line with this conclusion, no Ru metal nanoparticles could be observed by (non-AC) STEM for the 1Ru-SAC sample studied both before and after reduction (Fig. 4.2b and f). Surprisingly, no metal nanoparticles could be observed neither for the Ru-SAC materials prepared by same protocol at loadings up to 5 wt.%, indicating that any Ru particles or clusters formed need to be of subnanometer dimensions. In contrast, Ru metal nanoparticles could clearly be discerned in the image of Ru-NP, with a mean Ru particle size of 3.2 ± 2.5 nm (Fig. 4.2e).

The Ru phases of the Ru/ZrO₂ catalysts were further characterized by XAS. In line with the STEM analysis, 1Ru-NP showed a typical whiteness of a metallic Ru reference (Fig. 4.3). Although the 5Ru-SAC catalyst contains 5 times more Ru, the edge position of 5Ru-SAC shifted to a higher energy and its whiteness intensity increased as well compared to 1Ru-NP catalyst (Fig. 4.3a), indicative of a higher Ru oxidation state for the 5Ru-SAC catalyst. Moreover, both the whiteness intensity increased and edge position shifted towards higher energy upon decreasing of the Ru loading, indicating that Ru on average had an increasingly higher oxidation state upon lowering the Ru weight loading. When Ru weight loading was decreased to 0.5 wt.%, the catalyst exhibited a XANES spectrum very similar to the RuO₂ rather than the metallic Ru reference, confirming that the Ru phase in 0.5Ru-SAC is positively charged.

Fig. 4.3 and Table 4.5 summarize the EXAFS data fitting results. As seen from the Fourier transform (R space) of the EXAFS spectra, the 1Ru-NP catalyst exhibited a significant Ru-Ru contribution at a distance of 2.68 Å with an average coordination number of 11.4, which is comparable with that of the Ru⁰ reference. In line with the variations observed for the near edge region, this Ru-Ru peak intensity and hence coordination number gradually drop with decreasing weight loading. The small, first shell Ru-Ru coordination number seen for 1Ru-SAC, suggests that only a small fraction of the Ru is present as small metal clusters in the reduced 1Ru-SAC catalyst (no nanoparticles are detected by STEM). When the Ru loading level was further decreased to 0.5 wt.%, the Ru-Ru contribution completely vanished. Indeed, only one prominent peak at ~ 1.99 Å resulting from the Ru-O contribution was detected, demonstrating that the 0.5Ru-SAC is a fully atomically dispersed catalyst. As these samples were reduced at 450 °C for 5 h prior to EXAFS analysis, it can be inferred that the Ru-O ligands observed in the EXAFS analysis were not attributed to a bulk RuO_x phase, but originated from the interaction between Ru atoms and the ZrO₂ support. Indeed, the DFT calculations shown below suggest that the atomically dispersed sites consist of RuO_x species strongly bound to the zirconia surface, with the oxygen originating from a surface hydroxyl. It is worth to notice that calcined 1Ru-SAC also exhibited a XANES spectrum resembling that of the RuO₂ reference, indicating that Ru⁴⁺ like species are also dominant in the calcined 1Ru-SAC. Both the first shell and second Ru-Ru interaction (~ 3.2 Å) are lacking in the corresponding R space plot (Fig. 4.3e and Table 4.5), confirming that Ru species are present as isolated single atoms rather than bulk RuO₂, consistent with the absence of Ru metal nanoparticles in the STEM images. Therefore, it can be concluded

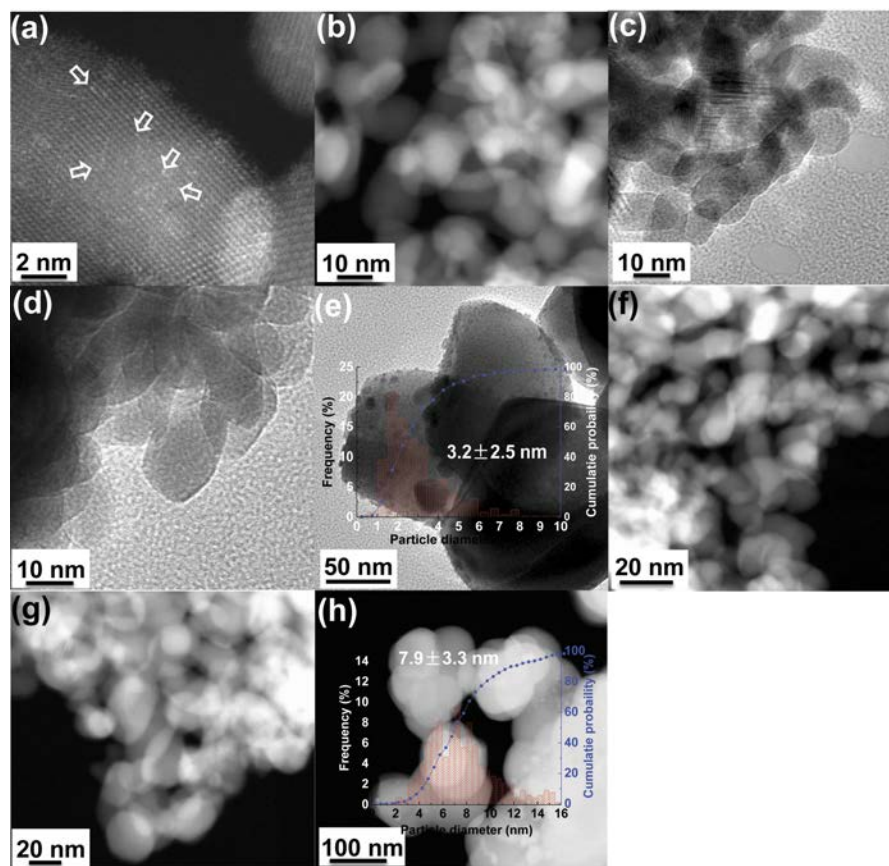


Fig. 4.2. (a) AC-TEM images of 1Ru-SAC,[45] STEM images of (b) 1Ru-SAC, (c) 5Ru-SAC, (d) 2Ru-SAC, (e) 1Ru-NP and (f) calcined 1Ru-SAC, (g) spent 1Ru-SAC and (h) spent 1Ru-NP after three CO oxidation cycles.

that a fully atomic dispersion of the Ru phase could also be achieved at a Ru loading of 1 wt.% without reduction.

CO adsorption on supported Ru catalysts is another versatile approach to monitor the properties, such as oxidation and coordination states, of supported metal catalysts and has proven to be very powerful for the analysis of SAC.[16] FT-IR spectra of freshly reduced catalysts were recorded at liquid nitrogen temperature after exposure to CO, with $p(\text{CO})$ gradually being increased to 0.3 mbar (Fig. 4.4). Not to expose the freshly reduced catalyst to the atmosphere, the freshly prepared samples were transferred to a glove box and subsequently loaded in the FT-IR cell under inert atmosphere. Then the cell was directly cooled down to -188 °C, with a drying step not being necessary for this protocol.

Fig. 4.4a shows the FT-IR spectrum of the fresh, reduced 1Ru-SAC catalyst after CO adsorption. Three features located at 2121, 2061, and 2023 cm^{-1} were detected and assigned to one

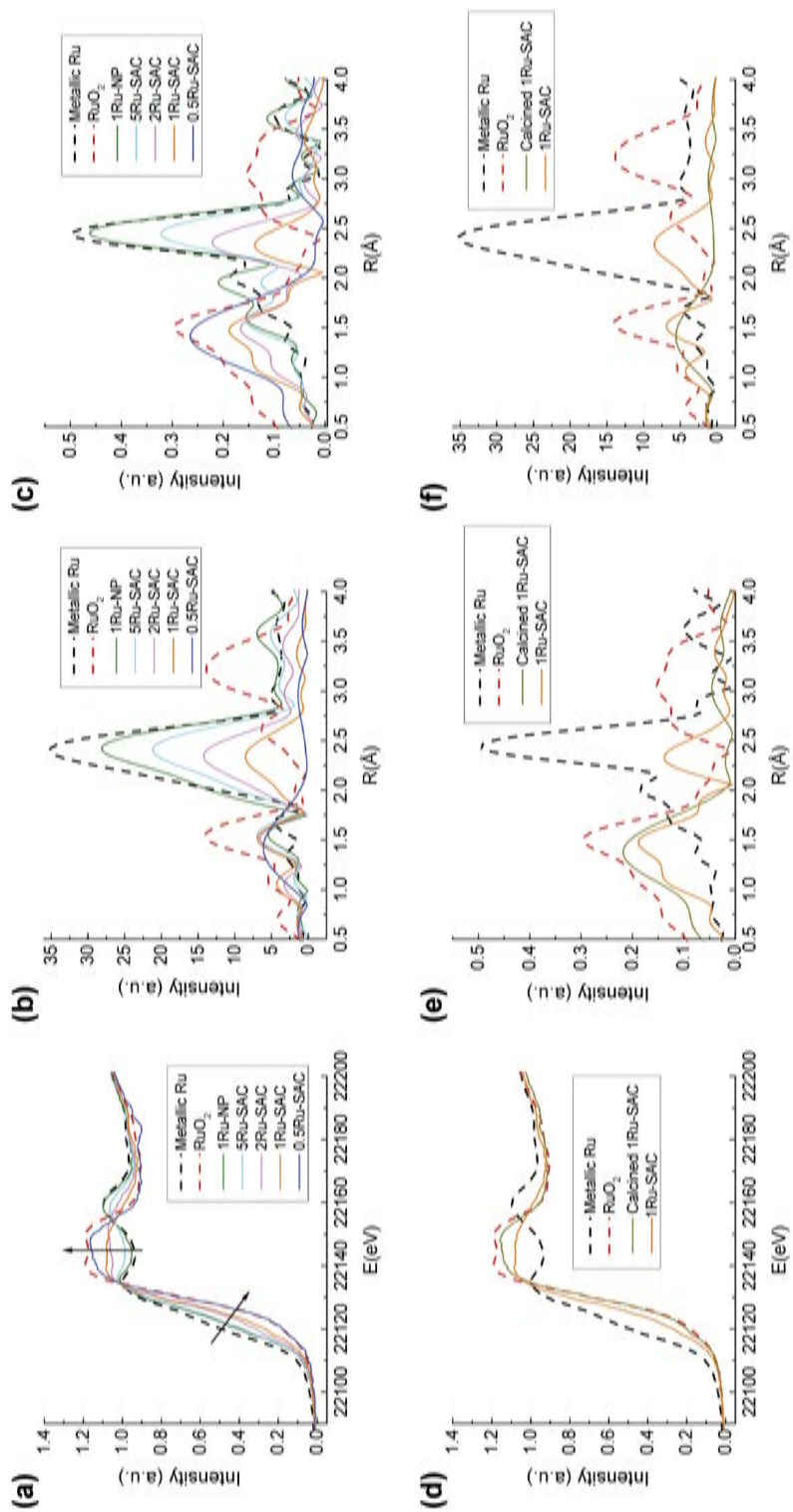


Fig. 4.3. (a) XANES spectra, (b) k^2 -weighted, (c) k^3 -weighted Fourier transform spectra from the EXAFS of the reduced Ru/ZrO₂ catalysts and references; (d) XANES spectra, (e) k^2 -weighted, (f) k^3 -weighted Fourier transform spectra from EXAFS of calcined 1Ru/ZrO₂ and reduced 1Ru/ZrO₂ catalyst and references.

Table 4.5. Overview of the physicochemical properties of the Ru/ZrO₂ catalysts.

Sample	Particle size (nm) ^a	Dispersion (%) ^b	IR bands (cm ⁻¹) ^c	EXAFS fitting results			
				Neighbor	N ^d	R ^d (Å)	σ ^d
1Ru-NP	3.2 ± 2.5	18	2003-2035	Ru	11.4	2.68	0.004
				O	1.56	1.97	0.01
5Ru-SAC	ND	ND	2126, 2067,	Ru	9.25	2.68	0.005
			2021, 2003	O	1.24	1.96	0.001
2Ru-SAC	ND	ND	ND	Ru	5.4	2.68	0.004
				O	2.1	1.99	0.003
1Ru-SAC	ND	ND	2121, 2061,	Ru	3.0	2.68	0.003
			2003	O	2.7	1.99	0.003
0.5Ru-SAC	ND	100 ^e	2122, 2059,	Ru	0	ND	ND
			2017	O	3.6	1.99	0.002
Calcined 1Ru-SAC	ND	100 ^e	2054, 2019	Ru	0	ND	ND
				O	2.9	1.97	0.0001
Ru foil				Ru	12	2.68	0.004
RuO ₂				O	6	1.98	0.003

^a is determined by HAADF-STEM; b is obtained from H₂ chemisorption, c is the FT-IR bands of Ru-CO vibration, samples used for FT-IR measurements are non-air exposed, d: N, R and σ² are the coordination number, interatomic distance, Debye–Waller factor, respectively, e is assumed based on the fact that 0.5Ru-SAC and calcined 1Ru-SAC are fully atomically dispersed.

or two CO molecules adsorbed on cationic, single atom Ru sites based on the DFT calculations shown below. The broad nature of the peaks was attributed to different Ru locations expected to lead to a broadened spectral envelope. Notably, upon increasing the CO pressure, no shifts were seen for the peak maxima and this lack of coverage dependence is highly indicative of the mono-atomic nature of the catalyst.[16] The spectral features at 2194 and 2174 cm⁻¹, which appeared at higher CO pressures, were assigned to CO on ZrO₂, in line with literature.[52–54]

The FT-IR spectra of 1Ru-SAC obtained in our work are very similar to those reported earlier by Guglielminotti *et al.* for reduced Ru/ZrO₂, synthesized with a self-prepared zirconia support.[54] No particle size data or information on dispersion is reported for this catalyst, except for chemisorption results that show a majority of the Ru to be exposed to the surface. The chemisorption results were considered as ‘odd’ by the authors and the FT-IR data were subsequently interpreted assuming that Ru was presented as fully reduced Ru⁰ nanoparticles/crystallites, with the assignment of the bands to Ruⁿ⁺(CO)_{1,2} species being linked to oxidized Ruⁿ⁺ species at the surface of the crystallites. The broadness of the observed bands was thought to be the result of crystallites of various sizes or a different level of contamination by oxygen. Mihaylov *et al.* extensively studied CO adsorption on an oxidized Ru/ZrO₂ sample prepared on a home-made monoclinic ZrO₂ support and activated at 400 °C under oxygen.[53] Temperature-dependent FT-IR studies after (isotope-labeled) CO adsorption prompted these authors to propose Ru³⁺(CO)₃ and Ru²⁺(CO)₃ species to contribute to the bands observed at ca. 2130

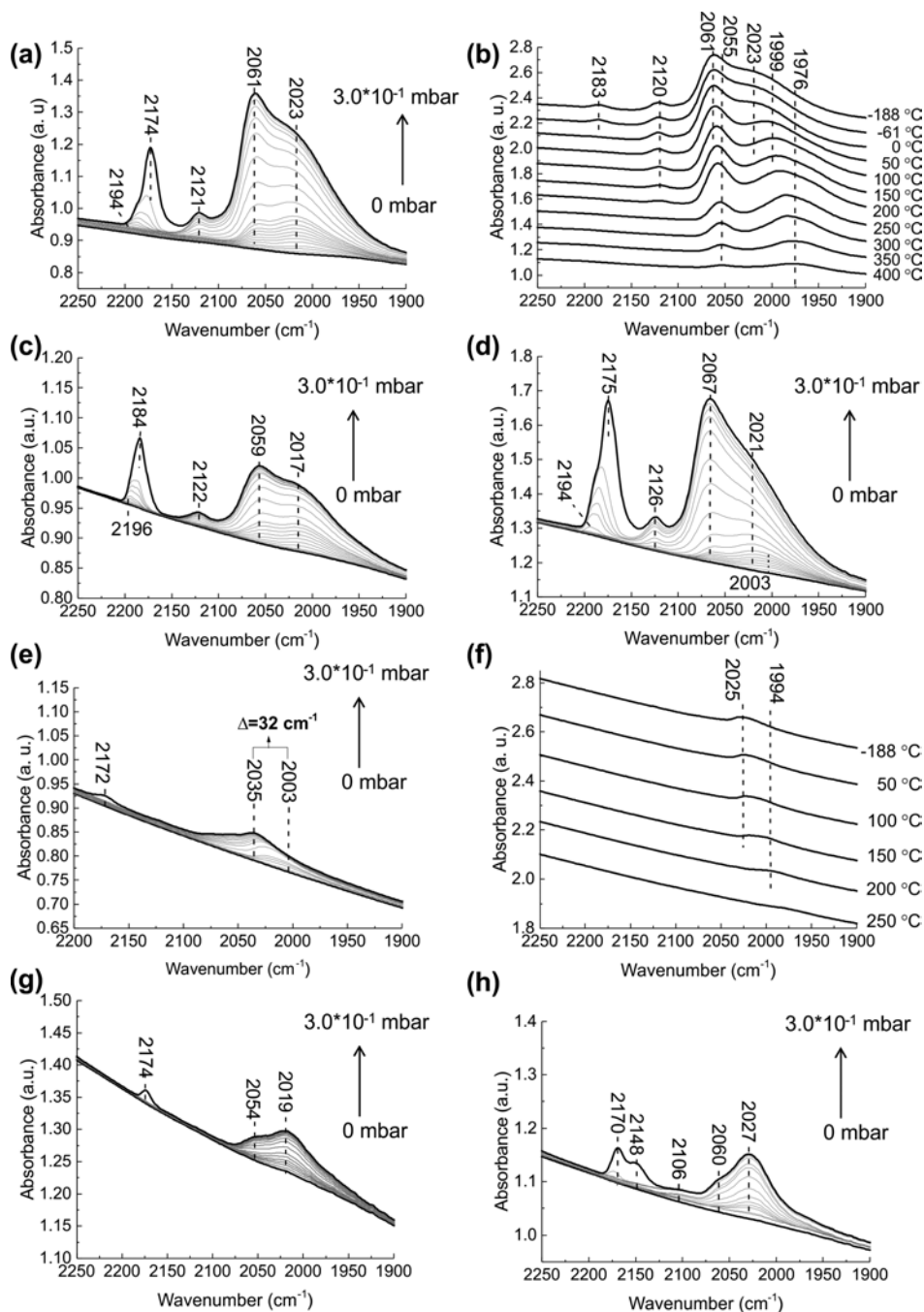


Fig. 4.4. FT-IR spectra of (a) fresh, reduced 1Ru-SAC as a function of CO pressure,[51] (b) CO desorption on reduced 1Ru-SAC as function of temperature under 10^{-6} mbar vacuum, reduced (c) 0.5Ru-SAC, (d) 5Ru-SAC as a function of CO pressure at -188 °C, (e) reduced Ru-NP at -188 °C as function of CO pressure, (f) CO desorption on reduced Ru-NP as function of temperature under 10^{-6} mbar vacuum, FT-IR spectra of (g) calcined 1Ru-SAC and (h) reduced 1Ru-SAC after exposing to air as function of CO pressure at -188 °C.

and 2070 cm⁻¹ and 2070 and 2000 cm⁻¹, respectively. The spectral features are thus somewhat similar to the FT-IR spectra, shown in Fig. 4.4a, albeit less similar than the spectra reported by Guglielminotti *et al.* for the reduced Ru/ZrO₂ sample.[54] The highly oxidized nature of the Ru in this material and the lack of information on metal dispersion or particle size furthermore make direct comparison, including the spectral assignments, rather difficult. In our case, supported by the HAADF-STEM, EXAFS and DFT (see below) results, we attribute the observed features in the CO-FT-IR spectrum of freshly reduced 1Ru-SAC to the lower-valent, cationic nature of the supported single Ru atoms and the broadness to the different locations that these single Ru cations can be bound at on the support material (Table 4.1, 2 and 3).

The FT-IR spectra were also recorded for 1Ru-SAC catalyst after CO exposure under vacuum with gradual heating of the sample from liquid nitrogen temperature up to 400 °C (Fig. 4.4b). Under high vacuum (10⁻⁶ mbar) at -188 °C, the band centered at 2174 cm⁻¹, attributed to Zr⁴⁺-CO species, decreased in intensity and blue shifted to 2183 cm⁻¹, while no change was observed in the Ru-CO region. The band located at 2183 cm⁻¹, thought to involve more electrophilic Zr⁴⁺ species only fully disappeared at 0 °C.[52] In the Ru-carbonyl region, the bands at 2120 and 2023 cm⁻¹ decreased gradually upon heating and vanished completely at 250 °C. Similarly, Mihaylov *et al.* also noted the disappearance of a band at ca. 2130 cm⁻¹ upon heating to 200 °C.[53] Upon increasing the temperature, the lower wavenumber bands developed some additional structural complexity, with bands centered at 2055 and 1976 cm⁻¹ attributed to geminal CO adsorbed on ruthenium cations starting to develop from 200 °C, and being stable up to 400 °C. On the other hand, the DFT calculations reported below also reveal the rather labile character of Ru(CO)₃ species, which could in principle explain the loss of peaks around 2120 cm⁻¹ upon desorption of one CO molecule at 200 °C and consequent transition from Ru²⁺(CO)₃ species to Ru²⁺(CO)₂ species. Relatedly, for a Ru/TiO₂ system bands assigned to Ru³⁺(CO)₂ or Ru²⁺(CO)₃ species (observed at 2151-2132 and 2090-2070 cm⁻¹) could be removed by evacuation at 200 °C, whereas bands associated with Ru²⁺(CO)₂ complexes, located at lower frequencies (2101-2080 and 2038-2023 cm⁻¹) remained up to 350 °C.[55]

After CO exposure, freshly reduced 0.5Ru-SAC also showed three Ru-CO vibrations at 2121, 2059 and 2017 cm⁻¹ (Fig. 4.4c), very similar to 1Ru-SAC. As 0.5Ru-SAC is fully monoatomic, this suggests that the small fraction of small Ru clusters detected in 1Ru-SAC by EXAFS, do not contribute much to the observed IR spectrum. For 5Ru-SAC, which is more of a mixture of SAC and subnanometer metal particles, a band located at 2003 cm⁻¹ appeared first, which can be attributed to CO linearly adsorbed on Ru metal particles.[56] After CO adsorption being saturated for this band, the three features located at 2126, 2067, and 2021 cm⁻¹ also developed for this catalyst and increased linearly in intensity as a function of CO pressure, again suggesting the presence of a large amount of Ru single atoms, in line with EXAFS analysis, even at this high weight loading.

Fig. 4.4g shows the FT-IR spectra of calcined 1Ru-SAC after CO adsorption. Two main peaks located at 2054 and 2019 cm⁻¹ were observed in the Ru-CO region. Notably, the peak positions did not shift upon increasing CO pressure, which is again indicative of isolated, single sites, in line with XAS analysis. However, the band centered at 2121 cm⁻¹ was absent in the FT-IR

spectra of calcined 1Ru-SAC and the band intensity was much lower than for the reduced samples under the same CO pressure. Similar, but less extensive weakening of CO adsorption was also observed for air-stored reduced 1Ru-SAC. As shown in Fig. 4.4h, after exposing to air overnight, Three bands related to Ru-CO vibration centered at 2106, 2060 and 2027 cm^{-1} were observed, among which 2106 cm^{-1} was also related to geminal CO adsorbed on cationic, single atom Ru sites (Table 4.2). The intensity of these bands decreased significantly compared to that in the spectra of the non-air exposed counterpart at the same CO pressure (Fig. 4.4a). In fact, a comparison of the XAS of the reduced 1Ru-SAC before and after air exposure confirmed that the Ru atoms on average were more oxidized (data not shown).

For comparison, CO adsorption on the nanoparticulate catalyst 1Ru-NP was also investigated. As expected, very different CO adsorption and desorption behavior was observed for the 1Ru-NP catalyst (Fig. 4.4e). Upon CO exposure, a single band appeared in the Ru-carbonyl region centered at around 2003 cm^{-1} and attributed to CO linearly adsorbed on metallic Ru nanoparticles (Fig. 4.4e).[56] At higher CO pressure, this band gradually blue shifted gradually to 2035 cm^{-1} due to the dipole-dipole interaction of adsorbed CO molecules. Reversely, upon vacuum exposure and heating, the Ru^0 -CO band decreased in intensity and red shifted back to a lower wavenumber at $\sim 1994 \text{ cm}^{-1}$, and vanished completely at 250 °C. Clearly, the temperature for complete CO desorption seen for the nanoparticle catalyst is much lower than that of the Ru single atom catalysts (400 °C), indicating that the Ru^{n+} -CO interaction is stronger than the Ru^0 -CO one. A similar conclusion was drawn by Ding *et al.* as they found that the FT-IR band related to CO adsorption on Pt nanoparticles could be removed upon O_2 exposure at 100 °C, whereas the Pt single atoms still strongly held on to adsorbed CO at the same temperature.[27]

Taken together, the STEM, EXAFS and CO-FT-IR characterization results demonstrate the loading-dependent dispersion of the Ru phase and that the atomicity of the solid catalysts increased gradually with decreasing metal loading. (Predominantly) Ru single atom catalysts with metal loading up to 1 wt.% were thus prepared successfully via a simple wet impregnation method, with 0.5Ru-SAC being fully monoatomic and with even 5Ru-SAC containing a large fraction of the metal as single atoms. The CO adsorption experiments suggested that Ru single atoms exhibited a much stronger CO bonding ability compared to the Ru nanoparticles.

4.3.3. DFT calculations of single Ru species dispersed on ZrO_2

Ru single atoms are expected to be rather mobile and may diffuse with moderate barriers due to their high free surface energy.[57] However, the liquid phase hydrogenation results suggested that Ru single atoms loaded on ZrO_2 were fairly stable and can resist sintering under these highly polar, high temperature reducing conditions.[45] Further insight into the formation, nature of the single atom sites in the Ru/ ZrO_2 materials and their interaction with CO was obtained from DFT calculations. The structure and electronic nature of atomically dispersed Ru species on tetragonal ZrO_2 (t- ZrO_2) (101) and (156) surfaces, to connect to earlier work by the group of Pacchioni,[57] as well as on monoclinic ZrO_2 (), was investigated in detail.

Five distinct models of Ru adsorption on ZrO₂ were considered, 1) adsorption of atomic Ru, (Ru)_{ad}; 2) adsorption of a RuO complex, (RuO)_{ad}; 3) adsorption of a RuO₂ complex, (RuO₂)_{ad}; 4) adsorption of a RuO₃ complex, (RuO₃)_{ad}; and 5) incorporation of Ru at a Zr surface lattice site, (Ru)_{lattice}. In the case of adsorbed atomic Ru, Ru is only bound to lattice oxygens of the ZrO₂ surface. The (RuO)_{ad}, (RuO₂)_{ad}, (RuO₃)_{ad} cases can be seen as the result of the interaction of a Ru atom with one, two, or three surface OH groups with release of 1/2 H₂, H₂ and 3/2 H₂, respectively. It is important to note that the reaction of surface OH groups with supported metal atoms to form O-M complexes and 1/2 H₂ is often exothermic.[58] In the last case, Ru is simply replacing Zr in the lattice. The formal oxidation state of Ru has been attributed by inspecting its coordination sphere. Assuming that the lattice oxygen anions in zirconia are in an O²⁻ state, and cannot therefore be reduced any further, only the oxygen ad-atoms from the RuO_x fragment determine the Ru oxidation state. Therefore, we have assigned Ru⁰ to (Ru)_{ad}, Ru^I to (RuO)_{ad}, Ru^{II} to (RuO₂)_{ad}, Ru^{IV} to (RuO₃)_{ad}. In the case of incorporation of Ru in the zirconia lattice, we attribute this to the Ru atom in the same oxidation state of the Zr cation, i.e. Ru^{IV}. The data related to the CO adsorption on (RuO_x) ZrO₂ are summarized and shown in the experimental section (Table 4.1,2 and 3).

As shown above, the FT-IR measurements of CO adsorption on 1Ru-SAC sample show blue-shifted bands at ~ 2174 and ~ 2194 cm⁻¹ attributed to CO adsorption on m-ZrO₂ (11) surface Zr⁴⁺ sites and a set of bands red-shifted with respect to the gas phase by 2121, 2061 and 2023 cm⁻¹. A summary of the relevant calculation results is summarized in Fig. 4.5 as well as Tables 4.1, 4.2 and 4.3. Clearly, when CO is bound to a Ru atom anchored to the oxide surface via Ru-O bonds, its C-O stretching frequency is always red-shifted compared to free CO, despite the presence of a positive charge on Ru and the positive oxidation state of the metal atom. This indicates that there is enough electron density on Ru to give rise to a substantial back-donation of charge to CO, but also to activate other adsorbed molecules and act as an active catalytic center.

Given the obtained experimental FT-IR spectra (Fig. 4.4a) and the high stability of adsorbed Ru atoms, (RuO)_{ad} and (RuO₂)_{ad} complexes are considered as promising candidates to describe the structure of the single Ru atoms on zirconia. Indeed, these two Ru species are formally derived from the reaction of a Ru atom with one or two surface OH groups and the resulting complexes have strong Ru-O bonds that should prevent the diffusion of the Ru atoms. In particular, the RuO units are bound by 3.76 eV on t-ZrO₂ (101), and by 3.96-4.06 eV on m-ZrO₂ (11). An even higher binding energy is found on the stepped t-ZrO₂ (156) surface, 5.14 eV. These large binding energies suggest a low mobility of the RuO species on the surface.

In the experimental FT-IR spectra of 1Ru-SAC, the band at 2023 cm⁻¹ correlates with the one at 2061 cm⁻¹. In this respect, a single CO adsorption model should be ruled out, while the formation of germinal CO structures must be considered. As shown in Fig. 4.5, two bands shifted by 2039/1972 cm⁻¹ (terrace), 2044/1975 cm⁻¹ (step) on t-ZrO₂, and 2036/1963 cm⁻¹ on m-ZrO₂ (terrace) were calculated for the (CO)₂(RuO)_{ad} geminal CO complex. The corresponding intensities show that the band at higher frequencies is more intense. These calculated vibrations correspond with the bands at 2061 and 2023 cm⁻¹, observed in the experimental FT-IR spectra. The assignment is even more convincing if we consider that there is an overestimate of

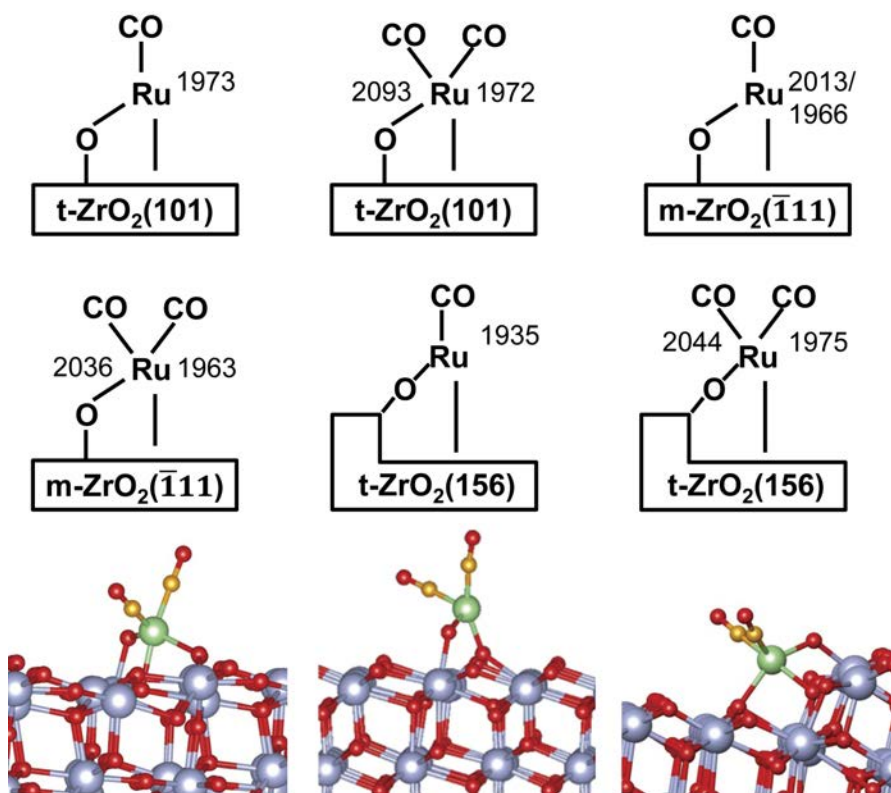


Fig. 4.5. Schematic representation of the RuO models of single atom Ru complexes formed on the surface of a zirconia-based catalyst. The bottom entry is geminal CO molecules on RuO₂ structures grafted on m-ZrO₂ (), t-ZrO₂ (101) and t-ZrO₂ (156). O, Zr, Ru and C are red, grey, green and gold spheres, respectively.[51]

the computed red-shift by about 20 cm⁻¹ due to the limitations of the PBE+U approach (see discussion above). Furthermore, both CO molecules are strongly bound to the (RuO)_{ad} complex, which are expected to be thermally very stable with respect to CO desorption. Using a Redhead equation for first-order desorption processes,[59] $\Delta E_{\text{des}} = RT_{\text{des}} (\ln v T_{\text{des}} - 3.64)$, and using a pre-factor $v = 10^{13} \text{ s}^{-1}$, one can conclude that thermal desorption of CO is possible for temperatures above 277–327 °C. Indeed, the FT-IR spectra, shown in Fig. 4.4b, recorded at 350 °C still show the presence of CO-Ru species. Thus, we propose that the (RuO)_{ad} species, where a Ru atom is formally bound to an O atom from a surface hydroxyl group, and anchored to the surface via another coordinative bond, is a good structural representation for the single atom site in the real catalyst.

4.3.4. Catalyst stability in gas atmosphere

4.3.4.1. *In-situ* reduction of calcined 1Ru-SAC

As suggested by the *ex-situ* EXAFS analysis, the calcined parent material, but not the final reduced 1Ru-SAC catalyst contained isolated Ru atoms only. Indeed, for the reduced samples, full atomic dispersed was achieved at a Ru loading of 0.5 wt.% or lower, with the reduced 1Ru-SAC being mostly but not fully atomically dispersed (as no nanoparticles are detected by HAADF-STEM, but some Ru-Ru scattering was seen in the EXAFS data). This suggests that the reduction step needs to be tightly controlled and that the Ru-Ru interactions seen for 1Ru-SAC are the result of sintering upon reduction of the atomically dispersed calcined precursor material. To better understand the genesis of single Ru atoms during the catalyst synthesis procedure and their stability in H₂ atmosphere, the reduction step was measured with *in-situ* XAS. The calcined 1Ru-SAC system was reduced *in-situ* under pure H₂ flow by gradually heating to 450 °C, after which this temperature was kept constant for over 5 h, to mimic the reduction step of the catalyst preparation process.

Changing the atmosphere from air to H₂ gas at RT showed little effect on the Ru XAS data (Fig. 4.6a). Upon heating, an obvious drop in whiteness intensity was observed at 100 °C, and also the edge position was shifted by 5 eV from 22129 to 22124 eV (Fig. 4.6c), similar to the changes observed during the *in-situ* reduction of re-oxidized 1Ru-SAC sample (Fig. 4.8a and b), indicating a decrease in the oxidation state of the Ru atoms present. After that, only slight changes were observed in the XANES profiles when raising the temperature further to 450 °C. The FT data shows that at 450 °C, the Ru-O interaction disappeared (Fig. 4.6d), whereas a Ru-Ru interaction was seen to develop. Indeed, the Ru-Ru coordination number of the catalyst after 450 °C reduction increased to 5.4, after which it remained unchanged for 5 h (Table 4.6). These results show that while some sintering occurs, most of the Ru single atoms must be stable against high temperature H₂ reduction at high metal loading.

4.3.4.2. *In-situ* O₂ treatment

To test the stability of the catalyst materials under oxidizing conditions, the reduced 1Ru-SAC catalyst was gradually heated in a pure O₂ flow to 300 °C. Once exposed to pure O₂ at RT, the intensity of the whiteness increased significantly for the 1Ru-SAC sample, although no obvious edge position shift was observed, indicating an increase in Ru oxidation degree. Surprisingly, the EXAFS data shows that the initial Ru-Ru interactions in the reduced 1Ru-SAC catalyst disappeared upon oxidation (Fig. 4.7a), indicating that the small metallic Ru clusters, considered minority species that form by sintering during the reduction step in the catalyst synthesis, can be re-dispersed back into single atoms even at RT under an oxygen-rich environment. The regeneration of single atoms from small clusters has been reported previously, but at much higher temperatures.[33,60] For example, Moliner *et al.* have shown that Pt nanoparticles (~1-1.5 nm) disappeared gradually with isolated Pt atoms appearing simultaneously after exposing a reduced Pt-CHA-2 material to O₂ at 500 °C.[60] Likewise, Peterson *et al.* also demonstrated that small Pd clusters as a result of Pd single atom reduction

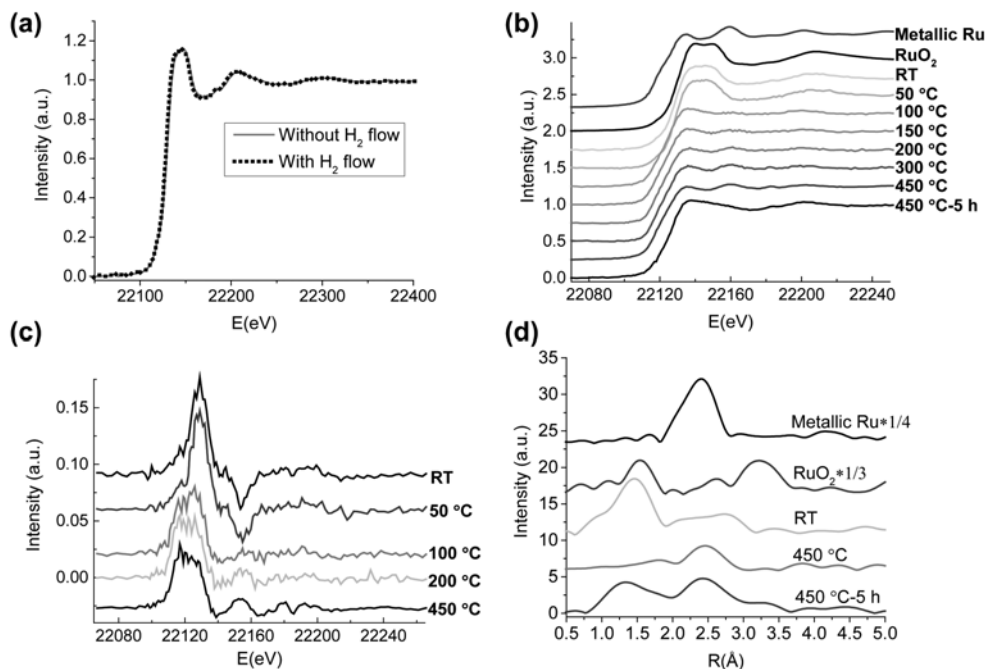


Fig. 4.6. (a) EXAFS spectra of calcined 1Ru-SAC before and after H_2 exposing at RT, temperature-resolved (b) XANES spectra, (c) the first derivatives of the XANES spectra and (d) changes in k^3 -weighted Fourier transform spectra from EXAFS of calcined 1Ru-SAC upon reduction.

during CO oxidation process can transform back to isolated Pd atoms after O_2 oxidation at 700 °C with the help of XAS analysis.[33] Peterson *et al.* claimed that desorption of surface OH groups of the support played a key in the Pd cluster redispersion at these high temperatures. [33] In our case, the small Ru clusters detected by XAS in the reduced sample might only be associated with each other very loosely rather than by strong Ru-Ru metallic bonds and can be re-oxidized easily under O_2 flow, causing the disappearance of the Ru-Ru scattering after O_2 exposure at room temperature.

The XANES profiles remained practically unchanged upon heating up to 250 °C, i.e. over the temperature range of the CO oxidation measurements, demonstrating that the Ru single atoms are sintering resistant and stable to calcination at elevated temperature in an O_2 rich environment. This resembles the observation of Duan *et al.*, in which Fe_2O_3 supported Pt single atoms are stable at 250 °C under O_2 atmosphere.[30] At $T > 250$ °C, both edge position and whiteline intensity started to change, with the edge position moving to higher energy and whiteline intensity increasing, indicating the formation of more oxidized Ru species. Correspondingly, at 300 °C, a new peak started to appear at 2.8 Å in the FT data, which increased in intensity upon prolonged treatment (Fig. 4.7c). This peak corresponds neither to a first nor second shell Ru-Ru interaction and the assignment of this peak is currently not clear.

Table 4.6. Summary of EXAFS fitting results for *in-situ* gas treatments.

Condition	Neighbor	N	R(Å)	(Å)
<i>In-situ</i> H ₂ reduction of calcined 1Ru-SAC				
Air-RT	Ru	0	ND	ND
	O	2.9	1.97	<0.001
H ₂ -RT	Ru	0	ND	ND
	O	3.4	1.96	0.002
H ₂ -450 °C	Ru	5.4	2.65	0.013
	O	0.6	1.98	0.005
H ₂ -450 °C-5 h *	Ru	5.1	2.7	0.008
	O	3.3	1.97	0.006
<i>In-situ</i> O ₂ oxidation of reduced 1Ru-SAC				
Air-RT	Ru	3.0	2.68	0.003
	O	2.7	1.99	0.003
O ₂ -RT	Ru	0	ND	ND
	O	3.4	1.98	0.03
O ₂ -300 °C	Ru	0	ND	ND
	O	2.8	1.96	<0.001
O ₂ -300 °C-2 h *	Ru	0	ND	ND
<i>In-situ</i> O ₂ oxidation of reduced 1Ru-NP				
Air-RT	Ru	0	ND	ND
	O	3.6	1.99	0.002
O ₂ -RT	Ru	10.5	2.68	0.0033
	O	0.79	1.92	0.0001
O ₂ -300 °C	Ru	7.9	2.70	0.0094
	O	1.74	1.97	0.0005
O ₂ -300 °C-2 h *	Ru	7.4	2.69	0.0041
	O	1.95	1.97	0.0011
<i>In-situ</i> CO reduction of reduced 1Ru-SAC				
Air-RT	Ru	3.0	2.68	0.003
	O	2.7	1.99	0.003
CO-RT	Ru	4.5	2.68	0.007
	O	2.8	1.99	0.003
CO-250 °C	Ru	8.9	2.67	0.009
	O	0.5	1.98	0.008
CO-250 °C-2 h *	Ru	10	2.69	0.005
	O	ND	ND	ND

* The EXAFS spectrum was collected after cooling down to RT.

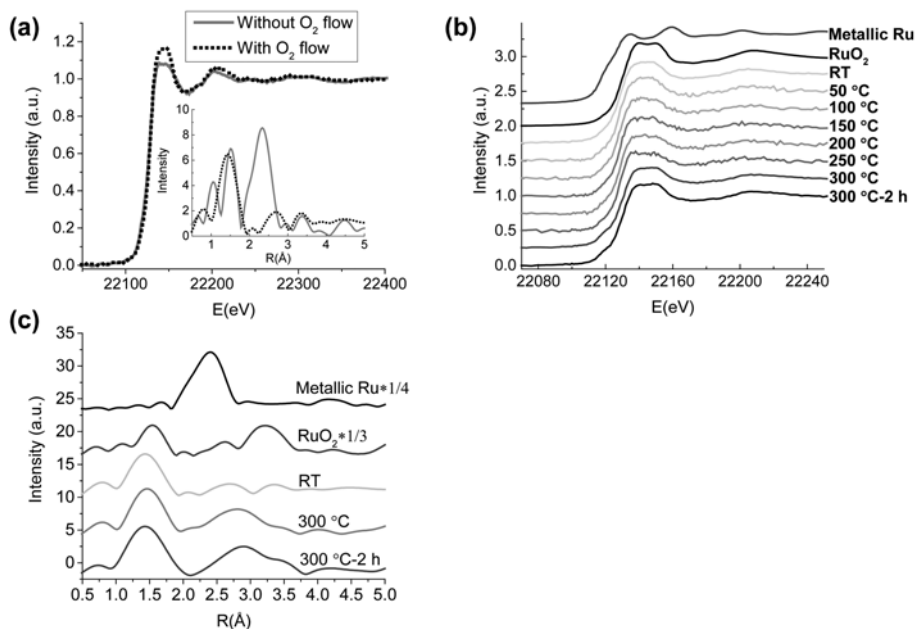


Fig. 4.7. (a) EXAFS spectra of 1Ru-SAC before and after O_2 exposure at RT, temperature-resolved (b) XANES spectra and (c) k^3 -weighted Fourier transform spectra from EXAFS of 1Ru-SAC upon heating under O_2 .

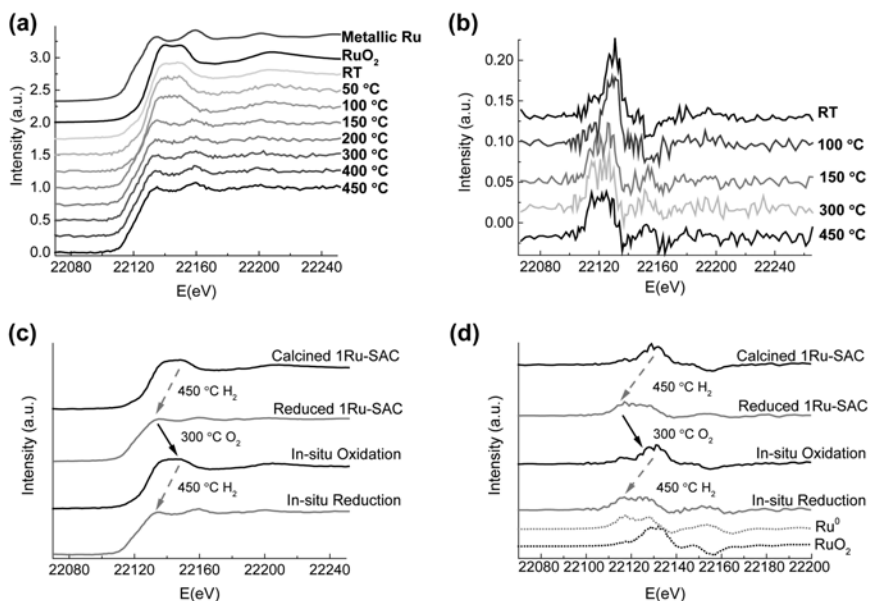


Fig. 4.8. Temperature-resolved (a) XANES spectra of *in-situ* reduction of 1Ru-SAC right after *in-situ* O_2 treatment (b) the first derivatives of corresponding XANES spectra and (c) XANES spectra and their derivatives upon redox cycling between Ru clusters and single atoms.

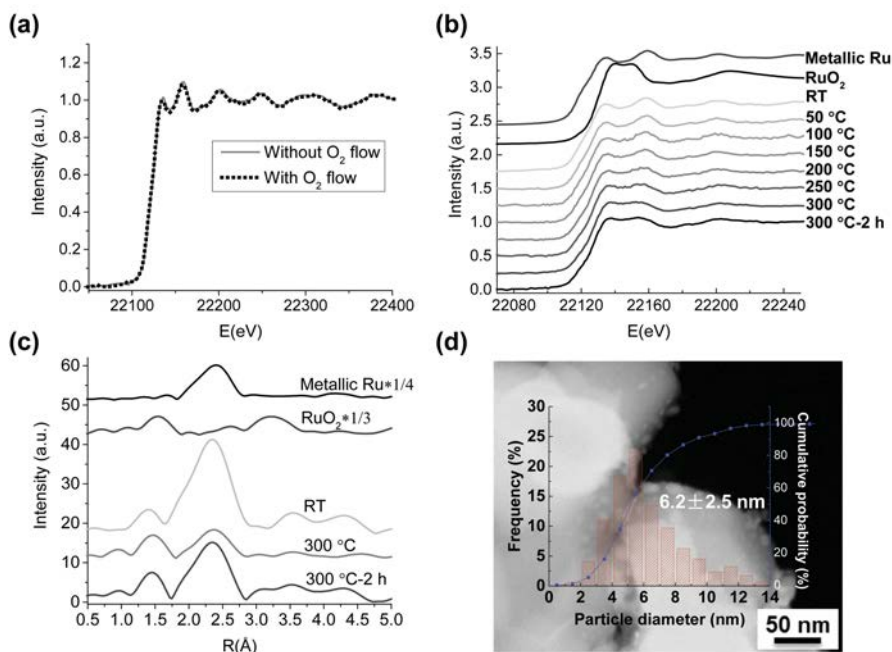


Fig. 4.9. (a) EXAFS spectra of 1Ru-NP before and after O₂ exposing at RT, temperature-resolved (b) XANES spectra and (c) k^3 -weighted Fourier transform spectra from EXAFS of 1Ru-NP, and (d) STEM image of 1Ru-NP after O₂ treatment.

To get more insight into the reversibility of the changes seen, the sample was again reduced *in-situ* right after the oxidation process described above. The onset temperature for the reduction was ~ 150 °C with the edge position shifting from 22130 to 22124 eV (Fig. 4.8b). No evidence for a further reduction was observed at higher temperature (Fig. 4.8a and b), which is in good agreement with the observation in the temperature-resolved reduction of the fully atomically dispersed calcined sample. Interestingly, the XAS data seems to suggest that any changes in the 1 wt.% Ru/ZrO₂ single atom catalyst are reversible and that the reduced single-atom state of the catalyst can be readily re-attained by simply changing the reduction/oxidation conditions. As shown in Fig. 4.8c and d, reduction of calcined 1Ru-SAC at 450 °C resulted in the formation of small Ru clusters, showing a rather metallic whiteline and edge absorption. Switching to a pure O₂ atmosphere, those Ru clusters could again be re-oxidized upon increasing the temperature, giving rise to a XANES profile resembling the calcined 1Ru-SAC. Remarkably, Ru clusters could be reformed upon subsequent reduction of the oxidation sample in H₂ at 450 °C, a whiteline intensity and edge absorption equal to that of reduced 1Ru-SAC was reached eventually, indicating same overall Ru speciation was obtained after this treatment.

For comparison, the reduced 1Ru-NP catalyst was also re-oxidized *in-situ* in a pure O₂ flow. In strong contrast to the Ru oxidation observed for 1Ru-SAC at RT, no change was seen for 1Ru-NP before and after O₂ exposure at RT (Fig. 4.9a). Upon heating under oxygen, the Ru nanoparticles did gradually oxidize, as evidenced by the increase in whiteline intensity

together with the edge position shift towards higher energy in the temperature-dependent XAS experiments (Fig. 4.9b). Accordingly, the Ru-Ru scatter decreased considerably when comparing the 300 °C and RT data (Fig. 4.9c). Upon prolonged exposure (2 h at 300 °C), the intensity of both Ru-Ru scattering and RuO₂ second-shell feature increased, however. This would be in line with the TEM analysis that showed significant sintering for the 1Ru-NP system after this oxidation treatment, with the average Ru particle size increasing from 3.2 ± 2.5 to 6.2 ± 2.5 nm (Fig. 4.9d). Thus, it is suggested that the Ru nanoparticles are transformed into a larger metallic Ru particles covered by a thin layer of RuO_x after O₂ treatment at elevated temperature. As noted above, such Ru/RuO_x core-shell nanoparticles were considered responsible for the high activity in CO oxidation by Aßmann *et al.*, [48] and are held responsible for the enhanced catalytic activity seen for 1Ru-NP upon reuse as noted above. In any case, the results demonstrate the differences in stability under high temperature, oxidizing conditions between the single atom and nanoparticulate catalyst materials, the former being rather stable while the latter is suffering from sintering and oxidation.

4.3.4.3. *In-situ* CO treatment

Catalyst structure and stability were also investigated in a CO rich environment. Although clear Ruⁿ⁺-CO vibrations are seen in the FT-IR spectrum of the reduced 1Ru-SAC catalyst after CO dosing, no differences were observed in the XAS spectra of 1Ru-SAC catalyst before and after CO exposure (Fig. 4.10a). Coordination of CO to the single atoms sites would be difficult to discern given the similar EXAFS phase shift and backscattering amplitude functions of C and O.[61] This result also suggests that CO is not able to reduce Ru atoms at RT. At higher temperatures, changes were seen under CO, however, with progressive reduction of the 1Ru-SAC catalyst being suggested by the gradual decrease of the whiteline intensity in the temperature-resolved XANES experiments. Eventually, a rather metallic Ru like XANES spectrum was achieved after 2 h treatment in CO atmosphere at 250 °C. Correspondingly, the Ru-Ru coordination number doubled compared to the initial value at the end of this CO treatment (Table 4.6), indicating the production of metallic Ru clusters.

Such gas induced sintering of metal single atoms was also reported by Duan *et al.*[30] The authors found that Fe₂O₃-supported Pt single atoms will sinter into clusters with an average particle size of around 1 nm by both CO and H₂ at 250 °C.[30] In our case, the Ru SAC material is indeed unstable against CO reduction, similar to the observation of Duan *et al.*, whereas it shows good stability in the presence of H₂. The different stability of the Ru SAC material observed in H₂ and CO atmosphere is probably due to different reduction mechanisms. Parkinson and co-workers demonstrated that the CO induced coalescence of single atom to clusters was also encountered for both Pd and Pt/Fe₃O₄(001) SAC systems after CO exposure at room temperature, and they attributed the enhanced mobility of single atoms to the formation of strong single atom-CO bonding which in turn weakened the metal-support interaction, facilitating the diffusion of single atoms into subnanometer metal clusters.[62,63] The single atom-carbonyl species was the only one to be seen diffusing in their *in-situ* scanning tunneling

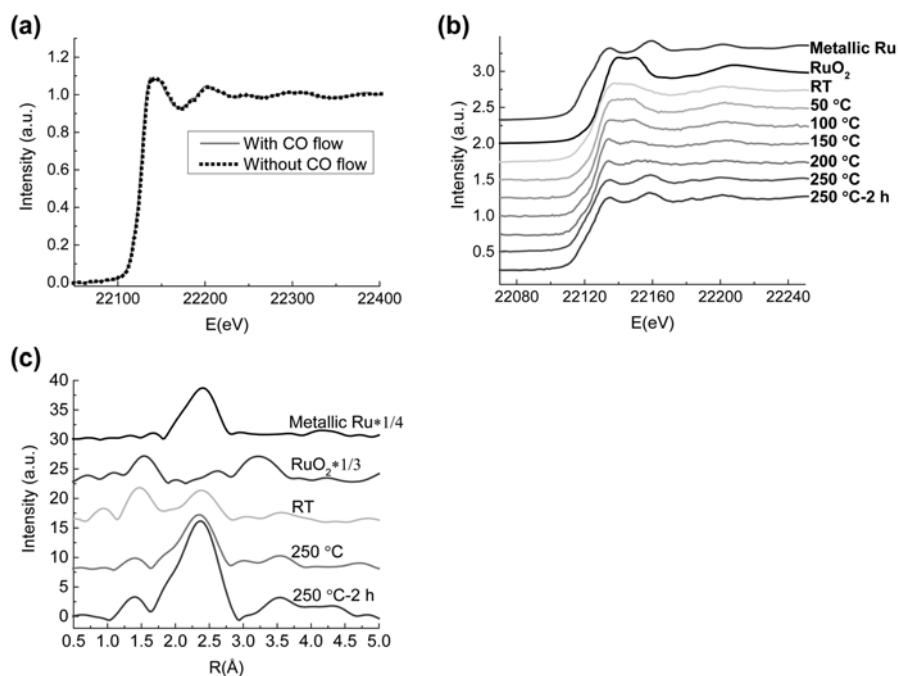


Fig. 4.10. (a) EXAFS spectra of 1Ru-SAC before and after CO exposing at RT, temperature-resolved (b) XANES spectra and (c) k^3 -weighted Fourier Transform spectra from EXAFS of 1Ru-SAC in a CO rich environment.

microscopy analysis, whereas larger particles were found to be immobile.[63] The observation from CO desorption experiments that Ru-carbonyl interactions are strong and stable up to 350 °C under high vacuum would be in line with this.

For H₂ reduction, H₂ molecules dissociatively adsorb on metal atoms, while spillover effects onto the support are known to weaken the metal-support interaction and thus induce mobility of the single atoms.[30,64] Bradley *et al.* demonstrated that a SMSI played a key role in the stability of single atoms against H₂ induced aggregation. They compared the stability of Pt single atoms supported on different materials (i.e., TiO₂, SiO₂ and Al₂O₃) under H₂ atmosphere at 550 °C and found that the TiO₂ supported catalysts are more sintering resistance than the Al₂O₃ and SiO₂ counterparts due to the strong bonding between the Pt single atoms and the TiO₂ support. [65] In addition to the beneficial effect strong bonding of the single atom to the support has on stability, previous studies have also suggested that the enhanced catalytic activity of SAC in CO oxidation can be attributed to such SMSI effects.[36,37]

4.4. Conclusions

In this PhD thesis chapter, we report on a set of stable fully atomically dispersed Ru/ZrO₂ catalysts and study their dispersion as function of weight loading. The structure of the solid catalysts

under investigation is studied with aberration-corrected HAADF-STEM, FT-IR of CO stepwise adsorption and Extended X-ray Absorption Fine Structure (EXAFS). Catalyst characterization shows that both calcined 1Ru-SAC and reduced 0.5Ru-SAC contain only single Ru atoms. Temperature-resolved XAS experiments confirm that Ru SAC shows good thermal stability in both O₂ and H₂ atmosphere at elevated temperature, whereas it can be reduced gradually to metallic Ru by CO. Remarkably, the metal phase of the 1Ru-SAC catalyst could be reversibly changed by sequential redox cycling, turning the small metallic Ru clusters that are present in addition to single atoms in the reduced catalyst, to single atoms by an oxidation treatment and vice versa by reduction. The results thus provide more insight into the genesis and dynamics of single atom sites as function of temperature and environmental conditions. In contrast, a nanoparticle containing catalyst suffered from obvious metal sintering upon oxidation and converted into a Ru/RuO₂ core-shell species. When tested in CO oxidation under net oxidizing conditions, the Ru SAC catalysts showed enhanced activity towards CO conversion compared to its nanoparticulate counterpart, as evidenced by the lower T_{50%} (90 °C vs 150 °C, respectively). In line with the *in-situ* XAS experiments, catalytic recycling tests further demonstrated that Ru SAC is highly resistant to deactivation under oxidizing conditions, offering potential for applications in other oxidation reactions.[66,67]

References

1. H. Li, H. Zhang, X. Yan, B. Xu, J. Guo, *New Carbon Mater.* 33 (2018) 1–11.
2. G. Kyriakou, M.B. Boucher, A.D. Jewell, E.A. Lewis, T.J. Lawton, A.E. Baber, H.L. Tierney, M. Flytzani-Stephanopoulos, E.C.H. Sykes, *Science* 335 (2012) 1209–1212.
3. S. Liang, C. Hao, Y. Shi, *ChemCatChem* 7 (2015) 2559–2567.
4. R.A. Van Santen, *Acc. Chem. Res.* 42 (2009) 57–66.
5. B. Roldan Cuenya, F. Behafarid, *Surf. Sci. Rep.* 70 (2015) 135–187.
6. Y. Liu, G. Zhao, D. Wang, Y. Li, *Natl. Sci. Rev.* 2 (2015) 150–166.
7. S. Cao, F.F. Tao, Y. Tang, Y. Li, J. Yu, *Chem. Soc. Rev.* 45 (2016) 4747–4765.
8. M. Turner, V.B. Golovko, O.P.H. Vaughan, P. Abdulkin, A. Berenguer-Murcia, M.S. Tikhov, B.F.G. Johnson, R.M. Lambert, *Nature* 454 (2008) 981–983.
9. J. Lin, B. Qiao, N. Li, L. Li, X. Sun, J. Liu, X. Wang, T. Zhang, *Chem. Commun.* 51 (2015) 7911–7914.
10. S. Vajda, M.J. Pellin, J.P. Greeley, C.L. Marshall, L.A. Curtiss, G.A. Ballentine, J.W. Elam, S. Catillon-Mucherie, P.C. Redfern, F. Mehmood, P. Zapol, *Nat. Mater.* 8 (2009) 213–216.
11. J. Liu, *ACS Catal.* 7 (2017) 34–59.
12. X.F. Yang, A. Wang, B. Qiao, J. Li, J. Liu, T. Zhang, *Acc. Chem. Res.* 46 (2013) 1740–1748.
13. B. Qiao, J.X. Liang, A. Wang, C.Q. Xu, J. Li, T. Zhang, J.J. Liu, *Nano Res.* 8 (2015) 2913–2924.
14. Z.P. Liu, C.M. Wang, K.N. Fan, *Angew. Chem. Int. Ed.* 45 (2006) 6865–6868.
15. H. Wei, X. Liu, A. Wang, L. Zhang, B. Qiao, X. Yang, Y. Huang, S. Miao, J. Liu, T. Zhang, *Nat. Commun.* 5 (2014) 5634.
16. B. Qiao, A. Wang, X. Yang, L.F. Allard, Z. Jiang, Y. Cui, J. Liu, J. Li, T. Zhang, *Nat. Chem.* 3 (2011) 634–641.
17. S.F.J. Hackett, R.M. Brydson, M.H. Gass, I. Harvey, A.D. Newman, K. Wilson, A.F. Lee, *Angew. Chem. Int. Ed.* 119 (2007) 8747–8750.
18. Z. Zhang, Y. Zhu, H. Asakura, B. Zhang, J. Zhang, M. Zhou, Y. Han, T. Tanaka, A. Wang, T. Zhang, N. Yan, *Nat. Commun.* 8 (2017) 16100.
19. A. Wang, J. Li, T. Zhang, *Nat. Rev. Chem.* 2 (2018) 65–81.
20. J. Jones, H. Xiong, A.T. DeLaRiva, E.J. Peterson, H. Pham, S.R. Challa, G. Qi, S. Oh, M.H. Wiebenga, X.I. Pereira Hernandez, Y. Wang, A.K. Datye, *Science* 353 (2016) 150–154.
21. P. Liu, Y. Zhao, R. Qin, S. Mo, G. Chen, L. Gu, D.M. Chevrier, P. Zhang, Q. Guo, D. Zang, B. Wu, G. Fu, N. Zheng, *Science* 352 (2016) 797–800.
22. H. Yan, H. Cheng, H. Yi, Y. Lin, T. Yao, C. Wang, J. Li, S. Wei, J. Lu, *J. Am. Chem. Soc.* 137 (2015) 10484–10487.
23. C.T. Campbell, *Nat. Chem.* 4 (2012) 597–598.
24. J.D. Kistler, N. Chotigkrai, P. Xu, B. Enderle, P. Praserthdam, C.Y. Chen, N.D. Browning, B.C. Gates, *Angew. Chem. Int. Ed.* 53 (2014) 8904–8907.
25. G. Spezzati, Y. Su, J.P. Hofmann, A.D. Benavidez, A.T. DeLaRiva, J. McCabe, A.K. Datye, E.J.M. Hensen, *ACS Catal.* 7 (2017) 6887–6891.
26. B.C. Gates, M. Flytzani-Stephanopoulos, D.A. Dixon, A. Katz, *Catal. Sci. Technol.* 7 (2017) 4259–4275.
27. K. Ding, A. Gulec, A.M. Johnson, N.M. Schweitzer, G.D. Stucky, L.D. Marks, P.C. Stair, *Science* 350 (2015) 189–92.
28. B. Han, R. Lang, B. Qiao, A. Wang, T. Zhang, *Chin. J. Catal.* 38 (2017) 1498–1507.
29. Y.T. Kim, K. Ohshima, K. Higashimine, T. Uruga, M. Takata, H. Suematsu, T. Mitani, *Angew. Chem. Int. Ed.* 45 (2006) 407–411.
30. S. Duan, R. Wang, J. Liu, *Nanotechnology* 29 (2018) 204002–204010.

31. J.H. Kwak, J. Hu, D. Mei, C.W. Yi, D.H. Kim, C.H.F. Peden, L.F. Allard, J. Szanyi, *Science* 325 (2009) 1670–1673.
32. W. Deng, A.I. Frenkel, R. Si, M. Flytzani-Stephanop, *J. Phys. Chem. C* 112 (2008) 12834–12840.
33. E.J. Peterson, A.T. DeLaRiva, S. Lin, R.S. Johnson, H. Guo, J.T. Miller, J. Hun Kwak, C.H.F. Peden, B. Kiefer, L.F. Allard, F.H. Ribeiro, A.K. Datye, *Nat. Commun.* 5 (2014) 4885.
34. O. Korotkikh, R. Farrauto, *Catal. Today* 62 (2000) 249–254.
35. I.H. Kim, H.O. Seo, E.J. Park, S.W. Han, Y.D. Kim, *Sci. Rep.* 7 (2017) 40497–40508.
36. O. Goerke, P. Pfeifer, K. Schubert, *Appl. Catal. A Gen.* 263 (2004) 11–18.
37. M. Moses-Debusk, M. Yoon, L.F. Allard, D.R. Mullins, Z. Wu, X. Yang, G. Veith, G.M. Stocks, C.K. Narula, *J. Am. Chem. Soc.* 135 (2013) 12634–12645.
38. L. Liu, A. Corma, *Chem. Rev.* 118 (2018) 4981–5079.
39. L. DeRita, S. Dai, K. Lopez-Zepeda, N. Pham, G.W. Graham, X. Pan, P. Christopher, *J. Am. Chem. Soc.* 139 (2017) 14150–14165.
40. Y. Chen, T. Kasama, Z. Huang, P. Hu, J. Chen, X. Liu, X. Tang, *Chem. Eur. J.* 21 (2015) 17397–17402.
41. H. Over, M. Muhler, *Prog. Surf. Sci.* 72 (2003) 3–17.
42. W. Shi, X. Liu, J. Zeng, J. Wang, Y. Wei, T. Zhu, *Chin. J. Catal.* 37 (2016) 1181–1192.
43. P.C. Hicks, B.S. Lennon, *J. Catal.* 54 (1978) 372–383.
44. J.T. Kiss, R.D. Gonzalez, *J. Phys. Chem.* 88 (1984) 892–897.
45. J. Ftouni, A. Muñoz-Murillo, A. Goryachev, J.P. Hofmann, E.J.M. Hensen, L. Lu, C.J. Kiely, P.C.A. Bruijninx, B.M. Weckhuysen, *ACS Catal.* 6 (2016) 5462–5472.
46. B. Ravel, M. Newville, *J. Synchrotron Radiat.* 12 (2005) 537–541.
47. T. Bligaard, R.M. Bullock, C.T. Campbell, J.G. Chen, B.C. Gates, R.J. Gorte, C.W. Jones, W.D. Jones, J.R. Kitchin, S.L. Scott, *ACS Catal.* 6 (2016) 2590–2602.
48. J. Aßmann, D. Crihan, M. Knapp, E. Lundgren, E. Löffler, M. Muhler, V. Narkhede, H. Over, M. Schmid, A.P. Seitsonen, P. Varga, *Angew. Chem. Int. Ed.* 44 (2005) 917–920.
49. S.H. Joo, J.Y. Park, J.R. Renzas, D.R. Butcher, W. Huang, G.A. Somorjai, *Nano Lett.* 10 (2010) 2709–2713.
50. J. Singh, E.M.C. Alayon, M. Tromp, O. V. Safonova, P. Glatzel, M. Nachtegaal, R. Frahm, J.A. van Bokhoven, *Angew. Chem. Int. Ed.* 47 (2008) 9260–9264.
51. H.V. Thang, S. Tosoni, F. Liu, P. Bruijninx, G. Pacchioni, *ChemCatChem* 10 (2018) 2634–2645.
52. S. Kouva, K. Honkala, L. Lefferts, J. Kanervo, *Catal. Sci. Technol.* 5 (2015) 3473–3490.
53. M. Mihaylov, O. Lagunov, E. Ivanova, K. Hadjiivanov, *J. Phys. Chem. C* 115 (2011) 13860–13867.
54. E. Guglielminotti, F. Boccuzzi, M. Manzoli, F. Pinna, M. Scarpa, *J. Catal.* 192 (2000) 149–157.
55. E. Guglielminotti, G.C. Bond, *J. Chem. Soc. Faraday Trans.* 86 (1990) 979–987.
56. J. Robbins, *J. Catal.* 115 (1989) 120–131.
57. H.Y.T. Chen, S. Tosoni, G. Pacchioni, *J. Phys. Chem. C* 119 (2015) 10856–10868.
58. P. Schlexer, G. Pacchioni, *Top. Catal.* 60 (2017) 459–470.
59. P.A. Redhead, *Vacuum* 12 (1962) 203–211.
60. M. Moliner, J.E. Gabay, C.E. Klier, R.T. Carr, J. Guzman, G.L. Casty, P. Serna, A. Corma, *J. Am. Chem. Soc.* 138 (2016) 15743–15750.
61. M.K. Neylon, C.L. Marshall, A.J. Kropf, *J. Am. Chem. Soc.* 124 (2002) 5457–5465.
62. G.S. Parkinson, Z. Novotny, G. Argentero, M. Schmid, J. Pavelec, R. Kosak, P. Blaha, U. Diebold, *Nat. Mater.* 12 (2013) 724–728.
63. R. Bliem, J.E.S. van der Hoeven, J. Hulva, J. Pavelec, O. Gamba, P.E. de Jongh, M. Schmid, P. Blaha, U. Diebold, G.S. Parkinson, *Proc. Natl. Acad. Sci. U. S. A.* 113 (2016) 8921–6.

64. R. Bliem, J. Van Der Hoeven, A. Zavodny, O. Gamba, J. Pavelec, P.E. De Jongh, M. Schmid, U. Diebold, G.S. Parkinson, *Angew. Chem. Int. Ed.* 54 (2015) 13999–14002.
65. S.A. Bradley, W. Sinkler, D.A. Blom, W. Bigelow, P.M. Voyles, L.F. Allard, *Catal. Lett.* 142 (2012) 176–182.
66. K. Yamaguchi, N. Mizuno, *Angew. Chem. Int. Ed.* 41 (2002) 4538–4542.
67. B.Z. Zhan, M.A. White, T.K. Sham, J.A. Pincock, R.J. Doucet, K.V.R. Rao, K.N. Robertson, T.S. Cameron, *J. Am. Chem. Soc.* 125 (2003) 2195–2199.

5

ZrO₂ Supported Noble Metal Catalysts: Influence of Isolated Atoms on Catalyst Performance

Abstract

As many supported noble metal catalyzed reactions are known to be structure sensitive, thorough understanding of such structure-performance relationships is necessary to design cost effective catalysts. In this chapter, a series of ZrO_2 supported Pd and Pt catalysts are prepared via wet impregnation to investigate the influence of atomicity on catalytic performance in different types of reactions. Metal dispersion of those catalysts is demonstrated to be loading-dependent, with the population of isolated single metal atoms increasing as metal loading goes down. Fully monoatomically dispersed catalysts are obtained at 0.05 and 0.1 wt.% for Pt and Pd, respectively. The influence of dispersion on catalyst performance is assessed in gas and liquid phase reactions, including CO oxidation, propane dehydrogenation, cinnamaldehyde hydrogenation and selective 1,3-butadiene hydrogenation. The experimental results clearly show that catalyst performance in terms of activity and selectivity for CO oxidation and the selective hydrogenation of butadiene and cinnamaldehyde positively correlates with the amount of isolated single metal atoms present. Catalyst activity in cinnamaldehyde hydrogenation is furthermore found to be independent of weight loading once full dispersion is reached, suggesting that single atoms are the catalytically relevant species. For propane dehydrogenation, the influence of dispersion is more limited. Overall, the Pd materials outperformed their Pt counterparts in all targeted reactions. In CO oxidation, the $T_{50\%}$ (the 50% CO conversion temperature) of Pd/ ZrO_2 is at least 30 °C lower compare to that of Pt/ ZrO_2 . In addition, while a Pt single atom catalyst is unable to catalyze cinnamaldehyde hydrogenation and exhibited poor performance in butadiene hydrogenation, the Pd SAC showed good performance in both the gas and liquid phase hydrogenation reactions. In particular, the Pd/ ZrO_2 SAC displayed exceptional activity in selective butadiene hydrogenation. In the presence of a large excess of propene, butadiene is fully converted at 70 °C with 96% butenes selectivity and no detectable propene hydrogenation with a turnover frequency of 2.89 s^{-1} at 50 °C, an 8 fold increase over the most active catalyst reported. The catalyst showed stable performance for 60 h time on stream, making it a promising candidate for further development.

5.1. Introduction

Supported noble metal catalysts are widely employed for various important industrial processes. [1,2] A downside of the use of noble metals is that they are scarce, which makes them expensive, especially considering the increase in demand for these materials, for example for application in heterogeneous catalysts.[3] A promising solution to this problem is to create cost effective catalysts by reducing metal particle size. As catalysis is generally a surface phenomenon, decreasing the particle size of supported noble metal nanoparticles results in an increase in the fraction of noble metal atoms exposed to the surface, in turn increasing the catalytic activity on a per metal basis and thus the general efficiency of noble metal use.[4] The ultimate limit of downsizing a nanoparticle is to achieve full monoatomic dispersion, with all the metal atoms being isolated and exposed to the surface. Such single atom catalysts (SACs) are receiving much attention currently and can be regarded as a new frontier in heterogeneous catalysis.[1,5] It should be noted that single atoms are also expected to be present in traditional nanoparticle-based solid catalysts, with abundance depending on the adopted synthesis method and applied reaction conditions. Indeed, when aiming for the understanding of structure-activity and structure-sensitivity relationships, one should realize that both nanoparticles and more highly dispersed metal atoms can both be present under reaction conditions and will contribute differently to catalyst performance. An intermediate situation is encountered with so-called pseudo-SAC,[6] highly dispersed catalysts containing metal species ranging from small clusters or particles of up to tens of loosely associated atoms, i.e. without strong metal-metal interactions.[7,8]

Many routes are being developed for the on purpose synthesis of single atom catalysts, including physical vapor deposition, atomic layer deposition and wet chemical approaches. [9–12] Although it is possible to precisely control catalyst structure and dispersion on an atomic scale with these approaches, these methods are generally expensive and not scalable.[4,13] Therefore, access to (pseudo)-SAC via traditional wet chemical approaches would be highly attractive given their simplicity and applicability for use in industrial scale preparations. Wet chemical methods, including wet impregnation, co-precipitation and deposition-precipitation, have now indeed been successfully applied to fabricate single atom catalysts loaded on various supports.[12,14–16] Indeed, fully atomically dispersed catalyst can be achieved at a broad range of metal loading from 0.03 to 1.5 wt.% depending on the fabrication routes, metal precursors and supports.[10,17]

Given that reactions can be governed by different structure sensitivity relationships, the effect of decreasing dispersion to the single atom level can have both a positive or negative effect on catalyst performance.[18] For the majority of the examples, downsizing of metal clusters to isolated atoms has shown a positive effect on performance. For example, Zhang and co-workers pioneered a series of iron oxide-supported (pseudo) single atom catalysts that showed superior catalytic activity in CO oxidation, water gas shift (WGS) and nitroarene hydrogenation.[8,17,19,20] Other examples include the beneficial effect of isolated noble metal atoms on selectivity in chemoselective reduction processes. For example, graphene-supported isolated Pd atoms,[11] γ -alumina supported Pd-Cu single-atom alloys[21] and mesoporous

Al_2O_3 supported Pt single atom catalysts[12] were demonstrated to be highly selective towards alkadiene hydrogenation in alkene-rich streams, without the over-hydrogenation of the formed alkenes to alkanes that is shown by their nanoparticle-based analogues.

If the single atoms are the relevant catalytically active species remains a subject of discussion and should be established on a per-reaction/catalyst combination basis. For example, for CO oxidation and WGS the involvement of single atoms has been disputed. Ding *et al.* for example claimed that Pt nanoparticles were the active sites for efficient CO oxidation and WGS, while single Pt atoms only served as spectators in these two reactions.[22] However, other reports suggest that these reactions are in fact catalyzed by isolated metal atoms. Indeed, Yang *et al.* reported that Pt (or Au) SAC stabilized on both reducible oxides (CeO_2 , FeO_x , TiO_2) and irreducible supports (silica, zeolites, alumina and carbon nanotube) showed the highest catalytic efficiency in WGS. [23] DeRita *et al.* compared the effect of metal dispersion on CO oxidation activity over Pt/ TiO_2 catalysts with different weight loadings and found isolated Pt atoms to exhibit a two times higher turnover frequency than 1 nm Pt particles towards CO conversion.[24] Moses-Debusk *et al.* in turn demonstrated that inert $\theta\text{-Al}_2\text{O}_3$ supported Pt SAC is also highly active for CO oxidation.[25] Similar controversies are also encountered for the role of SAC in reactions other than CO oxidation and WGS. For example, Rossell *et al.* showed that magnetite-supported palladium single-atoms were unable to catalyze the hydrogenation of alkenes, whereas Pd clusters of low atomicity showed outstanding catalytic performance.[26] Likewise, Narula *et al.* reported that atomic Pd on θ -alumina was unable to catalyze NO oxidation, while supported Pd nanoparticulate catalysts are excellent NO oxidation catalysts.[27] On the other hand, the same authors demonstrated single Pt atoms stabilized by the same support were highly active for this reaction.[28] Given the above and keeping in mind that traditional synthesis methods can often give rise to a rather broad distribution in metal speciation, ranging from single atoms to nanoparticles in one and the same catalysts, it is essential further explore the structure-sensitivity relationships for noble metal SAC in different reactions.[4]

Previously, we reported on a fully monoatomically dispersed Ru/ ZrO_2 catalyst that could be easily obtained at 1 wt.% metal loading via a simple wet impregnation method.[29] This Ru/ ZrO_2 catalyst was used in liquid phase levulinic acid hydrogenation and, as shown by aberration corrected scanning transmission electron microscopy (AC-STEM), many of the single Ru atoms of the catalyst surprisingly survived the high temperature and pressure, polar liquid phase reaction conditions for several reuse cycles, albeit accompanied with some sintering.[29] Here, we extend this single atom family to include ZrO_2 -supported Pd and Pt SAC. A series of Pd and Pt/ ZrO_2 catalysts with different metal loadings and dispersions were prepared and tested in CO oxidation, cinnamaldehyde hydrogenation, propane dehydrogenation and 1,3-butadiene hydrogenation in a propene-rich stream to investigate the influence of atomicity on catalytic performance in different types of reactions, including gas and liquid phase reactions and oxidation and reduction reactions. Our results demonstrate that single atoms can promote the reaction rate of oxidation as well as hydrogenation reactions. Notably, the 0.05 wt.% Pd/ ZrO_2 catalyst proved to be excellent in selective butadiene hydrogenation, showing the highest reported activity for selective butadiene removal from a propene feedstock.

5.2. Experimental Section

5.2.1. Catalyst synthesis

All chemicals were used as received without any further purification. For the preparation of the catalyst materials the following chemicals have been used: tetraammineplatinum(II) nitrate ($\geq 50\%$ Pt basis, $\text{Pt}(\text{NH}_3)_4(\text{NO}_3)_2$) and tetraamminepalladium(II) nitrate (10 wt.% solution in water, $\text{Pd}(\text{NH}_3)_4(\text{NO}_3)_2$) were obtained from Sigma-Aldrich, while the monoclinic ZrO₂ support (Daiichi Kikenso RC-100) was obtained from Degussa. All the gases were provided by Linde.

The Pd and Pt/ZrO₂ catalyst was prepared via wet impregnation, similar to the method used for the preparation of Ru/ZrO₂. [29] The ZrO₂ support was first dried at 120 °C for 2 h to remove humidity. Subsequently, the slurry of the support and demi-water was stirred at room temperature for 30 min, followed by dropwise addition of 10 mL metal precursor solution after which the slurry was stirred for 3 h. After elimination of water under vacuum at 60 °C, the catalyst was dried at 60 °C overnight in air, calcined at 500 °C for 3.5 h with a heating ramp of 5 °C/min under a pure N₂ flow of 100 mL/min, followed by its reduction at 450 °C with a ramp rate of 5 °C/min for 5 h, under a pure H₂ flow of 80 mL/min. The catalysts were prepared with weight loadings ranging from 0.05 to 1 wt.% and are denoted as XM/ZrO₂ in which X being equal to the noble metal (M) weight loading.

5.2.2. Catalyst characterization

High angle annular dark field (HAADF) STEM images were taken at Lehigh University using an aberration-corrected JEM ARM 200CF microscope operating at 200 kV.

FT-IR measurements after CO adsorption were conducted in two ways: (1) to study a freshly reduced, inertly handled catalyst sample, the tube used for calcination/reduction was flushed with pure N₂ for 30 min, sealed and transported into a nitrogen-filled glovebox immediately to avoid any potential air oxidation or water adsorption. A self-supported wafer (10-15 mg) was pressed at 3.5 tons for 10 s and positioned in a well-sealed transmission IR cell equipped with CaF₂ windows inside the glovebox, no drying step was conducted; (2) alternatively, after reduction, reduced catalysts were stored in air rather than in the glovebox. 15-20 mg of the catalyst was pressed into a self-supported pellet and placed into a well-sealed cell with CaF₂ window. The wafer was activated at 300 °C (10 °C/min) under high vacuum (10⁻⁶ mbar) to remove adsorbed water. Subsequently, the cell was cooled down to -188 °C to record the spectra.

Fourier-transform infrared (FT-IR) spectra were recorded in transmission mode on a Perkin-Elmer 2000 instrument. The cell was evacuated to 10⁻⁶ mbar and cooled down to -188 °C with liquid nitrogen. Spectra were taken upon CO (10% in He, purity 99.9%) adsorption on the sample at stepwise increasing pressures.

X-ray Absorption Spectroscopy (XAS) measurements were taken at ESRF (Grenoble, France) at DUBBLE BM26 beamline. The glovebox-stored catalyst was packed in a capillary reactor (1 mm external diameter, 0.01 mm wall thickness) and supported with two plugs of quartz wool to give a catalyst bed length of 0.8 cm. The XAS measurements of the references were performed in transmission mode, while Pd and the Pt/ZrO₂ catalysts were analyzed in fluorescence mode.

All the acquired XAS spectra were subsequently processed in Athena and analyzed in Artemis, both part of a XAS data analysis software package using IFEFFIT.[30]

Hydrogen chemisorption experiments were performed on a Micromeritics ASAP 2020 instrument. The catalyst was reduced at 250 °C for 2 h. After reduction, the sample was degassed for 1 h at 250 °C. The sample was then cooled to 40 °C at which the H₂ adsorption isotherm was measured.

5.2.3. Catalytic performance testing

5.2.3.1. Propane dehydrogenation

For propane dehydrogenation a protocol described elsewhere was followed.[31] Catalytic tests were performed in a fixed-bed plug flow reactor set-up. 0.5 mg of noble metal (sieve fraction of 75-150 µm) was packed into a 1 cm OD rectangular quartz tube reactor (ID = 3 mm × 6 mm) and diluted with SiC (sieve fraction of 212-425 µm) to a total volume of 0.4 mL. Prior to the experiment, the system was flushed with 20 mL/min He until no air was detected by GC. After that, the catalyst was heated to 680 °C unless otherwise specified and then, a gas feed composition of 2 mL/min propane and 10 mL/min He was introduced to the system. All gas lines were heat-traced to 200 °C. In addition, liquid water was introduced into the reactor using a saturator at a rate of 1.6 mg/min at 65 °C. The output gas was analyzed by an online Interscience Compact GC equipped with an Rtx-wax and Rtx-1 column in series and an Rtx-1, Rt-TCEP and Al₂O₃/Na₂SO₄ column in series, both sets connected to an FID detector. The propane conversion (*X*) and propylene selectivity (*S*) were calculated based on the following equations:

$$X = \frac{\text{moles of propane inlet} - \text{moles of propane outlet}}{\text{moles of propane inlet}} \times 100\%$$

$$S = \frac{\text{moles of propylene} \times 100}{\text{moles of propylene} + \frac{\text{moles of CH}_4}{3} + \frac{2 * \text{moles of C2 hydrocarbons}}{3} + \frac{\text{moles of CO}}{3} + \frac{\text{moles of CO}_2}{3}}$$

For the recycling tests, the spent catalyst was regenerated *in-situ* in a 10 mL/min flow of 20% O₂/He at 580 °C (heated from room temperature) for 2 h.

5.2.3.2. CO oxidation

Catalytic tests were performed in a fixed-bed plug flow reactor set-up. Typically, a fixed amount (0.5 mg) noble metal (sieve fraction of 75-150 µm) was packed into a 1 cm OD rectangular quartz tube reactor (ID = 3 mm × 6 mm) and diluted with SiC (sieve fraction of 212-425 µm) to a total volume of 0.4 mL. After that, the catalyst was exposed to reagent gas consisting of 20 mL/min CO (10% in He, purity 99.9%) and 20 mL/min pure O₂. Catalyst activity was evaluated as function of a temperature gradient from 30 to 300 °C with a ramp of 2 °C/min. Catalyst thermal stability was tested by temperature cycling. The output gases were analyzed by nondispersive

FT-IR gas analysis and mass spectrometry. The gas concentration was calibrated with different concentrations of CO in O₂. Temperature for 50% CO conversion ($T_{50\%}$) was used as an index to evaluate catalyst activity and CO conversion (X) was calculated based on the following equation:

$$X = \frac{\text{Moles of CO inlet} - \text{Moles of CO outlet}}{\text{Moles of CO inlet}} \times 100\%$$

5.2.3.3. *Trans-cinnamaldehyde hydrogenation*

Hydrogenation of a 10 wt.% *trans*-cinnamaldehyde (CAL) solution in toluene was performed in a 40 mL stainless Parr batch autoclave for 2 h at a stirring speed of 1250 rpm. In a typical experiment, 80 mg of catalyst, 2 g cinnamaldehyde and 18 g toluene were loaded in the autoclave. 0.2 g biphenyl was also added as internal standard. Then the autoclave was purged three times with argon after which the reaction mixture was heated to 60 °C and charged with 5 bar H₂. This was taken as the starting point of the reaction and liquid samples were taken regularly during the reaction. The reaction mixture was analyzed by a gas chromatograph (Hewlett–Packard 5890 Series with auto sampler) fitted with an HP5 capillary column (30 m × 0.32 mm × 0.25 μm i.d.).

5.2.3.4. *1,3-Butadiene hydrogenation*

For selective butadiene hydrogenation a protocol described elsewhere was followed.[12] To compare the catalytic performance of 1 and 0.05 wt.% M/ZrO₂ catalysts under the same reaction conditions, the 1% Pd and Pt/ZrO₂ catalysts were diluted 20 times with pure ZrO₂ support. A fixed amount of noble metal (10 μg) was used for all the catalytic runs. In a typical experiment, 20 mg (ZrO₂ support diluted) catalyst (sieve fraction of 90-150 μm) and 180 mg of alumina was packed in a stainless tube.[12] A gas mixture of 2 v% 1,3-butadiene, 20 v% propylene, 16 v% H₂ and balance He at a flow rate of 20 mL/min was introduced and catalyst performance assessed as function of ascending temperature (30-100 °C). GC analysis was done at a few selected temperatures after stabilization at that point for at least 10 min.

Butadiene and propene conversion (X) and product selectivities (S) are defined as follows:

$$X_i(\%) = \frac{\text{Moles}_{0,i} - \text{Moles}_{t,i}}{C_{0,i}} \times 100\%$$

$$S_{t,p}(\%) = \frac{\text{Moles}_{t,p}}{\text{Moles}_{0, \text{buta}} - \text{Moles}_{t, \text{buta}}} 100\%$$

Where Moles_{0,i} is initial concentration butadiene or propene, Moles_{t,i} is butadiene or propene concentration at time t , and Moles_{t,p} is the moles of product i at time t .

5.3. Results and Discussion

5.3.1. Characterization of fresh catalysts

Fig. 5.1 shows the STEM images of Pt and Pt loaded ZrO_2 catalysts for selected loadings. In contrast to the $1\text{Ru}/\text{ZrO}_2$ catalyst reported before,[29] several Pd nanoparticles (particle size smaller than 1.5 nm, insufficient number for statistical analysis) were still observed at 1 wt.% for the $1\text{Pd}/\text{ZrO}_2$ catalyst (highlighted in yellow dashed circles), although a considerable fraction of Pd was found to be dispersed as isolated Pd atoms over the sample. It should be noted that despite the small Z contrast, detection of single Pd atoms is difficult, but possible in these images. The $1\text{Pt}/\text{ZrO}_2$ catalyst showed a lower dispersion at this weight loading, with many more metal nanoparticles being detected compared to its Pd counterpart. Based on examination of 6 different locations, all detected Pt clusters and nanoparticles were found to be smaller than 2 nm, but the number of Pt clusters/particles did not allow a particle size distribution to be determined. Again, a large amount of atomic Pt could also be found on the ZrO_2 surface, however. As can be seen in Fig. 5.1, the number of metal clusters/nanoparticles detected clearly decreased upon decreasing the metal loading. STEM analysis showed the Pd and Pt catalysts to be fully atomically dispersed at weight loadings of 0.5 and 0.1 wt.%, respectively. By inference, catalyst weight loadings lower than these respective thresholds are also considered (predominantly) monoatomic.

The local information obtained by STEM analysis was complemented by XAS analysis to get bulk characterization information. While no nanoparticles or clusters were detected in a series of different STEM images of $0.5\text{Pd}/\text{ZrO}_2$, the XAS data suggested a considerable amount of reduced Pd clusters to be present on the catalyst. As shown in Fig. 5.2, the edge position of 0.5Pd -SAC catalyst is similar to the metallic Pd rather than the PdO reference and the EXAFS spectrum and associated FT data do show Pd-Pd coordination (Fig. 5.2b and c). The discrepancy between the STEM and XAS results highlight the importance of complementary bulk analysis, but might also be due to some inevitable small batch-to-batch differences. Unfortunately, the strongly adsorbing zirconia support precluded XAS analysis at lower loadings catalyst, with even overnight measurements not giving data of sufficient quality. In any case, to err on the side of caution, the samples at 0.5 wt.% and higher are regarded as possibly having both single atoms and nanoparticles/clusters present with the single atoms becoming more and more dominant as loading goes down.

FT-IR analysis after CO adsorption did allow also for the lower weight loadings to be analyzed. After CO exposure at liquid nitrogen temperatures, a band located around 2063 cm^{-1} appeared for $1\text{Pt}/\text{ZrO}_2$ (Fig. 5.3a). This band is normally attributed to CO linearly adsorbed on metallic Pt nanoparticles.[32] No band typically associated with bridging CO adsorbed on large Pt particles was observed in the region $1800\text{--}2000\text{ cm}^{-1}$, however.[32] Previous studies also pointed out that CO adsorbed on isolated Pt atoms may also be detected in a region similar to the vibration of linearly adsorbed CO on Pt^0 . Indeed, Qiao *et al.* reported that CO adsorption on FeO_x supported single Pt atoms gave a vibration at around 2080 cm^{-1} . [20] Likewise, Zhang *et al.* showed that a $\text{Pt}/\text{m-Al}_2\text{O}_3$ SAC exhibited a CO-Pt vibration at 2087 cm^{-1} . [12] Lou *et al.* compared

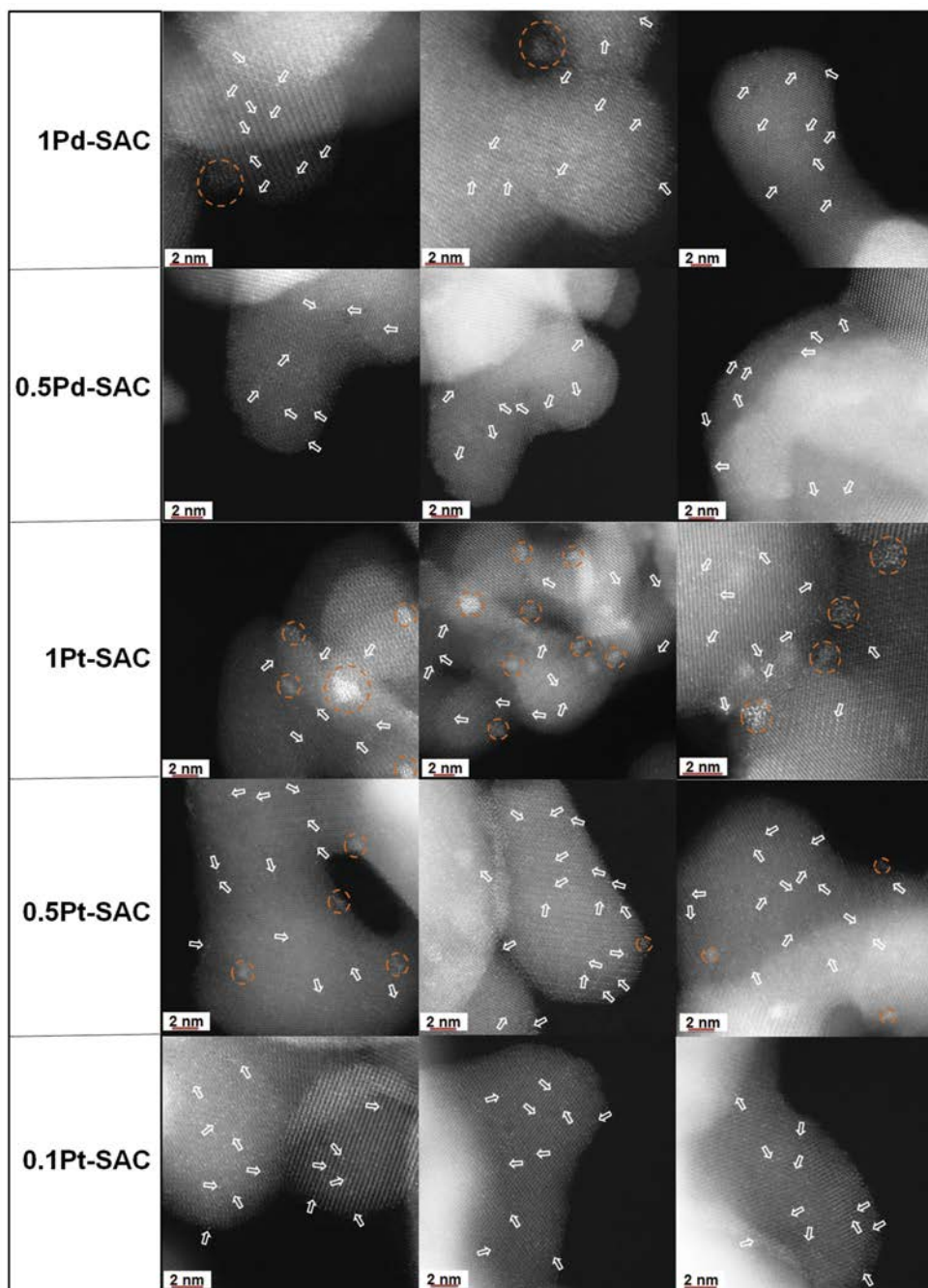


Fig. 5.1. AC-STEM images of Pd and Pt/ZrO₂ catalysts at different metal loadings. Single supported atoms are indicated with arrows, nanoparticles/clusters are highlighted with a dashed circle.

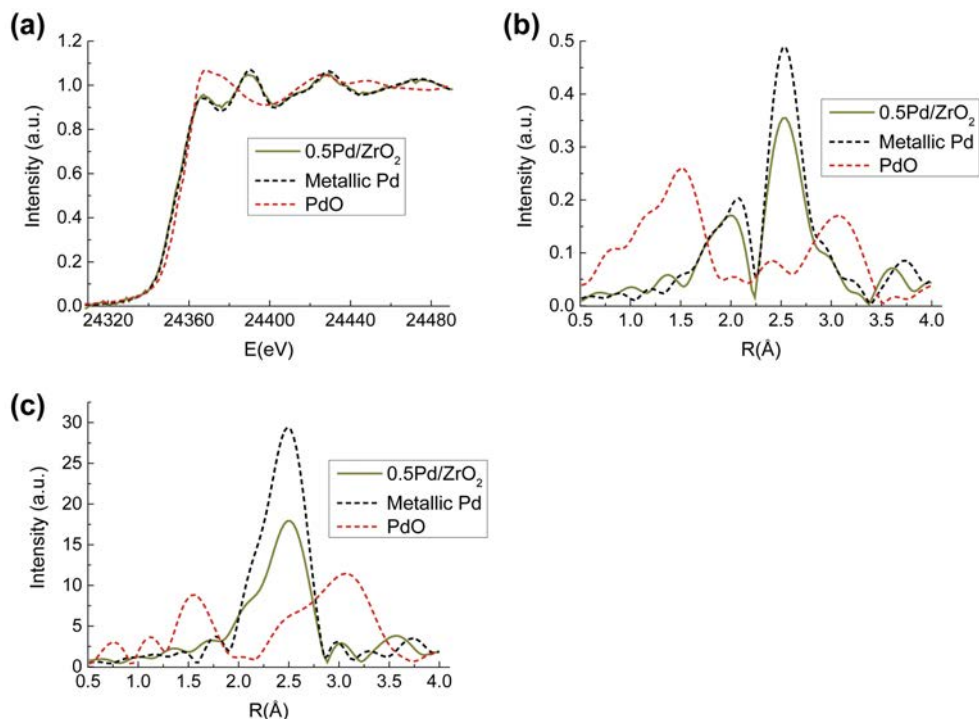


Fig. 5.2. (a) XANES spectra, (b) k^1 and (c) k^3 -weighted Fourier transform spectra from EXAFS of glovebox stored 0.5Pd/ZrO₂ catalyst and references.

CO adsorption of isolated Pt atoms on various metal oxide supports with DRIFTS, attributing vibrations at 2030 cm⁻¹ to CO linearly adsorbed on Pt nanoparticles and vibrations in the range of 2060-2076 cm⁻¹ to CO adsorption on Pt isolated atoms.[33] While the vibration seen for 1Pt/ZrO₂ would fall in the latter category, we cannot fully attribute this peak to CO adsorption on isolated atoms rather than on nanoparticulate Pt. Indeed, upon CO dosing, the CO-Pt vibration gradually blue-shifted to higher wavenumbers, an observation typically attributed to dipole-dipole interactions of CO adsorbed on Pt clusters or nanoparticles, something which would be in line with the Pt dispersion seen in the TEM images (Fig. 5.1).[24] At high CO coverage, a CO-Zr⁴⁺ band appeared and centered around 2205-2200 cm⁻¹, red shifting gradually upon CO dosing.[34] The spectra for lower Pt loadings essentially showed the same features. Notably, the shift seen for CO-Pt band maxima upon increasing CO pressure got smaller upon lowering the Pt loading, decreasing from 18 cm⁻¹ to 11 and 4 cm⁻¹ for 1, 0.1 and 0.05Pt/ZrO₂, respectively. This is indicative of an increase in dispersion and mono-atomicity upon decreasing Pt loading, in line with the TEM results. Especially for 0.05Pt/ZrO₂, a shift of only 4 cm⁻¹ band shift was observed (Fig. 5.3c), similar to the result reported by Zhang *et al.*, who observed a 3 cm⁻¹ red shift when CO readily desorbed from alumina supported isolated Pt atoms.[12] These results suggest that 0.05Pt/ZrO₂ is (almost) fully atomically dispersed. Meanwhile, a new band centered

around 2137 cm⁻¹ was observed for 0.05Pt/ZrO₂ catalyst and attributed to multicarbonyl adsorption on monatomic Pt, again demonstrating the increased atomicity at lower weight loadings (Fig. 5.3c).[32]

The IR spectra of freshly reduced Pd/ZrO₂ exposed to CO were also collected at liquid nitrogen temperature and are shown in Fig. 5.4. After introducing CO into the IR cell, three bands centered at 2086, 1970 and 1923 cm⁻¹ were observed for 1Pd/ZrO₂. The same bands were also observed for the 0.5, 0.1 and 0.05Pd/ZrO₂ catalysts, with the shift of the band located at 2086-2094 cm⁻¹ as function of CO coverage decreasing gradually upon the decreasing of Pd loading level, again indicating increased dispersion.

These spectra are similar to those reported by Guerrero-Ruiz *et al.* for reduced Pd/ZrO₂, also synthesized with a monoclinic ZrO₂ support.[35] No particle size information was reported for this catalyst, but chemisorption analysis suggested that only 12% of the Pd atoms were exposed to the surface after reduction at 500 °C.[35] The authors assigned the band observed at 2080 cm⁻¹ to CO linearly adsorbed on Pd⁰ and the 1976 and 1916 cm⁻¹ vibrations to bridged CO on Pd. Also here, interpretation is not unambiguous, however, as a similar shift of band for linearly adsorbed CO-Pd⁰ band was reported for a highly dispersed Pd catalyst. Lear *et al.* could not detect any Pd particles on an alumina-supported Pd catalyst by TEM,[36] and CO chemisorption suggested a very high Pd dispersion of up to 97%. In their case, three CO-Pd

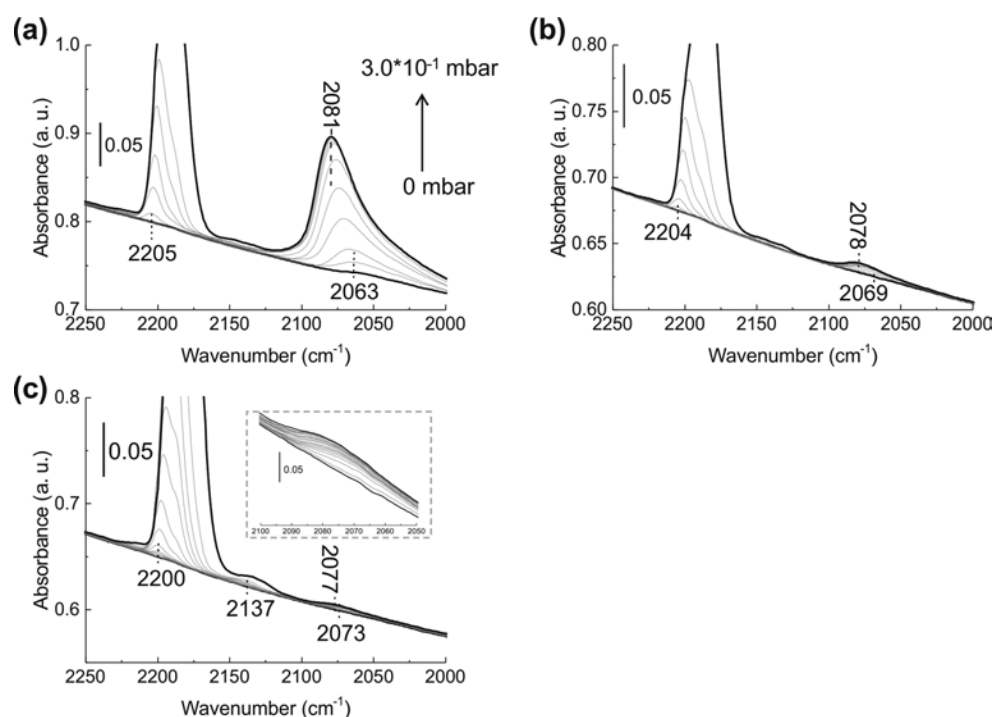


Fig. 5.3. FT-IR spectra of freshly-reduced, glovebox stored (a) 1Pt/ZrO₂, (b) 0.1Pt/ZrO₂ and (c) 0.05Pt/ZrO₂ as a function of CO pressure at liquid N₂ temperature.

bands located at 2065, 1915 and 1830 cm^{-1} (μ_3 bridge-bonded CO-Pd^0) appeared after the first CO pulse, which shifted by 12, 9 and 8 cm^{-1} to 2077, 1924, 1838 cm^{-1} at saturation coverage of CO, respectively.[36] As shown above in TEM images (Fig. 5.1), no Pd nanoparticles could be found for 0.5Pd/ZrO₂ and the weight loading of 0.05Pd/ZrO₂ is extremely low, essentially guaranteeing full dispersion. Nevertheless, the band located in the region of 1900-2000 cm^{-1} is still observed also for this 0.05Pd/ZrO₂ catalyst. Moreover, the peak maxima of spectral features at 1967 and 1923 cm^{-1} do not shift as function of CO pressure, something that would not be expected if originating from bridged CO adsorbed on Pd clusters/nanoparticles. In general, only few studies are available that report CO adsorption on supported isolated Pd atoms. Piernavieja-Hermida *et al.* attributed bands seen for Pd/TiO₂ SAC at 2160 and 2116 cm^{-1} , obtained by atomic layer deposition, to CO adsorbed on Pd²⁺ and Pd⁺ sites, with the 2160 cm^{-1} vibration being related to the CO adsorption on Pd single atoms, whereas the 2116 cm^{-1} band was attributed CO adsorption on Pd nanoparticles.[37] The bands located between 2000-1900 cm^{-1} were also seen by the authors and assigned to bridged CO on large Pd particles.[37] Spezzati *et al.* extensively investigated the catalytic behavior of isolated Pd atoms loaded on CeO₂ for CO oxidation with the help of CO-FTIR spectroscopy at 50 °C.[38] They found that isolated Pd atoms were stabilized as PdO and PdO₂ in a CO/O₂ environment, exhibiting bands at 2096 and 2137 cm^{-1} , respectively,[38] demonstrating that CO adsorbed on Pdⁿ⁺ single atom sites may also exhibit a peak in the region below 2100 cm^{-1} . In our case, given the multiple Pd species present in the 1 and 0.5 wt.% samples, as suggested by TEM and EXAFS, the small shift seen forces a tentative assignment of the band located at 2103 cm^{-1} to CO linearly adsorbed on small Pd particles. CO adsorbed on the Pd single atoms present on these materials, which might adsorb at a similar wavelength, possibly then do not contribute much to the observed IR spectrum. Given the lack of shift, the bands at 1970 and 1923 cm^{-1} are assumed to be correlated to CO-Pd single atom vibrations, however, the precise assignment is as of yet unclear. CO-IR data of air-stored samples further demonstrated that the small Pd clusters suggested by the IR spectra of 0.1 and 0.05Pd/ZrO₂ materials are in fact loosely associated with each other and can be easily oxidized into single atoms after exposure to air.

Interestingly, once exposed to air, one additional band located at 2133 cm^{-1} was observed for 0.5Pd/ZrO₂. This band has been attributed to bicarbonyl-Pd²⁺ species.[38] This is reminiscent of the observations made in chapter 4, where we reported that small Ru clusters in 1Ru/ZrO₂ can redisperse as single atoms upon exposure to an O₂ flow at room temperature. The Pd speciation in the air stored 0.1Pd/ZrO₂ catalyst seemed even more complex. Different from the spectra obtained for the freshly reduced material, CO adsorption gave rise to the appearance of 4 bands at 2089, 2100, 2138 and 2245 cm^{-1} . The assignment of these bands is not yet clear, but it is worth to note that no shifts were seen for the maxima of these bands upon CO stepwise adsorption up to 0.01 mbar and this lack of coverage dependence is highly indicative of the mono-atomic nature of the species responsible.[20] Surprisingly, when the CO pressure was higher than 0.01 mbar (the dot spectrum in Fig. 5.5b), the band located at 2100 cm^{-1} blue shifted to 2107 gradually whereas the band at 2138 cm^{-1} slightly red shifted to 2134 cm^{-1} , perhaps due to non-identical coordination environments of isolated Pd species.[12] For the air exposed 0.05Pd/ZrO₂ catalyst

no appreciable signal could be obtained other than CO-Zr vibrations (data not shown), again suggesting that CO adsorption on the (oxidized) Pd single atoms is weak.

Taken together, the characterization data suggest the dispersion of ZrO₂ supported Pt and Pd catalysts to be metal loading dependent with the atomicity of the catalysts increasing upon decreasing of metal loading. In particular, the 0.05Pt/ZrO₂ and 0.1 and 0.05Pd/ZrO₂ seem to be fully atomically dispersed catalysts.

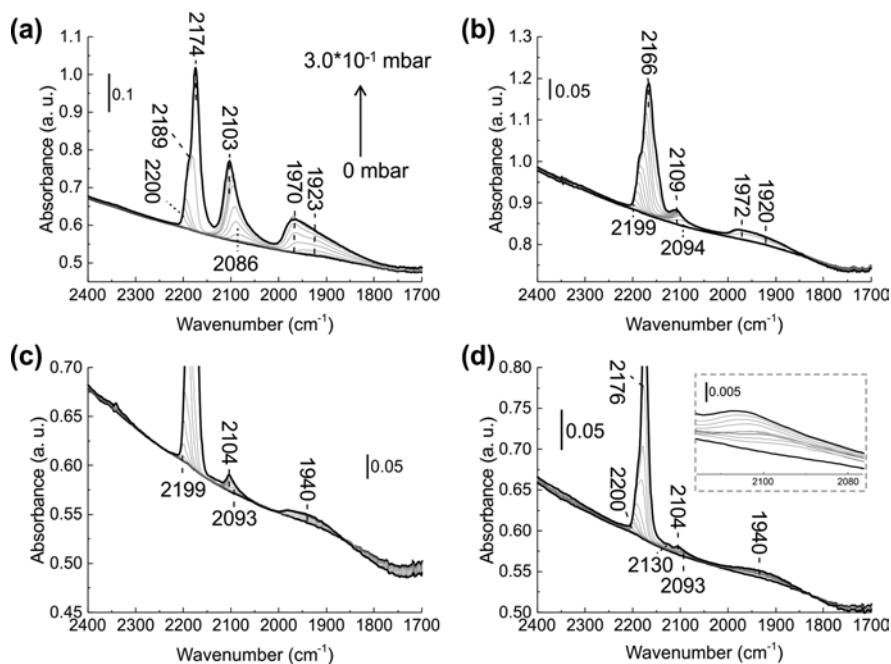


Fig. 5.4. FT-IR spectra of glovebox stored (a) 1Pd/ZrO₂, (b) 0.5Pd/ZrO₂, (c) 0.1Pd/ZrO₂ and (d) 0.05Pd/ZrO₂ as a function of CO pressure at liquid N₂ temperature.

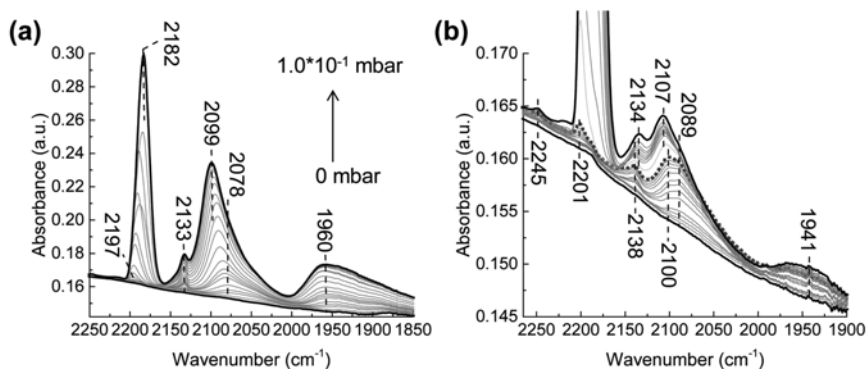


Fig. 5.5. FT-IR spectra of air stored (a) 0.5Pd/ZrO₂ and (b) 0.1Pd/ZrO₂ as a function of CO pressure at liquid N₂ temperature.

5.3.2. Catalyst performance testing

5.3.2.1. Propane dehydrogenation

Propane dehydrogenation is becoming increasingly important industrially and supported Pt and Pd normally show both good activity and selectivity for this reaction.[39] Previous reports suggested that propane dehydrogenation is often structure sensitive. For example, Zhu *et al.* intensively investigated the size effect of Pt nanoparticles on propane dehydrogenation performance and found that larger Pt clusters promoted the selectivity towards propene, but inhibited propane conversion.[40] Liu *et al.* reported that zeolite MCM-22 supported subnanometric Pt species (considered a combination of Pt single atoms and fine clusters) were more reactive and stable than a catalyst containing Pt nanoparticles of 1-5 nm for propane dehydrogenation at 550 °C.[41]

In this section, the Pd and Pt loaded ZrO₂ catalysts studied here were tested under the propane dehydrogenation reaction condition established by Xiong *et al.*[31] The standard reaction conditions entailed 6 h runs at 680 °C and H₂O saturated He gas was added into the reaction flow to mitigate the coke formation during treatment.[31] As we wanted to keep the gas hourly space velocity (GHSV) the same for all the experiments, the catalysts with weight loadings lower than 0.5 wt.% were not tested due to limitations in the accuracy of the mass flow controller used. Under the applied conditions, all catalysts initially showed a relatively high propane conversion, but suffered from fast deactivation early on in the run, after which little variation was observed (Fig. 5.6-5.8). The same main products were observed for all the catalysts, i.e. CH₄, CO, H₂, CO₂ and propene as well as trace amounts of C₂H₄ and C₂H₆ (selectivity below 1%) (Fig. 5.6-5.8). Methane, ethane and ethene are products of propane cracking, which is the main side reaction that can occur under propane dehydrogenation conditions.[39] The formation of CO and CO₂ can be attributed to steam reforming of propane followed by water-gas-shift reaction (WGS),[42–44] both of which are thermodynamically favored over dehydrogenation in the presence of water (Fig. S5.1).[44]

The results obtained with the ZrO₂ based catalysts can be compared with those obtained for the benchmark Pt-Sn/CeO₂ catalyst previously reported by Xiong *et al.* and tested here again in the same reactor setup (Fig. 5.6).[31] In the report of Xiong *et al.*, the generation of a small amount of CO was also observed but no further explanation was given.[31] Under identical reaction conditions but without water addition, conversion of propane stabilized at ~18% for the Pt-Sn/CeO₂ catalyst after a fast, initial deactivation. Two main products, propylene (72% carbon selectivity) and CH₄ (27%) (Fig. 5.6g and i), were detected, whereas less than 0.5% CO was produced indicating that dehydrogenation and cracking dominated in the absence of water. With water added to the feed to limit coke formation, propane conversion increased to around 27%, but at the expense of a small drop in both dehydrogenation and cracking activity with selectivity of propylene and methane decreasing to 60% and 15%, respectively. These values are similar to those achieved previously by Xiong *et al.*[31] CO and CO₂ are now detected with selectivities of 12% and 8% (Fig. 5.6g and h), respectively, demonstrating that steam reforming and WGS are taking place in the presence of water.

The results obtained for the 0.5 and 1Pt/ZrO₂ catalysts, tested at the same total metal loading at 680 °C with water present, is summarized in Fig. 5.6. Both catalysts show very similar catalytic performance, with an initial propane conversion of around 70% that rapidly dropped and stabilized at around 20%. Initially CO is the main product (about 68%), but gradually selectivity shifts towards propene as the main product. Again, similar propene (45% and 39%) and methane (19% and 16%) selectivities were seen for the 1 and 0.5 Pt/ZrO₂ materials, respectively, after 6 h reaction. These results suggest that the differences in original dispersion of the fresh 1 and 0.5 catalysts are not reflected in catalyst performance under these conditions. As shown in Fig. 5.7, performing the reaction with 1Pt/ZrO₂ at a lower temperature of 600 °C, led to a drop in propane conversion of 50%, with selectivity dropping to 22% after 6 h, and a concomitant increase in CO₂ selectivity to 45%, in line with thermodynamic expectations (Fig. S5.1). CH₄ production was also inhibited at lower temperature with a selectivity of 6%, which is only 1/3 of the value obtained at 680 °C. These results suggest that steam reforming followed by WGS are preferred at lower reaction temperatures at the expense of dehydrogenation and cracking, in contrast to Xiong *et al.* who noted that dehydrogenation was preferred at lower reaction temperature for the Pt-Sn benchmark material.[31] Longer term stability of 1Pt/ZrO₂ was also evaluated by multiple recycling (Fig. 5.8), with the spent catalyst being regenerated *in-situ* followed the method reported by Xiong *et al.*[31] No obvious changes in propene production were observed, demonstrating that the state reached by the catalyst after early exposure to the reaction conditions is stable, also after repetitive regeneration.

The Pd loaded ZrO₂ catalysts gave results qualitatively similar to the Pt catalysts (Fig. 5.6d-f). Although the Pd dispersions again differed for the 0.5 and 1% Pd/ZrO₂ materials, no difference was observed with respect to activity and selectivity for those two catalysts, showing a propane conversion that stabilized at around 17% after initial deactivation. Different from the steady increase in propene selectivity seen during reaction for the Pt catalysts, the maximum propene selectivity of 47% is rapidly reached after 0.5 h, after which it remains constant. The Pd and Pt/ZrO₂ catalysts thus proved less selective towards propylene at similar conversion than the Pt-Sn/CeO₂ benchmark, mainly as a result of enhanced steam reforming and WGS activity.

That the two Pd and two Pt M/ZrO₂ materials show such similar catalytic performance, regardless of differences in original dispersion, taken together with the recycling results suggests that the materials may evolve to give a similar catalyst composition, i.e. nanoparticle size and degree of dispersion, upon exposure to the demanding reaction conditions. Indeed, Xiong *et al.* pointed also out that Pt-Sn/Al₂O₃ catalyst suffered irreversible activity loss upon reusing due to the metal sintering.[31] Likewise, Liu *et al.* found that zeolite (MCM-22) supported subnanometric Pt species slowly grew into bigger particles under propane dehydrogenation conditions at 550 °C. [41]

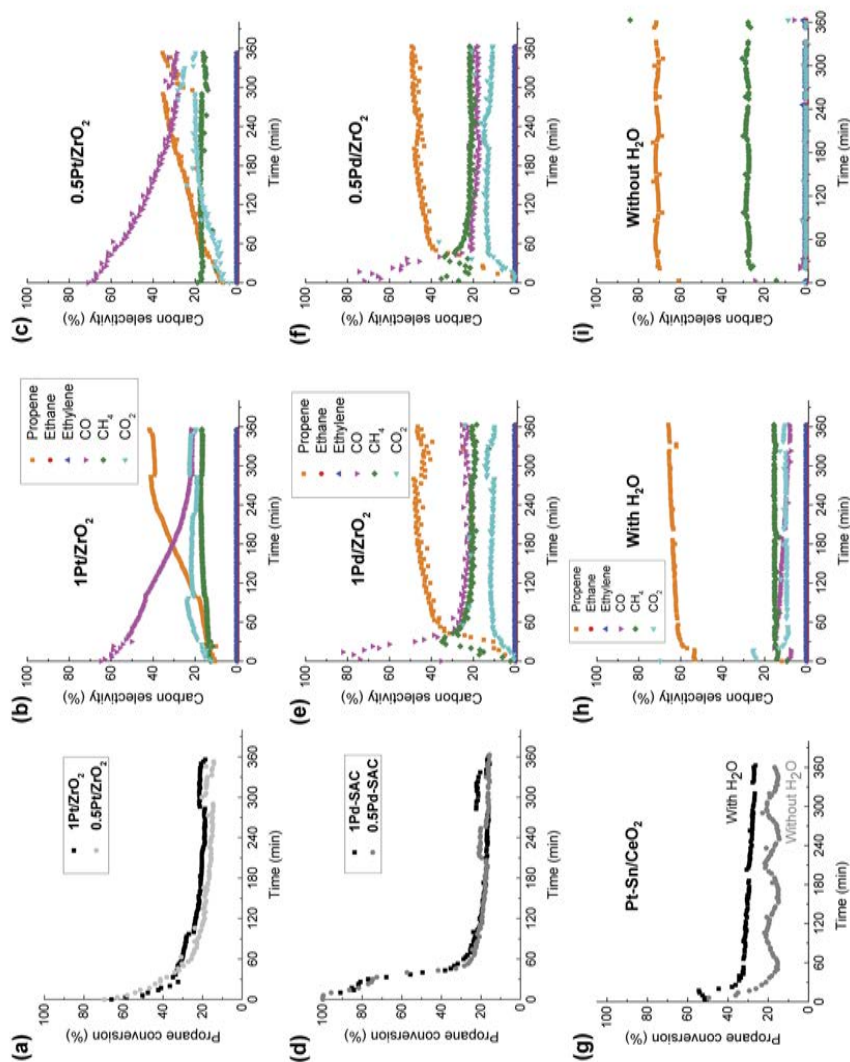


Fig. 5.6. (a) Propane conversion for Pt/ZrO₂ and (b)-(c) the corresponding product selectivity for (b) 1 wt.% and (c) 0.5 wt.% catalysts; (d) propane conversion for Pd/ZrO₂ and (e)-(f) the corresponding product selectivity for (b) 1 wt.% and (c) 0.5 wt.% catalysts as function of time at 680 °C with water addition; (g) propane conversion of Pt-Sn/CeO₂ benchmark catalyst previously reported by Xiong *et al.*[31] at 680 °C and the corresponding gas product selectivities (h) with and (i) without water addition.

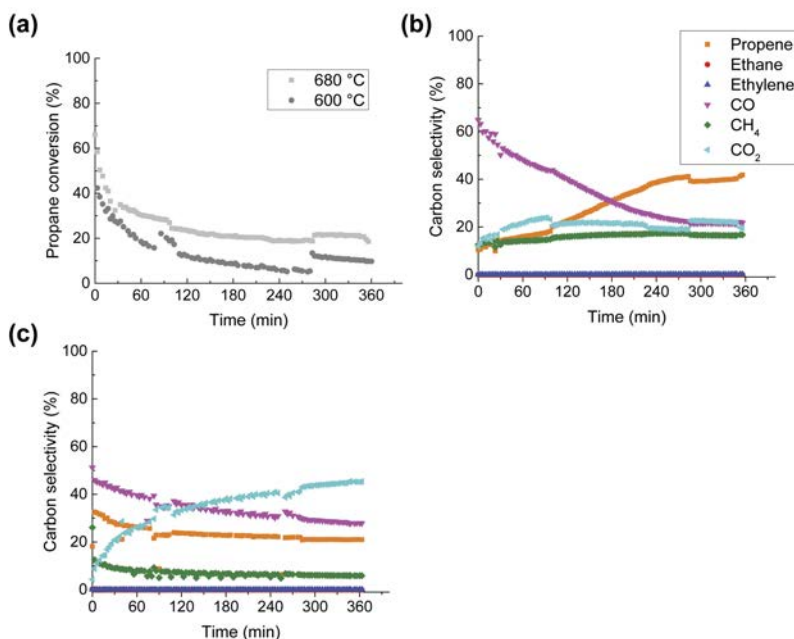


Fig. 5.7. (a) Temperature effect on propane conversion, and the corresponding product selectivity at (b) 680 °C and (c) 600 °C with 1Pt/ZrO₂ as catalyst in the presence of water as function of time.

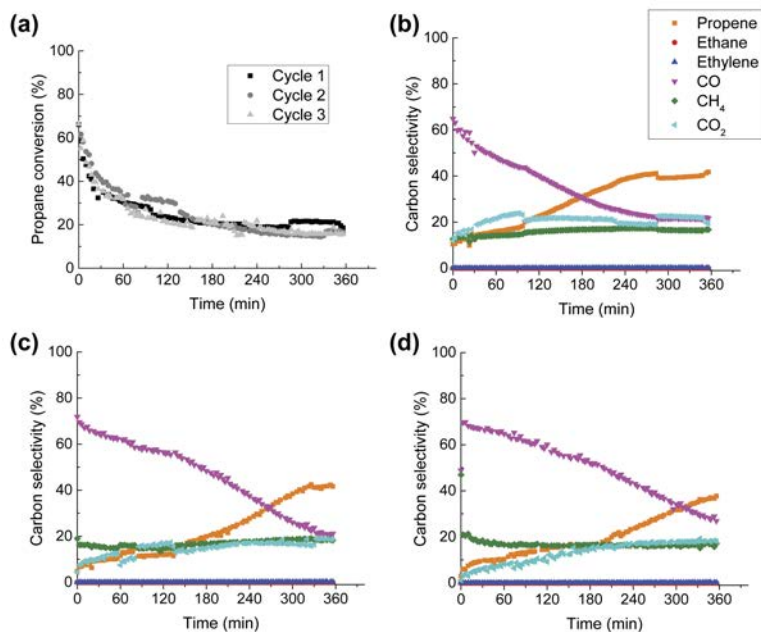


Fig. 5.8. (a) Propane conversion of 1Pt/ZrO₂ at 680 °C under identical reaction conditions at different cycles, the corresponding product selectivities at (b) cycle 1, (c) cycle 2 and (d) cycle 3.

5.3.2.2. CO oxidation

CO oxidation was selected as probe reaction to evaluate catalyst performance under oxidative conditions. CO conversion was investigated over a temperature range of 30 to 300 °C as function of weight loading, keeping the fixed total amount of noble metal loaded into the reactor. Fig. 5.9a summarizes the catalytic activity of the Pt catalysts. Clearly, CO oxidation over 1Pt/ZrO₂ occurred at temperatures higher than 150 °C, reaching 50% CO conversion at 192 °C. When the Pt loading decreased to 0.5 wt.%, both light-off temperature and 50% CO conversion temperature ($T_{50\%}$) were shifted lower temperature, being 120 °C and 160 °C, respectively. The Pd/ZrO₂ showed the same effect, as shown in Fig 5.9b and Table 5.1. The 1Pd/ZrO₂ catalyst exhibited a $T_{50\%}$ of 146 °C, indicating that Pd is more reactive than Pt for this reaction. Likewise, Xu *et al.* predicted the catalytic activity of graphene supported Pd SAC to be higher than Pt based on the theoretical calculations.[45] Again, lowering the weight loading increased catalytic activity as the $T_{50\%}$ shifted to 130 °C for 0.5Pd/ZrO₂. These results could reflect the larger fraction of single atoms at lower loadings and suggest that catalysts with higher atomicity are more catalytically active in CO oxidation. Indeed, several examples have been reported showing that supported isolated noble metal dispersed on various metal oxides are crucial for low temperature CO oxidation. [25,38] For example, Moses-DeBusk *et al.* demonstrated that the catalytic activity of θ -Al₂O₃ supported Pt single atom catalysts was 6 fold higher compared to a nanoparticulate counterpart at 20% CO conversion.[25] While no examples could be found for CO oxidation activity of Pd SAC supported on a non-reducible oxide, Spezzati *et al.* investigated the catalytic behavior of highly dispersed Pd/CeO₂ nanorods in CO oxidation, reporting activity at a temperature as low as 50 °C. The Pd single atoms detected by AC-TEM and CO-FT/IR were thought to be pivotal to the high CO oxidation activity.[38]

Catalyst stability was again evaluated by recycling, this time without any intermediate regeneration step. The Pd catalysts proved not only to be more active but also more stable than their Pt counterparts, as upon recycling, both the 1 and 0.5Pt/ZrO₂ showed a slight deactivation, with $T_{50\%}$ increasing by ~10 °C after 3 cycles. For the Pd catalysts this shift was only ~5 °C. The observed deactivation might be due to partial reduction and clustering of the positively charged single atoms. Peterson *et al.* investigated the nature of isolated Pd during CO oxidation over a Pd/La₂O₃-alumina catalyst via *operando* XAS.[46] They found that the deactivation seen for Pd/La₂O₃-alumina catalyst after one time use was accompanied by the appearance of a Pd-Pd contribution, indicating the transformation of Pd single atoms into Pd clusters.[46] Taken together, the ZrO₂-supported Pd and Pt are shown to efficiently catalyze CO oxidation under mild conditions and the presence of single metal atoms is thought to have a beneficial effect on the catalytic activity. Under the same reaction conditions, the Pd catalyst outperforms its Pt counterpart, both in terms of activity and stability.

5.3.2.3. Cinnamaldehyde hydrogenation

Cinnamaldehyde (CALD) hydrogenation is often used as probe reaction to study the structure sensitivity in liquid phase chemoselective reduction.[47] Cinnamaldehyde contains two

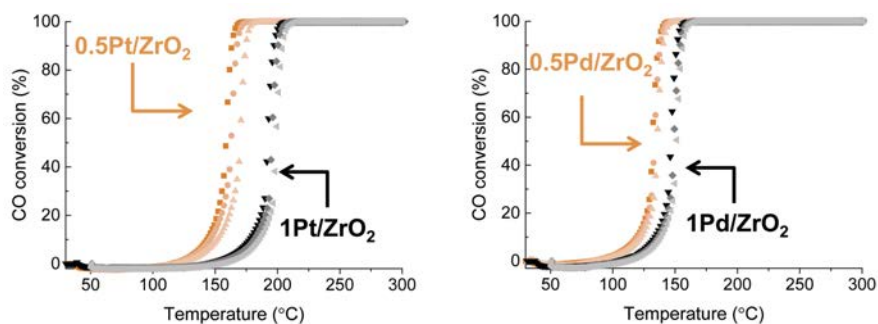


Fig. 5.9. Catalytic activity and stability upon reuse as a function of reaction temperature over (a) Pt and (b) Pd catalysts (lighter symbol color represents higher recycle number).

Table 5.1. Catalytic performance of Pt and Pd loaded ZrO₂ catalysts in CO oxidation.

Cycle No.	T _{50%} (°C)			
	1Pt/ZrO ₂	0.5Pt/ZrO ₂	1Pd/ZrO ₂	0.5Pd/ZrO ₂
1	192	160	146	130
2	196	164	149	133
3	199	170	151	136

reducible functional groups, i.e. C=C and C=O bonds,[48] with reduction of the former yielding hydrocinnamaldehyde (HCAL) and the latter cinnamyl alcohol (CALC). Both of these two intermediates can also be further hydrogenated into 1-phenylpropanol (PP).[49] Particle size dependent performance has been often noted for this reaction, with Durndell *et al.* for example demonstrating that the turnover frequency of CALD hydrogenation over Pt/SiO₂ catalysts was invariant regardless of Pt particle size over 2-15 nm, whereas selectivity towards C=O hydrogenation products was structure sensitive and strongly preferred over large metal particles.[50] Studying the reverse reaction, Hackett *et al.* investigated the performance of different Pd/Al₂O₃ catalysts in the oxidation of CALC, and reported a nonlinear increase in catalytic activity when Pd particles size dropped from 4.7 nm to 0.13 nm (single atoms), while CALD selectivity was structure insensitive over the same range.[51]

Although Pt group metals have been demonstrated to be active in cinnamaldehyde hydrogenation,[52,53] our Pt single atom catalysts showed poor CALD hydrogenation ability under identical reaction or even more forcing reaction conditions (20 bar H₂ and 90 °C). The Pd/ZrO₂ catalysts, however, did exhibit good catalytic activity for this reaction (Fig. 5.10). Only a single product, HCAL was detected by GC regardless of Pd loading and dispersion, showing that C=C rather than C=O bond hydrogenation is preferred. This is in line with the structure sensitivity shown by traditional nanoparticle-based Pd catalysts, for which smaller particle sizes in the range of 1.3-5.7 nm preferred C=C reduction over C=O reduction.[54]

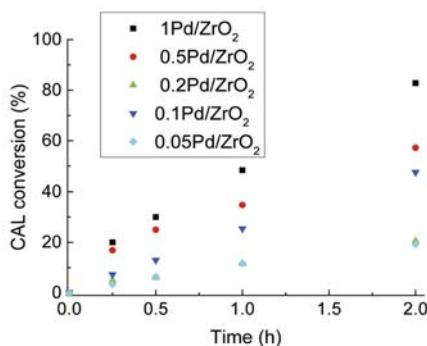


Fig. 5.10. Cinnamaldehyde conversion over Pd/ZrO₂ as a function of time at 60 °C under 5 bar H₂ in toluene as solvent, applying the same total amount of catalyst.

As the mass balance of substrate and products (CALD + HCAL) was always higher than 95% as determined by GC analysis, only CALD conversion is given to compare catalytic activity between catalysts. Fig. 5.10 shows CALD conversion as function of time and as function of Pd loading. 1Pd-SAC exhibited 83% CAL conversion after 2 h reaction. As expected, the CAL conversion dropped with decreasing of metal loading to 57% and 21% for the 0.5% and 0.2% Pd/ZrO₂ catalysts, respectively. Interestingly, the lowest loading Pd catalysts (0.1 and 0.05%) performed better than expected, showing CALD conversions of up to 47% and 20%, respectively. This corresponds to a HCAL productivities of 1.3 and 1.1 mol_{HCAL} mol_{Pd}⁻¹ s⁻¹, for 0.1 and 0.05Pd/ZrO₂, respectively, values which are around 5 times higher than that of the 1Pd-SAC catalyst (0.23 mol_{HCAL} mol_{Pd}⁻¹ s⁻¹). With H₂ chemisorption analysis revealing that 1Pd/ZrO₂ exhibited a surface Pd dispersion of 59%, this resulted in a turnover frequency (TOF) of 0.4 s⁻¹ for 1Pd/ZrO₂. With the 0.1 and 0.05Pd-/ZrO₂ being considered to be (almost) fully atomically dispersed, TOF values of 0.1Pd/ZrO₂ and 0.05Pd/ZrO₂ were calculated to be 1.3 and 1.1 s⁻¹, a threefold increase compared to the 1Pd/ZrO₂ catalyst. It is also worth to notice that 0.1 and 0.05 Pd/ZrO₂ catalysts exhibited a very similar TOF, indicating that catalytic activity is independent from metal loading. Assuming that different adsorption sites (with intrinsically different TOFs) are equally populated at low loadings, SAC would indeed be expected to show loading-independent TOFs, as previously suggested by Qiao *et al.* and as demonstrated, for example, for the Au/FeO_x catalyst system in CO oxidation.[17] Relatedly, Xu *et al.* demonstrated that both of reaction rate and TOF were constant in the gas phase hydrogenation of 1,3-butadiene once the Au phase was fully atomically dispersed.[55] The monoatomic Pd catalysts were thus found to be active in cinnamaldehyde hydrogenation, preferentially hydrogenating the olefinic bond, showing a threefold increase in activity compared over the 1Pd/ZrO₂ catalyst, which contains both Pd single atom and nanoparticles.

5.3.2.4. 1,3-Butadiene selective hydrogenation in excess propene

1,3-Butadiene is found as an impurity in propene feedstocks used for the synthesis of polypropylene, a polymer produced on enormous scale. Selective hydrogenation of this

butadiene impurity in the presence of the large excess of the alkene is highly industrially relevant, as it can poison polymerization catalysts used for polyolefin production.[56] In addition to selectivity reduction of butadiene over propene, overhydrogenation of the butenes formed to butane should also be avoided. This provides a considerable challenge to supported metal hydrogenation catalysts. Precious transition metals (Pd, Pt) are often used to catalyze this process given their excellent hydrogenation ability, but suffer from poor selectivity.[57] Therefore, the development of more active and selective catalysts is still highly desired for this reaction. Recently, several investigations have shown that supported isolated metal atoms or single atom alloys exhibit high selectivity for butadiene removal from alkene feedstocks via semihydrogenation.[11,12,21] We therefore also tested the catalytic performance of the Pd and Pt/ZrO₂ catalysts with different atomicity in semi-hydrogenation of 1,3-butadiene.

Light-off curves were determined for each catalyst material over a temperature range of 30 to 100 °C in the presence of excess propene, keeping the amount of noble metal fixed between runs. Fig. 5.11 shows the catalytic performance of high and low weight loading Pt and Pd catalysts, tested at the same total metal loading and selected to illustrate the selectivity of fully monoatomic and lower dispersion materials. Of the materials tested, 0.05Pd/ZrO₂ clearly stood out, showing superior performance for this important industrial reaction. 100% conversion of 1,3-butadiene was observed at about 70 °C for 0.05Pd/ZrO₂ to give a 96% butenes yield, without any detectable hydrogenation of propene into propane (Fig. 5.11a). The major component of the generated butenes is 1-butene, which is the most desirable product (Fig. 5.11c). The selectivity to 1-butene is around 65%, comparable to what has been reported for a graphene supported single Pd atom catalyst (0.25 wt.%).[11] Temperature has a minor effect on butenes selectivity with 0.05Pd/ZrO₂ at less than full conversion of 1,3-butadiene, indicating that isomerization and overhydrogenation into butane are secondary processes. The TOF for butenes formation over 0.05Pd/ZrO₂ at 50 °C was calculated to be 2.89 s⁻¹ (assuming 100% Pd dispersion). To the best of our knowledge, this TOF value is the highest value so far reported for selective hydrogenation of 1,3-butadiene among the supported single-atom and modified nanoparticle-based catalysts that exhibited high butene selectivity (>99%), including Pt, Pd, Au and bimetallic catalysts (Table S5.1). Indeed, the activity of 0.05Pd-/ZrO₂ towards 1,3-butadiene conversion is two orders of magnitude higher than that of bimetallic Pt-Cu single atom alloy catalyst[55] and about eight fold higher than that of a graphene supported Pd single atom catalyst[11] under comparable conditions. The durability of 0.05Pd/ZrO₂ was further tested at 70 °C for 60 h. As shown in Fig. 5.11d, almost no change was observed for 0.05Pd/ZrO₂ in term of butadiene and propene conversion over the entire run, except for a small drop slight drop of butenes selectivity (< 3%), showing the long term stability of the Pd single atom catalyst against deactivation. Moreover, the 0.05Pd catalyst proved to be very stable over a broad range of temperatures, no poisoning was observed even at temperature as low as 50 °C (Fig. 5.12a). In contrast, the 1Pd/ZrO₂ catalyst of lower dispersion showed a considerably decreased activity with butadiene conversion being only 9% at 50 °C (TOF 0.49 s⁻¹), which is 1/10 of that found for 0.05Pd/ZrO₂ catalyst (Fig. 5.11a). The selectivity of 1Pd/ZrO₂ was also demonstrated to be lower than that of 0.05Pd/ZrO₂. For example, full conversion was achieved at 70 °C for both 1 and 0.05

Pd/ZrO₂. The butenes selectivity and propene conversion of the former at this temperature were 86% and 10% (Table 5.2), respectively, whereas a nearly 100% butenes selectivity was observed for the latter catalyst without transforming the propene feedstock.

It is well documented that Pt is less active and selective than Pd for selective hydrogenation of 1,3-butadiene.[57] Indeed, 0.05Pt/ZrO₂ catalyst showed a much lower activity than its Pd counterpart, with butadiene only starting to be converted at temperatures higher than 80 °C (Fig. 5.11), at which a nearly full conversion was already achieved for the Pd catalysts. The 0.05Pt/ZrO₂ catalyst was also less selective. For example, butanes were detected at a butadiene conversion as low as 2%, although no propene conversion was observed. The 0.05Pt/ZrO₂ also proved less stable, with an increase in conversion from 7% to 21% seen within 1 h of reaction at 100 °C (Fig. 5.12d), accompanied by a decrease in butenes selectivity from 93% to 89%.

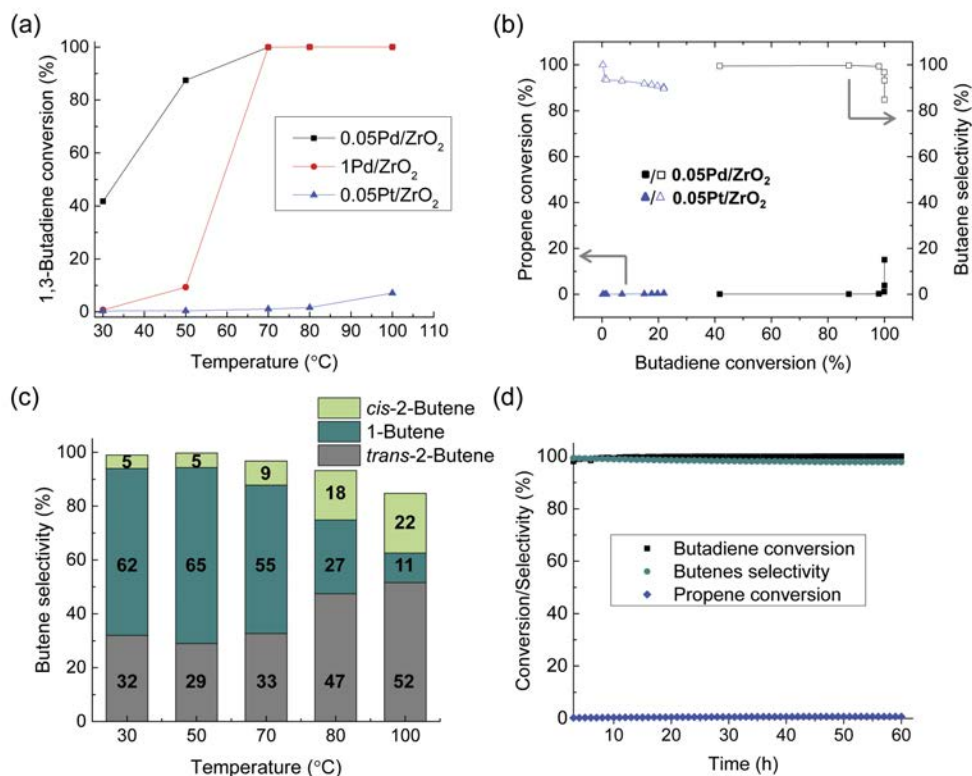


Fig. 5.11. (a) 1,3-Butadiene conversion as a function of temperature and (b) propene conversion and butenes selectivity as a function of butadiene conversion over different fresh catalysts; (c) butenes selectivity for 0.05Pd/ZrO₂ at different temperatures, (d) long term stability test for 0.05Pd/ZrO₂ at 70 °C.

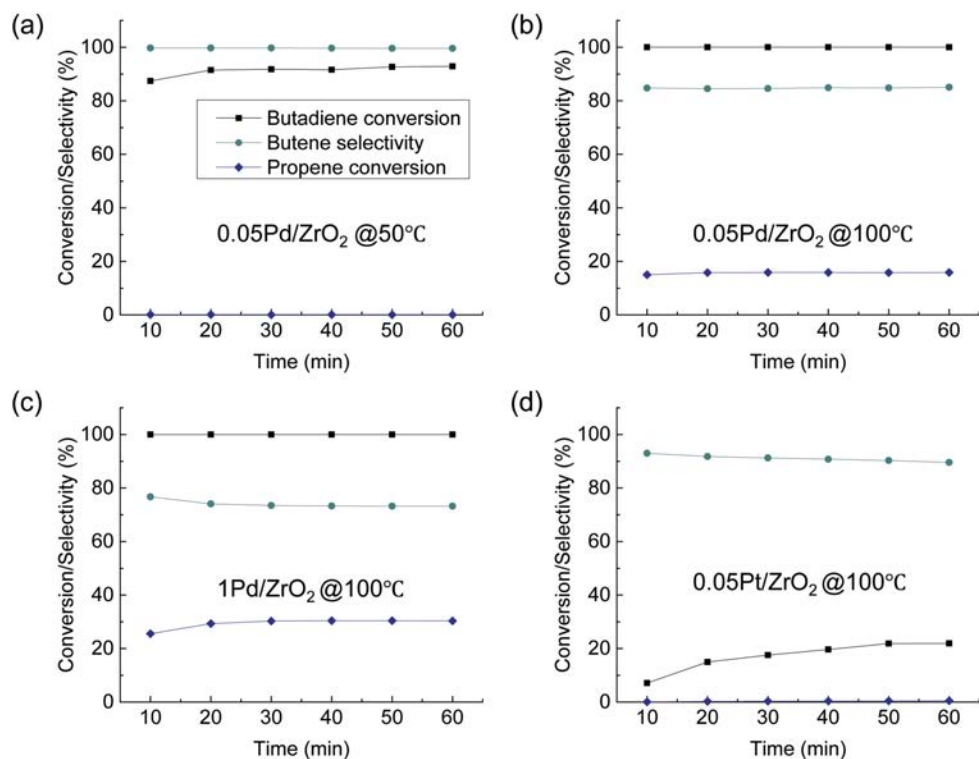


Fig. 5.12. Catalyst stability of 0.05Pd/ZrO₂ at (a) 50 °C and (b) 100 °C, (c) 1Pd/ZrO₂ and (d) 0.05Pt/ZrO₂ at 100 °C.

Table 5.2. Summary of catalytic activity of catalysts at different temperatures.

		Temperature (°C)				
		30	50	70	80	100
0.05Pd/ZrO ₂	Butadiene (C ^a ,%)	42	87	100	100	100
	Butene (S ^b ,%)	99	100	97	93	85
	Propene (C,%)	<1	<1	1	4	15
1Pd/ZrO ₂	Butadiene (C,%)	<1	9	100	100	100
	Butene (S,%)	100	99	86	81	77
	Propene (C,%)	<1	<1	10	17	26
0.05Pt/ZrO ₂	Butadiene (C,%)	<1	<1	1	2	7
	Butene (S,%)	100	100	94	93	93
	Propene (C,%)	<1	<1	<1	<1	<1

^a:conversion; ^b: selectivity.

5.4. Conclusions

In this PhD thesis chapter, a series of Pd and Pt catalysts of different weight loadings have been prepared via a simple wet impregnation procedure and the nature of loaded metal species studied by XAS, FT-IR after CO adsorption and AC-TEM. The latter already showed that large amounts of isolated metal atoms are presented in the 1 wt.% catalysts. In addition, the metal dispersion is weight loading dependent and the atomicity of catalysts increased upon lowering the metal weight loading, with fully monoatomic dispersions being found for catalysts of 0.1 wt.% and lower. The influence of atomicity on catalyst performance was probed in oxidation, dehydrogenation and hydrogenation reactions. Both the Pd and Pt/ZrO₂ catalysts exhibited only a moderate ability to produce propene via propane dehydrogenation, regardless of differences in dispersion of the fresh catalyst. In contrast, the results demonstrate the Pd and Pt catalysts of higher dispersion to perform better in the CO oxidation reaction, suggesting that the single atoms show a higher activity. Degree of dispersion also proved to be key to catalyst performance in both gas and liquid phase hydrogenation reactions. An increase in turnover frequency of around three and six-fold was observed in cinnamaldehyde and 1,3-butadiene hydrogenation, respectively, when comparing catalysts containing (some) nanoparticles with fully atomically dispersed materials. Notably, for cinnamaldehyde hydrogenation, the turnover frequency was found to be independent from metal loading for the SAC. Excitingly, the 0.05 wt.% Pd/ZrO₂ SAC showed excellent catalytic performance in the semi-hydrogenation of 1,3-butadiene as impurity in a propene-rich stream, combining the highest activity reported so far, with excellent butene selectivity and stability over 60 h time on stream. The ZrO₂-supported Pt and, in particular, Pd-based SAC thus proved highly versatile catalysts for a broad range of reactions.

References

1. A. Wang, J. Li, T. Zhang, *Nat. Rev. Chem.* 2 (2018) 65–81.
2. L. Liu, A. Corma, *Chem. Rev.* 118 (2018) 4981–5079.
3. S. Liang, C. Hao, Y. Shi, *ChemCatChem* 7 (2015) 2559–2567.
4. X.F. Yang, A. Wang, B. Qiao, J. Li, J. Liu, T. Zhang, *Acc. Chem. Res.* 46 (2013) 1740–1748.
5. Y.G. Wang, D. Mei, V.A. Glezakou, J. Li, R. Rousseau, *Nat. Commun.* 6 (2015) 6511.
6. G. Vilé, D. Albani, N. Almora-Barrios, N. López, J. Pérez-Ramírez, *ChemCatChem* 8 (2016) 21–33.
7. M. Dhiman, V. Polshettiwar, *J. Mater. Chem. A* 4 (2016) 12416–12426.
8. H. Wei, X. Liu, A. Wang, L. Zhang, B. Qiao, X. Yang, Y. Huang, S. Miao, J. Liu, T. Zhang, *Nat. Commun.* 5 (2014) 5634.
9. J. Jones, H. Xiong, A.T. DeLaRiva, E.J. Peterson, H. Pham, S.R. Challa, G. Qi, S. Oh, M.H. Wiebenga, X.I. Pereira Hernandez, Y. Wang, A.K. Datye, *Science* 353 (2016) 150–154.
10. P. Liu, Y. Zhao, R. Qin, S. Mo, G. Chen, L. Gu, D.M. Chevrier, P. Zhang, Q. Guo, D. Zang, B. Wu, G. Fu, N. Zheng, *Science* 352 (2016) 797–800.
11. H. Yan, H. Cheng, H. Yi, Y. Lin, T. Yao, C. Wang, J. Li, S. Wei, J. Lu, *J. Am. Chem. Soc.* 137 (2015) 10484–10487.
12. Z. Zhang, Y. Zhu, H. Asakura, B. Zhang, J. Zhang, M. Zhou, Y. Han, T. Tanaka, A. Wang, T. Zhang, N. Yan, *Nat. Commun.* 8 (2017) 16100.
13. M. Dhiman, V. Polshettiwar, *ChemCatChem* 10 (2018) 881–906.
14. X. Gu, B. Qiao, C. Huang, W. Ding, K. Sun, E. Zhan, T. Zhang, J. Liu, W. Li, *ACS Catal.* 4 (2014) 3886–3890.
15. J. Lin, A. Wang, B. Qiao, X. Liu, X. Yang, X. Wang, J. Liang, J. Li, J. Liu, T. Zhang, *J. Am. Chem. Soc.* 135 (2013) 15314–15317.
16. S. Yang, J. Kim, Y.J. Tak, A. Soon, H. Lee, *Angew. Chem. Int. Ed.* 55 (2016) 2058–2062.
17. B. Qiao, J.X. Liang, A. Wang, C.Q. Xu, J. Li, T. Zhang, J.J. Liu, *Nano Res.* 8 (2015) 2913–2924.
18. R.A. Van Santen, *Acc. Chem. Res.* 42 (2009) 57–66.
19. J. Lin, B. Qiao, N. Li, L. Li, X. Sun, J. Liu, X. Wang, T. Zhang, *Chem. Commun.* 51 (2015) 7911–7914.
20. B. Qiao, A. Wang, X. Yang, L.F. Allard, Z. Jiang, Y. Cui, J. Liu, J. Li, T. Zhang, *Nat. Chem.* 3 (2011) 634–641.
21. F.R. Lucci, J. Liu, M.D. Marcinkowski, M. Yang, L.F. Allard, M. Flytzani-Stephanopoulos, E.C.H. Sykes, *Nat. Commun.* 6 (2015) 8550.
22. K. Ding, A. Gulec, A.M. Johnson, N.M. Schweitzer, G.D. Stucky, L.D. Marks, P.C. Stair, *Science* 350 (2015) 189–192.
23. M. Yang, M. Flytzani-Stephanopoulos, *Catal. Today* 298 (2017) 216–225.
24. L. DeRita, S. Dai, K. Lopez-Zepeda, N. Pham, G.W. Graham, X. Pan, P. Christopher, *J. Am. Chem. Soc.* 139 (2017) 14150–14165.
25. M. Moses-Debusk, M. Yoon, L.F. Allard, D.R. Mullins, Z. Wu, X. Yang, G. Veith, G.M. Stocks, C.K. Narula, *J. Am. Chem. Soc.* 135 (2013) 12634–12645.
26. M.D. Rossell, F.J. Caparrós, I. Angurell, G. Muller, J. Llorca, M. Seco, O. Rossell, *Catal. Sci. Technol.* 6 (2016) 4081–4085.
27. C.K. Narula, L.F. Allard, M. Moses-DeBusk, G.M. Stocks, Z. Wu, *Sci. Rep.* 7 (2017) 560–567.
28. C.K. Narula, L.F. Allard, G.M. Stocks, M. Moses-DeBusk, *Sci. Rep.* 4 (2015) 7238–7241.
29. J. Ftouni, A. Muñoz-Murillo, A. Goryachev, J.P. Hofmann, E.J.M. Hensen, L. Lu, C.J. Kiely, P.C.A. Bruijninx, B.M. Weckhuysen, *ACS Catal.* 6 (2016) 5462–5472.
30. B. Ravel, M. Newville, *J. Synchrotron Radiat.* 12 (2005) 537–541.
31. H. Xiong, S. Lin, J. Goetze, P. Pletcher, H. Guo, L. Kovarik, K. Artyushkova, B.M. Weckhuysen, A.K. Datye, *Angew. Chem. Int. Ed.* 56 (2017) 8986–8991.

32. E. V. Benvenutti, L. Franken, C.C. Moro, C.U. Davanzo, *Langmuir* 15 (1999) 8140–8146.
33. Y. Lou, J. Liu, *Ind. Eng. Chem. Res.* 56 (2017) 6916–6925.
34. S. Kouva, K. Honkala, L. Lefferts, J. Kanervo, *Catal. Sci. Technol.* 5 (2015) 3473–3490.
35. A. Guerrero-Ruiz, S. Yang, Q. Xin, A. Maroto-Valiente, M. Benito-Gonzalez, I. Rodriguez-Ramos, *Langmuir* 16 (2000) 8100–8106.
36. T. Lear, R. Marshall, J. Antonio Lopez-Sanchez, S.D. Jackson, T.M. Klapötke, M. Bäumer, G. Rupprechter, H.J. Freund, D. Lennon, *J. Chem. Phys.* 123 (2005) 174706.
37. M. Piernavieja-Hermida, Z. Lu, A. White, K.B. Low, T. Wu, J.W. Elam, Z. Wu, Y. Lei, *Nanoscale* 8 (2016) 15348–15356.
38. G. Spezzati, Y. Su, J.P. Hofmann, A.D. Benavidez, A.T. DeLaRiva, J. McCabe, A.K. Datye, E.J.M. Hensen, *ACS Catal.* 7 (2017) 6887–6891.
39. J.J.H.B. Sattler, J. Ruiz-Martinez, E. Santillan-Jimenez, B.M. Weckhuysen, *Chem. Rev.* 114 (2014) 10613–10653.
40. J. Zhu, M.L. Yang, Y. Yu, Y.A. Zhu, Z.J. Sui, X.G. Zhou, A. Holmen, D. Chen, *ACS Catal.* 5 (2015) 6310–6319.
41. L. Liu, D.N. Zakharov, R. Arenal, P. Concepcion, E.A. Stach, A. Corma, *Nat. Commun.* 9 (2018) 6511.
42. Y. Li, X. Wang, C. Song, *Catal. Today* 263 (2016) 22–34.
43. C. Resini, L. Arrighi, M.C.H. Delgado, M.A.L. Vargas, L.J. Alemany, P. Riani, S. Berardinelli, R. Marazza, G. Busca, *Int. J. Hydrogen Energy* 31 (2006) 13–19.
44. C. Resini, M.C. Herrera Delgado, L. Arrighi, L.J. Alemany, R. Marazza, G. Busca, *Catal. Commun.* 6 (2005) 441–445.
45. G. Xu, R. Wang, F. Yang, D. Ma, Z. Yang, Z. Lu, *Carbon* 118 (2017) 35–42.
46. E.J. Peterson, A.T. DeLaRiva, S. Lin, R.S. Johnson, H. Guo, J.T. Miller, J. Hun Kwak, C.H.F. Peden, B. Kiefer, L.F. Allard, F.H. Ribeiro, A.K. Datye, *Nat. Commun.* 5 (2014) 4885.
47. Y. Chen, T. Kasama, Z. Huang, P. Hu, J. Chen, X. Liu, X. Tang, *Chem. Eur. J.* 21 (2015) 17397–17402.
48. P. Gallezot, D. Richard, *Catal. Rev. Sci. Eng.* 40 (1998) 81–126.
49. S. Bhogeswararao, D. Srinivas, *Catal. Lett.* 140 (2010) 55–64.
50. R. Li, W. Yao, Y. Jin, W. Jia, X. Chen, J. Chen, J. Zheng, Y. Hu, D. Han, J. Zhao, *Chem. Eng. J.* 351 (2018) 995–1005.
51. S.F.J. Hackett, R.M. Brydson, M.H. Gass, I. Harvey, A.D. Newman, K. Wilson, A.F. Lee, *Angew. Chem. Int. Ed.* 119 (2007) 8747–8750.
52. A.J. Plomp, H. Vuori, A.O.I. Krause, K.P. de Jong, J.H. Bitter, *Appl. Catal. A Gen.* 351 (2008) 9–15.
53. A. Giroir-Fendler, D. Richard, P. Gallezot, *Catal. Lett.* 5 (1990) 175–182.
54. F. Jiang, J. Cai, B. Liu, Y. Xu, X. Liu, *RSC Adv.* 6 (2016) 75541–75551.
55. X. Zhang, H. Shi, B.Q. Xu, *Angew. Chem. Int. Ed.* 44 (2005) 7132–7135.
56. N. Masoud, L. Delannoy, C. Calers, J.J. Gallet, F. Bournel, K.P. de Jong, C. Louis, P.E. de Jongh, *ChemCatChem* 9 (2017) 2418–2425.
57. H. Yi, H. Du, Y. Hu, H. Yan, H.L. Jiang, J. Lu, *ACS Catal.* 5 (2015) 2735–2739.

Supplementary Material

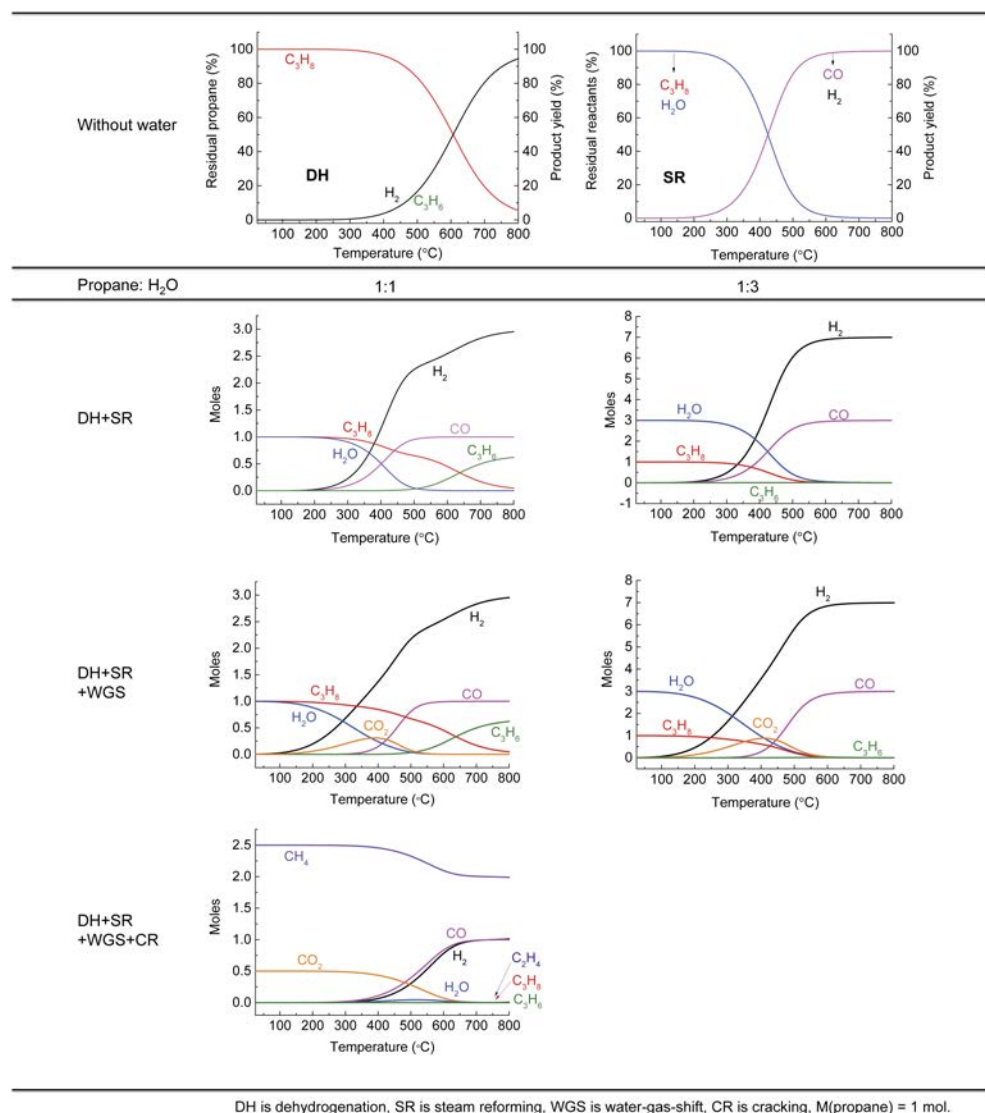


Fig. S5.1. Thermodynamic data of different reactions under different condition as a function of temperature under atmospheric pressure.

Fig. S5.1 presents the thermodynamic equilibrium for the dehydrogenation (DE), steam reforming (SR), water-gas-shift (WGS) and cracking (CR) reactions expected to occur under the applied experimental conditions. Clearly, temperatures higher than 400 °C and 300 °C are required for propane dehydrogenation and steam forming under atmospheric pressure, respectively, indicating that steam reforming is thermodynamically favored. When H₂O is

introduced, water starts to convert into H_2 at 150 °C as a result of SR and WGS and the conversion of water increases with the increasing of temperature until full conversion at 550 °C. WGS is favored over the temperature range of 150-400 °C, while dehydrogenation only occurs after the full consumption of steam. Increasing the amount of H_2O (propane: H_2O =1:3) in the feed does not significantly effect SR or WGS, but gives rise to complete inhibition of DE over whole temperature range.

Table S5.1. Summary of reported catalysts with high butene selectivity (S.).

Catalyst	Particle Size (nm)	[Buta] ^a : ^b [H ₂] ([Buta]:[Prop] ^b)	T (°C)	Buta C. ^c (%)	Butene S. (%)	ATOF ^d (s ⁻¹)	TOF (s ⁻¹)	Note
0.05Pd/ZrO ₂	Single atom	1:8 (1:10)	50	87	> 99	2.89	2.89	This work
0.05Pd/ZrO ₂	Single atom	1:8 (1:10)	30	41	> 99	1.32	1.32	This work
Pd ₁ /graphene	Single atom	1:2.5 (1:37)	47	95	100	0.35	0.35	[1]
ALD 30Al/Pd/Al ₂ O ₃	2.3	1:2.5 (1:37)	100	99	100	0.08	ND	[2]
Au ³⁺ /ZrO ₂	Single atom	1:45 (ND)	120	85	100	0.42	0.42	[3]
0.2Pt/m-Al ₂ O ₃ -H ₂	Single atom	1:8 (1:10)	50	93	100	0.12	0.12	[4]
Pt ₁ @Cu/Al ₂ O ₃	Single atom	1:16 (1:10)	50	27	100	0.01	0.01	[5]
Au/CNTs-1	3.2 ^e	1:72 (ND)	150	56	100	ND	0.14	[6]
Au3Ag1/SiO ₂	3.1	1:67 (1:100)	120	~35	100	ND	5.4*10 ⁻³	[7]

^a Buta: butadiene; ^b Prop: propene; ^c C.: conversion; ^d ATOF is the reaction rate without taking account of metal dispersion; ^e Particle size in nm was calculated through the equation: $d = 1.12 / D$. Where D is the metal dispersion.[8]

References

1. H. Yan, H. Cheng, H. Yi, Y. Lin, T. Yao, C. Wang, J. Li, S. Wei, J. Lu, *J. Am. Chem. Soc.* 137 (2015) 10484–10487.
2. H. Yi, H. Du, Y. Hu, H. Yan, H.L. Jiang, J. Lu, *ACS Catal.* 5 (2015) 2735–2739.
3. X. Zhang, H. Shi, B.Q. Xu, *Angew. Chem. Int. Ed.* 44 (2005) 7132–7135.
4. Z. Zhang, Y. Zhu, H. Asakura, B. Zhang, J. Zhang, M. Zhou, Y. Han, T. Tanaka, A. Wang, T. Zhang, N. Yan, *Nat. Commun.* 8 (2017) 16100.
5. F.R. Lucci, J. Liu, M.D. Marcinkowski, M. Yang, L.F. Allard, M. Flytzani-Stephanopoulos, E.C.H. Sykes, *Nat. Commun.* 6 (2015) 8550.
6. X. Zhang, Y.C. Guo, Z. Cheng Zhang, J. Sen Gao, C.M. Xu, *J. Catal.* 292 (2012) 213–226.
7. N. Masoud, L. Delannoy, C. Calers, J.J. Gallet, F. Bournel, K.P. de Jong, C. Louis, P.E. de Jongh, *ChemCatChem* 9 (2017) 2418–2425.
8. T. Lear, R. Marshall, J. Antonio Lopez-Sanchez, S.D. Jackson, T.M. Klapötke, M. Bäumer, G. Rupprechter, H.J. Freund, D. Lennon, *J. Chem. Phys.* 123 (2005) 174706–174719.

6

Summary and Outlook

6.1. Main Findings of this Research

Heterogeneous catalysis plays a central role in many chemical processes, such as petroleum refining, renewable energy production, medicine manufacturing, fine chemicals production and automotive exhaust treatment. The main task of heterogeneous catalysis scientists is to develop catalytic materials that exhibit high activity and selectivity towards the formation of desired reaction products and a long life-time in the targeted application. However, this is not an easy task as catalyst activity, selectivity and stability are controlled by various factors.

In **Chapter 1**, we briefly discussed the importance of heterogeneous catalysis, the effect of morphology on catalyst performance and provided some example of the causes of catalyst deactivation, including often-reversible coke formation and poisoning by impurities that can be removed by regeneration or pretreatment, as well as irreversible metal sintering and support deconstruction that should be prevented by using different strategies. Recently, Single Atom Catalysis (SAC) has become a very active new frontier in heterogeneous catalysis, not only because of the very promising performance shown by some of these SAC materials, but also because conceptually they fill the gap between homogeneous and heterogeneous catalysts. We also reviewed the fabrication, characterization, catalytic performance and high stability of SACs in various catalytic applications. In the different Chapters of this PhD Thesis, we have studied the effect of the choice of catalyst support, support modification as well as metal dispersion on the performance of metal oxide-supported, precious metal-based catalysts. In what follows, we will summarize the main findings of this research work.

In the last decades, the production of chemicals and transportation fuels from bio-based feedstock has emerged as a potential green alternative for fossil-derived materials and fuels. For example, hydrogen has received much attention as a clean and renewable energy carrier. Aqueous phase reforming (APR), initially developed and explored by the group of Dumesic and coworkers,[1–3] produces H_2 from biomass-derived oxygenates, such as sugar alcohols, dissolved in water and is considered rather effective given the relatively low reaction temperature used compared to the conventional steam reforming, and the associated lack of CO production and undesired substrate decomposition side-reactions. $Pt/\gamma-Al_2O_3$ has been commonly used as an APR catalyst, showing good activity, high H_2 selectivity and limited alkane formation. However, it has also been demonstrated that the alumina support can be attacked by water under typical APR conditions and transformed into crystalline boehmite.

In order to improve the catalyst stability in APR reactions of biomass-derived oxygenates, we studied a support modification strategy. More specifically, in **Chapter 2**, we reported that the hydrothermal stability of a Pt/Al_2O_3 catalyst in the APR of glycerol can be enhanced by support silylation, followed by calcination and reduction with tetraethylorthosilicate as silicon source. The APR of a 5% glycerol solution was selected as a model reaction and performed at 225 °C and 30 bar of He under semi-batch conditions, this approach allows for an initial assessment of activity and, upon catalyst recycling, possible catalyst deactivation. Catalyst characterization showed that silica deposition did not significantly alter the catalyst morphology, but resulted in a partial coverage of the active platinum phase. FT-IR spectra before and after

surface modification confirmed that Al-O-Si bonds are formed at the expense of specific surface Lewis acid sites of the alumina support, giving rise to the generation of Brønsted acid sites. The total acidity, however, was found to decrease upon surface modification. As a result of Brønsted acid site formation and partial Pt blockage, the catalytic activity for APR of glycerol, as evidenced by the H₂ production rates, decreased upon modification. Based on XRD, STEM, ²⁷Al NMR and TGA characterization of the (recycled) solid catalysts, silica modification effectively slowed down the support transformation process. An 8 h overcoating treatment ultimately increased the lifetime of the catalyst three times from 12 to 36 h compared to the non-modified catalyst. These results clearly show that silica deposition can considerably improve the stability of a Pt/Al₂O₃ APR catalyst in polar aqueous media (Fig. 6.1).

Catalytic hydrogenation of biomass-derived levulinic acid (LA) into γ -valerolactone (GVL) is also an important catalytic process in the field of catalysis for renewables. It has received much attention given the relative ease of LA synthesis and the manifold potential applications of GVL. However, previous work of our group showed that a Ru/TiO₂-P25 catalyst lost its catalytic activity upon recycling in LA hydrogenation at 150 °C under 30 bar H₂ in dioxane as solvent. The observed deactivation of the Ru/TiO₂-P25 catalyst was attributed to Ru surface coverage by reduced Ti species as demonstrated by aberration corrected scanning transmission electron microscopy (AC-STEM), a phenomenon which is known as Strong Metal Support Interaction (SMSI). It has been reported that the choice of the support oxide and solvent has a profound influence on catalyst performance in liquid-phase hydrogenation reactions. Therefore, in **Chapter 3**, we have examined the effect of the TiO₂ support type on Ru catalyst performance, in particular stability, under the same LA hydrogenation reaction conditions. Different titania supports, namely rutile, anatase and the mixture of these two phases (better known as TiO₂ P25) were selected as support oxides. A set of Ru/TiO₂ catalysts was prepared via a wet impregnation method, with similar metal loading and Ru particle size for fair comparison, and their stability assessed by multiple recycling runs under batch reactor conditions. The activity results demonstrated that the Ru/P25 and Ru/Anatase catalyst materials showed considerable loss of

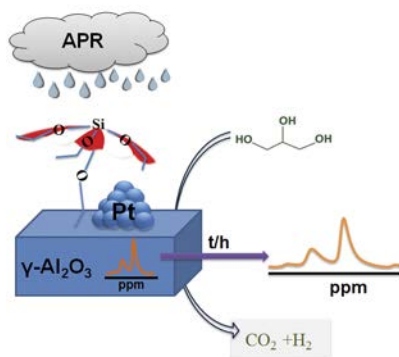


Fig. 6.1. Silica deposition of a Pt/Al₂O₃ aqueous phase reforming (APR) catalyst is an effective route to improve the overall catalyst stability in the APR reaction of glycerol.

activity upon recycling. In contrast, an initial activity increase was observed for the rutile-phase supported Ru catalyst (Fig. 6.2a). Characterization by TEM, TGA and FT-IR spectroscopy after CO adsorption demonstrated that the observed deactivation for (mixed) anatase supported catalysts could be attributed to SMSI rather than coke formation and metal sintering, with the rutile phase showing a better stability against this support oxide reduction. That the Ru/Rutile catalyst was highly stable was also demonstrated in a continuous flow reactor system, with this catalyst exhibiting the best performance over 3 days of time-on-stream. Notably, SMSI formation under the applied, relatively mild conditions only occurred in the presence of organic acids, such as LA or valeric acid, indicating that these acids play a key role in the encapsulation of the active metal phase (Fig. 6.2b). When water is used as solvent at 90 °C under 45 bar H_2 , all these three catalysts suffered activity losses to different extents. Characterization suggested that the acid-induced SMSI is limited or absent, but Ru sintering is observed for all three catalysts under study. These results clearly show that catalyst performance highly depends on the support structure and the solvent employed, and can provide useful information to select efficient catalysts for specific catalytic biomass conversion processes.

Recently, SAC, that is catalysis with solid materials containing single, isolated metal atoms as the active site, has developed into a new frontier in catalysis research due to the maximized atom efficiency of the supported metal and distinct catalytic performance in various reactions. Previously, we reported on a fully monoatomic Ru/ZrO₂ catalyst (at 1 wt.% metal loading), which was used for LA hydrogenation to GVL. No deactivation was observed for this Ru/ZrO₂ catalyst upon reuse and most of Ru single atoms survived the high temperature and pressure reaction conditions, suggesting them to be fairly stable. To follow up on this study, in **Chapter 4**, the structure, stability and performance of the Ru/ZrO₂ single atom catalyst was systemically investigated. A set of Ru/ZrO₂ catalysts with different loading (0.5-5 wt.%) was prepared by the same approach that previously gave a fully monoatomic 1 wt.% Ru/ZrO₂ (named as XRu-SAC, X is equal to metal loading). The structure of this SAC catalyst has been

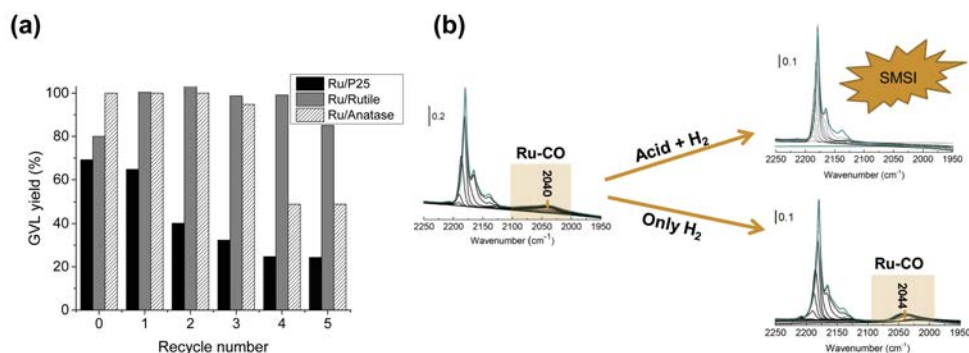


Fig. 6.2. (a) The yield of γ -valerolactone (GVL) as a function of recycling number in the catalytic hydrogenation of the biomass-derived levulinic acid (LA) and (b) organic acid plays a key role in the Strong Metal Support Interaction (SMSI) formation of TiO₂ support under mild liquid hydrogenation conditions.

studied with aberration-corrected HAADF-STEM, FT-IR spectroscopy after stepwise CO adsorption, Extended X-ray Absorption Fine Structure (EXAFS) and theoretical calculations. Catalyst characterization showed that the atomicity of these synthesized catalysts increased with decreasing metal loading, with the calcined 1Ru-SAC and reduced 0.5Ru-SAC materials being fully atomically dispersed. Temperature-resolved *in-situ* X-ray Absorption Spectroscopy (XAS) experiments confirm that the Ru SAC material showed good thermal stability in both O_2 and H_2 atmosphere at elevated temperature, whereas it can be reduced gradually to metallic Ru by CO. Remarkably, the Ru speciation in the 1 wt.% Ru SAC catalyst could be reversibly changed, from single atoms and small metallic Ru clusters to single atoms only by switching oxidation and reduction activation treatment. In contrast to the good stability of Ru SAC, a Ru nanoparticle-containing catalyst, synthesized for comparison, suffered from metal sintering and converted into a Ru/RuO₂ core-shell species after interacting with O_2 . In this Chapter, CO oxidation was employed as a probe reaction to investigate the catalytic performance of Ru-SAC materials. The $T_{50\%}$ (the temperature at which 50% of CO is converted) of 150 °C was 90 °C lower for the fully atomic dispersed Ru/ZrO₂ relative to its nanoparticle-containing counterpart (Fig. 6.3). Recycling tests further demonstrated that Ru SAC is highly resistant to deactivation under a strongly oxidizing environment.

Supported Pt and Pd catalysts have been widely used in different types of chemical reactions. In Chapter 5, we have further extended our research on SAC materials to also include Pt and Pd as supported single atoms. Aberration-corrected HAADF-STEM and FT-IR spectroscopy after CO adsorption showed that large amounts of isolated metal atoms were present in 1 wt.% catalysts and the atomicity of these catalysts increased with decreasing metal loading. Fully mono-atomically dispersed catalysts were obtained at 0.05 and 0.1 wt.% for Pt and Pd, respectively. The influence of atomicity on catalyst performance was probed in oxidation, dehydrogenation and hydrogenation reactions. Both the Pd/ZrO₂ and Pt/ZrO₂ catalysts exhibited only a moderate ability to produce propene via propane dehydrogenation, regardless of differences in dispersion

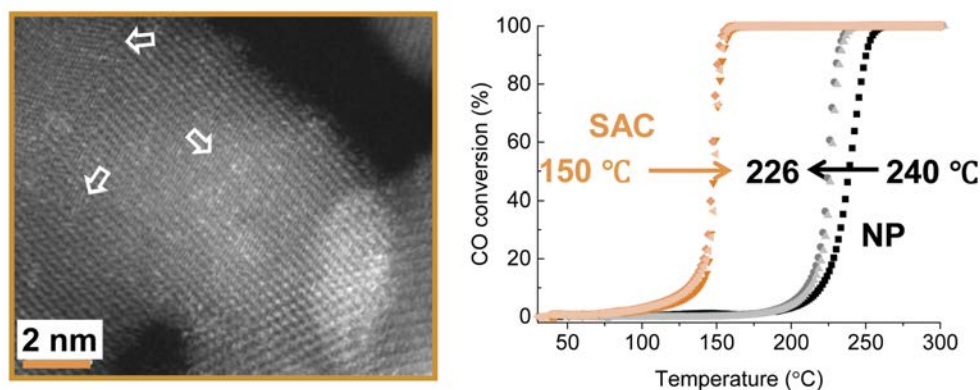


Fig. 6.3. Ru-based ZrO₂-supported Single Atom Catalyst (SAC) material and its excellent catalytic performance in CO oxidation. The $T_{50\%}$ (i.e., the temperature at which 50% of CO is converted) is lowered by 90 °C to 150 °C for the SAC Ru/ZrO₂ system with respect to its nanometric counterpart.

of the fresh catalyst. In contrast, the results demonstrated that Pd and Pt showed a higher activity in CO oxidation when present as supported single atoms (Fig. 6.4a). The degree of metal dispersion also proved to be the key to catalyst performance in both gas-phase and liquid-phase hydrogenation reactions. An increase in turnover frequency of around three-fold and six-fold is observed in cinnamaldehyde and 1,3-butadiene hydrogenation, respectively, when comparing solid catalysts containing (some) metal nanoparticles with fully atomically dispersed catalysts. Notably, for cinnamaldehyde hydrogenation, the turnover frequency was found to be independent from metal loading, for the SACs. Overall, the Pd materials outperformed the Pt counterparts in all targeted catalytic reactions. In CO oxidation, the $T_{50\%}$ of Pd/ZrO₂ is at least 30 °C lower when compared to that of Pt/ZrO₂. In addition, while the Pt-based SAC is unable to catalyze cinnamaldehyde hydrogenation and exhibited poor reactivity as well as low selectivity in butadiene hydrogenation, Pd-based catalysts showed good to excellent performance in both the gas phase and liquid phase hydrogenation reactions. In particular worth noting is the catalytic performance of the 0.05 wt.% Pd/ZrO₂ catalyst. This system shows a remarkable performance in the semi-hydrogenation of 1,3-butadiene as impurity in a propene-rich steam, combining the highest activity reported so far, with an excellent butene selectivity and stability over 60 h time-on-stream (Fig. 6.4b).

6.2. Some Perspectives on Future Research

In this PhD thesis, we study the effect of choice of catalyst support, support modification and metal dispersion on the performance of metal oxide supported catalysts. Based on catalyst performance in a range of reactions and catalyst characterization results, insights are gained into the structure-activity relationships governing these reactions, which can aid further



Fig. 6.4. (a) A Pd/ZrO₂ Single Atom Catalyst (SAC) showed good to excellent performance in various reactions and (b) excellent long-term stability of Pd/ZrO₂ SAC in selective butadiene hydrogenation in a propene-rich steam.

development of stable catalysts for targeted applications. However, more effort regarding catalyst synthesis optimization, the investigation of reaction mechanisms and the exploration of new applications is still needed.

Catalyst synthesis improvement. Fabrication of single atom catalysts (SAC) via conventional wet approaches is very attractive due to the simplicity of the preparation process. However, given the limited anchoring sites that play a key role in stabilizing single atoms of the supports, it is often difficult to synthesize SACs with high loadings via classical wet chemical synthesis approaches. This may hamper their practical application and as well as the structural and mechanistic studies.[4] Indeed, in Chapter 5 of this thesis, it is found that fully atomic dispersed Pt and Pd/ZrO₂ (monoclinic) catalysts prepared via a conventional wet impregnation approach could be only achieved at very low metal loading (0.1 wt.% and the below). Such low metal loadings make it difficult to get insight into the catalyst structure using techniques such as XAS. In order to solve this problem, further work can employ the oxides with abundant anchoring sites to prepare high weight loading SAC. It also requires more detailed investigations on the synthesis of defect-rich support oxides as well as characterization protocols to investigate defects within support oxides.

Support pre-treatment has been explored as a useful strategy to alter the properties of a given oxide matrix. For example, defect sites which can serve as anchoring sites to stabilize isolated metal atoms in reducible oxides, such as TiO₂, can be generated by high temperature reduction, chemical reduction or UV irradiation. Likewise, a recent study demonstrated that a ZrO₂ (monoclinic) support, normally considered as non-reducible support, rich in oxygen vacancies or surface defects could be generated after magnesiothermic reduction in H₂/Ar atmosphere.[5] Therefore, further studies could make use of this modified ZrO₂ material as a useful support to fabricate higher loadings of Pt and Pd/ZrO₂ SAC via our synthesis approach. The defects generated by the magnesiothermic reduction pretreatment process could help to stabilize single precious metal atoms on the ZrO₂ surface even at high metal loading.

Reaction mechanism investigations. In addition to the synthesis of high loading SAC, another challenge remaining in single atom catalysis is get detailed insight into catalytic pathways operating with atomically dispersed catalysts, knowledge which would provide useful information for the rational design of stable and efficient catalysts. In Chapters 4 and 5, it was observed that the noble metal loaded ZrO₂ SACs were very active in CO oxidation. Conventional supported nanoparticle-based Pt group metals used for CO oxidation are thought to operate via a Langmuir-Hinshelwood (L-H) mechanism in which the reaction takes place between chemisorbed reagents.[6] Previous studies show that the mechanism of CO oxidation on SAC is different from that of nanoparticle containing catalysts, and may as well be for other similar reactions that operate via an L-H mechanism on classical catalysts (e.g. the water gas shift reaction). CO oxidation on SAC is thought to operate via a modified L-H mechanism, i.e. O₂ and CO are adsorbed on one isolated metal atom rather than two adjacent neighboring atoms of metal clusters, forming a CO₃-single metal atom intermediate before CO₂ liberation.[7] The results described in this PhD thesis do not yet allow for the exact mechanism of ZrO₂ SAC catalyzed CO oxidation to be established. Further investigation using *in-situ* or *operando*

techniques, complemented by kinetic studies and theoretical calculations, could further address this. In fact, *in-situ* Diffuse Reflectance Infrared Fourier Transform Spectroscopy (DRIFT)[7] and *operando* X-ray Absorption Spectroscopy[8] have previously been successfully used to confirm the role of active sites and intermediates formation during the SAC catalyzed CO oxidation reaction.

New applications. Single atom catalysts are highly active in numerous reactions as discussed in chapter 1. In this PhD thesis, the catalytic performance of fabricated ZrO_2 SAC family indeed showed nice performance in CO oxidation, hydrogenation reactions in both gas and liquid phases. But there is still room left to explore new applications of industrial importance. For example, liquid oxidation is one of the most important transformations in organic synthesis and the aerobic oxidation of biomass-derived alcohols, such as polyols, 5-hydroxymethylfurfural and various sugars, to the corresponding aldehyde and carboxylic acid has received growing attention as it provides a green route for the synthesis of value-added chemicals.[9] Ru-based nanoparticle-containing catalysts have been reported to exhibit good performance for these kind of reactions and could tolerate diverse functional groups.[10,11] Such aerobic oxidation of alcohols has not yet been reported for Ru SAC. Promisingly, in Chapter 4, it has been demonstrated that our Ru SAC system was indeed more active and stable than its nanoparticle-based counterpart under net oxidizing conditions. The Ru SAC reported in this thesis could therefore also be explored in the aerobic oxidation of alcohols reactions in future studies.

References

1. R.D. Cortright, R.R. Davda, J.A. Dumesic, *Nature* 418 (2002) 964–967.
2. R.R. Davda, J.A. Dumesic, *Chem. Commun.* 10 (2004) 36–37.
3. D.M. Alonso, J.Q. Bond, J.A. Dumesic, *Green Chem.* 12 (2010) 1493–1513.
4. P. Liu, Y. Zhao, R. Qin, S. Mo, G. Chen, L. Gu, D.M. Chevrier, P. Zhang, Q. Guo, D. Zang, B. Wu, G. Fu, N. Zheng, *Science* 352 (2016) 797–800.
5. A. Sinhamahapatra, J.P. Jeon, J. Kang, B. Han, J.S. Yu, *Sci. Rep.* 6 (2016) 27218–27226.
6. R.J. Baxter, P. Hu, J. *Chem. Phys.* 116 (2002) 4379–4381.
7. M. Moses-Debusk, M. Yoon, L.F. Allard, D.R. Mullins, Z. Wu, X. Yang, G. Veith, G.M. Stocks, C.K. Narula, *J. Am. Chem. Soc.* 135 (2013) 12634–12645.
8. M.A. Newton, D. Ferri, G. Smolentsev, V. Marchionni, M. Nachtegaal, *Nat. Commun.* 6 (2015) 8675–8681.
9. S.E. Davis, M.S. Ide, R.J. Davis, *Green Chem.* 15 (2013) 17–45.
10. D.S. Mannel, S.S. Stahl, T.W. Root, *Org. Process Res. Dev.* 18 (2014) 1503–1508.
11. B.Z. Zhan, M.A. White, T.K. Sham, J.A. Pincock, R.J. Doucet, K.V.R. Rao, K.N. Robertson, T.S. Cameron, *J. Am. Chem. Soc.* 125 (2003) 2195–2199.



Nederlandse Samenvatting

List of Publications

Acknowledgements

Curriculum Vitae

Samenvatting in het Nederlands

Heterogene katalyse speelt een centrale rol in veel chemische processen, waaronder olieraffinage, het zuiveren van uitlaatgassen, en in de productie van bulk- en fijnchemicaliën, medicijnen, en hernieuwbare energiedragers. De belangrijkste taak van onderzoekers op het gebied van heterogene katalyse is het ontwikkelen van nieuwe katalytische materialen met een hoge activiteit en selectiviteit voor de gewenste producten en een lange levensduur. Dit is echter geen makkelijke taak omdat katalytische activiteit, selectiviteit en stabiliteit door verschillende factoren worden bepaald. In dit proefschrift is onderzoek gedaan naar een specifieke categorie heterogene katalysatoren, materialen waarbij een katalytisch actieve metaalcomponent afgezet wordt op een dragermateriaal. Daarbij is gekeken naar het effect van de keuze van de soort dragermateriaal en modificatie daarvan op katalytische stabiliteit en naar het effect van deeltjesgrootte van de metaalcomponent op katalytische activiteit en selectiviteit.

Hoofdstuk 1 beschrijft eerst het belang van heterogene katalyse, het effect van morfologie op de werking van de katalysator, en enkele voorbeelden van manieren van deactiveren van een katalysator. Hieronder vallen de (vaak reversibele) vorming van koolstofafzettingen, en vergiftiging door onzuiverheden, oorzaken van deactivering die kunnen worden verholpen door regeneratie of voorbehandeling. Ook worden irreversibele processen als metaal-*sintering* en de afbraak van het dragermateriaal beschreven. Deze moeten worden voorkomen met andere strategieën. Een nieuw onderzoeksveld in de heterogene katalyse is katalyse door één enkel, geïsoleerd atoom, in het Engels *Single Atom Catalysis* (SAC) genoemd. De interesse in dit nieuwe onderzoeksveld komt niet alleen door de hoge activiteit die deze SAC-materialen laten zien, maar ook omdat ze een conceptuele brug vormen tussen de homogene en heterogene katalyse. Een kort overzicht van de recente literatuur over SACs is gegeven, waarin het maken, de karakterisering, de katalytische werking en de hoge stabiliteit van SACs in verschillende katalytische processen worden beschreven.

In de afgelopen decennia is de productie van chemicaliën en brandstoffen uit biomassa naar voren getreden als een groen alternatief voor fossiele materialen en grondstoffen. Een voorbeeld van een product dat uit biomassa verkregen kan worden is waterstof, een schone en vernieuwbare energiedrager. Waterstof kan bijvoorbeeld worden gemaakt uit zuurstofhoudende organische moleculen zoals suikeralcoholen. Opgelost in water kunnen suikeralkoholen door middel van het zogeheten *Aqueous phase reforming* (APR) process omgezet worden in waterstof. Het APR process is oorspronkelijk ontwikkeld en onderzocht door de onderzoeksgroep van Dumesic [1–3]. APR is vrij efficiënt, gezien de relatief lage reactietemperatuur ten opzichte van het meer gebruikelijke stoom-*reforming*. Ook treden er weinig ongewenste zijreacties op, zoals de productie van CO of het ongecontroleerd verlies van het substraatmateriaal. Een Pt/g-Al₂O₃ katalysator wordt vaak gebruikt als APR-katalysator, gezien de hoge activiteit, hoge H₂ selectiviteit en lage alkaanvorming, die deze katalysator laat zien. Echter is ook aangetoond dat de aluminadrager niet stabiel is en kan worden aangetast door water onder APR condities, waardoor het kristallijne boehmiet wordt gevormd.



Om de stabiliteit van de katalysator in APR reacties te verhogen, hebben we een strategie onderzocht om het dragermateriaal te modificeren. In **Hoofdstuk 2** beschrijven we hoe de hydrothermale stabiliteit van Pt/Al₂O₃ in de APR van glycerol kan worden verbeterd door silylering van het dragermateriaal, met tetraethylorthosilicaat als bron van silicium, gevolgd door calcinatie en reductie. APR van een 5% glyceroloplossing werd gekozen als modelreactie, bij 225 °C en 30 bar He onder *semi-batch* condities. Op deze manier kan niet alleen de initiële activiteit van de katalysator worden bestudeerd, maar ook de eventuele deactivering van de katalysator na hergebruik. Uit karakterisering van de katalysator blijkt dat de afzetting van silica geen groot effect heeft op de morfologie van de katalysator. Echter wordt het actieve platina wel deels bedekt. FT-IR spectra van het materiaal voor en na modificatie van het oppervlak bevestigen dat Al-O-Si bindingen zijn gevormd ten koste van specifieke Lewiszuurcentra op het aluminaoppervlak. Hierdoor worden nieuwe Brønsted zure plaatsen gevormd. De totale zuurheid van het materiaal daalt als gevolg van de oppervlaktemodificatie. Als gevolg van het vormen van Brønsted zure plaatsen en de gedeeltelijke blokkering van het Pt metaal, daalt de katalytische activiteit voor APR van glycerol, wat blijkt uit een afname van de snelheid van H₂ productie. Op basis van XRD, STEM, ²⁷Al NMR en TGA karakterisering van de (hergebruikte) vaste katalysatoren, is vastgesteld dat de omvorming van het dragermateriaal langzamer gaat wanneer het gemodificeerd is met silica. Een behandeling van 8 uur voor het afzetten van een silicaaagje verlengt de levensduur van de katalysator met een factor drie, van 12 tot 36 uur. Deze resultaten laten duidelijk zien dat de afzetting van silica de stabiliteit van de Pt/Al₂O₃ in waterige oplossingen aanzienlijk kan verhogen (Fig. 1).

We hebben ook de omzetting van levulinezuur (Engels: *levulinic acid*, LA) naar γ -valerolacton (GVL) bestudeerd. Dit is een belangrijke reactie, omdat LA vrij eenvoudig uit biomassa kan worden gemaakt en GVL vele mogelijke toepassingen heeft. Echter is uit eerder onderzoek in onze onderzoeksgroep gebleken dat een Ru/TiO₂-P₂₅-katalysator voor deze reactie deactiveerde na hergebruik in LA hydrogenatie bij 150 °C en onder 30 bar H₂ in dioxaan als oplosmiddel. Het proces van deactivering van de Ru/TiO₂-P₂₅-katalysator werd onderzocht met aberratie-

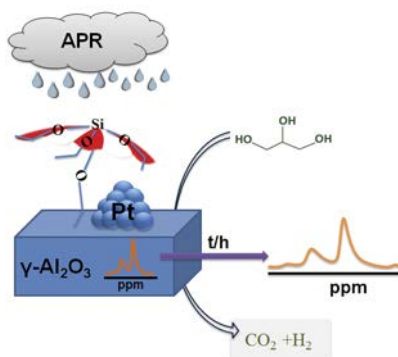


Fig. 1. Afzetting van silica op een Pt/Al₂O₃ *aqueous phase reforming* (APR) katalysator is een effectieve manier om de stabiliteit van de katalysator te verhogen in de APR reactie van glycerol.

gecorrigeerde *scanning* transmissie elektronenmicroscopie (AC-STEM). Hieruit bleek dat het Ru oppervlak werd bedekt met gereduceerde Ti verbindingen. Deze sterke interactie tussen de drager en het metaal staat in het Engels bekend als *Strong Metal Support Interaction* (SMSI).

Het is bekend dat de keuze van het dragermateriaal en oplosmiddel een grote invloed hebben op de activiteit van de katalysator in hydrogenatiereacties in vloeistoffase. In **Hoofdstuk 3** bestuderen we daarom het effect van het type TiO_2 -drager op de werking van de Ru katalysator, in het bijzonder de stabiliteit, onder dezelfde reactiecondities van LA hydrogenatie. Drie verschillende titaniadragers werden onderzocht, namelijk rutiel, anataas en een mengsel van deze twee fasen (beter bekend als TiO_2 -P25). Een set Ru/ TiO_2 -katalysatoren werd gemaakt via de zogenaamde natte-impregnatiemethode, met vergelijkbaar metaalgehalte en Ru deeltjesgrootte. De stabiliteit van de katalysatoren werd vastgesteld door iedere katalysator meerdere malen te testen in een batchreactor. Uit de verkregen resultaten blijkt dat de activiteit van de Ru/P25- en Ru/anataaskatalysatoren sterk daalt bij hergebruik. Daarentegen werd een initiële stijging in activiteit geobserveerd voor de Ru/rutieltkatalysator (Fig. 2a). Karakterisering met TEM, TGA en FT-IR spectroscopie na CO adsorptie liet zien dat de geobserveerde deactivatie voor katalysatoren op (gemengde) anataasdragers toegeschreven kan worden aan SMSI, en niet aan de vorming van koolstofafzettingen of metaal-sintering. De rutiefase vertoonde een hogere stabiliteit tegen de reductie van het dragermateriaal. De hoge stabiliteit van de Ru/rutieltkatalysator werd ook aangetoond in een stroomreactor, waar deze katalysator de beste werking vertoonde gedurende een experiment van drie dagen. Ook werd gezien dat, onder deze relatief milde reactieomstandigheden, het proces van SMSI alleen plaatsvond in aanwezigheid van organische zuren, zoals LA of valeriaanzuur. Hieruit blijkt dat deze zuren een belangrijke rol spelen in de inkapseling van de actieve metaalfase (Fig. 2b). Wanneer water gebruikt wordt als oplosmiddel bij 90 °C onder 45 bar H_2 , vertonen alle drie katalysatoren een verlies in activiteit van verschillende omvang. Karakteriseringsstudies tonen aan dat zuurgeïnduceerde SMSI niet of nauwelijks plaatsvindt, maar voor alle drie katalysatoren wordt Ru-sintering geobserveerd. Deze

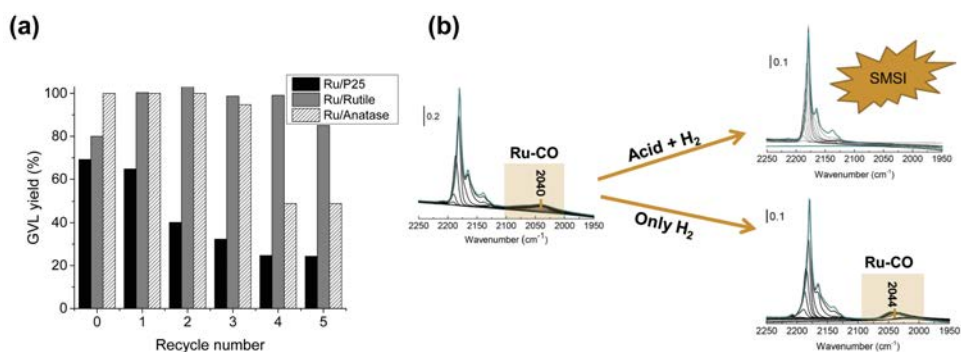


Fig. 2. (a) De opbrengst van γ -valerolacton (GVL) als functie van het aantal reactiecycli in de katalytische hydrogenatie van levulinezuur (LA) uit biomassa. (b) Organische zuren spelen een belangrijke rol in de modificatie van TiO_2 -dragers door middel van sterke interacties tussen metaal en dragermateriaal (SMSI) onder milde hydrogenatiecondities in de vloeistoffase.

resultaten laten duidelijk zien dat de werking van een katalysator dus sterk afhankelijk is van de structuur van het dragermateriaal en van het gebruikte oplosmiddel. Deze informatie kan worden gebruikt om efficiënte katalysatoren te selecteren voor specifieke katalytische processen voor de conversie van biomassa of afvalstromen.

Een nieuwe ontwikkeling in het katalyseonderzoek is SAC, katalyse door vaste stoffen met enkele, geïsoleerde metaalatomen als actieve centra. Grote voordelen van SAC zijn de zeer hoge atomefficiëntie van het metaal en de bijzonder goede katalytische werking in verschillende reacties. We hebben eerder een monoatomaire Ru/ZrO₂-katalysator bestudeerd (met 1 % massa metaal). Deze werd gebruikt voor de hydrogenatie van LA tot GVL. Er werd geen deactivering geobserveerd bij hergebruik en het grootste deel van de Ru atomen bleef apart bij de hoge temperatuur en druk tijdens de reactie, wat impliceert dat ze vrij stabiel zijn. Als vervolg op deze studie, is in Hoofdstuk 4 de structuur, stabiliteit en werking van de Ru/ZrO₂-katalysator met enkele, geïsoleerde atomen systematisch onderzocht. Ru/ZrO₂-katalysatoren met verschillende hoeveelheden metaal werden gemaakt met dezelfde methode die eerder de volledig monoatomaire 1 % massa Ru/ZrO₂-katalysator gaf. Katalysatoren werden gemaakt met 0.5-5 % massa Ru, genaamd XRu-SAC, waarbij X de hoeveelheid metaal is. De structuur van deze SAC katalysatoren werd bestudeerd met aberratie-gecorrigeerde HAADF-STEM, FT-IR spectroscopie na stapsgewijze CO adsorptie, theoretische berekeningen en EXAFS (waarbij de fijnstructuur in het röntgenabsorptiespectrum wordt geanalyseerd). Uit karakterisering bleek dat katalysatoren met lagere hoeveelheden metaal een hogere fractie losse atomen bevatten. De gecalcineerde 1Ru-SAC- en gereduceerde 0.5Ru-SAC-materialen bevatten enkel losse Ru atomen. *In situ* röntgenabsorptiespectroscopiemetingen (XAS) bij verschillende temperaturen bevestigen dat het Ru SAC-materiaal een hoge thermische stabiliteit heeft in zowel O₂ als H₂ atmosfeer bij hoge temperatuur, terwijl het langzaam kan worden gereduceerd tot metallisch Ru door CO. Met behulp van een reductieve activatiebehandeling kunnen de afzonderlijke Ru atomen in de SAC-katalysator met 1 massaprocent Ru worden omgezet in kleine metallische Ru clusters. Opmerkelijk genoeg is dit proces reversibel: bij een oxidatieve behandeling worden de metaalclusters weer omgezet in losse metaalatomen. In tegenstelling tot de goede stabiliteit van Ru SAC, is een katalysator met Ru nanodeeltjes gevoelig voor metaal-*sintering*. In dit geval werden na interactie met O₂ Ru/RuO₂ kern-schilnanodeeltjes gevormd. In dit hoofdstuk is CO-oxidatie gebruikt als een testreactie om de katalytische werking van Ru SAC-materialen te onderzoeken. De T_{50%} (de temperatuur waarbij 50% van CO is omgezet) van 150 °C voor de volledig mono-atomaire Ru/ZrO₂ was 90 °C lager dan voor de katalysator met nanodeeltjes (Fig. 3). Hergebruiktests lieten ook zien dat Ru SAC zeer resistent is tegen deactivatie onder sterk oxiderende omstandigheden.

Katalysatoren met Pt en Pd op een dragermateriaal worden veel gebruikt in verschillende soorten chemische reacties. In Hoofdstuk 5 hebben we ons onderzoek naar SAC materialen verder uitgebreid naar Pt en Pd als losse atomen op het dragermateriaal ZrO₂. Aberratie-gecorrigeerde HAADF-TEM en FT-IR spectroscopie na CO adsorptie tonen aan dat grote aantallen geïsoleerde metaalatomen aanwezig zijn in katalysatoren met een 1% massabelading van het edelmetaal. De fractie losse atomen neemt toe met afnemende hoeveelheden metaal.

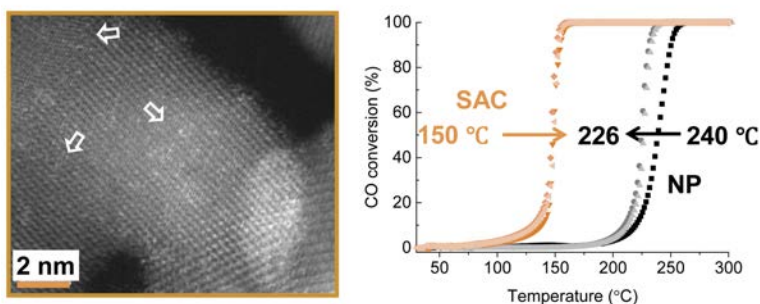


Fig. 3. Een katalysator met losse Ru atomen (SAC) op een ZrO_2 drager. De uitstekende katalytische werking in de CO oxidatiereactie. De $T_{50\%}$ (de temperatuur waarbij 50% van de CO is omgezet) daalt met 90 °C tot 150 °C als Ru nanodeeltjes worden vervangen door losse atomen.

Volledig monoatomaire katalysatoren werden verkregen voor respectievelijk 0.05 en 0.1 % Pt en Pd. De invloed van de fractie losse atomen op katalytische werking werd onderzocht in oxidatie-, dehydrogenatie- en hydrogenatiereacties. Zowel de Pd/ZrO_2 - als de Pt/ZrO_2 -katalysatoren vertonen een matig vermogen om propaan te produceren via propaandehydrogenatie, onafhankelijk van hoe fijnverdeeld de metalen zijn in de verse katalysator. Pd en Pt vertonen echter een hogere activiteit in CO-oxidatie wanneer de metalen aanwezig zijn als losse atomen op een drager (Fig. 4a). De fractie van losse metaalatomen bleek cruciaal voor de werking van de katalysator voor hydrogenatiereacties in zowel gasfase als vloeistoffase. Een drievoudige en zesvoudige toename in omzettingfrequentie werd gezien in de hydrogenatie van respectievelijk cinnamaldehyde en 1,3-butadien, voor vaste katalysatoren met enkel losse metaalatomen ten opzichte van katalysatoren waarbij het metaal (deels) aanwezig is als nanodeeltjes. De omzettingfrequentie van cinnamaldehyde blijkt ook onafhankelijk van de totale

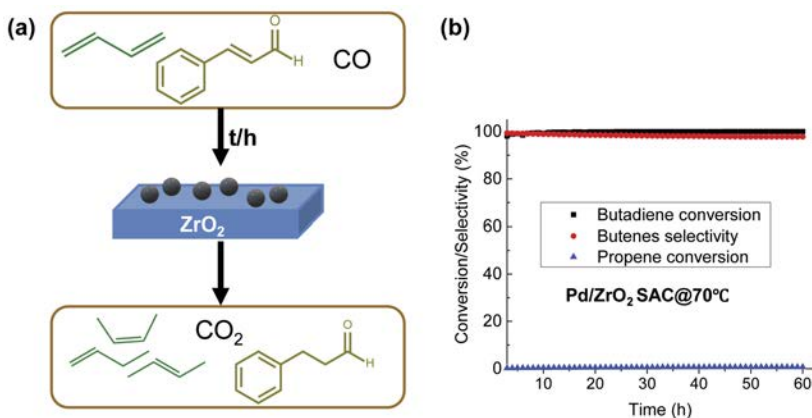


Fig. 4. (a) Een Pd/ZrO_2 -katalysator met afzonderlijke atomen (SAC) vertoont goede tot uitstekende werking in verschillende reacties. (b) De uitzonderlijke langetermijnstabiliteit van Pd/ZrO_2 SAC in de selectieve hydrogenering van butadien in een propenrijke stroom.

hoeveelheid metaal voor SACs. Katalysatoren met Pd waren effectiever dan materialen met Pt voor alle geteste katalytische reacties. In de CO-oxidatiereactie was de T_{50} van Pd/ZrO₂ meer dan 30 °C lager dan die van Pt/ZrO₂. Terwijl de Pt-SAC de hydrogenatie van cinnamaldehyde niet kon katalyseren en een lage reactiviteit en selectiviteit had in de hydrogenering van butadieen, vertoonden de Pd-katalysatoren goede tot uitstekende werking in hydrogenatiereacties in zowel de gas- als vloeistoffase. In het bijzonder verdient de katalytische werking van de 0.05 % massa Pd/ZrO₂-katalysator aandacht. Dit systeem vertoont opmerkelijke activiteit in de semi-hydrogenatie van 1,3-butadieen in een propenrijke stroom en combineert daarmee de hoogste activiteit tot dusverre beschreven met een uitstekende selectiviteit voor buteen en hoge stabiliteit gedurende een experiment van 60 uur (Fig. 4b).

List of Publications and Presentations

Publications

Fang Liu, Chukwuemeka Okolie, Ryan M. Ravenelle, John C. Crittenden, Carsten Sievers, Pieter C.A. Bruijninx, Bert M. Weckhuysen. "Silica Deposition as an Approach for Improving the Hydrothermal Stability of an Alumina Support During Glycerol Aqueous Phase Reforming" *Appl. Catal. A Gen.*, **2018**, 551, 13-22.

Ho Viet Thang, Sergio Tosoni, Fang Liu, Pieter C.A. Bruijninx, Gianfranco Pacchioni. "Nature of Sintering- Resistant, Single- Atom Ru Species Dispersed on Zirconia- Based Catalysts: A DFT and FTIR Study of CO Adsorption". *ChemCatChem*, **2018**, 10, 2634-2645.

Dilek Boga, Fang Liu, Pieter C.A. Bruijninx, Bert M. Weckhuysen. "Aqueous-Phase Reforming of Crude Glycerol-Effect of Impurities on Hydrogen Production" *Catal. Sci. Technol.*, **2016**, 6, 134-143.

Fang Liu, Jamal Ftouni, Pieter C.A. Bruijninx, Bert M. Weckhuysen. "Phase-Dependent Stability and Substrate-Induced Deactivation by Strong Metal-Support Interaction of Ru/TiO₂ Catalysts for the Hydrogenation of Levulinic Acid", *in preparation*.

Fang Liu, Herrick Schaink, Ad van der Eerden, Ramon Oord, Bert M. Weckhuysen, Pieter C.A. Bruijninx. "A Highly Stable Ru/ZrO₂ Single Atom Catalyst: Structure, Genesis, Stability and Application in CO Oxidation", *in preparation*.

Oral Presentations

Fang Liu, Jamal Ftouni, Homer Genuino, Li Lu, Christopher J. Kiely, Bert M. Weckhuysen, Pieter C.A. Bruijninx. "Genesis, Structure and Stability of Single Atom M/ZrO₂ catalysts and Their Application in Catalytic Oxidation and Hydrogenation". 18th Netherlands' Catalysis and Chemistry Conference (NCCC), Noordwijkerhout, the Netherlands, 2018.

Fang Liu, Jamal Ftouni, Pieter C.A. Bruijninx, Bert M. Weckhuysen. "On the Stability and Deactivation of Ru/TiO₂ Catalysts in Hydrogenation of Levulinic Acid". 13th European Congress on Catalysis (EUROPACAT), Florence, Italy, 2017.

Fang Liu, Dilek Boga, Chukwuemeka Okolie, Carsten Sievers, Pieter C.A. Bruijninx, Bert M. Weckhuysen. "Aqueous Phase Reforming of Pure and Crude Glycerol: Catalyst Stability and Deactivation Studies". 16th Netherlands' Catalysis and Chemistry Conference (NCCC), Noordwijkerhout, the Netherlands, 2016.



Acknowledgements

September 26th, 2013 I landed in Schiphol and started my first morning in the Netherlands. It is never easy to adapt to a completely new culture and living environment. I still remember that at that time, I was a shy and quiet girl. After a 5 years' study in the Inorganic Chemistry and Catalysis group of Utrecht University, I've grown into an open and sonsy person. Now my amazing journey in the Netherlands is nearly finishing. I appreciate all the kind people I met in Holland and thank them for their help, support and company.

I would like to first thank my supervisor Prof. Bert Weckhuysen for giving me the opportunity to conduct my PhD in such a great and international research group. I want to thank you for sharing your knowledge through the meetings. Especially in the final year, your constructive feedback pointed out a clear direction to me on the structure build-up of my thesis, which has been invaluable for finalizing the document.

I also want to particularly thank my daily supervisor Prof. Pieter Bruijninx. Pieter, I am so lucky to have you as my daily supervisor. I understand it is not an easy job to guide a shy Chinese PhD student, but you are always so patient, kind and willing to offer help. Your keen insight and detailed guidance allow me to grow immensely into an independent researcher, writer and presenter.

Oscar, Fouad, Pascal, Marjan, Ad (Mens), Hans and Jan Willem; thank you all to maintain the good research atmosphere in the lab. None of my work would be possible without your help. Dymph, many thanks for your patient help in arranging documents, forwarding emails and many more. Also, I would like to show my great sincere gratitude to Ad (van de Eerden), Herrick, Ramon, Rolf and Miguel. Thank you all for helping me with experimenting, data analysis and sharing your knowledge with me.

The majority of my working time has been spent in the biomass lab and high-pressure lab. Chris, Ana, Khaled, Homer, Beatriz, Egor, Robin, Frank, Miguel, Nono, Carolien and Wirawan, thanks a lot for sharing the chemicals and working space with me. Also, I would like to thank Ara and Laura for their helping to start my experiments in my first year.

In the past years, I have spent a lot of grateful times with my friends and colleagues. First up is our VIP lunch and the fifth-floor group members, Sandra, Sang-Ho, Pasi, Ivan, Özgün, Nono, Tao, Thomas, Donglong, Pierre, Yann, Jamal, Abishek, Gareth, Bo (Feng) and Joel. I will remember all the dinners and parties, weekly cakes we had together. Sandra and Donglong, special thanks to you for taking the responsibility being my paranymphs. Also, I really appreciate the precious time I spent with our baking group team members, Nazila, Lisette, Iris (and Sandra), I did enjoy our sweet time and those delicious cakes we made together. Heba, Ru-Pan, Jose, Marte, Ahmed, Ties and Federica, thanks a lot for your encouragement and company in the last phase of my

PhD period. I feel so relaxing and was refreshed after talking with you. I would like to give a special thanks to Marte for perfectly translating my English summary into Dutch.

I shared many great times with the following people at lunch, coffee breaks, borrels, labuitjes and parties: Anne-Eva, Baira, Carlos, Charlotte, Dilek, Ilse, Jelle, Jeroen, Jessi, Jogchum (Oenema), Jochem (Wijten), Joris, Jovana, Katinka, Koen, Katarína, Lars, Leila, Laurens, Lennart, Matthias, Marisol, Marjolein, Mark, Nynke, Paul, Pengfei, Peter, Remco, Rogier, Rosa, Roxanna, Sam, Sander, Stanislav, Suzanne, Silvia, Thomas (Hartman), Tom (van Deelen), Wouter, Ying and Zoran.

My special thanks to Elena, Joe, Roy, Fiona, Jamal, Robin and Pieter. Thanks a lot for your help with my job search.

五年前，尤得知自己被公派录取的深夜，辗转反侧，不知道自己在陌生的荷兰会有着怎么样的境遇。所幸一路走来，一直被暖暖的热心和关爱所包裹。在准备出国之前，张少辉师兄一直耐心的指导我如何办理各种繁琐的手续，事无巨细的回答整理行装的问题。到荷兰最初的几个月也一直帮助我适应环境，带我参加各种社交活动。感谢罗文豪师兄在我到来第一天带我参观实验室，感谢博洋师兄，王刚师兄在学习，NIOK考试以及生活中给予的帮助。

Warande 89 号，至今在我看来都是一个神奇和充满温暖回忆的地方。不知是系统故意安排还是冥冥之中注定，我们一个公寓内都是中国人。朝文，小D，晓臣，Tim，还有同一届来的茂哥，波波，玉珑，张浩，杨欣，施杰，瑞学，郭勇，陈晨，纪元，宏凯。大家互相切磋厨艺，一起出行采购，共同努力学习新技能。这份热闹冲淡了乡愁和对家的思念。

人生之幸事乃得些许挚友。友如文静，黎明前的黑暗中，互相鼓励；友如馨蔚，虽为新交亦相谈甚欢，引为知己。成康，谢谢你在气相实验反应条件摸索阶段提供的无私帮助。富强，非常感谢你在生活习惯上包容。感谢Biopharm的海丽，宴娜，飞龙，伟栾师姐，丹丹师姐，一楠师姐和菱蕾，谢谢你们这几年组织的美食和那些共度的欢乐时光。此外，还有诸多在乌特勒支大学认识的朋友们，李梦，小于，韦萱，陈婧，广贤，翟鹏，子丹，李婧，陈建明，文涛师兄，郎一飞，玉玺，子丹，曾慧 玉茹... ..得友如此，人生无憾矣！

人生就像一场公路旅行，有人上车有人离去。曾经的室友，邻居及好友或回国，或搬去了其他地方亦或留在乌村继续探索科学的奥妙。我也即将要离开这个充满了回忆的地方。物理距离虽然陡然增长，但是心的距离却不会因此而消退。我亲爱的朋友们，感谢你们在这几年里带给我陪伴和感动。无论你们现在身在何方，都衷心祝愿你们在以后生活中心想事成，事业有成！

在此，我也想衷心的感谢我的硕士导师何占航教授和实验室的同门们，在我申请读博时全力支持，在读博过程中关心问候；林林，硕越，谢谢你们千里迢迢从弗莱堡飞来作为家人代表参加我的答辩，这些情谊我会永远放在心底。

感谢老爸老妈小姨三叔在这几年来对我的支持，你们是最坚强的后盾。谢谢哥哥嫂子们对父母的悉心照顾，让我可以毫无后顾之忧的追寻我自己的梦想。

娄博士，感谢这五年来有你并肩同行，共品博士生活的酸甜苦辣，余生愿做你身边的一株木棉，一起迎接未来的风霜、雾霭、流岚和虹霓！

Thank you all for everything! My beloved colleagues and friends, I wish all the best to your future!

Curriculum Vitae

Fang Liu was born on July 15, 1988 in Henan, China. After finishing high school in 2006, she began her undergraduate studies in Chemistry at Henan Normal University, China. From 2010 till 2013, she was studying Inorganic Chemistry and earned her Master degree at Zhengzhou University under the supervision of Prof. Zhan-Hang He. Her master project was a collaboration with the Institute of Medicine of Zhengzhou University, China, and entitled “Preparation and Properties of Silver-based Nanomaterials for Biological and Environmental Applications”. Afterwards she moved to the Netherlands and carried out her PhD research in the Inorganic Chemistry and Catalysis group of the Debye Institute of Nanomaterials Science of Utrecht University, under the supervision of Prof. dr. ir. Bert M. Weckhuysen and Prof. dr. Pieter C.A. Bruijninx. Her research on “Support Stability and Strong Metal-Support Effects in Catalysis: From Nanoparticles to Single Atoms” is described in this PhD thesis.

